WERKZEUGMASCHINEN
WERKZEUGMASCHINEN

ERGEBNISSE AUS DER PRODUKTIONSTECHNIK

This thesis provides a framework of efficient experimental and analytical substructuring methods for the reliable prediction of spindle-holder-tool assembly dynamics. Specifically, the prediction of the tool tip Frequency Response Functions (FRFs) as well as the tool tip-Spindle Integrated Displacement Sensors (SIDS) transfer functions for a main spindle equipped with contactless displacement sensors. Here, the holder-tool assembly is modelled analytically whereas the spindle substructure is modelled experimentally.

For achieving high-quality experimental response models, three important aspects are researched. Firstly, strategies for measurement of displacement-to-force compliances are systematically compared and assessed. Secondly, two new methods for the identification of rotational compliances are proposed based on a modal parameter approach and commercially available rotational accelerometers. Thirdly, an experimental method for obtaining the interface flange-SIDS transfer function matrix and corresponding measurement uncertainty is developed and validated. This is required for prediction the tool tip-SIDS transfer function along with propagated uncertainty bounds.

A significant challenge in the analytical response modelling of holder-tool assemblies is that features like joint parameters cannot practically be modeled a priori and require additional reference measurements for their parametrization. This thesis proposes an extended tool model updating approach, where FRFs of the holder-tool assembly measured in an offline, freely constrained state are used for feature parameterization. Using this approach, a priori unknown parameters like joint stiffness and effective diameter of the fluted segment are reliably identified and validated for several different holder-tool assemblies. Furthermore, methods for the accurate beam modelling of various holder features such as balancing holes, tapered segment and holder-inserted tool segment were developed, analyzed and systematically validated.

Another valuable contribution of this thesis is demonstrating the utility of the predicted tool tip and tool tip-SIDS FRFs for estimating process forces and virtual workpiece quality. In this regard, the practical integration of the developed substructuring methods with an existing virtual quality framework is presented and successfully implemented to estimate process forces and workpiece quality for different milling operations and tool assemblies.

ISBN 978-3-98555-160-6

Substructuring Methods for Efficient Prediction of Spindle-Holder-Tool Assembly Dynamics

Prateek Chavan

Prateek Chavan

Substructuring Methods for Efficient Prediction of Spindle-Holder-Tool Assembly Dynamics

WZL | RWTH AACHEN UNIVERSITY

Fraunhofer IPT

Edition Wissenschaft Apprimus

Substructuring Methods for Efficient Prediction of Spindle-Holder-Tool Assembly Dynamics

Substrukturierungsmethoden zur effizienten Prognose der Spindel-Halter-Werkzeug-Dynamik

Von der Fakultät für Maschinenwesen
der Rheinisch-Westfälischen Technischen Hochschule Aachen
zur Erlangung des akademischen Grades eines
Doktors der Ingenieurwissenschaften
genehmigte Dissertation

vorgelegt von

Prateek Satish Chavan

Berichter/in:

Univ.-Prof. Dr.-Ing. Christian Brecher
Univ.-Prof. Dr.-Ing. Kai-Uwe Schröder

Tag der mündlichen Prüfung: 01. März 2023

ERGEBNISSE AUS DER PRODUKTIONSTECHNIK

Prateek Chavan

Substructuring Methods for Efficient Prediction of Spindle-Holder-Tool Assembly Dynamics

Herausgeber:
Prof. Dr.-Ing. T. Bergs
Prof. Dr.-Ing. Dipl.-Wirt. Ing. G. Schuh
Prof. Dr.-Ing. C. Brecher
Prof. Dr.-Ing. R. H. Schmitt

Band 18/2023

Bibliografische Information der Deutschen Nationalbibliothek
Die Deutsche Nationalbibliothek verzeichnet diese Publikation in der Deutschen Nationalbibliografie; detaillierte bibliografische Daten sind im Internet über https://portal.dnb.de abrufbar.

Prateek Chavan:

Substructuring Methods for Efficient Prediction of Spindle-Holder-Tool Assembly Dynamics

1. Auflage, 2023

Gedruckt auf holz- und säurefreiem Papier, 100% chlorfrei gebleicht.

Wissenschaftsverlag des Instituts für Industriekommunikation und Fachmedien
an der RWTH Aachen
Steinbachstr. 25, 52074 Aachen
Internet: www.apprimus-verlag.de, E-Mail: info@apprimus-verlag.de

Printed in Germany

ISBN 978-3-98555-160-6

D 82 (Diss. RWTH Aachen University, 2023)

Vorwort

Die vorliegende Arbeit entstand während meiner Zeit als wissenschaftlicher Mitarbeiter am Werkzeugmaschinenlabor (WZL) der RWTH Aachen.

Meinem Doktorvater Herrn Prof. Dr.-Ing. Christian Brecher gilt mein besonderer Dank für die Betreuung dieser Arbeit. Sein Vertrauen sowie die fachlichen Diskussionen waren immer Ansporn und haben wesentlich zum Gelingen dieser Arbeit beigetragen. Ebenso bedanke ich mich bei Herrn Prof. Dr.-Ing. Kai-Uwe Schröder für die Übernahme des Koreferats, die kritische Durchsicht meiner Arbeit sowie die wertvollen Anmerkungen. Herrn Prof. Dr.-Ing. Georg Jacobs danke ich für die Übernahme des Vorsitzes in meinem Promotionsverfahren.

Mein Dank gilt allen Mitarbeitern des Werkzeugmaschinenlabors, die mich in den letzten Jahren trotz anfänglicher Sprachschwierigkeiten herzlich aufgenommen und unterstützt haben. Dies gilt besonders für meine ehemaligen Oberingenieure Herr Dr. Marcel Fey, Herr Stephan Neus sowie Herr Dr. Alexander Epple. Ohne Eure Hilfsbereitschaft und die konstruktiven Diskussionen wäre diese Arbeit so nicht möglich gewesen. Auch Herrn Dr. Birk Brockmann möchte ich für seine stetige Motivation während meiner Promotion danken. Für die langjährige freundliche Zusammenarbeit danke ich meinen ehemaligen Kollegen Herrn Robert Spierling, Herrn Dr. Frederik Wellmann, Herrn Dr. Simo Schmidt, Herrn Dr. Alexander Hassis und Herrn Dr. Tobias Motschke. Für die tatkräftige Unterstützung bei der Durchführung zahlreicher experimenteller Untersuchungen sowie für die Einspannung von unzähligen Fräswerkzeugen bedanke ich mich bei Herrn Karsten Meier, Herrn Axel Kaunzner und Herrn Johannes Windelen. Ein besonderer Dank geht an Herrn Anton Strachkov, Herrn Matthäus Loba und Herrn Marian Wiesch für ihre Unterstützung bei der Durchführung und Auswertung von Messungen mit spindelintegrierten Wegsensoren.

Während meiner Zeit am Lehrstuhl haben mich zahlreiche Studierende und Auszubildende begleitet. Für deren unermüdlichen Einsatz möchte ich mich bei Herrn Alexander Steinert, Herrn Janis Ochel, Herrn Robert Meyer, Frau Lisa Larsen, Herrn Matthäus Loba, Frau Franziska Plum, Herrn Lennard Vorwerk-Handing, Herrn Nico Lange und Herrn Florian Wulff bedanken. Es macht mich stolz, dass die meisten meiner studentischen Hilfskräfte und Abschlussarbeiter als wissenschaftliche Mitarbeiter zu meinen Kollegen am Lehrstuhl wurden.

Der Deutschen Forschungsgemeinschaft (DFG) danke ich für die finanzielle Unterstützung des Projekts „Experimentelle Substrukturkopplung zur Schwingungsanalyse in Werkzeugmaschinen“ (GZ: BR 2905/55-2), auf dessen Ergebnissen diese Arbeit im Wesentlichen basiert.

Für die sorgfältige und akribische Korrektur dieser Arbeit bedanke ich mich bei Herrn Dr. Alexander Hassis, Herrn Alex Steinert und Herrn Matthäus Loba.

Ein liebevoller Dank gebührt meinen Eltern Kavita und Satish Chavan für die uneingeschränkte Unterstützung in jeglichen Lebenslagen und für ihre Hingabe, mit der sie mir meine Ausbildung ermöglicht haben. Auch meiner Schwester Pallavi danke ich für den stetigen Rückhalt.

Schließlich danke ich zutiefst meiner Frau Saskia für ihr Verständnis und ihre Geduld an den langen Arbeitstagen und vielen Wochenenden, die ich dieser Arbeit gewidmet habe. Ohne Deinen Rückhalt und Deine Aufmunterung wäre diese Arbeit nicht möglich gewesen.

Bruchsal, im Mai 2023 Prateek Satish Chavan

Brief Summary

This thesis provides a framework of efficient experimental and analytical substructuring methods for the reliable prediction of spindle-holder-tool assembly dynamics. Specifically, this implies the prediction of the tool tip Frequency Response Functions (FRFs) as well as the tool tip-Spindle Integrated Displacement Sensors (SIDS) transfer functions for a main spindle equipped with contactless displacement sensors. Here, the holder-tool assembly is modelled analytically whereas the spindle substructure is modelled experimentally. The knowledge of the spindle-holder-tool assembly dynamics is indispensable for a variety of applications such as prediction of stability behavior, process forces, tool deflection during cutting as well as virtual surface quality.

For achieving high-quality experimental response models, three important aspects are researched. Firstly, strategies for measurement of displacement-to-force compliances are systematically compared and assessed. Secondly, two new methods for the identification of rotational compliances are proposed based on a modal parameter approach and commercially available rotational accelerometers. Thirdly, an experimental method for obtaining the interface flange-SIDS transfer function matrix and corresponding measurement uncertainty is developed and validated. This is required for prediction the tool tip-SIDS transfer function along with propagated uncertainty bounds.

A significant challenge in the analytical response modelling of holder-tool assemblies is that certain features like joint parameters cannot practically be modeled a priori and require additional reference measurements for their parametrization. Instead of using FRFs of the tool clamped in the machine spindle, this thesis utilizes the measurement of reference FRFs in an offline, freely constrained state of the tool assembly. A precise feature parameterization is made possible by the developed extended tool model updating approach. Using this approach, a priori unknown parameters like joint stiffness and effective diameter of the fluted segment are reliably parameterized and validated for several different holder-tool assemblies in a completely offline manner. Furthermore, methods for the accurate beam modelling of various holder features such as balancing holes, tapered segment and holder-inserted tool segment were developed, analyzed and systematically validated.

Another valuable contribution of this thesis is demonstrating the utility of the predicted tool tip and tool tip-SIDS FRFs for estimating process forces and virtual workpiece quality. In this regard, the practical integration of the developed substructuring methods with an existing virtual quality framework is presented and successfully implemented to estimate process forces and workpiece quality for different milling operations and tool assemblies.

Kurzzusammenfassung

Die vorliegende Dissertationsschrift stellt effiziente experimentelle und analytische Substrukturierungsmethoden für die zuverlässige Vorhersage der Dynamik von Spindel-Halter-Werkzeug-Baugruppen bereit. Konkret werden der Nachgiebigkeitsfrequenzgänge (engl.: Frequency Response Functions, FRFs) an der Werkzeugspitze sowie Übertragungsfunktionen zwischen Werkzeugspitze und spindelintegrierten Verlagerungssensoren (engl.: Spindle Integrated Displacement Sensors, SIDS) prognostiziert. Dabei wird die Halter-Werkzeug-Baugruppe analytisch modelliert, während die Spindel-Substruktur experimentell abgebildet wird. Die effiziente Vorhersage der Spindel-Halter-Werkzeug-Dynamik bildet die Grundlage für eine Vielzahl an Berechnungen wie die Vorhersage des Stabilitätsverhaltens, der Prozesskräfte sowie der virtuellen Oberflächenqualität.

Zur Erzielung qualitativ hochwertiger experimenteller Response-Modelle werden drei zentrale Aspekte erforscht. Als Erstes werden Strategien zur Messung von translatorischen Nachgiebigkeiten systematisch verglichen und methodisch bewertet. Zweitens werden zwei neue Methoden zur Identifikation von rotatorischen Nachgiebigkeiten erarbeitet, die auf einer modalen Umrechnung und auf Rotationsbeschleunigungsmessungen basieren. Drittens wird eine Mess- und Auswertungsmethode zur Ermittlung der Matrix der Werkzeugschnittstelle-SIDS-Übertragungsfunktion unter Berücksichtigung von Messunsicherheiten vorgestellt und validiert. Dies ist für die Vorhersage der Werkzeugspitze-SIDS-Übertragungsfunktion mit entsprechenden Konfidenzintervallen erforderlich.

Eine wesentliche Herausforderung bei der analytischen Response-Modellierung von Halter-Werkzeug-Baugruppen besteht darin, dass bestimmte Eigenschaften (z. B. Fügestellenparameter) a priori praktisch nicht modelliert werden können und somit zusätzliche Referenzmessungen für ihre Parametrisierung erfordern. In dieser Arbeit werden solche Referenzmessungen in Form von FRFs nicht am eingebauten Werkzeug, sondern offline im frei eingespannten Zustand gemessen. Der erarbeitete und validierte Ansatz des Modelabgleichs mit erweitertem Werkzeug ermöglicht eine präzise Identifikation der a priori unbekannten Eigenschaften im nicht-eingebauten Zustand. Darüber hinaus werden Ansätze für die genaue Modellierung verschiedener Haltermerkmale wie Wuchtbohrungen, eine Kegelgeometrie sowie eingespannte Werkzeugsegmente entwickelt, analysiert und systematisch validiert.

Ein bedeutender Beitrag dieser Arbeit ist die Darstellung des Nutzens der vorhergesagten Werkzeug- und Werkzeug-SIDS-FRFs zur Ermittlung der Prozesskräfte und der virtuellen Werkstückqualität. In diesem Zusammenhang wird die praktische Integration der entwickelten Substrukturierungsmethoden in bestehenden Ansätzen zur Ermittlung der virtuellen Qualität vorgestellt und erfolgreich validiert.

Table of Contents

Inhaltsverzeichnis

Formula Symbols and Abbreviations

Formelzeichen und Abkürzungsverzeichnis

Uppercase letters

Großbuchstaben

Identifier	Unit	Description
A	m^2	Area
A_c	mm^2	Cross-section area of undeformed chip
A_r	-	Scaling factor for modal mass of r^{th} mode
$\boldsymbol{B}$	-	Signed Boolean matrix
$\boldsymbol{C}$	Ns/m	Viscous damping matrix
E	Pa	Youngs modulus
F_a	N	Axial cutting force
F_c	N	Cutting force
F_{dyn}	N	Dynamic cutting force component
F_{ext}	N	Excitation force
$F_{i,j}$	N	Force acting in i^{th} direction of the j^{th} cutting edge
F_q	N	Force in q^{th} DOF or at q^{th} coordinate
F_r	N	Radial cutting force
F_{rel}	N	Relative Force
F_{stat}	N	Static cutting force component
F_t	N	Tangential cutting force
F_{abs}^{T}	N	Absolute force acting on tool
F_{abs}^{W}	N	Absolute force acting on workpiece
G	Pa	Shear modulus
$\boldsymbol{G}_g$	var.	Oriented compliance matrix
$\boldsymbol{G}_{ij}^{k}$	var.	Compliance matrix between DOFs *j* and *i* of structure *k*
H	µm/N	Displacement-to-force FRF
$H_{xx,abs}$	µm/N	FRF from absolute displacement and absolute excitation in x-direction
$H_{xx,a/r}$	µm/N	FRF from absolute displacement and relative excitation in x-direction

$H_{xx,rel}$	µm/N	FRF from relative displacement and relative excitation in x-direction
$H^{2abs}_{xx,abs}$	µm/N	Two times absolute FRF in x-direction based on absolute FRFs
$H^{2abs}_{xx,a/r}$	µm/N	Two times absolute FRF in x-direction based on absolute FRFs from relative excitation
I	m^4	Area moment of inertia
I_{eq}	m^4	Equivalent area moment of inertia
J	kgm^2	Rotational inertia
$\boldsymbol{K}$	N/m	Stiffness matrix
L	mm	Length of beam
L	µm/Nm	Displacement-to-moment FRF
L_o	mm	Overhang length
LB_{amp}	var.	Lower bound of confidence interval on amplitude
LB_{pha}	rad	Lower bound of confidence interval on phase
LR	var.	Lower residual
M_z	Nm	Moment about z
$\widehat{M}_r$	kg	Modal mass of r^{th} mode
$\boldsymbol{M}$	kg	Mass matrix
N	rad/N	Rotation-to-force FRF
N_b	-	Number of measurement blocks
P	rad/Nm	Rotation-to-moment FRF
Q	var.	Excitation vector at an unassembled substructure coordinate
$\boldsymbol{R}$	var.	Residue matrix
S	mm	Distance between impact locations
U	var.	Vector of deflections at an assembled structure coordinate
UB_{amp}	var.	Upper bound of confidence interval on amplitude
UB_{pha}	rad	Upper bound of confidence interval on phase
UR	var.	Upper residual
V	m	Transverse beam deflection (function of x)
W_i^{abs}	-	Weightage on amplitude error of i^{th} mode

W_i^f	-	Weightage on frequency error of i^{th} mode
$\boldsymbol{Y}$	var.	Compliance matrix of uncoupled system
$\boldsymbol{Y}^i$	var.	Compliance matrix of i^{th} structure
Z	-	Standard normal variable

Lowercase letters

Kleinbuchstaben

a_e	mm	Axial depth of cut
a_p	mm	Radial depth of cut
a_r	-	Dimensionless frequency number of r^{th} mode
b	mm	Uncut chip width
b_r	-	Dimensionless frequency number of r^{th} mode
c_{xf}	Ns/m	Translational damping
$c_{\theta M}$	Nms/rad	Rotational damping
d	mm	Distance between impact locations
d_{cc}	mm	Diameter cooling channel
d_{eff}	mm	Effective diameter
d_h	mm	Depth of unbalance hole
d_{out}	mm	Outer diameter
d_s	mm	Shank diameter
f_s	Hz	Sampling frequency
f_i	Hz	Eigenfrequency of i^{th} mode
f_i^m	Hz	Measured eigenfrequency of i^{th} mode
f_n	Hz	Spindle speed in Hz
f_t	Hz	Tooth meshing frequency
f_z	mm	Feed per tooth
h	mm	Undeformed chip thickness
h_d	mm	Depth of balancing hole
j	-	Imaginary unit
k_c	N/mm^2	Specific cutting force
k_{qc}	N/mm^2	Specific cutting force in q^{th} direction
k_{qe}	N/mm	Edge force coefficient in q^{th} direction

k_{xf}	N/m	Translational stiffness
$k´$	-	Shear coefficient
$k_{\theta M}$	Nm/rad	Rotational stiffness
m	kg	Mass of accelerometer
m_{eq}	kg	Equivalent mass
m_c	-	KIENZLE exponent
n	min^{-1}	Spindle speed
p_k	rad/s	k^{th} complex pole
p_k^*	rad/s	k^{th} complex conjugate pole
q	var.	Excitation vector at an unassembled substructure coordinate
t	s	Time
u	var.	Vector of deflections at an unassembled substructure coordinate
v_f	mm/min	Feed velocity
v	m	Transverse beam deflection (function of x and t)
x	m	Displacement in x-direction
x_{rel}	m	Relative displacement in x-direction
x_{abs}^T	m	Absolute displacement of tool in x-direction
x_{abs}^W	m	Absolute displacement of workpiece in x-direction
$\dot{x}$	m/s	Velocity in x-direction
$\ddot{x}$	m/s^2	Acceleration in x-direction
y	m	Displacement in y-direction
y_{act}	m	Actual TCP position in y-direction
y_{corr}	m	Corrected TCP position in y-direction
y_{dyn}	m	Dynamic TCP deflection in y-direction
y_{stat}	m	Static TCP deflection in y-direction

Greek Letters

Griechische Buchstaben

α_{pq}^r	var.	FRF between DOFs p and q with mass at DOF r
β	°	Helix angle

$\mathbf{\Gamma}$	-	Transformation matrix
Δ	var.	Operator for confidence interval
θ_Z	rad	Rotation about z
ξ	-	Structural damping loss factor
ρ	kg/m^2	Density
ρ_{eq}	kg/m^2	Equivalent density
σ_{ImH}	µm/N	Uncertainty of imaginary part of *H*-term
σ_{ReH}	µm/N	Uncertainty of real part of *H*-term
$\Phi_{i,j}$	var.	Modal vector in i^{th} direction of j^{th} node
ϕ_j	rad	Angular position of j^{th} cutting edge
ψ	rad	Angular deflection of beam
ω	rad/s	Angular velocity

Abbreviations

Abkürzungen

ANN	Artificial Neural Networks
ARM	Analytical Response Model
CAD	Computer-Aided Design
CMS	Component Mode Synthesis
DFG	Deutsche Forschungsgemeinschaft
DOF	Degree Of Freedom
EBB	EULER-BERNOULLI Beam
EBBM	EULER-BERNOULLI Beam Model
ERM	Experimental Response Models
ETMU	Extended Tool Model Updating Approach
FBS	Frequency Based Substructuring
FEM	Finite Element Method
FFT	Fast FOURIER Transformation
FRF	Frequency Response Function
HSK	Hohlschaftkegel (German)
IBS	Impulse Based Substructuring
IRF	Impulse Response Function

LM	LAGRANGE Multiplier
LSCF	Least Squares Complex Frequency
LSFD	Least Squares Frequency Domain
LVDT	Linear Variable Differential Transducer
MCT A	Machine Tool A
MCT B	Machine Tool B
MIMO	Multiple Input Multiple Output
MPC	Multi-Point Constraint
NC	Numeric Control
NVH	Noise Vibration Harshness
PDE	Partial Differential Equation
PVC	Polyvinyl Chloride
RCSA	Receptance Coupling Substructuring Analysis
SDE	Spring-Damper Element
SDOF	Single Degree of Freedom
SIDS	Spindle Integrated Displacement Sensors
SIFS	Spindle Integrated Piezoelectric Force Sensors
SIMO	Single Input Multiple Output
SISO	Single Input Single Output
SNR	Signal-to-Noise Ratio
STL	Stereolithography
TB	TIMOSHENKO Beam
TBM	TIMOSHENKO Beam Model
TCP	Tool Center Point
vCMM	Virtual Coordinate Measurement Machine
WQM	Workpiece Quality Monitoring
WZL	Werkzeugmaschinenlabor (German)
2D	Two-dimensional
3D	Three-dimensional

1 Introduction

The oriented Frequency Response Function (FRF) between the workpiece and tool of a milling machine significantly determines the allowable material removal rate without instability, surface quality as well as achievable form accuracy [BREC17a]. This dynamic behavior is further determined by the compliance behavior of all components and joints of the machine lying within the force flux. This includes the milling tool assembly, main spindle, machine column and bed, feed drives, workpiece table, workpiece itself, etc. Among these elements, the milling tool is frequently changed as per cutting requirements, thereby changing the dynamic behavior with each variation of tool dimensions. Figure 1.1 illustrates the influence of different tool assemblies on the vibration behavior at the tool tip. Despite a significant structural influence, several industries require a variety of milling tool assemblies to meet the growing demands of flexibility. Especially in the case of tool and die manufacturers, where milling represents 47 % of the manufacturing processes and requires up to 450 different milling tools [BOOS18]. Since the measurement of the tool tip dynamics for each combination of tool and machine spindle is not feasible, there is a strong motivation for its efficient prediction. With the prediction of the tool tip dynamics, an inference about the response to external excitation as well as stability behavior can be achieved.

Another motivating aspect is the growing research and industrial interest in the integration of various sensors in the main spindle for the estimation of milling forces, tool life and process condition, among others [ABEL10; CAO17]. In [BREC18b; BREC19c], an arrangement of Spindle Integrated Displacement Sensors (SIDS) was proposed, such that axial, radial and rotational deflections of a shaft mounted disc could be measured. The corresponding deflections were utilized for the estimation of milling forces and combined with a model-based material removal simulation, such that, a process parallel prediction of the milled surface quality could be achieved. However, the force estimation requires the knowledge of the tool tip-to-SIDS transfer function for each tool assembly. This further underlines the need for the efficient prediction of the spindle-holder-tool assembly dynamics.

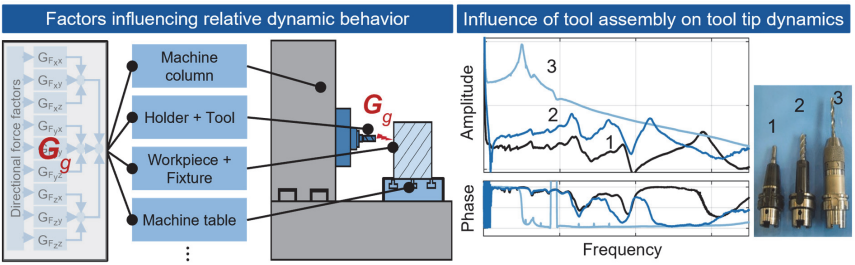

Figure 1.1 Tool dynamics as a factor influencing the dynamic behavior of a machine tool

Experimental-analytical dynamic substructuring offers a possibility for efficiently predicting the dynamic behavior of different combinations of the spindle-holder-tool as-

semblies. Here, the compliance behavior of each machine at the spindle-holder interface is determined experimentally while the dynamic behavior of the holder-tool assembly is modelled analytically. These behaviors are usually described in the frequency domain. Subsequently, with the application of mathematical boundary conditions at the interface, the analytical and the experimental models are coupled, such that the dynamic behavior at the tool tip of the spindle-holder-tool assembly can be predicted.

Although this tool coupling approach has gained research interest in the past decade, the industrial application is still limited by the challenges in the reliable analytical and experimental modelling. Some of the challenges regarding the experimental characterization of the spindle-holder interface include the difficulty in obtaining rotational compliances as well as choosing the appropriate measurement strategies given the variety of available actuator and sensor technologies. With respect to analytical modelling of the holder-tool assembly, the efficient and reliable identification of the properties of the holder-tool joint remains a major challenge. Furthermore, the extension of the tool coupling framework to include the SIDS, which can measure rotational deflections as well, has not been explored in literature.

Therefore, the focus of this thesis is on researching experimental and analytical modelling strategies for the reliable prediction of the tool tip FRF as well as the tool tip-SIDS transfer function for any combination of spindle-holder-tool assembly. In this thesis, only shaft mills and thermal shrink-fit holders are considered because of their importance in finishing operations and the presence of non-negligible holder-tool joint dynamics.

A further goal of this thesis is to demonstrate the utility of the predicted FRFs for the efficient estimation of process forces and monitoring of workpiece surface quality. In this regard, the SIDS deflections measured during the milling operation are evaluated with the predicted tool tip-SIDS transfer function to obtain an estimation of the process forces. The estimated forces are then used in combination with the predicted tool tip stiffness as well as a material removal simulation to allow a process parallel estimation of the milled surface quality.

The results presented in this thesis were achieved as part of the research project ‘Experimental substructure coupling for vibration analysis in machine tools’ (BR 2905/55-2) funded by the German Research Foundation (Deutsche Forschungsgemeinschaft, DFG). Part of the results have been published in: [BREC16a; BREC21; BREC22].

Einleitung

Das gerichtete Nachgiebigkeitsverhalten zwischen Werkstück und Werkzeug einer Fräsmaschine bestimmt maßgeblich das zulässige, stabile Zerspanvolumen, die Oberflächenqualität sowie die erreichbare Formgenauigkeit [BREC17a]. Dieses wird wiederum durch das Nachgiebigkeitsverhalten aller im Kraftfluss liegenden Bauteile und Fügestellen der Maschine bestimmt. Dazu gehören u. a. die Werkzeugbaugruppe, die Hauptspindel, der Maschinenständer, das Maschinenbett, die Vorschubantriebe, der Werkstücktisch sowie das Werkstück selbst. Von diesen Komponenten wird das Fräswerkzeug je nach Zerspanungsanforderung häufig gewechselt, wodurch sich das dynamische Verhalten auch ändert. Abbildung 1.1 veranschaulicht den Einfluss unterschiedlicher Werkzeugbaugruppen auf das Schwingungsverhalten an der Werkzeugspitze. Um den wachsenden Anforderungen an die Flexibilität gerecht zu werden, ist es für viele Branchen unvermeidbar, einen großen Bestand an verschiedenen Werkzeugbaugruppen zu unterhalten. Dies gilt insbesondere für den Werkzeug- und Formenbau, wo das Fräsen 47 % der Fertigungsprozesse darstellt und bis zu 450 verschiedene Fräswerkzeuge benötigt werden [BOOS18]. Da die Vermessung des Schwingungsverhaltens für jede Kombination von Werkzeug und Maschinenspindel nicht praktikabel ist, gibt es eine starke Motivation für ihre effiziente Vorhersage. Mit der Prognose der Werkzeugdynamik im eingespannten Zustand können Rückschlüsse über die Schwingungsantwort auf Selbst- und Fremderregungen gezogen werden.

Ein weiterer motivierender Aspekt ist das wachsende Interesse in Forschung und Industrie an der Integration verschiedener Sensoren in die Hauptspindel, u. a. zur Schätzung von Fräskräften, Werkzeugstandzeiten und Prozesszustand [ABEL10; CAO17]. In [BREC18b; BREC19c] wurde eine Anordnung von spindelintegrierten Wegsensoren (SIDS) vorgestellt, mit der axiale, radiale sowie rotatorische Auslenkungen einer wellenmontierten Scheibe gemessen werden können. Die entsprechenden Auslenkungen wurden zur Abschätzung der Fräskräfte herangezogen und mit einer modellbasierten Abtragsimulation kombiniert, sodass eine prozessbegleitende Vorhersage der gefrästen Oberflächenqualität erreicht werden konnte.

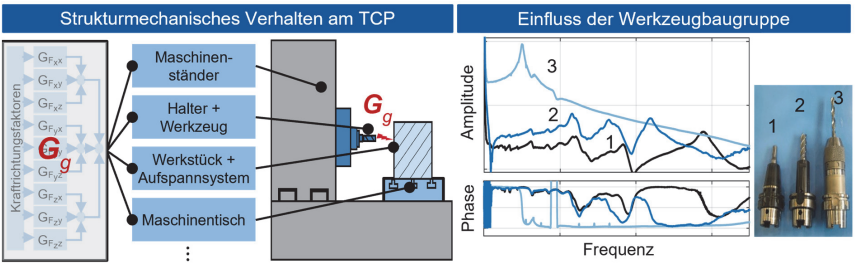

Abbildung 1.1 Einfluss verschiedener Werkzeuge auf das dynamische Maschinenverhalten

Die Kraftabschätzung erfordert allerdings die Kenntnis der Werkezug-SIDS Übertragungsfunktion für jede Werkzeugbaugruppe. Dies unterstreicht die Notwendigkeit einer effizienten Vorhersage der Dynamik der Spindel-Halter-Werkzeug-Baugruppe.

Die experimentell-analytische dynamische Substrukturierung bietet eine Möglichkeit zur effizienten Vorhersage des dynamischen Verhaltens verschiedener Kombinationen von Spindel-Halter-Werkzeug-Baugruppen. Dabei wird das Nachgiebigkeitsverhalten jeder Maschine an der Werkzeugschnittstelle experimentell bestimmt, während das dynamische Verhalten der Halter-Werkzeug-Baugruppe analytisch modelliert wird. Diese beiden Verhalten werden in der Regel im Frequenzbereich beschrieben. Anschließend werden die analytischen und die experimentellen Modelle durch die Anwendung mathematischer Randbedingungen gekoppelt, sodass das dynamische Verhalten an der Werkzeugspitze der Spindel-Halter-Werkzeug-Baugruppe vorhergesagt werden kann.

Obwohl dieser Ansatz der Werkzeugankopplung im letzten Jahrzehnt an Forschungsinteresse gewonnen hat, ist die industrielle Anwendung weiterhin durch die Herausforderungen bei der zuverlässigen analytischen und experimentellen Modellierung begrenzt. Zu den Herausforderungen bei der experimentellen Charakterisierung der Spindel-Halter-Schnittstelle gehören die Ermittlung der rotatorischen Nachgiebigkeit sowie die Wahl der geeigneten Messstrategien angesichts der Vielfalt der verfügbaren Aktor- und Sensortechnik. Bei der analytischen Modellierung der Halter-Werkzeug-Baugruppe bleibt die effiziente und zuverlässige Bestimmung der dynamischen Eigenschaften der resultierenden Fügestelle eine große Herausforderung. Darüber hinaus wurde die Erweiterung der Werkzeugankopplung um die SIDS, welche auch rotatorische Auslenkungen ermitteln können, in der Literatur noch nicht untersucht.

Daher liegt der Schwerpunkt dieser Arbeit auf der Erforschung experimenteller und analytischer Modellierungsstrategien zur zuverlässigen Vorhersage des Nachgiebigkeitsfrequenzgangs an der Werkzeugspitze sowie der Übertragungsfunktion zwischen Werkzeugspitze und SIDS für jede beliebige Kombination von Spindel-Halter-Werkzeug-Baugruppen. In dieser Arbeit werden nur Schaftfräser mit Schrumpffutter als Halter betrachtet, da sie für die Schlichtbearbeitung relevant sind und eine nicht zu vernachlässigende Dynamik der Halter-Werkzeug-Verbindung aufweisen.

Ein weiteres Ziel dieser Arbeit ist es, die Nützlichkeit der vorhergesagten Nachgiebigkeitsfrequenzgänge für die effiziente Abschätzung von Prozesskräften und die Überwachung der Oberflächenqualität von Werkstücken zu demonstrieren. Zu diesem Zweck werden die während des Fräsvorgangs gemessenen SIDS-Auslenkungen mit der vorhergesagten Übertragungsfunktion zwischen Werkzeugspitze und SIDS ausgewertet, um eine Schätzung der Prozesskräfte zu erhalten. Die geschätzten Kräfte werden dann in Kombination mit der vorhergesagten Werkzeugspitzensteifigkeit sowie einer Materialabtragsimulation verwendet, um eine prozessparallele Abschätzung der gefrästen Oberflächenqualität zu erzielen.

Die in dieser Arbeit vorgestellten Ergebnisse wurden im Forschungsprojekt "Experimentelle Substrukturkopplung zur Schwingungsanalyse in Werkzeugmaschinen" erarbeitet. Dieses Projekt wurde von der Deutschen Forschungsgemeinschaft gefördert (Projektzeichen BR 2905/55-2). Ein Teil der Ergebnisse wurde bereits in [BREC16a; BREC21; BREC22] veröffentlicht.

2 Literature Review

Stand der Forschung und Technik

This chapter aims to introduce the reader to the theoretical background regarding the subject matter of this thesis. In this context, methods for predicting process forces during milling are briefly explained along with current approaches for their experimental measurement and estimation (Section 2.1). Subsequently, it is necessary to understand the vibration behavior of structures and its modelling (Section 2.2). Here, the focus is on the continuous modelling of beam-like structures, as this approach is utilized for the modelling of milling tool assemblies in Chapter 5. A major part of the literature survey is devoted to the introduction and discussion of the concept of dynamic substructuring and its applications (Section 2.3 and 2.4). Among the applications, the problem of experimental-analytical tool coupling is discussed in greater detail so as to understand the latest trends and limitations of literature. Finally, the chapter is concluded by a summary of the deficits and research gaps in relevant, current literature (Section 2.5).

2.1 Process forces in milling

Prozesskräfte beim Fräsen

The milling process involves intermittent material removal using a rotating and defined cutting edge. Due to the combined rotation and feed velocity, the cutting edges trace a trochoidal path, such that each tooth creates a varying but periodic chip thickness. Figure 2.1 illustrates a half radial immersion, up milling operation with a four toothed cutter. The intermittent nature of cutter engagement is an important source of external excitation for the machine tool. Additionally, an unfavorable dynamic compliance between the tool and workpiece can result in significant modulation of the undeformed chip thickness, which can lead to the phenomenon of regenerative chatter. Thus, the prediction, measurement or estimation of milling forces is crucial for design of machine tools, for time-domain stability calculations, tool life estimation, process monitoring, surface quality predictions, etc.

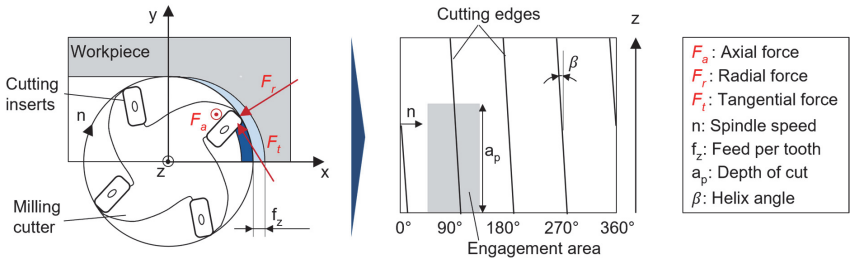

Figure 2.1 Sketch of half immersion up milling with the unwound cutter circumference
Skizze eines Halbtauchfräsens im Gegenlauf und der abgewickelte Fräsermantel

2.1.1 Prediction of milling forces

Prognose der Fräskräfte

In the pioneering work of F. W. TAYLOR from the early 20th century, a relation between cutting force (F_c) and the cross-section area of the chip (A_c) was identified [TAYL07; WALL08],

$$F_c = k_c \cdot A_c = k_c \cdot h \cdot b \tag{2.1}$$

where, k_c represents the empirically obtained specific cutting force, h is the undeformed chip thickness and b the uncut chip width. Subsequently, several authors investigated and improved upon the above relation. A significant improvement was proposed by KIENZLE in [KIEN52], where a more realistic, non-linear relation between the specific cutting force and undeformed chip thickness was identified from cutting trials,

$$k_c = k_{c1.1} \cdot h^{-m_c}. \tag{2.2}$$

Substituting in Eq. 2.1, the cutting force can be given as,

$$F_c = k_{c1.1} \cdot h^{1-m_c} \cdot b. \tag{2.3}$$

Here, $k_{c1.1}$ represents the cutting force for removing a chip of undeformed thickness and height of 1 mm, whereas m_c is a material constant. Although these values can be obtained from cutting trials with the required combination of workpiece and tool material, they are influenced by a verity of prevailing factors (rake angle, cutting speed, chip upsetting, etc.). Furthermore, the influencing factors themselves show varying degrees of interdependence. [DENK11]

The linearization of the KIENZLE equation (Eq. 2.2) enables the consideration of the specific cutting force (k_{qc}) as a constant, such that [ALTI12],

$$F_q = k_{qc} \cdot h \cdot b + k_{qe} \cdot b. \tag{2.4}$$

Here, q represents the direction of the force resolution. The edge coefficient k_{qe}, enables the consideration of the friction between the tool edge and the workpiece such that a non-zero friction force exists even when no shearing occurs ($h = 0$). For deriving the equations for milling forces, consider the half immersion up milling operation in Figure 2.1. Here, only a single tooth is in contact with the workpiece at any point of time. The characteristic variation of the chip thickness with the angle of tool rotation is approximated as,

$$h(\phi) = f_z \cdot \sin(\phi). \tag{2.5}$$

The presence of a cutter helix angle ($\beta > 0$) allows for a smoother entry and exit of the cutting edge from the workpiece. To calculate the total force acting on the j^{th} cutting edge in the tangential, radial and axial directions, the linearized formulation from Eq. (2.4) is applied first to an infinitesimal axial segment dz of the cutting edge. The corresponding differential equations of the forces for the engagement angle of ϕ_j are as follows,

$$dF_{t,j}(\phi_j) = \left(k_{tc} \cdot h(\phi_j) + k_{te}\right) \cdot dz \tag{2.6}$$

$$dF_{r,j}(\phi_j) = \left(k_{rc} \cdot h(\phi_j) + k_{re}\right) \cdot dz \tag{2.7}$$

$$dF_{a,j}(\phi_j) = \left(k_{ac} \cdot h(\phi_j) + k_{ae}\right) \cdot dz. \tag{2.8}$$

The integration of the above equation along the depth of cut a_p gives the total cutting force at the corresponding cutting edge. This can be transformed to obtain the force acting at the Tool Center Point (TCP) in the tool coordinate system (see Figure 2.1),

$$F_{x,j}(\phi_j) = -F_{t,j} \cdot \cos(\phi_j) - F_{r,j} \cdot \sin(\phi_j) \tag{2.9}$$

$$F_{y,j}(\phi_j) = F_{t,j} \cdot \sin(\phi_j) - F_{r,j} \cdot \cos(\phi_j) \tag{2.10}$$

$$F_{z,j}(\phi_j) = F_{a,j}(\phi_j). \tag{2.11}$$

In case multiple teeth are involved simultaneously in cutting, their individual force components can be transformed to the tool coordinate system and added vectorially to obtain the total force acting at the TCP or tool tip. Now the prediction of the forces from Eq. (2.9) to (2.11) requires the knowledge of specific cutting forces or cutting coefficients k_{qc}, k_{qe}. These unknown coefficients are identified empirically using mainly two approaches: i) mechanistic identification, ii) orthogonal to oblique transformation [ALTI12].

In the widely used mechanistic identification, milling trials are conducted for the required tool-workpiece combination keeping constant radial immersion and depth of cut while the feed rates are varied [ALTI12]. The corresponding process forces per tool revolution are usually measured using a dynamometer. These are then averaged by the number of teeth and equated to the analytically obtained average force expression. The unknown coefficients are then identified using linear regression or other fitting strategies. Although this approach offers a convenient and simple identification of the coefficients, the validity of the values is limited to a narrow band of prevailing cutting conditions.

BUDAK et al. proposed the use of parameters obtained from orthogonal cutting trials such as shear stress, friction coefficient and shear angle for the evaluation of cutting coefficients of an oblique cut [BUDA96]. This enables the convenient use of orthogonal cutting database for the evaluation of generic oblique cutting coefficients. However, the assumptions of the orthogonal to oblique transformation make it difficult to apply to end mills with complex geometries.

Independent of the approach, the identification of cutting coefficients and the accurate prediction of milling forces remains challenging due to the underlying assumptions, approximations and uncertainties. This is especially valid for complex tool geometries and engagement conditions. Therefore, the experimental measurement of forces using dynamometers or estimation from sensor signals is more favorable in many situations.

2.1.2 Measurement / estimation of process forces

Experimentelle Ermittlung von Prozesskräften

The approaches for process parallel measurement of cutting forces can be broadly classified into direct and indirect approaches (Figure 2.2). The direct approach refers to the use of dynamometers within the force flux and in immediate proximity to the cutting processes. Thus, commercially available rotating [KIST19b] as well as stationary [KIST19a] dynamometers have been used in laboratory environment, mostly for measuring reference cutting forces [BUDA94; ALBR05; MILF05; SAAD18]. Their applicability in industrial practice is severely limited due to high procurement costs, reduced working space, and due to the modification of the dynamic behavior between workpiece and tool. Since the dynamometer is placed within the force flux, its intrinsic dynamics interacts with the machine dynamics, which can lead to a significant reduction of the measurable frequency bandwidth. For obtaining a usable measurement bandwidth, the compensation of the intrinsic dynamics of the dynamometer is unavoidable. For example, SCIPPA et al. suggest the use of a disturbance KALMAN filter for compensating the influence of the dynamometer dynamics from the force measurements [SCIP15]. Due to the above-mentioned difficulties, several works in literature strive to estimate process forces indirectly, based on additional structure-integrated sensors or using available sensors of the machine tool drive and control system.

Motor currents of the main spindle and servomotors have been commonly utilized in literature for estimating tangential and normal cutting forces [ALTI92; JEON02; BREC15; ASLA18]. The main advantage here is that cutting forces can be estimated independent of tool-workpiece combination and without additional sensors. However, considerable effort is required for modelling the feed-drive system, motor dynamics, friction behavior as well as filter tuning for compensating the structural vibration modes.

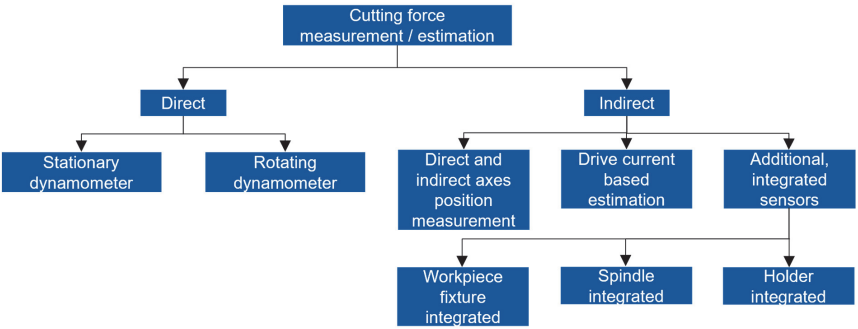

Figure 2.2 Broad classification of experimental methods for process force monitoring

Einordnung der experimentellen Methoden zur Überwachung der Prozesskräfte

An alternative is provided in [FEY16; XI21], where the difference between the direct (linear scale) and indirect measurement system (motor encoder) of the feed drive is used to predict the experienced axes loads. This method requires the measurement of

position and velocity dependent errors along with the position dependent stiffness of each feed drive. In contrast to motor current, the difference in position measurements show a nearly linear relation to axes force according to [XI21].

In literature, several additional sensors such as strain gauges, accelerometers, eddy-current and piezoelectric sensors have been considered for process force estimation. Apart from accelerometers, the additional sensors must be integrated within a machine structure to allow precise force estimation. The commonly used structures for integrating additional sensors are, tool holders [FRAU15; CHEN17; PRO-21], workpiece fixtures [MÖHR10] and main spindles [PARK02; ALBR05; DENK12; BREC18b; POST19].

A major focus in literature has been on researching spindle integrated vibration, force and displacement sensors for monitoring process forces, as can be seen in the number of review papers [MATS09; ABEL10; CAO17]. Unlike workpiece or holder integrated sensors, they are not limited to specific tool or workpiece dimensions. In addition, they do not significantly change the dynamic properties of the machine tool. A series of papers by PARK and ALTINTAS first proposed piezoelectric Spindle Integrated Force Sensors (SIFS) [PARK02; PARK04; ALTI04; PARK06], based on the concept of a 'force-ring' [HOFF99], for estimating milling forces. Here, piezoelectric force sensors are applied in the force flux at the bolting holes of the spindle flange, such that cutting forces cause a change in the preload of the piezoelectric sensors. Later, ALBRECHT et al. proposed a more cost effective and robust approach of using capacitive displacement sensors which measure the radial deflection of the spindle shaft relative to the housing [ALBR05]. Such a system can be termed as Spindle Integrated Displacement Sensors (SIDS). To further increase the industrial applicability, POSTEL et al. proposed the used of spindle mounted accelerometers for the estimation of both, tool tip deflection as well as cutting forces [POST19; POST20]. As part of a research project at the WZL, a special arrangement of non-contact SIDS was used to measure radial as well as axial displacements of a disc mounted on the spindle shaft during milling [BREC18b; BREC19c] (Figure 2.3a). The thermo-elastic shaft deflections measured by the SIDS were compensated using the novel approach from [FEY19]. With the information of axial displacements, the radial-axial cross compliance could be compensated, such that an accurate estimation of axial cutting forces was made possible.

The main disadvantage of using spindle integrated sensors is that they are located away from the generation of cutting forces and thus the dynamic behavior between the tool tip and sensor location must be compensated from the measurements. This implies that the tool tip to sensor transfer function is required for each holder-tool assembly. Even different overhang lengths of the same holder-tool assembly can significantly influence the transfer function. Since the measurement of the transfer function for each combination requires considerable effort, a method for its prediction is highly desirable. Once this transfer function is available from experiments or from predictions, a disturbance KALMAN filter [PARK02; ALBR05; POST19] or direct inversion method [BREC18b; BREC19c] (Figure 2.3b) can be applied to obtain the cutting forces.

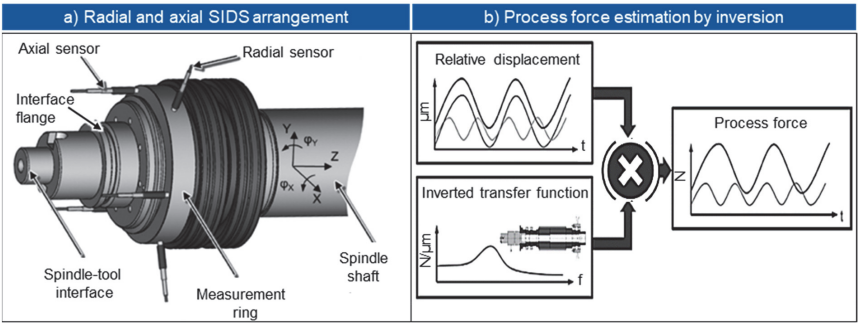

Figure 2.3 a) Arrangement of SIDS and b) method for process force estimation [BREC18b]
a) Anordnung von SIDS und b) Verfahren zur Kraftabschätzung [BREC18b]

To reduce the measurement effort for obtaining tool tip-sensor transfer functions, PARK et al. proposed using a substructuring approach for predicting the tool tip-SIFS transfer function for simulated end mills of different lengths [PARK06]. However, the transfer functions of end mills of the same diameter and for the same holder could be predicted. Additionally, the rotational compliances (displacement-to-moment) between the interface flange and sensor were assumed to be rigid due to the difficulties in measuring them. In [POST19], the system was divided into the holder-tool substructure and the spindle substructure with acceleration sensors. With such a substructuring formulation, the transfer function prediction is not limited to a specific holder-tool combination. Here as well, merely the translational transfer functions (displacement-to-force) between the interface flange and accelerometers were considered.

Due to the arrangement of three radial and three axial SIDS in [BREC18b; BREC19c], it is possible to not only measure the radial and axial deflections but also the rotational deflections of the spindle shaft about tangential directions (φ_X and φ_Y in Figure 2.3). This opens the possibility of considering rotational transfer functions between the interface flange and the SIDS in the substructuring calculations such that a more realistic prediction of the tool tip-SIDS transfer function may be achieved. The measurement and consideration of rotational transfer functions is not possible with previously proposed methods from literature.

Another important aspect to be considered in the application of spindle integrated sensors is that of measurement uncertainty and its propagation. Due to the spatial separation between the point of force application (tool tip, interface flange) and point of force or displacement measurement (SIDS, accelerometer, etc.), a poor Signal-to-Noise Ratio (SNR) can be expected. Although the disturbance KALMAN filter approach attenuates high frequency noise, the explicit quantification and propagation of measurement uncertainty through the tool coupling calculations has not been researched in literature.

2.2 Modelling of structural dynamics

Modellierung der Strukturdynamik

The time-varying displacement, velocity and acceleration response of a structure to dynamic loading can be termed as its dynamic behavior. The mathematical modelling of structural dynamics involves defining the degree of abstraction, listing of assumptions, creation of a visual depiction and finally deriving the corresponding differential equations of motion. The solution of these equation while considering the method of excitation then gives the resulting vibration or dynamic behavior. [CRAI06]

The mathematical model of the dynamic behavior is derived mainly based on the abstraction of the real structure as a discrete or continuous model.

2.2.1 Discrete models

Diskrete Modelle

A rigid, point mass with a single degree of freedom (SDOF) attached to the surroundings via a spring represents the simplest discrete, vibratory system. In some cases, simple machine structures can be approximated as distributed SDOF systems. In most cases, real machine tool structures are complex, three dimensional (3D) structures that cannot be modelled with sufficient accuracy using SDOF models. The Finite Element Method (FEM) is an established method in industrial and research practice for numerically approximating the static and dynamic behavior of continuous, linear structures. Essentially, the continuous structure is spatially discretized into a finite number of continuous elements, where each element is abstracted usually with linear or quadratic functions. This results in a mesh of elements connected to each other via nodes of varying degrees of freedom (DOFs). Based on the assigned material properties and the trial function of the element, the discretized mass ($\boldsymbol{M}$), stiffness ($\boldsymbol{K}$) and, if required, damping matrix ($\boldsymbol{C}$) of the entire structure can be obtained. Subsequently, the non-homogeneous Newtonian equation of motion can be solved to obtain the time response to a dynamic exciting force F_{ext},

$$\boldsymbol{M}\ddot{\mathrm{x}}(t) + \boldsymbol{C}\dot{\mathrm{x}}(t) + \boldsymbol{K}x(t) = F_{ext}(t). \tag{2.12}$$

Often, the dynamic characteristics of machine tools is evaluated based on the (undamped) eigenvalues and corresponding mode shape vectors. These are also derived from the above three system matrices by solving the undamped eigenvalue problem,

$$\left|-\boldsymbol{M}\omega^2 + \boldsymbol{K}\right| = 0. \tag{2.13}$$

In the case of general viscous damping, the damped eigenvalues and vectors can be calculated using a state space formulation of Eq. (2.12) [CRAI06]. The obtained modal parameters (eigenvalues and vectors) are the basis for the efficient calculation of nodal FRFs using modal superposition. For further details on the finite element analysis of structural vibrations, readers are referred to the following textbooks: [CRAI06; LINK14; GASC21].

2.2.2 Continuous models

Kontinuierliche Modelle

Mathematical models which describe the exact structure mechanical behavior (under certain assumptions) using analytical Partial Differential Equations (PDEs) are referred to as continuous models. However, setting up and solving the required system of equations is feasible merely for simple beam, shell and plate structures. In this thesis, the dynamic behavior of the holder-end mill assembly is represented using the back-to-back coupling of continuous beam elements (refer Chapter 5). Hence, this subsection focuses on providing a summary and relevant details about different continuous beam modelling approaches based on [HAN99; CRAI06; RAO06]. Here, the focus is on modelling the two-dimensional transverse vibrations using the following engineering beam theories: EULER-BERNOULLI and the TIMOSHENKO beam theory.

EULER-BERNOULLI Beam (EBB)

Consider the undeformed, linear elastic uniform beam shown in Figure 2.4a. Under transverse vibration, an arbitrary segment of the EULER-BERNOULLI beam (shaded) will deform as shown in Figure 2.4b. The shear forces and bending moments acting at both ends of the incremental segment are also illustrated. The transverse and rotational deflections of the segment are represented by v and ψ, respectively. The defining characteristic of the EBB is that a plane perpendicular to the neutral axis remains perpendicular during bending deformation as well. In addition, the rotational inertia associated with the rotation of the cross-section about the θ_z direction is assumed negligible compared to the translational inertia. The PDE of motion can be obtained by applying NEWTON'S second law to the illustrated beam segment,

$$\mathrm{EI}\frac{\partial^4 v(x,t)}{\partial x^4} + \rho \mathrm{A}\frac{\partial^2 v(x,t)}{\partial t^2} = 0. \tag{2.14}$$

Solving the above equation is more convenient by separating the spatial and temporal components by assuming the following general solution,

$$v(x,t) = V(x)\cdot\sin(\omega t). \tag{2.15}$$

Substituting the above relation in Eq. (2.14), and solving the fourth order PDE, the following general solution is achieved,

$$V(x)\cdot = \mathrm{C}_1\cdot\cos(\lambda\cdot x) + \mathrm{C}_2\cdot\sin(\lambda\cdot x) + \mathrm{C}_3\cdot\cosh(\lambda\cdot x) + \mathrm{C}_4\cdot\sinh(\lambda\cdot x) \tag{2.16}$$

Now, for substructuring calculations, the free vibration behavior (in terms of FRFs) at the ends of an EBB with unconstrained boundary conditions (free-free) is required. Applying such boundary conditions, the coefficients C_1, C_2, C_3 and C_4 can be found and the corresponding eigenvalue problem can be setup. BISHOP and JOHNSON presented a closed form solution for obtaining the direct and cross FRFs at the ends of an EBB for different boundary conditions without explicitly solving the eigenvalue problem [BISH55; BISH11]. This convenient approach has been widely used in literature for the frequency based substructure modelling of holder-tool assemblies as EBB. However, a key disadvantage of the EBB is the inherent overestimation of the eigenfrequencies

due to the ignorance of shear deformation and rotary inertia. Thus, the EBB provides a dynamically stiffer estimation, especially for thick beams and higher modes [ERTÜ06].

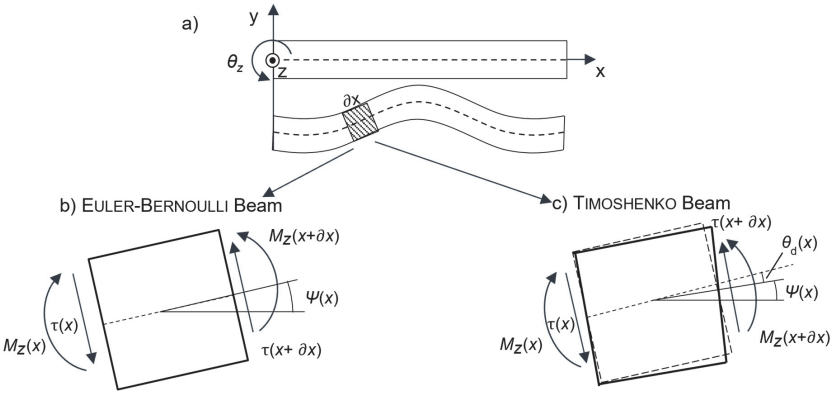

Figure 2.4 Sketches of beam segments under bending deformation
Skizzen von Balkensegmenten unter Biegeverformung

Several beam theories have been proposed to address the drawbacks of the EBB. For example, the RAYLEIGH beam proposes a slight improvement by considering the rotational inertia of the beam cross-section [STRU77]. However, this leads to only a marginal correction of the overestimation as the shear distortion is still ignored. The shear beam model adds the effect of shear distortion but without consideration of the rotational inertia. This is a considerable improvement especially for thick beams, where the shear effects are more dominant than the rotational effects [HAN99]. The PDEs of motion for these theories are listed in Table 2.1 along with the mathematical terms corresponding to each considered effect.

TIMOSHENKO Beam (TB)

In the landmark papers from 1921-22, TIMOSHENKO proposed a beam model which accounted, additionally to the EBB, for the rotational inertia effect as well as the shear dependent distortion due to bending [TIMO21; TIMO22]. Figure 2.4c shows an incremental segment of a TB under bending without time dependency for brevity. The slope at the end of the TB differs from that of the EBB by an angle θ_d such that planes normal to the neutral axis do not remain perpendicular during bending. Due to the consideration of shear, the TB model can accurately predict the eigenfrequencies and mode shapes compared to the EBB model. This is especially valid for non-slender beam and higher eigenfrequencies. The fourth order PDE of motion has two dependent variables v and ψ such that the non-homogenous equations of motion are given as follows,

$$\rho A \frac{\partial^2 v(x,t)}{\partial t^2} - k' GA \left(\frac{\partial^2 v(x,t)}{\partial x^2} - \frac{\partial \psi(x,t)}{\partial x} \right) = F_{ext}(x,t) \tag{2.17}$$

$$\rho I \frac{\partial^2 \psi(x,t)}{\partial t^2} - \frac{\partial^2 \psi(x,t)}{\partial x^2} - k' GA \left(\frac{\partial v(x,t)}{\partial x} - \psi(x,t) \right) = 0 \tag{2.18}$$

Now, the vibration behavior of the TB with free-free end conditions is of interest for the analytical modelling of tool assemblies. The setting up and solving of the eigenvalue problem is, however, much more complex here, due to the coupling of the transverse and rotational deflections. Thus, a closed form solution for obtaining the FRF matrix at the ends of a TB does not exist. In an important contribution, ARISTIZABAL-OCHOA proposed a classical formulation of the eigenvalue problem for TB such that the mode shapes and natural frequency could be derived for generalized end conditions [ARIS04]. This approach was first utilized by ERTÜRK for obtaining the compliance matrix at the ends of segments of the tool beam model [ERTÜ06] and is addressed in more detail in Section 5.2.

Table 2.1 PDEs of motion for different beam theories (summarized from [HAN99])
Bewegungsgleichungen diverse Balkentheorien (zusammengefasst aus [HAN99])

Beam models	PDE of motion	Transverse inertia	Bending	Shear deformation	Rotary inertia
EULER-BERNOULLI	$\rho A \frac{\partial^2 v(x,t)}{\partial t^2} + EI \frac{\partial^4 v(x,t)}{\partial x^4} = F_{ext}(x,t)$	✓	✓	✗	✗
RAYLEIGH	$\rho A \frac{\partial^2 v(x,t)}{\partial t^2} + EI \frac{\partial^4 v(x,t)}{\partial x^4} - \rho I \frac{\partial^4 v(x,t)}{\partial x^2 \partial t^2} = F_{ext}(x,t)$	✓	✓	✗	✓
Shear	$\rho A \frac{\partial^2 v(x,t)}{\partial t^2} - k' GA \left(\frac{\partial^2 v(x,t)}{\partial x^2} - \frac{\partial \psi(x,t)}{\partial x} \right) = F_{ext}(x,t)$ $\frac{\partial^2 \psi(x,t)}{\partial x^2} + k' GA \left(\frac{\partial v(x,t)}{\partial x} - \psi(x,t) \right) = 0$	✓	✓	✓	✗
TIMOSHENKO	$\rho A \frac{\partial^2 v(x,t)}{\partial t^2} - k' GA \left(\frac{\partial^2 v(x,t)}{\partial x^2} - \frac{\partial \psi(x,t)}{\partial x} \right) = F_{ext}(x,t)$ $\rho I \frac{\partial^2 \psi(x,t)}{\partial t^2} - \frac{\partial^2 \psi(x,t)}{\partial x^2} - k' GA \left(\frac{\partial v(x,t)}{\partial x} - \psi(x,t) \right) = 0$	✓	✓	✓	✓

2.3 Dynamic substructuring

Dynamische Substrukturierung

The paradigm of 'divide and conquer' or breaking down complex problems into smaller, easier problems is of fundamental importance in engineering sciences. The first applications of this paradigm in the field of structural dynamics began in the 1960s. Large aerospace structures were subdivided into smaller, unique structures and analyzed individually due to the prevailing limitations of computational capacities [PRZE63; CRAI68]. Subsequently, compatibility and force equilibrium conditions were applied to the interface between the substructures to obtain the behavior of the assembly. In the same decade, the approach of representing dynamic behavior using a selection of

mode shape vectors such as normal, rigid body, constraint and attachment modes was proposed and further developed in the 70s [GLAD64; RUBI75; CRAI77]. With this Component Mode Synthesis (CMS) approach, a considerable model reduction could be achieved as merely a combination of '*m*' mode shape vectors could describe relevant dynamic behavior instead of the nodal information of '*n*' DOFs of the discretized structure (where $m << n$). Thus, model reduction became an essential component of dynamic substructuring, especially, when large structural models were involved.

There was already an early interest in including experimentally obtained mode shapes within the framework of CMS for achieving a realistic modal basis [MACN71; KLOS71]. With improvements in experimental testing equipment as well as computing capabilities, first attempts were made in the 1980s at coupling experimental and analytical models using Frequency Based Substructuring (FBS) [CROW84]. Here, the research focus was mainly on the synthesis of FRFs of structures with simple modifications of lumped masses and stiffnesses. These initial approaches were impedance based, where the measured FRF matrix had to be inverted for the coupling calculations. JETMUNDSON et al. improved on the impedance based approaches by proposing a formulation that directly utilized the measured FRFs and did not require their inversion [JETM88].

An important developmental step in FBS was the dual reformulation of JETMUNDSON's approach by DE KLERK et al in [KLER06]. Here, LAGRANGE Multipliers (LM) serve to apply the force equilibrium at the interface nodes and a single signed Boolean matrix is required to define the coupling relationships. The resulting elegant reformulation was termed as LAGRANGE Multipliers Frequency Based Substructuring (LM FBS).

In recent years, efforts have been made to apply the experimental-analytical FBS methods to complex, real-world problems such as wind turbine dynamics [VOOR10; HAEU21], automotive NVH [SEIJ16] and machine tool dynamics (refer Section 2.4), among others. However, experimental substructuring still remains a challenge. The current challenges with respect to FBS in general and specific to its application in machine tools are discussed in Subsection 2.3.2 and Section 2.4 respectively.

2.3.1 Substructuring domains

Domänen der Substrukturierung

Although frequency based methods have gained popularity in the past decade, the dynamics of substructures can equally be described in physical, analytical, modal, state space and time domains. Figure 2.5 illustrates the different domains in which a substructure such as a beam can be represented along with the transformation methods between the domains. A brief introduction to each domain is provided in the following. For a more detailed description and formulations of each domain, the reader is referred to the review by DE KLERK in [KLER08b] as well as ALLEN et al. [ALLE20].

In the physical domain, the dynamics are expressed in terms of physical displacements of the structure (spatial description). This can be for both, discretized as well as continuous models. In case of complex, discretized structures, the mass, stiffness and

damping matrices are required for calculation of the nodal displacements. On the other hand, simple structures can often be abstracted and modelled as continuous beam or plate elements. Here, analytical PDEs must be solved with boundary conditions to obtain the continuous displacement field. Although continuous models are not extensively used in classical substructuring, the modelling of simple, beam-like structures as continuous analytical beams can be advantageous in many cases. Especially for quick and reliable estimations without the use of proprietary meshing software and algorithms, continuous models may be preferable. Substructures represented in the physical domain can easily be transformed to other domains without loss of information (except for model reduction through modal truncation).

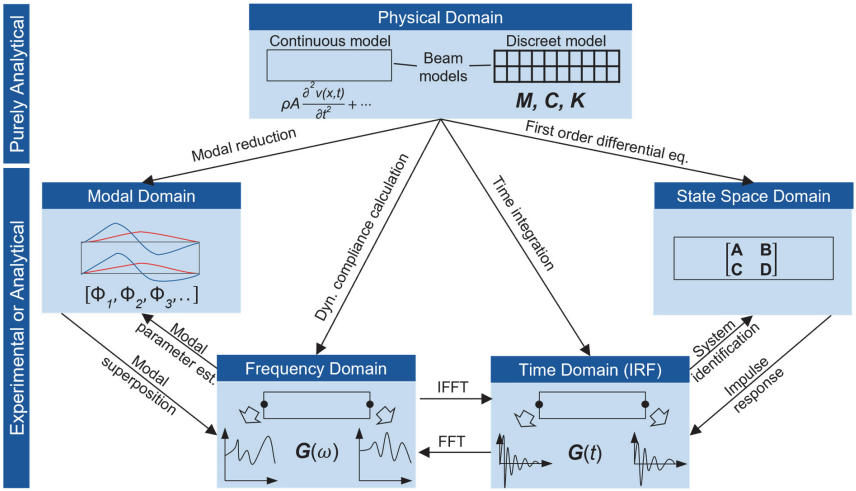

Figure 2.5 Domains of substructuring (based on [KLER08b; SEIJ16])

Domänen der Substrukturierung (angelehnt an [KLER08b; SEIJ16])

In the modal representation or CMS, substructure dynamics are expressed by a linear combination of mode shape vectors instead of nodal deflections. This inherently leads to a reduction of the problem as the number of modes considered is usually much smaller than number of DOFs of a discretized structure. Different CMS techniques utilize different types of mode shape vectors and consequently result in different reduction basis.

Frequency domain representation involves the description of structural behavior at discreet points and DOFs using frequency response functions. The harmonic response can be expressed in terms of dynamic stiffness or receptance. Since FRFs can be obtained experimentally with relatively low measurement effort, the coupling of experimentally and analytically derived models is convenient in the frequency domain. In this thesis, the experimentally obtained frequency based substructure models are termed as Experimental Response Models (ERMs), whereas the analytically (or numerically) obtained models are termed as Analytical Response Models (ARMs).

The time domain analogy of an FRF is the Impulse Response Function (IRF) and it captures the temporal vibration response to an impulse excitation. The corresponding Impulse Based Substructuring (IBS) technique using IRF was proposed in [RIXE10]. Although, experimental models can be obtained in this domain as well, the practical implementation of IBS is limited. This is mainly because the condition of ideal Dirac-impulse cannot be achieved experimentally with an impact hammer. In addition, noise on the measured signal leads to instabilities in the coupling results [RIXE11].

As an alternative to modal parameter estimation required for CMS techniques, SU and JUANG proposed the use of system identification methods for describing substructure dynamics [SU94]. Here the identified transfer functions are expressed as a state-space model with displacement and velocity as independent state variables. The advantages of the state-space formulation are: firstly, a vast number of system identification techniques from control theory can be applied and secondly, the handling of arbitrary viscous damping becomes convenient such that damped eigenvalues and eigenvectors can be easily calculated. However, practical implementation is limited due to unavoidable system identification procedures based on the input, output data (refer to the works of SJÖVALL and ABRAHAMSSON [SJÖV06; SJÖV07b; SJÖV07a; SJÖV08]).

For the problem of structural modification, both, the modified as well as unmodified structure must be described in the same domain, so that the interface compatibility and interface force equilibrium conditions can be applied. Ideally, one of the components should be described experimentally as experimental-analytical coupling provides a more realistic prediction of dynamics as long as accurate models are obtained. Out of all the domains, the frequency based coupling of analytical and experimental models has high industrial relevance because of the following advantages:

i) No system identification or modal parameter estimation from frequency response data is required.
ii) FRFs can be easily measured (in many cases) without significant equipment cost and effort.
iii) The transformation from physical to frequency domain is possible without truncating the influence of higher modes.
iv) Measured FRFs inherently contain influence of higher modes.

Despite the above advantages, the practical implementation of experimental-analytical FBS still has several challenges. These are discussed in the following subsection.

2.3.2 Challenges in experimental-analytical FBS

Herausforderungen bei der experimentellen-analytischen FBS

To illustrate the major challenges, an exemplary coupling problem shown in Figure 2.6 is discussed. Consider two plate-like substructures *Q* and *R* in the 3D space, which are to be coupled at their three interface nodes to give the assembly *S*. Here, *Q* represents a fixed-free structure whose dynamics is to be obtained experimentally. Whereas *R* represents a simulated structure who's unconstrained (free-free) dynamic behavior is required for the coupling calculation. The aim is to predict the driving point FRFs at

node or coordinate 4 of the assembly. The equation for coupling the two substructures at their interfaces using the LM FBS formulation [KLER06] is given as,

$$\boldsymbol{Y}^S = \boldsymbol{Y} - \boldsymbol{Y}\boldsymbol{B}^T\left(\boldsymbol{B}\boldsymbol{Y}\boldsymbol{B}^T\right)^{-1}\boldsymbol{B}\boldsymbol{Y}. \tag{2.19}$$

The coupling equation requires the experimental response model containing the compliance matrix of measured, direct and cross-FRFs at interface nodes ($\boldsymbol{Y}^Q$). Also, the analytical response model containing the compliance matrix of simulated direct and cross-FRFs at the coordinates of R, $\boldsymbol{Y}^R$ is required.

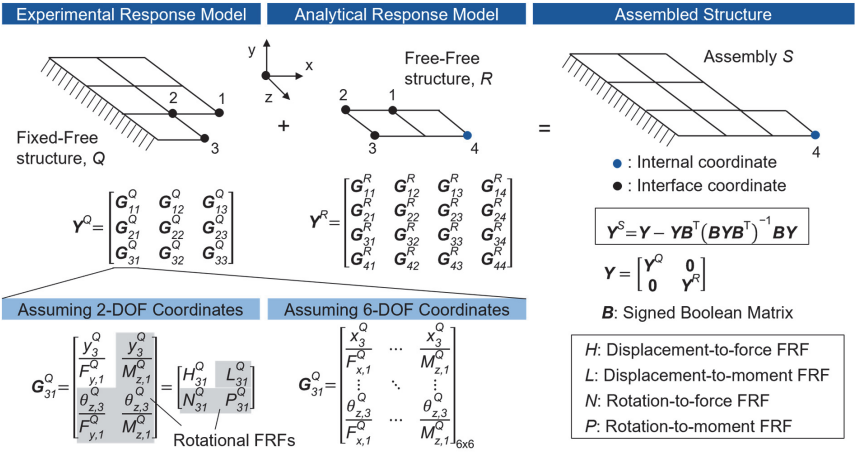

Figure 2.6 Example of frequency based substructure coupling
Beispiel einer frequenzbasierten Substrukturkopplung

Now, the size of the compliance matrices (or response models) depends on the number of substructure coordinates to be considered (internal and interface) as well as on the number of DOFs of each coordinate. For an exact coupling of 3D substructures, all six DOFs of the interface coordinates must be considered. For the below example with merely three interface coordinates of P and four coordinates of Q, response models of sizes $[\boldsymbol{Y}^Q]_{18x18}$ and $[\boldsymbol{Y}^R]_{24x24}$ are necessary. This means that 324 FRFs must be obtained experimentally for the response model of Q. Under the assumption that the interface and internal nodes only have two DOFs, say, y- and θ_x-direction, then the size of the response models reduce to $[\boldsymbol{Y}^Q]_{6x6}$ and $[\boldsymbol{Y}^R]_{8x8}$. Still 36 FRFs must be measured. As an example, an element of the response model $\boldsymbol{Y}^Q$ is shown in Figure 2.6 with its FRFs considering two and six DOFs per coordinate. The calculation of the LM FBS equation gives the dynamics of the assembly in the fully occupied matrix $\boldsymbol{Y}^S$. The prediction of FRFs at coordinate 4 are available at the appropriate rows and columns of this matrix. Based on the above coupling problem, the following challenges become clear:

1. Measurement of rotational FRFs: As seen in the contents of $\boldsymbol{G}_{31}^{Q}$, rotational FRFs make up for 75 % of the compliance matrix for the 6-DOF as well as the chosen 2-DOF coordinates cases. The importance of considering rotational FRFs in coupling calculations has been extensively discussed in literature [DUAR95; LIU99]. However, their direct measurement is extremely challenging. This is because, the application of a pure moment at a point on a structure (for e.g., $M_{z,1}^{Q}$) is not practical with conventional measurement technology. Current approaches for pure moment excitation using magnetostrictive rods, twin shaker arrangement or synchronized hammers require significant measurement effort and have not gained wide acceptance in experimental substructuring. Even the direct measurement of dynamic angular displacement or rotation (for e.g., $\theta_{z,3}^{Q}$) is challenging with conventional accelerometers.

Over the past decades several techniques have emerged to measure or estimate rotational compliances. DUARTE and EWINS [DUAR00] assign the available techniques into following six categories: i) block, ii) mass additive, iii) finite-difference, iv) estimation, v) angular transducers, and vi) laser-based techniques. In the following, two relevant and popular techniques are discussed: the finite difference method (iii) and use of angular transducers (v) (see Figure 2.7). For details on the other techniques refer to the comprehensive review in [DUAR00].

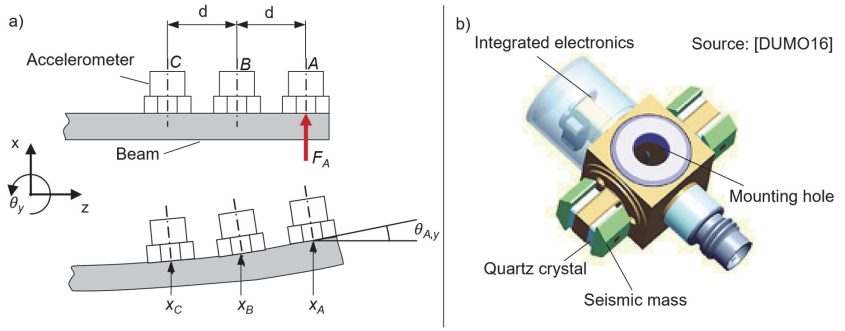

Figure 2.7 a) Backward difference method for beam end; b) Rotational accelerometer [DUMO16]

a) Rückwärtsdifferenzmethode für ein Balkenende b) Winkelbeschleunigungssensor [DUMO16]

The finite difference method is based on the relationship that rotational deflections are derivatives of the translational deflections. Thus, rotational compliance can be approximated from the measured displacement-to-force FRFs (*H*-terms) without additional structural attachments. Consider the 2D cantilever beam in Figure 2.7a with closely spaced accelerometers. Here, the rotational compliances at the free end of the beam (*A*) can be approximated based on the translational FRFs measured at coordinates *A*, *B* and *C* separated by the distance d. This corresponds to the second order finite backwards difference method. The transformation matrix ($\boldsymbol{\Gamma}$) for first, second and nth-order

backwards difference method are obtained by applying the TAYLOR series expansion at coordinate *A* [SATT80; ANSI84; DUAR00],

$$\text{first order, } \boldsymbol{\Gamma}_f = \begin{bmatrix} 0 & 1 \\ -\frac{1}{d} & \frac{1}{d} \end{bmatrix}; \text{ second order, } \boldsymbol{\Gamma}_s = \frac{1}{2d}\begin{bmatrix} 0 & 0 & 2d \\ 1 & -4 & 3 \end{bmatrix}. \tag{2.20}$$

The measured compliance matrix containing translational FRFs, $\boldsymbol{H}_{ABC}$ can then be transformed to obtain the collocated compliance matrix at *A* including rotational FRFs,

$$\begin{aligned} \boldsymbol{G}_{AA} &= [\boldsymbol{\Gamma}_s] \cdot [\boldsymbol{H}_{ABC}] \cdot [\boldsymbol{\Gamma}_s]^T \\ &= \frac{1}{2d}\begin{bmatrix} 0 & 0 & 2d \\ 1 & -4 & 3 \end{bmatrix} \cdot \begin{bmatrix} H_{CC} & H_{CB} & H_{CA} \\ H_{CB}^T & H_{BB} & H_{BA} \\ H_{CA}^T & H_{BA}^T & H_{AA} \end{bmatrix} \cdot \frac{1}{2d}\begin{bmatrix} 0 & 0 & 2d \\ 1 & -4 & 3 \end{bmatrix}^T. \end{aligned} \tag{2.21}$$

In the practical implementation of this method by [DUAR00], the rotation-to-moment FRFs (denoted by *P*) showed a much greater degree of noise contamination than the rotation-to force FRFs (denoted by *N*), especially at lower frequencies. Similar results were achieved in [ELLI12], where the second order central difference method was implemented for simple beam structures. The problem of noise sensitivity and amplification still remains a significant hurdle in application of estimation methods.

The development of the new generation of rotational accelerometers was motivated by the need to measure angular accelerations experienced during automotive collision testing [KINS08; DUMO16]. Commercially available rotational accelerometers from KISTLER INSTRUMENTE GMBH are based on the shear cut arrangement of two piezoelectric quartz systems (Figure 2.7b). In such an arrangement, linear accelerations are self-cancelling and the measured output is related only to the experienced rotational acceleration. This sensor thus allows for the direct and convenient measurement of rotation-to-force FRFs using impact or shaker excitation. However, the *P*-term still cannot be directly measured due to the practical difficulties in creating pure moment excitation. Also, the use of rotational accelerometers in experimental dynamic substructuring of complex, real world structures has not yet been extensively studied in literature. Only laboratory-scale implementations of FBS coupling of simple, freely constrained beams and plates using such sensors has been demonstrated in [DROZ18a; DROZ18b]. However, the significant mass loading effect of rotational accelerometers in translational and rotational DOFs has not been addressed in these studies.

2. Interface discretization and dynamics: In the example from Figure 2.6, interface coordinates were given to be the discrete coordinates 1 to 3. However, in real coupling problems it is not always obvious how to appropriately discretize a structural joint [ALLE20]. Into how many coordinates should a structural joint (such as welded joints or bolted joints with overlapping pressure cones) be discretized, has not been addressed in literature. Apart from this, joints are not ideal stiff but rather have a finite, usually non-linear stiffness and damping behavior. An accurate a priori modelling of such non-linear joints is often not feasible, such that a parameterization from experimental data is unavoidable. Note that the problem of joint dynamics has two aspects:

firstly, choosing a suitable description or model of the joint and secondly, parameterizing the unknown variables of the joint model from experimental data. Examples of commonly used joints models are: spring-damper elements [TSAI88], point-mass model [MEHR13] and direct FRF description [TOL15; PARK08]. For the identification of model parameters, reference FRFs of the assembled substructures with the joint are measured. Subsequently the error between the rigidly coupled system FRF and reference FRF is minimized by optimizing the values of the unknown joint model parameters.

3. Measurement uncertainty: Experimentally obtained FRFs are subject to systematic and random errors. The inversion of the experimental response model in the coupling equation (Eq. (2.19)), invariably amplifies measurement errors and propagates them to the coupling predictions. Since FRFs are complex-valued vectors, the quantified uncertainty is also complex-valued, and its treatment is different from real-valued variables. Although coherence provides a measure of consistency in repeated measurements, it is not suitable for expressing complex uncertainty. This is because a complex-valued treatment of uncertainty is necessary for propagation through FBS coupling equations. Therefore, the quantification and propagation of uncertainty has become a topic of high relevance in the field of experimental substructuring.

The most common sources of systematic or bias errors are: incorrect, inconsistent position and orientations of dynamic excitation and response measurement equipment. Since bias errors are unavoidable in case of manual impact testing, De Klerk studied their influence on substructure coupling. It was shown that bias errors in impact location in collocated SISO FRFs can considerably propagate through FBS to the poles and zeros of the coupled system [KLER11].

On the other hand, random errors are stochastic perturbations of the measurement signal mainly due to sensor noise, random variation of impact location and environmental factors. Treating the measured FRF as a complex-valued random variable, a bivariate description of measurement uncertainty is often utilized [RIDL02; KIM07; MEGG18]. Kim and Schmitz illustrated the quantification of typical uncertainties encountered during impact testing. These are: the calibration coefficient, mass loading, cosine and stochastic uncertainty. It was shown that the uncertainty on the instrument calibration coefficient contributed the most to the quantified uncertainty [KIM07]. Meggitt pointed out that operator error during impact testing for SIMO and MIMO FRFs can lead to inter-FRF correlation, which must be considered in uncertainty quantification and propagation. Recently, Trainotti et al. presented in [TRAI20] a comprehensive discussion on the practical handling of measurement uncertainty within the context of FBS, especially for impact based measurement. Thus, the focus of the current literature has been on the quantification and propagation of uncertainty in manual impact-based experimental modelling as there are several sources of bias and random errors. The use of relative exciters such as piezoelectric, electrodynamic and electrohydraulic actuators has not been explored, as the absolute dynamic behavior is required for substructuring calculations.

2.4 Applications of dynamic substructuring in machine tools

Anwendungen der dynamischen Substrukturierung in Werkzeugmaschinen

This section presents the implementations of dynamic substructuring to milling machine structures. The goal of the applications has been to predict the influence of structural modifications on the dynamic behavior of the machine tool. In this context, the modifications can be classified into three categories: modification of structural components other than tools and workpieces (Subsection 2.4.1), workpiece coupling and material removal (Subsection 2.4.2) and change of milling tool assembly (Subsection 2.4.3).

2.4.1 Modification of general machine structures

Modifikation allgemeiner Maschinenstrukturen

The modification of structural components lying within the force flux directly impacts the working accuracy of machine tools. Such a modification can occur mainly in two ways: firstly, the change in position of structural components relative to each other can cause a change in vibration behavior; secondly, design changes in the dimension and geometry of structural members.

The simulation of position-dependent machine tool dynamics in a full FEM or co-simulation environment is usually computationally expensive due to the large number of nodes and DOFs involved (typically more than 10^6 DOFs). For efficient simulation of position dependency, LAW proposed a dynamic substructuring approach, where structural components are reduced using CMS and subsequently assembled at the interfaces for any position configurations [LAW13a; LAW13b; LAW13c]. This approach can be classified as coupling in the physical domain as all components are described numerically or analytically. An inherent problem in simulating varying axes positions is the application of constraints for non-conforming meshes. For this, LAW proposed an interpolation-based Multi-Point Constrain (MPC), where the displacements of the condensation node are the weighted average of the deflections of the varying interface nodes in contact.

Later, DANIELS also developed a similar, purely simulation framework, where structural components are reduced using the Dual CRAIG-BAMPTON formulation and saved in databanks of machine, workpiece, fixture and tool models [DANI17]. This allows for the efficient assembly of different configurations, such that relative FRFs can be synthesized between any tool and workpiece model for any machine position (Figure 2.8a). Furthermore, an alternate type of point-to-surface constraint called ‘RBE4’ was proposed in [BREC16b] for avoiding intermittent, mesh-dependent changes in dynamics during motion of linear axes. Within such a framework, time and frequency domain simulation of the milling process can be performed to obtain position dependent stability boundaries [DANI17]. Although promising first results were achieved by LAW and DANIELS, their work highlights the need to accurately model the structural joints in machine tools (bolted joints, ball screws, linear guideways, bearings etc.).

SEMM extended upon these methods by developing a more realistic treatment of joint damping effects for different axes positions [SEMM19a; SEMM19b]. Here, the effect of the variation of local damping due to the change in axes configuration (and corresponding mode shape) was considered. This led to a better prediction of modal damping than constant or global damping.

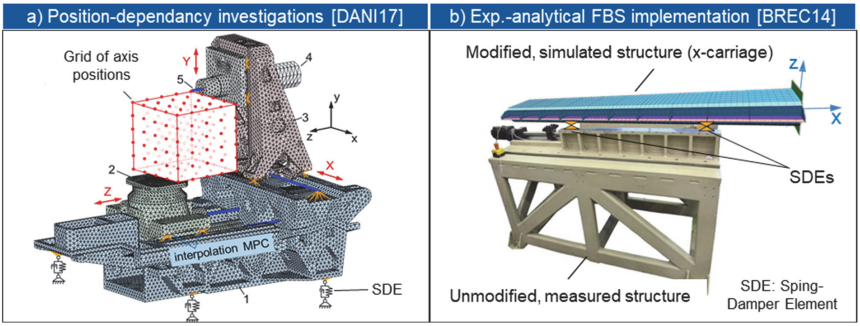

Figure 2.8 a) Milling machine model for simulating position dependent dynamics [DANI17]
b) Example of experimental-analytical FBS from [BREC14]

a) Simulationsmodell für die positionsabhängige Maschinendynamik [DANI17]
b) Beispiel der experimentell-analytische FBS nach [BREC14]

The most common design tasks in machine tool design are where only certain parts of an existing machine are modified or varied [ROMA94]. Thus, machine tool manufacturers often need to assess the effect of structural design changes of an existing machine on its dynamic behavior. This represents an ideal application for experimental-analytical FBS as the existing, unmodified structure can be modelled experimentally and the virtual design modification can be modelled analytically. In [BREC14], the analytical model of a slider (or carriage) was coupled with an experimental model of a test bench via joint models of the four guide way shoes (Figure 2.8b). It was shown that, merely the consideration of vertical DOF (z-direction) of the interface coordinates was sufficient to predict the FRF at the overhanging end of the assembled carriage in the z-direction. Here, the joints (guide way shoes) were modelled based on manufacturers data sheet and not included in the experimental model.

In the DFG sponsored research project ‘Experimental substructure coupling for vibration analysis of machine tools’, the multi-point, multi-DOF experimental-analytical coupling of machine structures was researched in detail (see summary at [DFG21]). A modelling approach was proposed here, which includes the joint interfaces in the experimental response model, such that elaborate joint modelling is completely avoided. As an example, an analytical model of a y-carriage was coupled to four guide shoes of the unmodified x-carriage using FBS (Figure 2.9). Here, the ERM was obtained from impact testing at the guide shoes in x and z-directions. It was shown that symmetry of the response model matrix as well as structural symmetry could drastically reduce the measurement effort. Thus, the prediction of the FRF at coordinate 5 could be achieved using merely four FRFs at symmetric coordinates 1 and 3 (or 2 and 4).

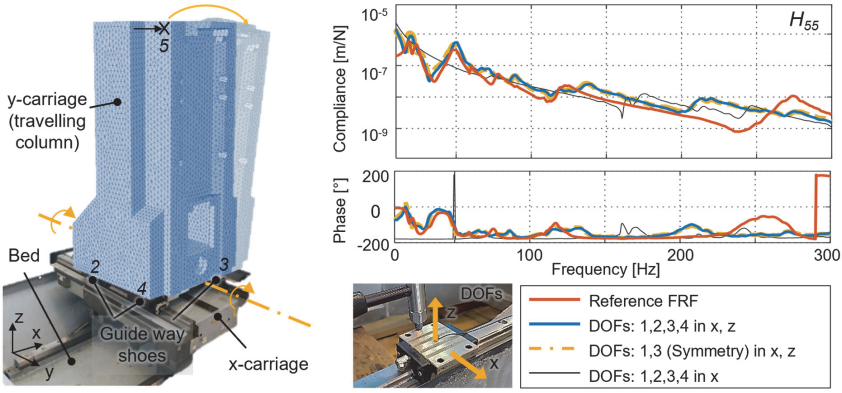

Figure 2.9 Frequency based multipoint coupling of machine carriage
Frequenzbasierte Mehrpunktankopplung eines Fahrständers

2.4.2 Workpiece coupling and material removal

Werkstückankopplung und Materialabtrag

With respect to workpiece-side dynamics, structural modification occurs mainly when the workpiece and fixture are attached to the machine table and when a significant volume of the workpiece is removed during machining. Thus, there are two main applications of dynamic substructuring for the prediction of the workpiece side compliance: coupling of the workpiece to the machine table and the simulation of the influence of material removal on the workpiece compliance.

The methods for workpiece holding in milling machines can be grouped into four categories: simple, standard, modular and special clamping devices [BREC19b]. The application of dynamic substructuring for workpiece coupling has been limited to simple and modular clamping, where the clamping can be discretized to individual points on the workpiece and machine structures. This reduces the problem to a multi-point, multi-DOF coupling problem, similar to coupling of machine structures to guide way shoes.

In [CHAV20], the frequency based, coupling of a workpiece to a machine table via four bolted joints was demonstrated. Here, the machine table was characterized experimentally, and the arbitrary geometry of the workpiece was modelled using the corresponding FEM model (Figure 2.10a). In many situations, it is necessary to raise the clamping height of the workpiece to allow for machining at the side walls. This can be realized using modular, zero-point clamping systems. However, the discreet, raised clamping elements introduce a significant compliance in the clamped assembly. BRECHER et al. proposed the use of a clamped adapter for experimentally obtaining the compliance matrix at the ends of the clamping element [BREC19a] (Figure 2.10b). Subsequently the FEM based analytical response model of the workpiece was coupled to the discrete clamping element to predict the dynamic behavior of the assembly.

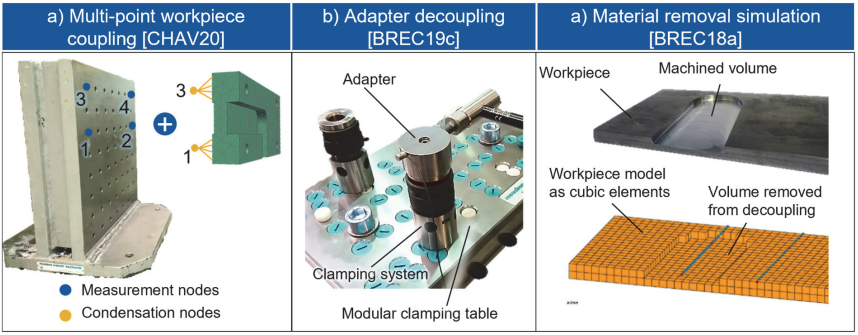

Figure 2.10 Substructuring techniques for predicting workpiece-side dynamics
Substrukturierungsverfahren zur Vorhersage werkstückseitiger Dynamik

With regards to material removal simulation, TUYUZ and ALTINTAS in [TUYS17] predicted the change in thin-walled workpiece dynamics during milling using a semi-analytical frequency based substructuring approach. This was realized by the frequency based decoupling of the removed material volume from the raw workpiece model. Alternate to frequency based approaches, BRECHER et al. utilized decoupling in physical domain for representing the material removal [BREC18a]. The efficiency of this approach lies in the use of a common mesh grid for both, the workpiece discretization as well as for the voxel representation in the engagement simulation. Thus, the workpiece is meshed using cubic elements, such that the element coordinates can be used for the voxel representation of the workpiece in a subsequent engagement simulation. The tool-workpiece engagement simulation then identifies the elements to be removed for a machining state. The elements are then recursively decoupled from the workpiece model in the physical domain such that the FEM model of the machined state is directly achieved (Figure 2.10c). Solution of the corresponding eigenvalue problem then gives the dynamic behavior of the machined workpiece.

2.4.3 Tool coupling

Werkzeugankopplung

Compared to the multipoint coupling of 3D structures like workpieces and machine carriages, the problem of coupling (abstracted) 2D tool models to a single coordinate of machine main spindles is less complex. However, the requirements of accuracy are much higher for prediction of tool dynamics, as these FRFs can then be utilized for estimating stability boundaries, process forces and workpiece quality. There are several challenges involved in the accurate prediction of tool dynamics using experimental-analytical FBS. To recognize these, the general tool coupling procedure is explained in the following along with the current research works.

In [SCHM00], the Receptance Coupling Substructuring Analysis (RCSA) approach was first proposed for tool coupling, where the spindle-side displacement-to-force re-

ceptance was obtained experimentally and the milling tool was simplified as an analytical EBB element. The main idea behind RCSA or experimental-analytical substructure coupling of milling tools is as follows: first, experimentally identify the absolute dynamic behavior of the spindle-machine substructure at a point, which is common to all assembled tools. In literature, the tool end of the interface flange is widely used as the common coupling point (Figure 2.11). Second, analytically model the milling tool to obtain their dynamic behavior at both ends in an unconstrained or freely constrained state. Third, couple the response models of both the substructures at the interface flange to obtain the dynamic behavior of the tool-spindle-machine assembly at the tool tip. The coupling is considered in a 2D plane (xz in Figure 2.11) with the assumption of negligible cross sensitivity between the radial directions (x and y). The current state of research with respect to experimental and analytical modelling is presented below.

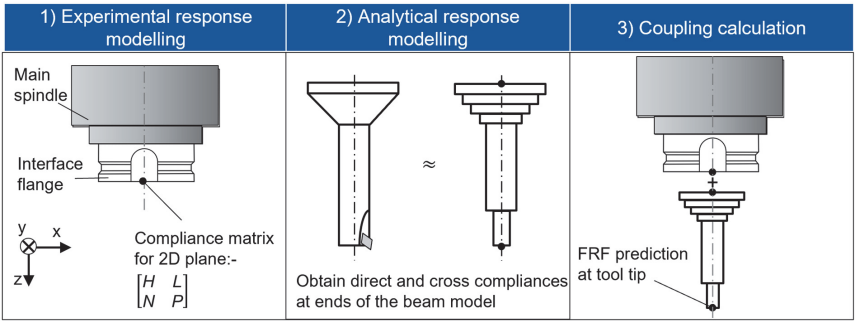

Figure 2.11 Illustration of the procedure for tool coupling

Skizze der Vorgehensweise für die Werkzeugkopplung

Experimental Response Modelling

In the early works of SCHMITZ et al. [SCHM00; SCHM01], only displacement-to-force terms were used in the experimental response model and the rotational terms were considered to be rigid. Later, PARK et al. showed that the consideration of rotational compliances resulted in a significant improvement of the prediction accuracy [PARK03]. However, as mentioned in Subsection 2.3.2, the accurate measurement or estimation of rotational compliances is not a trivial task. Specific to the problem of experimental response modelling in tool coupling, there are three main approaches for obtaining the rotational FRFs (Figure 2.12). These are discussed in the following.

In [PARK03], it is proposed to conduct impact tests (displacement-to-force) at the free end of a short and a long calibration blank inserted in a spindle-holder assembly. Based on these FRFs and non-linear equation formulations, the complete 2x2 compliance matrix at the free end of the holder-spindle assembly could be obtained. However, due to the use of calibration blanks, the identified response model is valid only for the utilized tool holder. Thus, the procedure must be repeated for each required tool holder.

Later, NAMAZI et al. extended PARK's method to identify the complete compliance matrix at interface flange instead of the tool holder end [NAMA07]. This allows for the coupling of different holder-tool assemblies. For obtaining the compliance matrix, displacement-to-force impact tests are required at the free as well as at the interface flange end of a holder-spindle assembly (coordinates *1* and *2* in Figure 2.12b). Subsequently, a reformulation of the coupling equations gives the compliance matrix at the interface flange without the holder.

In an alternative approach, SCHMITZ and DUNCAN [SCHM05] proposed the substructure decoupling of a standard holder (or adapter) for obtaining the translational and rotational compliances at the interface flange. This approach uses a more intuitive and elegant decoupling formulation compared to the equations required in previous methods. For solving the decoupling equations, first the complete compliance matrix at the free end of the adapter (coordinate 3 in Figure 2.12c) is necessary.

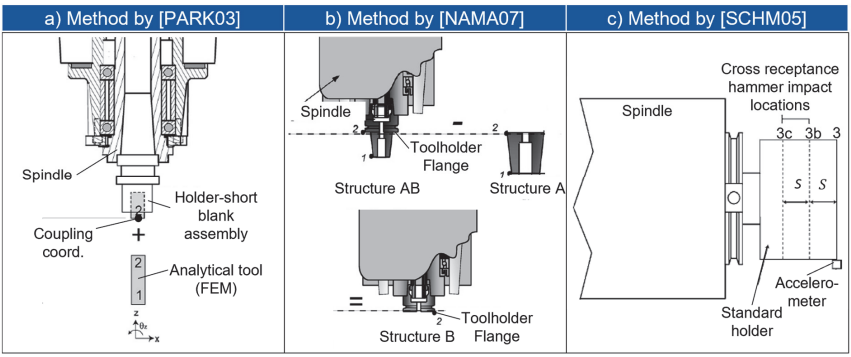

Figure 2.12 Methods for obtaining experimental response models: a) PARK et al. [PARK03], b) NAMAZI et al. [NAMA07], and c) SCHMITZ and DUNCAN [SCHM05]

Methoden zur Ermittlung von experimentellen Antwortmodellen von a) PARK et al. [PARK03], b) NAMAZI et al. [NAMA07], and c) SCHMITZ and DUNCAN [SCHM05]

For estimating the rotation-to-force FRF at coordinate 3, SCHMITZ proposes the use of the second order backwards difference method using three displacement-to-force FRFs measured at coordinated 3, 3b and 3c and applying Eq. (2.21) such that,

$$N_{33} = \frac{3H_{33} - 4H_{33\mathrm{b}} + H_{33\mathrm{c}}}{2S}. \tag{2.22}$$

Here, reciprocity is assumed between the N_{33} and L_{33}. For synthesizing the rotation-to-moment term, the following complex division formulation was proposed [SCHM05],

$$P_{33} = \frac{\theta_3}{M_3} = \frac{F_3 \cdot x_3 \cdot \theta_3}{x_3 \cdot M_3 \cdot F_3} = \frac{L_{33} \cdot N_{33}}{H_{33}} = \frac{(N_{33})^2}{H_{33}} = \frac{(L_{33})^2}{H_{33}}. \tag{2.23}$$

The analytical response model of the adapter is calculated using the closed form expressions for uniform free-free EBB and subsequently decoupled from the measured compliance matrix at 3.

The main advantage of this approach is the ease of application as well as low modelling and measurement effort. An important source of error in this method is the use of Eq. (2.23) for synthesizing P_{33}. This is because the equation involves the division of two complex vectors and invariably leads to the creation of spurious poles and zero shifting as observed by several authors [ALBE13a; ALBE13b; JI18; BREC16a; KUMA12]. To tackle this, ALBERTELLI showed that the partial differentiation of the *L*-term with respect to axial displacement gives the *P*-term for small axial displacements [ALBE13a]. Thus, P_{33} could be derived by applying the finite difference method,

$$P_{33} = \frac{3L_{33} - 4L_{3b3} + L_{3c3}}{2S}. \tag{2.24}$$

The synthesis of the *L* and *P*-terms in the above equation requires the measurement of nine displacement-to-force FRFs at three excitation locations, which represents significant measurement effort. An alternate method was provided by KUMAR and SCHMITZ [KUMA12], where a single FRF (H_{33}) is required for obtaining the rotational compliances. This is realized by fitting the poles of H_{33} using the closed form FRF expression for fixed-free EBBs from [BISH55]. More concretely, it involves the recursive variation of geometric parameters and solid damping factors of multiple fixed-free beams so as to match the poles of the measured FRF. The rotational FRFs can then be calculated based on the identified physical parameters of the hypothetical fixed-free beams. Although this method requires only a single FRF measurement, a considerable analysis effort is needed as each pole must be manually picked and fitted using the recursive algorithm.

Independent of the approach, experimental response modelling requires the measurement of absolute dynamic behavior, which is commonly obtained using an impact hammer (absolute excitation) and mounted acceleration sensor (absolute response). The systematic analysis and comparison of other measurement equipment (displacement sensors, vibrometer, piezoelectric shaker, etc.) with respect to their suitability for experimental response modelling of the spindle-machine substructure has not been addressed in literature.

Relative excitation between the workpiece and tool using, for example, piezoelectric, electrodynamic or electrohydraulic actuators is often utilized for performing experimental modal analysis of a machine tool or for measuring the oriented compliance function [BREC17a]. Such a setup has several advantages. Firstly, the simultaneous application of a static preload and dynamic excitation provides a realistic representation of cutting conditions and eliminates non-linear effects of joint clearance and play. Additionally, relative excitation actuators allow for a better setup alignment and repeatability such that bias errors associated with impact excitation are reduced. Furthermore, relative exciters such as piezoelectric actuators offer a wide excitation spectrum with flexible allocation of spectral energy. Despite the advantages, the question of whether and under which conditions the absolute vibration behavior can be obtained from relative excitation, has not been explored in literature.

Analytical Response Modelling

The freely constrained vibration behavior of the tool or tool assembly is usually modelled in literature as sequentially arranged analytical beam elements. Although FEM models can also deliver accurate ARMs, beam modelling has several associated advantages. The CAD models of tool assemblies required for FEM modelling are not readily available for each holder-tool combination. For beam modelling, the geometric measurement of the tool assembly with vernier calipers is often sufficient and is easily conducted in a workshop environment. Also, proprietary automated meshing algorithms are not required in case of beam modelling. The corresponding (manual) inspection of mesh quality is also avoided.

A holder-tool assembly, such as a thermal shrink fit and end mill assembly, has several structural features such as the tapered segment, unbalance holes, holder-tool contact, end mill flutes, etc. Analytical beam modelling in RCSA involves the abstraction of such tool assembly features into uniform cylindrical beam segments (or slices). The compliance matrices at and between the ends of the tool assembly are derived using the concept of end-to-end coupling. Here, the compliance matrices in free-free state are calculated at the ends of each beam slice using analytical beam theories. Subsequently, all slices are coupled to each other at their ends by applying compatibility and equilibrium conditions in the frequency domain (Figure 2.13a). This approach is different from the use of beam elements in FEM modelling, where the stiffness matrix of the discretized structure is derived based on the analytical stiffness of a uniform beam element. The derived mass and stiffness matrices are then used to solve the eigenvalue problem for the complete structure.

Alternate to FEM and classical beam modelling, FILIZ et al. proposed the use of spectral-TCHEBYCHEV method to solve the TIMOSHENKO beam equations [FILI09]. With such a method, the taper of the holder could be modeled more realistically as continuous beam segments with axially varying diameters (Figure 2.13b). An analysis of the error in the eigenfrequencies due to the assumption of constant diameter slices was found to be insignificant for the considered tapered holder [FILI09].

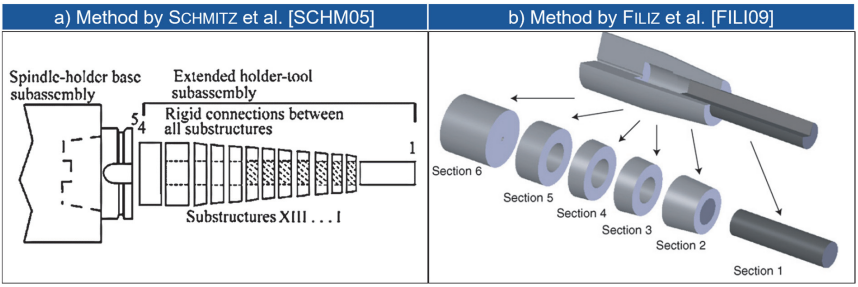

Figure 2.13 Analytical tool modelling according to a) [SCHM05] and b) [FILI09].
Analytische Werkzeugmodellierung nach a) [SCHM05] and b) [FILI09].

The most used beam theories in literature for tool assembly modelling are the EULER-BERNOULLI Beam Model (EBBM) [SCHM04; SCHM05; SCHM06; SCHM07; SCHM19; KUMA12] and TIMOSHENKO Beam Model (TBM) [ERTÜ06; MANC14; TUNC18; BREC21]. In case of the EBBM, BISHOP formulated closed-form expressions of translational and rotational compliances under different constraint conditions [BISH55]. Although these formulations are convenient and computationally efficient, the validity of EBBM is limited to slender beams (see Subsection 2.2.2).

On the other hand, the TBM of holder-tool assemblies has been shown to provide a more realistic representation their dynamics by considering rotational inertia and shear effects [NAMA07; ERTÜ06]. However, there exists no closed form expression for obtaining the FRFs. In [ERTÜ6], ERTÜRK argues that the classical eigen solution of a multisegmented beam is not feasible for tool modelling because each beam segment corresponds to four differential equations such that a beam of 'm' segments results in an eigenvalue problem of size 4m x 4m. The solution of the determinant of such a matrix with highly non-linear elements makes it extremely difficult to calculate higher order roots. In the same work, a solution of this problem is proposed, where the eigenvalue problem is solved for individual, freely constrained TIMOSHENKO beam segments. The model of the tool assembly is obtained by end-to-end receptance coupling of the individual beam segments. The resonance frequencies predicted by this method showed a good correspondence with those calculated by a FEM model without being as computationally expensive. This TBM approach provides a viable alternative for accurate modelling of beams without requiring CAD and FEM tool models and corresponding modelling software packages.

Apart from the beam modelling approach, two important challenges in creating reliable ARMs of tool holders are: i) the accurate modelling and identification of the holder-tool joint and ii) the accurate modelling of the complex fluted segment of the shaft mill.

The dynamic properties of the contact between a holder and end mill along its clamped length are difficult to obtain a priori. Therefore, several authors assume a model of the joint and parameterize the model properties indirectly, based on experimental results. One of the commonly used holder-tool joint models is the massless Spring-Damper Element (SDE) acting between the holder and overhanging tool [KIVA04; SCHM05; ÖZŞA09; ÖZŞA15] (Figure 2.14a). Such an element provides additional translational, rotational compliance and equivalent viscous damping that is caused by the joint contact.

PARK et al. [PARK08] pointed out that the consideration of joint inertia is necessary, where masses of the coupled structures are not several orders of magnitude higher. The authors proposed a formulation for identification of joint inertia, stiffness and damping for the bolted joints of modular tools. Like most of the methods for joint updating, this method also requires the measurement FRFs of the assembled spindle-holder-tool assembly.

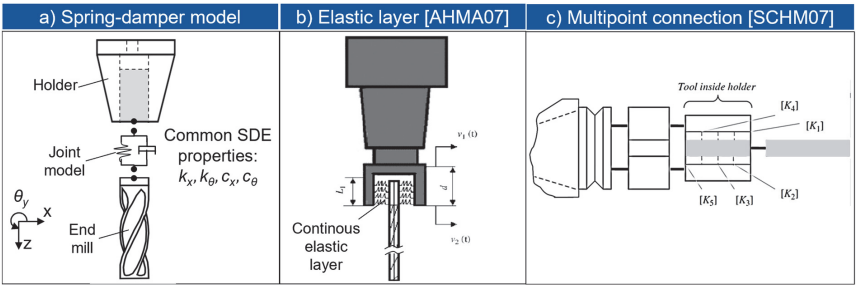

Figure 2.14 Schematic illustration of different joint modelling approaches
Darstellung der verschiedenen Ansätze zur Modellierung von Fügestellen

A more realistic model was proposed in [AHMA07], where the joint properties are represented not as a single SDE between holder and overhanging tool, but rather as a zero-thickness elastic layer along the clamped length. This allows for taking into consideration the variation of normal pressure and stiffness along the clamped length as well as surface roughness (Figure 2.14b). A simplification of the continuous layer model is the use of multiple, discrete and flexible connections between the holder and the inserted tool. SCHMITZ et al. proposed in [SCHM07] such a multiple connection joint model (Figure 2.14c). The values of the joint parameters at different positions along the clamped length were obtained from a corresponding FEM model with flexible contact interface. This allowed for an a priori prediction of TCP FRF specific to the considered holder-tool combination. Later in [SCHM19], this multipoint approach was implemented for 16 different combinations of tool diameter and lengths for an ER32 collet holder. Here, the parameters of the joint were updated using the tool tip FRF of the corresponding spindle-holder-tool assembly. The joint parameters were varied manually until a good correspondence between the measured and predicted TCP FRF was achieved. REZAEI et al. proposed an approach to directly identify the holder-tool joint FRFs at multiple points along the length of the holder using inverse RCSA [REZA12]. Due to the identification of multiple connection points at the holder, the effect of rotation is included implicitly and hence the rotational compliances were ignored. An alternate and direct approach for shrink fit holder joint modelling based on Hertzian contact theory and fractal geometry was developed by LIAO et al. [LIAO17]. Here, the contact stiffness is assumed to be a function of elastic deformation of micro-asperities in contact between the two surfaces.

Irrespective of the method employed for modelling the joint, the parameters of the joint model are obtained in majority of approaches by comparing the predicted tool tip FRF with an experimentally obtained tool tip FRF of the tool clamped in a machine spindle [KIVA04; AHMA07; PARK08; ÖZŞA15; SCHM19]. Subsequently, the error between prediction (from rigid coupling) and measurement is minimized by varying the joint parameters (usually translational, rotational stiffness and equivalent viscous damping factors). Three major disadvantages of such an approach are as follows:

Firstly, the analytical response model of the holder-tool assembly must be coupled with the experimentally derived spindle-interface receptance matrix to allow a comparison. This means that the errors and uncertainties associated with experimentally obtaining the spindle-interface receptance matrix are propagated in the predicted spindle-holder-tool tip FRF. FILIZ et al. recognized this issue in [FILI09]. Secondly, using the tip FRF in the spindle can lead to identification of incorrect joint parameters which do represent the dynamic behavior of the tool assembly over a larger frequency range [MATT16]. Thirdly, the blocking of the operating time of the machine tool, which is required for conducting the measurements with different holders-tool combinations is a further disadvantage.

The experimental identification of holder-tool assembly in an unclamped state (freely constrained) can overcome the above-stated limitations. MATTHIAS et al. demonstrated the identification of joint parameters between a collet holder and carbide blanks using tool tip FRFs measured in a freely constrained state of the holder-tool assembly [MATT16]. For this, the holder, including the standard spindle-holder interface, as well as the carbide blanks were modelled by receptance coupling of uniform cylindrical TIMOSHENKO beam segments. However, the modelling of the interface part of the holder as uniform cylindrical multi-segment beam introduces avoidable modelling errors. Especially since standard or normed interfaces are geometrically complex and may contain clamping groove, orientation notch, manual clamping holes, hollow tapered shank, balancing holes, etc., a beam modelling is insufficient. Also, the use of laser vibrometer for the free-free displacement (from velocity) measurement resulted in poor signal-noise ratio such that the location of anti-resonances could not be observed clearly. This limits the comparability of the predicted and measured FRF for joint identification.

Apart from the joint, the modelling of flutes of the end mill also represents a major challenge in analytical response modelling. The fluted segment of end mills has, depending on the number of teeth and helix angle, a complex cross-section, which varies along its length. KOPS and VO in [KOPS90] used a cylindrical beam with an equivalent diameter to represent the static stiffness behavior of an end mill. The variation of the area moment of inertia along the radial direction was ignored. They found that an equivalent diameter of 80 % of the tool diameter was suitable for representing the static bending behavior of the 2- and 4-fluted end mills used in the study. Subsequently, other authors have used the simplification of 80 % of tool diameter to represent the fluted segment for receptance coupling [NAMA07; LIAO17]. Later, KIVANC and BUDAK extended KOPS and VO's method by including the effect of the flute arcs on the area moment of inertia and also by considering the moment of inertia in two orthogonal directions [KIVA04]. In [ÖZŞA15], the fluted segment was divided into multiple segments and the area moment of inertia for the tool-end segment was first calculated for the corresponding cross-section using KIVANC and BUDAK's method. Then, the upper segments were rotated depending on the helix angle and the inertia about the fixed orthogonal coordinate system was calculated. A limitation of the methods presented in the literature is that an exact geometry of the flutes is not readily available and even if

it is available, the modelling of each end mill geometry is effortful and requires modelling expertise that might not be available in a workshop environment. The simplification of the equivalent diameter being 80 % of the fluted segment diameter gives a rough engineering estimate but cannot be satisfactorily representative for all combinations of number of teeth, helix angle, length of segments, cooling channels, etc.

There are other features on the holder-tool assembly, which also influence its dynamic behavior. These include balancing holes on the holder, the holder's taper, the hollow segment including the inserted tool, etc. In [SCHM06], the modelling of concentric beams using multipoint receptance coupling was proposed and compared with the equivalent composite beam approach. Nevertheless, the systematic modelling and abstraction of these holder features as uniform TIMOSHENKO beam elements has not been extensively studied in literature.

2.5 Deficits in available literature

Erkenntnisdefizite im Stand der Forschung

The current literature demonstrates the necessity of accurate analytical and experimental models for the reliable prediction of coupled dynamics. The identified research gaps specific to the topic of frequency based tool coupling are summarized in the following.

The experimental response modelling using the adapter decoupling approach from [SCHM05] offers an efficient method for obtaining the compliance matrix at the interface flange. Nevertheless, there are several aspects that require further research:

- The accurate measurement of displacement-to-force FRFs at the adapter is required not only for the compliance matrix but also for estimating the rotational compliances. However, the focus in literature has been merely on manual impact testing which is known to introduce several bias and random errors [KLER08a]. Other translational excitation and response measurement equipment such as piezoelectric shaker, displacement sensor, laser vibrometers, etc. have their own advantages and drawbacks. However, a systematic evaluation of the suitability of these equipment and their combinations for experimental response modelling has not been conducted. Especially the issue of utilizing absolute FRFs from relative excitation through piezoelectric actuators should be investigated as it may potentially improve measurement quality.
- The synthesis of rotation-to-moment FRF from translational FRFs using the straightforward complex division approach amplifies noise and leads to spurious poles. Other methods require significant experimental effort (as in [ALBE13a]) or considerable analysis effort (as in [KUMA12]). The transformation to modal domain offers the possibility to eliminate measurement noise and expand the compliance matrix with comparatively lesser analysis effort. This approach has not been explored for experiential response modelling of the spindle-adapter assemblies.

- Commercially available rotational accelerometers enable the direct measurement of rotation-to-force FRFs. However, the significant mass loading effect must be compensated from the rotational DOF before they can be applied for experimental response modelling.

With respect to analytical tool modelling, the following research gaps are identifiable:

- ARMs inevitably require model updating as the a priori modelling of holder-tool joint dynamics is not feasible. The common use of tool tip FRF in the clamped condition for parameterizing the joint model has several major disadvantages. On the other hand, the initial method by [MATT16] showed the potential of using freely constrained FRFs for efficient estimation of joint parameters. Further research is essential for improving upon the drawbacks of this methods such that the acceptance in industrial practice can be achieved.
- Moreover, an updating approach should be researched, where not only joint parameters but also other a priori unknown or difficult to estimate feature parameters can be identified using FRF measured in the freely constrained state.

The arrangement of spindle integrated displacement sensors developed at the WZL enables the measurement of radial, axial and rotational deflections of the shaft mounted disc. Nevertheless, the estimation of process forces and virtual quality using SIDS still requires the measurement of the tool tip-SIDS transfer function for each tool assembly. The extension of the tool coupling framework to include the SIDS plane has the potential to drastically reduce the measurement effort required for the estimation. However, there are several large gaps in research that must be addressed first:

- An experimental method for reliably obtaining the transfer function between the interface flange and SIDS, including the rotational compliances, should be researched.
- The treatment of measurement uncertainty, especially due to random noise, has not been discussed in literature in relation to tool tip-SIDS transfer functions. This is of high relevance due to the non-collocation of force application and response measurement. Thus, the quantification and propagation of uncertainty represents an important research gap.
- Based on purely predicted tool tip and tool tip-SIDS FRFs, a model-based framework such as in [KÖNI18] can be utilized for the estimation of workpiece surface quality. Such an integration of the substructuring framework with a virtual quality framework has not been explored in literature and would be highly desirable for industrial implementation.

3 Objectives and Modus Operandi

Zielsetzung und Vorgehensweise

During milling operations, tool change represents a frequent and usually significant structural modification of a component lying within the force flux. The resulting change in the machine dynamics influences the maximum achievable stable depth of cut as well as the quality of the milled surface. Since the measurement of each tool tip FRF in each machine is not feasible, the approach of frequency based experimental-analytical receptance coupling has been widely proposed in literature for an efficient prediction. However, the industrial applicability of this approach is still limited by the challenges in reliable experimental and analytical response modelling, as seen in the literature survey. With the increasing use of spindle integrated sensors, for not only force estimation but also providing surface quality estimates, the accurate prediction of spindle-holder-tool assembly dynamics has gained even more importance. Here as well, the application of substructuring approach can considerably reduce the required measurement effort.

The goal of this thesis is, therefore, to provide a framework of efficient analytical and experimental substructuring methods for the reliable prediction of the spindle-holder-tool assembly dynamics. Specifically, this implies the prediction of the tool tip FRF and the tool tip-SIDS transfer function for a spindle equipped with contactless displacement sensor system. To achieve the above stated goal, the identified gaps in current literature must be closed. A structural overview of the thesis is provided in Figure 3.1.

To improve the accuracy and efficiency of experimental response modelling at the interface flange using adapter decoupling, the following research questions should be answered:

a) How do absolute and relative measurement strategies compare with respect to their suitability for experimental response modelling? Can the advantages of relative excitation using piezoelectric actuators be utilized for obtaining the absolute dynamic behavior at the interface flange?
b) How can the disadvantages of complex division for synthesizing rotational compliances be overcome without significant experimental or analysis effort?

The accurate analytical response modelling of tool assemblies is often the aspect which limits the industrial applicability of the substructuring framework. This is mainly because the holder-tool features often cannot be modelled and parameterized a priori with reasonable effort. Since tool model updating using FRFs from the freely constrained state can significantly improve the efficiency and accuracy, the following research question arises,

c) How can a priori unknown parameters of the tool assembly model be precisely identified in a freely constrained state such that feature models (joint, fluted segment model, etc.) can be reliably parameterized and validated in a completely offline manner?

The prediction of the tool tip-SIDS FRFs additionally requires the measurement of the transfer functions between the interface flange and the SIDS. Unlike other spindle integrated sensor systems from literature, the SIDS arrangement from [BREC18b; BREC19c] allows for the convenient indirect measurement of the rotational deflections at the shaft-mounted disc. This leads to the following research question,

d) Which experimental and evaluation strategies should be used to obtain both, the translational and rotational transfer functions between the interface flange and SIDS for consideration in the coupling calculations?
e) In what way can the effect of GAUSSIAN random noise on the measured SIDS signal be quantified and propagated through the coupling calculations such that uncertainty bounds on the predicted tool tip-SIDS transfer function can be obtained?

A secondary objective of this work is the demonstration of the effectiveness of using the proposed tool coupling methods in combination with an existing framework for model-based prediction of virtual workpiece quality developed in [KÖNI18]. In this regard, the following research question arises,

f) How can the tool coupling and virtual quality frameworks be integrated such that a process parallel estimation of cutting forces and surface quality is achieved?

Chapter 4 deals with evaluating different measurement strategies as well as researching alternate approaches for synthesizing rotational compliances. Chapter 5 presents a method for analytical tool modelling and feature parameterization in freely constrained state. A method for tool tip-SIDS transfer function measurement, uncertainty quantification is proposed in Chapter 6. Finally, an approach for the integration of the tool coupling methods with an existing virtual quality framework is demonstrated in Chapter 7. The thesis in summarized and concluded in Chapter 8.

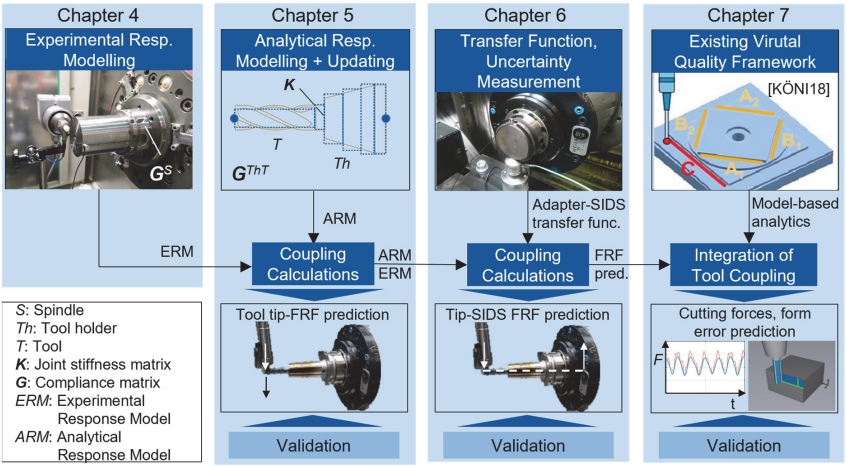

Figure 3.1 Overview of the contents of the chapters and their interlinkage
Überblick über die Inhalte der Kapitel und deren Verkettung

4 Experimental Response Modelling

Experimentelle Response Modellierung

Accurate experimental response models are necessary for successful frequency based substructure coupling. In this chapter, first, an overview of the mathematical formulation for tool coupling and the adopted convention for numbering the coupling planes is provided (Section 4.1). The displacement-to-force FRFs (*H*-terms) are required here for not only the coupling calculations, but also form the basis for estimating rotational compliances. Hence, Section 4.2 is dedicated to the evaluation of different measurement strategies with respect to their suitability for experimental response modelling. Finally, Section 4.3 describes two novel methods for obtaining the rotation-to-moment FRF (*P*-term) at the free end of the adapter. These are then compared with the complex division formulation by SCHMITZ [SCHM05] and suitable use cases for each method are provided.

4.1 Overview of tool coupling formulation

Überblick über die Formeln zur Werkzeugankopplung

In order to enable a better understanding of the substructuring methods researched in this thesis, a brief description of the adopted tool coupling approach, its mathematical formulation and conventions is presented. As seen in Subsection 2.4.3, the prevalent methods by NAMAZI et al. [NAMA07] and SCHMITZ et al. [SCHM05] enable obtaining the experimental response model of the spindle-machine substructure at the interface flange. In this work, the approach of decoupling of a simple cylindrical artifact or adapter from [SCHM05] is chosen because of two reasons: i) The measurement of the required FRFs at the adapter end is much easier than the method in [NAMA07]; ii) The computational implementation is also more simple and a non-linear solver is not required. However, the estimation of rotational compliances at the free end of the adapter now becomes necessary and is therefore addressed in Section 4.3.

Figure 4.1 illustrates the adopted approach for experimental response modelling and tool coupling. The goal is to experimentally obtain the response model at the interface flange coordinate, *4* of the interface-spindle substructure ($\boldsymbol{G}^{S}_{44}$). The starting point for this, is the experimental determination of the 2 x 2 FRF matrix at the free end of the assembled adapter, $\boldsymbol{G}^{A}_{33}$. This is the focus of the current chapter. Next, the free-free ARM of the cylindrical adapter is derived from a TIMOSHENKO beam model based on the method for generalized end conditions by ARISTIZABAL-OCHOA [ARIS04] (refer to Section 5.2). Subsequently, the ERM at the interface flange is found by decoupling the adapter dynamics as follows [SCHM05],

$$\boldsymbol{G}^{S}_{44} = \boldsymbol{G}^{a}_{34}(\boldsymbol{G}^{a}_{33} - \boldsymbol{G}^{A}_{33})^{-1}\boldsymbol{G}^{a}_{43} - \boldsymbol{G}^{a}_{44} \tag{4.1}$$

The inversion of the measured FRF matrix $\boldsymbol{G}^{A}_{33}$ in Eq. (4.1) inevitably leads to the amplification of the measurement noise and errors and thus motivates the need for accurate measurement and estimation of the components of $\boldsymbol{G}^{A}_{33}$, i.e. H^{A}_{33}, L^{A}_{33}, N^{A}_{33} and P^{A}_{33}.

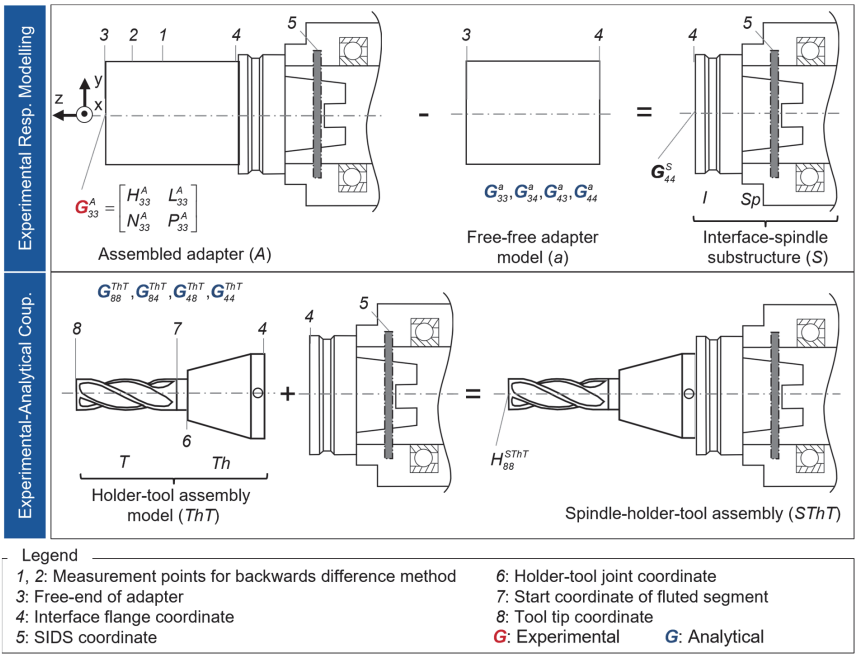

Figure 4.1 Adopted tool coupling formulation with coupling coordinates
Verwendete Formulierung zur Werkzeugkopplung mit Kopplungskoordinaten

Coordinate *5* in Figure 4.1 represents the disc mounted on the spindle shaft, where the SIDS measure displacements relative to the spindle housing. The dynamic behavior at coordinate *5* does not play any role in the coupling calculations for predicting tool tip behavior H_{88}^{SThT}. However, it is relevant for predicting the tool tip-SIDS transfer function H_{58}^{SThT} and is therefore considered in the corresponding measurement campaign (Section 6.2).

Once the ERM at coordinate *4* is obtained, any analytical holder-tool assembly model can be coupled to get the displacement-to-force FRF at the assembled tool tip [SCHM01; SCHM03],

$$H_{88}^{SThT} = H_{88}^{ThT} - \begin{bmatrix} H_{84}^{ThT} & L_{84}^{ThT} \end{bmatrix} \left(\boldsymbol{G}_{44}^{ThT} + \boldsymbol{G}_{44}^{SThT} \right)^{-1} \begin{bmatrix} H_{48}^{ThT} \\ N_{48}^{ThT} \end{bmatrix}. \tag{4.2}$$

An important aspect, which has not been highlighted in literature, is that the diameter of the adapter used for ERM should be equal to the interface end diameter of the tool to be coupled. A difference in diameters will lead to different stiffness conditions and incorrect coupling. Hence multiple adapters of different diameters are required for a range of tool holder diameters.

The experimental investigation and validation trails conducted in this thesis were implemented at two horizontal milling machines. Machine Tool A (MCT A) is a 4-axis

machine built in a cross-bed design with a working room diagonal of 1090 mm and a 42 kW main spindle. Machine Tool B (MCT B) is a 5-axis machine in cross-bed, travelling column design with a working room diagonal of 1250 mm and a 40 kW main spindle. A rotary swivel table provides the fourth and fifth axis on the workpiece side. Both machines are equipped with an HSK-A 63 tool interface.

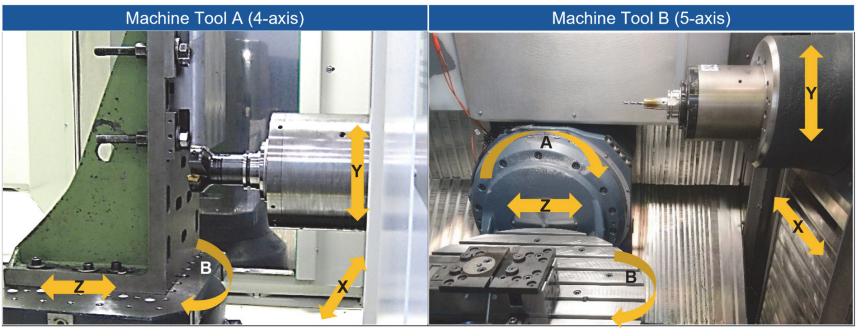

Figure 4.2 Machine tools used for experimental response modelling and validation trials
Verwendete Werkzeugmaschinen zur experimentellen Response-Modellierung

4.2 Measurement of translational compliances

Messung von translatorischen Nachgiebigkeiten

The component of the compliance matrix $\boldsymbol{G}^{A}_{33}$, which can directly be measured, is the displacement-to-force FRF H^{A}_{33}. This FRF along with further translational FRFs H^{A}_{32} and H^{A}_{31} serve as the basis for the estimation of rotational compliances, L^{A}_{33}, N^{A}_{33} and even P^{A}_{33}. Hence, it is essential to accurately and reliable measure displacement to force FRFs as errors in their estimation will propagate to 3/4$^{\text{th}}$ of the compliance matrix. This section, therefore, deals with the problem of accurate measurement of displacement-to-force FRFs using different measurement strategies. Here, the term ‘strategy’ implies the combination of excitation instrument, response measurement sensor as well as the measurement setup used. For the purpose of substructure coupling, the absolute dynamic behavior at the coupling coordinates is required. The most common strategy for obtaining this is by measuring the absolute displacement (from integrated accelerometer signal) due to an absolute excitation force (from impact hammer). Although the use of relative exciters such as piezoelectric or hydraulic actuators has several advantages, their application has not yet been considered in literature. Relative actuators allow for better structural excitation as the excitation spectrum can be designed as required, such that a good signal to noise ratio is achievable throughout the frequency range. The alignment and orientation errors of the excitation force associated with impact excitation is minimized here through the measurement setup. Therefore, the following section investigates under which conditions a relative excitation can be used for experimental response modelling.

4.2.1 Conditional equivalence of relative and absolute excitation

Bedingte Äquivalenz von relativer und absoluter dynamischer Erregung

The sketch of a relative excitation setup for MCT B in x-direction at coordinate *3* is shown in Figure 4.3a. Here, a piezoelectric actuator produces the relative excitation force, whereas a Linear Variable Differential Transducer (LVDT) measures the relative displacement between workpiece and tool. Additionally, one uniaxial acceleration sensor measures the absolute accelerations at the tool and workpiece side, each. Such a setup is common for the experimental investigation of the dynamic behavior of machine tools. Figure 4.3b shows the corresponding sketch for absolute excitation at the tool and workpiece side with the same acceleration sensor positions. Here, the absolute excitation force is introduced by an impact hammer.

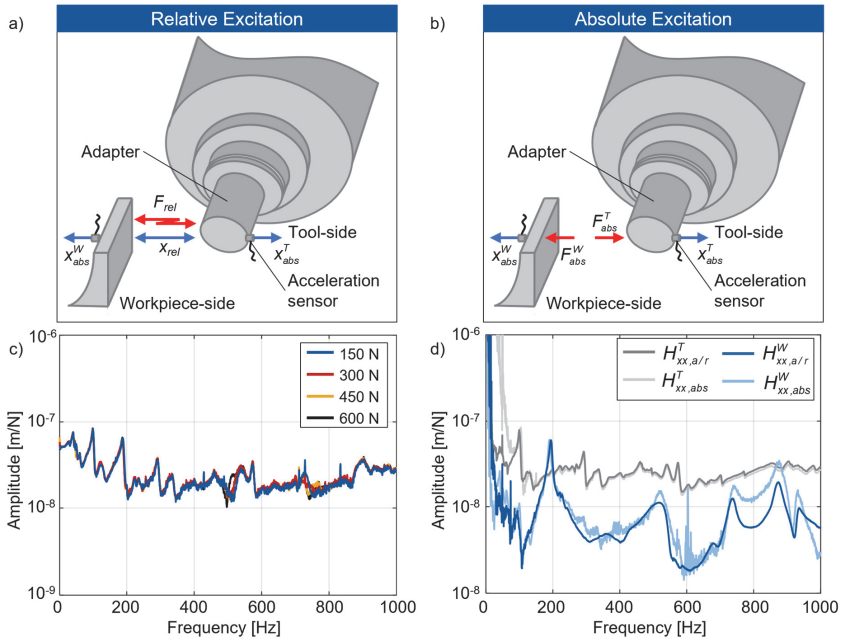

Figure 4.3 Sketches of measurement setups with a) relative and b) absolute excitations.
c) Effect of static preload variation on measured relative FRF, $H_{xx,rel}$
d) Comparison of absolute behavior from absolute and relative excitation

Skizzen von Messaufbauten mit a) relativer und b) absoluter Anregung.
c) Auswirkung der Variation der statischen Vorspannung auf $H_{xx,rel}$
d) Vergleich des Schwingungsverhaltens aus absoluter und relativer Anregung

In the case of relative excitation, assuming linear dynamics and that the ideal stiff actuator and the tool always remain in contact, it can be said that the relative displacement in x-direction is given by,

$$x_{rel} = x^T_{abs} + x^W_{abs} \tag{4.3}$$

where, the superscripts refer to the components (tool or workpiece) and the subscripts to the type of measurement or excitation (relative or absolute). The relative transfer function is then given by (based on [BRAV05]),

$$H_{xx,rel} = \frac{x_{rel}}{F_{rel}} = \frac{x^T_{abs} + x^W_{abs}}{F_{rel}} = \frac{x^T_{abs}}{F_{rel}} + \frac{x^W_{abs}}{F_{rel}} = H^T_{xx,a/r} + H^W_{xx,a/r} = H^{2abs}_{xx,a/r} \tag{4.4}$$

Here, the frequency dependence of the terms is implicit and dropped for brevity. The terms x^T_{abs}/F_{rel} and x^W_{abs}/F_{rel} are usual by-products of experimental machine characterization where, in additional to the relative displacement, the absolute displacements of the workpiece and tool side are also recorded. The summation of these two terms, $H^{2abs}_{xx,a/r}$ is called the 2-times absolute dynamic compliance (German: Zweifachabsolut) and gives the same response behavior as relative dynamic compliance. Now, in relative excitation, equal and opposite forces act on the workpiece and tool side. The force acting on the workpiece side usually causes a negligible displacement on the tool side (and vice versa). This is because of the various dynamically stiff components and joints lying within the force flux between the workpiece, machine structures and the tool. Thus the cross compliance between the workpiece and tool side is stiffer usually by several orders of magnitude. Assuming such dynamically stiff or isolated linear structures, it can be approximated that only the force component acting directly on a particular side causes a deflection on that side such that,

$$\begin{aligned} H^T_{xx,a/r} &= \frac{x^T_{abs}}{F_{rel}} \approx \frac{x^T_{abs}}{F^T_{abs}} = H^T_{xx,abs} \\ H^W_{xx,a/r} &= \frac{x^W_{abs}}{F_{rel}} \approx \frac{x^W_{abs}}{F^W_{abs}} = H^W_{xx,abs}. \end{aligned} \tag{4.5}$$

This is an important inference as it allows the measurement technician to take advantage of the consistent excitation signals and flexible design of the excitation power spectrum provided by relative dynamic actuators or shakers while still obtaining the absolute dynamic behavior. Nevertheless, due to the presence of non-linear joints such as bolted joints, ball bearings, guide shoes, tool interface, etc., the assumption of linearity should be checked before applying the above approximation. A quick check for the effect of non-linearity is the variation of static preload during relative dynamic excitation. As seen in Figure 4.3c, for the analyzed machine, the variation of static preload from 150 to 600 N did not result in any significant change of the dynamic compliance function. The assumption of dynamic separation can also be quickly checked experimentally by measuring the absolute deflection of one side due an absolute dynamic excitation at the other side. This cross compliance is usually several orders of magnitude smaller than the collocated FRFs. This was validated for the FRF at the free end of the cylindrical adapter in the 5-axis MCT B. Once these preconditions are checked, the approximation in Eq. (4.5) can be applied. The absolute dynamic behavior of each

side due to a relative excitation (by a piezoelectric actuator) and due to absolute excitation (by an impact hammer) is compared in Figure 4.3d. It can be observed that the absolute dynamic behavior of both, the workpiece as well as the tool side, exhibits a nearly identical behavior irrespective of the type of excitation and confirms the approximation of Eq. (4.5). Thus, if the conditions of linearity and negligible cross talk between the tool and workpiece table are fulfilled, the absolute and relative excitations produce equivalent results ($H^{T}_{xx,abs} = H^{T}_{xx,a/r}$).

Another way of checking the validity of Eq. (4.5), is to compare the 2-times absolute FRF from the complex addition of the absolute FRFs obtained from relative excitation ($H^{T}_{xx,a/r}$, $H^{W}_{xx,a/r}$), with the directly measured relative FRF, $H_{xx,rel}$. These are shown in Figure 4.4 along with the 2-times absolute FRF obtained from the addition of the absolute excitation FRFs,

$$H^{T}_{xx,abs} + H^{W}_{xx,abs} = H^{2abs}_{xx,abs} \tag{4.6}$$

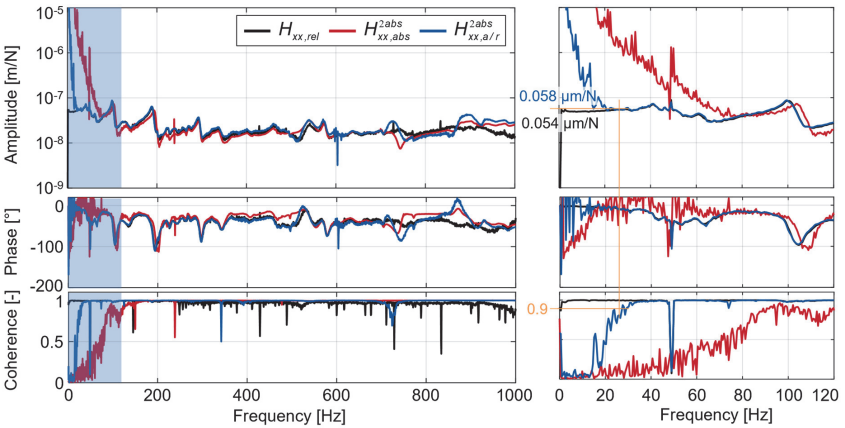

Figure 4.4 Comparison of relative FRFs
Vergleich von relativen FRFs

All three relative FRFs show a good correspondence throughout the measured frequency range indicating the validity of Eq. (4.4) and (4.5). The advantage of the relative excitation setup becomes very clear at lower frequencies (below 100 Hz). Note that both $H^{2abs}_{xx,a/r}$ and $H^{2abs}_{xx,abs}$ are based on measurements at the same location and with the same uniaxial acceleration sensors. However, in the relative excitation setup, the excitation force spectrum was chosen such that the lower frequencies were specifically excited with higher amplitudes. This resulted in better coherence and SNR up to 20 Hz for $H^{2abs}_{xx,a/r}$. This offers the possibility of estimating the static compliance based on the quasi-static compliance values where the coherence values start decreasing below 0.9. As an example, these values are extrapolated to 0 Hz assuming that there are no significant resonances below 20 Hz and the phase shift remains at 0°. The estimated value of 0.058 µm/N is close to the relative static compliance value of 0.054 µm/N

measured using the LVDT sensor. Thus, the combination of relative excitation and absolute acceleration measurement allows for the excitation and reliable measurement of a wide frequency range, including the lower quasi-static frequencies. Another inherent advantage of relative excitation is that the static preload eliminates mechanical play and clearances at the joints, such that a more realistic representation of the machine state during cutting can be achieved.

Of course, absolute excitation with modal shakers also allows for the flexible design of the excitation spectrum. However, it is not considered here for comparison because of the high procurement costs, greater space requirement, and significantly longer setup and measurement times compared to impact hammers. These disadvantages make modal shakers unsuitable for experimental response modelling for tool coupling.

4.2.2 Evaluation of measurement strategies

Bewertung von Messstrategien

Before different measurement strategies can be evaluated and compared, a discussion regarding the criteria for evaluation is necessary. An ideal strategy should achieve high measurement accuracy within the frequency range of interest by minimizing bias and random errors. On the other hand, measurements should be able to be conducted in a time and cost-effective manner. The evaluation criteria based on the above statements can be defined more formally as follows:

- *Frequency range*: In the context of conventional milling machines, the response model must be measured at least up to 1.5 – 2 kHz. Ideally, the response behavior at 0 Hz (static) should also be captured in the same setup or be extrapolated from the measured quasi-static response behavior. This is required for the subsequent prediction of the static compliance of the tool.
- *Scope of bias errors*: The exciter-sensor pair should be chosen such that the possibility of bias error especially due to orientation and positioning error is minimized.
- *Setup time*: Short setup and measurement times are highly essential for rapid measurement of the dynamic behavior at different positions and orientations.
- *Sensor mass loading*: Low mass (< 5 g) or contactless sensors are preferable as the subsequent mass cancellation and associated errors are avoided.
- *Measurement under rotation*: A setup, which allows the excitation and measurement of the spindle speed-dependent dynamic behavior at the adapter, is desirable.
- *Equipment costs*: High procurement costs of measurement equipment can potentially prohibit the widespread industrial application of the tool coupling framework. Hence, lower equipment procurement costs are favorable. The procurement cost of an accelerometer, impact hammer and required amplifiers is taken as a benchmark.

Three excitation instruments and three response measurement sensors, which are commonly used in literature and industrial practice, are evaluated for their suitability

for experimental response modelling. These include the conventionally used impact hammer and low-mass inertial accelerometer. Apart from this, a piezoelectric actuator and a linearly actuated impact hammer (see Figure 4.9) are considered. For dynamic response measurement at the adapter, a laser Doppler vibrometer and a LVDT displacement sensor are applied. The manufacturer's designation of each utilized instrument is specified in Table 4.1 along with the evaluation of their properties with respect to the above-defined criteria. In order to allow comparison and evaluation of the instruments, the criteria are expressed as statements, which can be applicable, partly applicable or not applicable.

Table 4.1 Evaluation of excitors and sensors with respect to derived criteria
Bewertung von Erregern und Sensoren anhand von abgeleiteten Kriterien

	Actuators			Sensors		
Properties / Criteria	**Impact hammer**	**Actuated impact hammer**	**Piezo-electric actuator**	**Accelero-meter**	**LVDT**	**Laser vibrometer**
Designation	Kistler 9724A5000	WZL Design	PI P-243.10	Brüel & Kjaer Type 4374	Solartron AX/1/S	Polytec VibroFlex Connect
Excitation/ meas. type	Absolute	Absolute	Relative	Absolute	Relative	Relative/ Absolute
Excitation/ meas. freq. range	0 – 3000 Hz (PVC tip) [MALI18]	0 – 3000 Hz (PVC tip) [MALI18]	0 – 10000 Hz	Approx. 5 – 26000 Hz	Approx. 0 – 2000 Hz	24 MHz (displace-ment)
Low scope of bias errors	◔	◕	●	●	◕	◕
Low setup and meas. Time	●	◕	◔	●	◔	◑
Meas. under rotation	◕	●	◔	◔	◔	●
Low equipment cost	● Benchmark	◕	◔	● Benchmark	●	◔
Negligible mass loading	-	-	-	◕	●	●

● : Applies fully ◕ ◑ ◔ : Applies partially ◔ : Does not apply

The evaluation in the above table highlights the constraints of each instrument and the fact that none of the instruments entirely fulfills all the criteria. Although the impact-based instruments fulfill many of the criteria, they suffer from the disadvantage of tip-dependent excitation spectrum [MALI18; PCB 21]. The piezoelectric actuator enables precise excitation in a wider frequency range but requires longer setup and measurement times. With respect to the sensors, the miniature, low-mass accelerometer meets all the necessary criteria except the ability to measure at 0 Hz and under rotation. Note that both, the LVDT sensor as well as the vibrometer, measure the relative deflection

between the adapter and the sensor holder (usually a magnetic base clamped to the workpiece table). If an externally placed holder such as a tripod is used for holding the laser source of the vibrometer, it is considered an absolute measurement.

Now, the three excitation instruments and three sensors allow for nine possible combinations or measurement strategies. In order to evaluate each combination and to understand practical limitations, each setup was implemented for the measurement of H_{33}^{A} at a Ø35 mm adapter clamped on MCT A. Prior to measurement, the preconditions for equivalence of absolute and relative excitation derived in Section 4.2.1 were validated and checked. FRFs for each sensor-exciter combination were measured with a sampling rate of 8 kHz and were windowed with 50 % overlapping HANN windows. The length of the window was adjusted, such that a resolution of 0.5 Hz could be achieved for each FRF. Five measurement repetitions were conducted to obtain the averaged FRF. Figure 4.5 shows three exemplary measurement setups for excitation with a piezoelectric actuator.

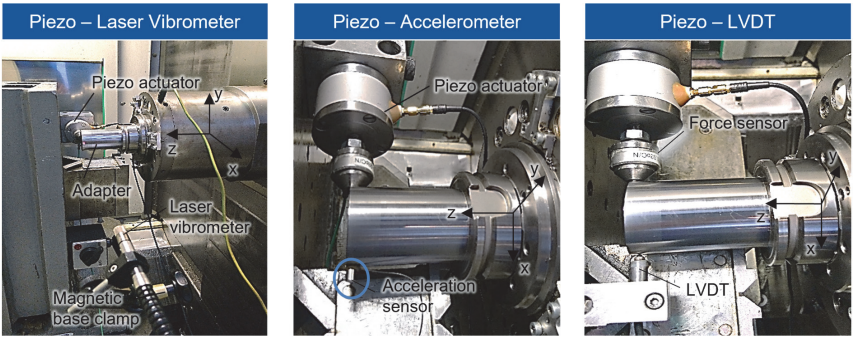

Figure 4.5 Measurement setups with piezoelectric actuator
Messaufbauten mit piezoelektrischem Erreger

The main effects, observations and implementation issues related to all the combinations are summarized in the following.

Firstly, it was observed, that nearly identical FRFs were obtained from manually operated and automatically actuated impact hammer, independent of the used sensor. Figure 4.6 (left) illustrates this for the case of the acceleration sensor. However, since the actuated impact hammer maintains relatively consistent orientation and impact location, the resulting FRFs are still considered to be more reliable and repeatable. The quality of manual impact excitation is largely dependent on operator skills.

Secondly, the combination of impact excitation (manual or actuated) and LVDT sensor proved to be problematic to implement and did not reliably produce acceptable FRFs. A probable cause for this was the occasional 'jumping' of the spring-loaded LVDT and short loss of contact with the adapter due to the impact at the radially opposite side. Thus, this combination is regarded as unsuitable and ruled out for the subsequent analysis.

Thirdly, the comparison of FRFs from piezo excitation with different sensors showed that the best coherence behavior throughout the frequency range could be achieved with the accelerometer. The FRFs from the other two sensors were susceptible to measurement noise especially at the anti-resonances or zeros as seen in the coherence plot in Figure 4.6 (right) at about 1200 Hz. Apart from this, the vibrometer FRF shows a resonance peak at 90.6 Hz, which is not observable in any other FRF. This peak most probably corresponds to the resonance of the magnetic base holder of the laser source. Since it is fixed on the workpiece table, it also experiences an excitation from the piezoelectric actuator. Thus, the fixation of sensor holding devices on the workpiece table should be set up with great care or avoided by using an external tripod, if possible.

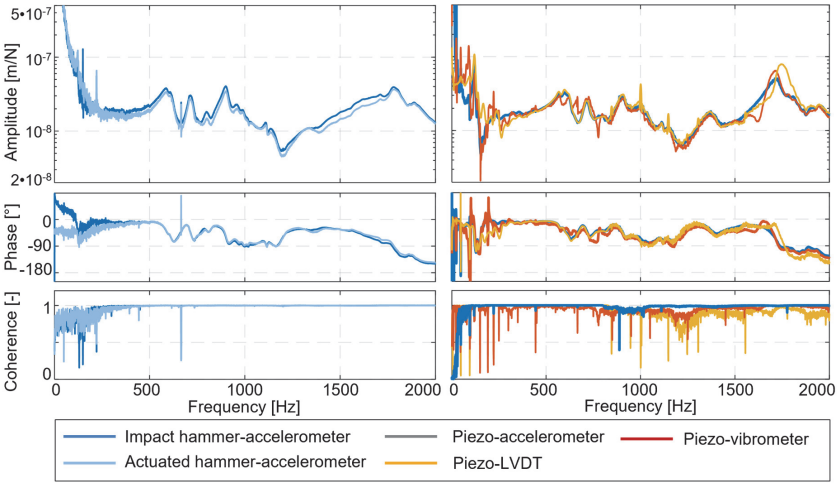

Figure 4.6 Comparison of H^{A}_{33} obtained from different measurement strategies

Vergleich der mit verschiedenen Messstrategien erhaltenen FRF, H^{A}_{33}

Fourthly, the accelerometer with piezoelectric actuator provided more reliable results at lower frequencies than with impact-based excitation. This effect is observable in Figure 4.6 (left) for MCT A as well as in Figure 4.4 for MCT B. Lower frequencies can be specifically excited with larger amplitudes with the piezoelectric actuator than with the PVC tip of the impact hammers. This results in better signal quality and coherence.

Based on the insights attained from the practical implementations, each combination or measurement strategy can now be rated with respect to the criteria derived for experimental response modelling. The evaluation of each combination is summarized in form of a matrix in Figure 4.7. The matrix illustrates, that the choice of excitation and response measurement is strongly dependent on the goals and constraints of the measurement campaign. For example, if good quality measurements are required at different machine positions with minimum effort, time and cost, the accelerometer-actuated hammer combination offers the best compromise. The drawback is that lower

frequencies (<100 Hz) are not measured reliably or require additional measurements with a soft rubber tip. Therefore, this combination is suitable for cases where the prediction of dynamic tool behavior is the primary goal. For example, in process stability calculations, the knowledge of tool-tip dynamic behavior is of greater importance than the static stiffness.

On the other hand, when highly accurate measurements are required in a wide frequency range, including quasi-static range, the accelerometer-piezoelectric actuator combination is most suitable. Since this strategy provides coherence above 0.9 up to 20 - 40 Hz, the static stiffness can be reliably extrapolated as shown in Figure 4.4. This strategy is best suited for applications of virtual quality prediction, where the accurate static and quasi-static response of the tool to forced excitation is essential.

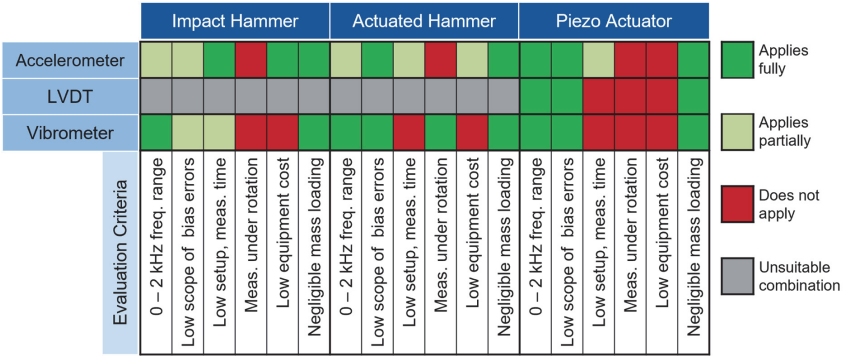

Figure 4.7 Evaluation matrix for different measurement strategies

Bewertungsmatrix für verschiedene Messstrategien

Based on the above analysis and comparisons, it can be summarized, that the combination of piezoelectric actuator and acceleration sensor is most suitable for measurement of displacement-to-force FRFs at non-rotating spindles. For measurement at different operating points of the spindle, the combination of vibrometer and the automatically actuated impact hammer is the only viable option out of the analyzed instruments. However, the high equipment costs associated with the vibrometer limits their use to laboratory environment. In future works the non-contact capacitive and inductive (eddy current) sensors should be evaluated for their suitability for experimental response modelling using the developed assessment criteria.

4.3 Identification of rotational compliances

Identifikation von rotatorischen Nachgiebigkeiten

In this section, two new methods for identifying the rotational compliances at the free end of the adapter are introduced, analyzed and compared with the method by SCHMITZ et al. [SCHM05]. Here, the focus is not on the method of excitation but rather on the synthesis of rotational compliances based on measured FRFs. The first method is based only on the measured displacement-to-force FRFs (Section 4.3.1). The second method explores the use of rotational accelerometer for the measurement of rotation-to-force FRFs and using these for synthesizing the rotation-to-moment FRF. A suitable method for cancellation of the significant mass loading effect on the rotational DOF is also provided (Section 4.3.2).

4.3.1 Modal parameter expansion method

Methode der modalen Expansion

This method requires the measurement of three displacement-to-force FRFs (H^A_{33}, H^A_{32}, H^A_{31}) on the adapter at constant distances d, identical to the approach in [SCHM05]. These are then used for determining the rotation-to-force FRF (N^A_{33}) using, for example, a second order finite backward difference method as shown in Subsection 2.3.2. Applying Eq. (2.21) for calculating N^A_{33},

$$N^A_{33} = \frac{3H^A_{33} - 4H^A_{32} + H^A_{31}}{2\mathrm{d}}. \tag{4.7}$$

Now, the available FRFs H^A_{33} and N^A_{33} are associated with the translational and rotational degrees of freedom respectively and represent the first column of the compliance matrix $\boldsymbol{G}^A_{33}$. A modal parameter estimation of these FRFs and subsequent expansion is therefore applied to identify the rotation-to-moment FRF P^A_{33}. For this, first, the global poles of the substructure are identified using the Least-Squares Complex Frequency (LSCF) algorithm and then the residues and residuals are estimated using the Least-Squares Frequency-Domain Residue (LSFD) estimator [GUIL03; PEET04]. This step delivers the pole vector p as well as the residue matrix $\boldsymbol{R}$, which has merely one row,

$$p = [p_1\ p_2\ \ldots p_\mathrm{n}] \text{ and } \boldsymbol{R}_{2\times 1\times \mathrm{n}} = \begin{bmatrix} \Phi_{x,3}\Phi_{x,3} \\ \Phi_{\theta,3}\Phi_{x,3} \end{bmatrix}. \tag{4.8}$$

Here n is the number of poles identified and x is merely the example direction of measurement. The mode shape (or eigenvector) associated with the rotational deflection ($\Phi_{\theta,3}$) is now easily obtained by the following simple manipulations,

$$\Phi_{\theta,3} = \boldsymbol{R}(2,1,\mathrm{n})/\Phi_{x,3}, \text{ where } \Phi_{x,3} = \sqrt{\boldsymbol{R}(1,1,\mathrm{n})}. \tag{4.9}$$

P^A_{33} is found by the superposition of modal parameters corresponding to rotational input and output degrees of freedom,

$$P_{33}^{A}(j\omega) = \sum_{k=1}^{n}\left(\frac{\Phi_{\theta,3}(k)\Phi_{\theta,3}(k)}{j\omega - p_k} + \frac{\left(\Phi_{\theta,3}(k)\Phi_{\theta,3}(k)\right)^{*}}{j\omega - p_k^{*}}\right). \tag{4.10}$$

Thus, the FRF matrix is expanded by utilizing the estimated modal parameters of the measurable FRFs. Since all FRFs are measured at the same coordinate, MAXWELL's reciprocal theorem can be applied to equate N_{33}^{A} with L_{33}^{A},

$$N_{33}^{A} = L_{33}^{A}. \tag{4.11}$$

In this way, all the components of $\boldsymbol{G}_{33}^{A}$ are obtained. For analysis, this approach was implemented for a simplified adapter-spindle assembly. The dynamic analysis of the assembly was conducted in an FEM environment. Figure 4.8a shows the FEM model with condensation nodes on the adapter representing the three impact locations in x-direction for H_{33}^{A}, H_{32}^{A} and H_{31}^{A}. Based on these three simulated FRFs, P_{33}^{A} is obtained using the SCHMITZ's formulation as well as the proposed approach. A comparison of both approaches shows that the formulation in [SCHM05] creates spurious poles after each zero which are not present in the reference FRF in Figure 4.8b. A characteristic of this complex division formulation is the spurious phase shift above 0° at the anti-resonances and the drop back to 0° at the spurious poles. The modal expansion approach, on the other hand, does not create spurious poles or phase shifts and corresponds well with the reference FRF. Another advantage of the proposed approach for real measurements is that the propagation of measurement noise to P_{33}^{A} is completely avoided due to the transformation in modal domain. Certainly, the limitation due to modal truncation is always associated with any modal truncation.

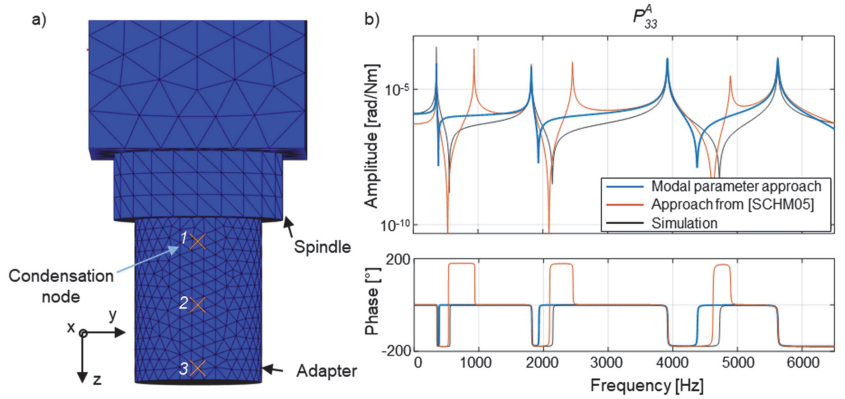

Figure 4.8 a) FEM model of adapter-spindle assembly;
b) comparison of P_{33}^{A} FRFs [BREC16a]
a) FEM-Model der Adapter-Spindel-Baugruppe;
b) Vergleich von P_{33}^{A} [BREC16a]

4.3.2 Use of rotational accelerometer

Verwendung von Winkelbeschleunigungssensor

The use of commercially available rotational accelerometers for the measurement of ERMs of machine tools has not yet been explored in literature. In the proposed method, a lateral rotational accelerometer of Type 8840 from KISTLER INSTRUMENTE GMBH is used in addition to the previously introduced miniature uniaxial accelerometer Type 4374 from BRÜEL & KJAER GMBH for obtaining the compliance matrix at the free end of an adapter. Figure 4.9 shows the rotational accelerometer mounted on a cylindrical adapter (ø35 mm, length 55 mm) using an M5 bolt such that the rotation about the y-axis at coordinate *3* ($\theta^A_{y,3}$) is measured. An important aspect, which must be considered while using a rotational accelerometer, is the resulting mass loading effect.

In this subsection, a method is proposed for cancellation of mass loading effect of the rotational accelerometer such that corrected rotation-to-force FRFs can be obtained at collocated (N^A_{33}) and non-collocated DOFs (N^A_{32}, N^A_{31}). The finite difference method can then be applied to the mass cancelled FRFs to estimate the rotation-to-moment FRF at coordinate *3* of the adapter (P^A_{33}). The mass of the rotational accelerometer including the cable, washer and bolt amounts to approx. 28 g. This mass is significantly greater than that of the uniaxial sensor (0.65 g) and can influence the vibration behavior of the adapter, such that its effect must be compensated before further analysis. The translational inertia effects of conventional accelerometer can be cancelled using structural modification technique [ÖZŞA10]. However, the compensation of mass loading effect on rotational compliances is not as simple and straightforward as for translational compliance functions.

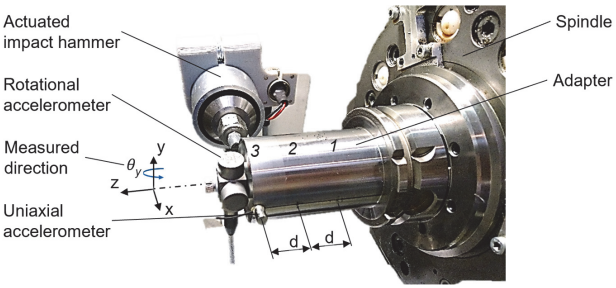

Figure 4.9 Adapter measurement setup with rotational accelerometer

Messaufbau mit Winkelbeschleunigungssensor

Only few research works have dealt with the problem of compensation of sensor mass loading from rotational FRFs. MAIA et al. [MAIA97] propose a 'Mass Uncoupling Method' for removing the rotational inertia effects of the commonly used T-block from rotational FRFs. CAKAR and SANLITURK [CAKA05] presented a general formulation for the elimination of sensor translational and rotational inertia based on the SHERMAN-MORRISON identity. The experimental implementation of this method for a simple overhanging beam and sensor mass showed promising results. Therefore, this method is

implemented and adapted here for the removal of inertia effects of the rotational accelerometer. The general formulation for obtaining an FRF (without inertia effects), α_{pq} at any DOF *p* due to excitation at DOF *q* with the presence of a (sensor) mass at DOF *r* is given as [CAKA05],

$$\alpha_{pq} = \frac{\alpha^r_{pq} + m\omega^2\left(\alpha^r_{rr}\alpha^r_{pq} - \alpha^r_{pr}\alpha^r_{rq}\right)}{1 + m\omega^2\alpha^r_{rr}} \tag{4.12}$$

Note that *p* and *q* can be translational or rotational DOFs, such that the term *m* can be understood as the translational or rotational inertia. Applying the above general formulation to the case of the adapter, where the effect of the sensor inertia *m* at coordinate *3* on the measured rotation-to-force FRF is to be cancelled ($p = \theta^A_{y,3}; q = x^A_3; r = x^A_3$),

$$\alpha_{\theta_{y,3}x_3} = \frac{\alpha^{x_3}_{\theta_{y,3}x_3}}{1 + m\omega^2\alpha^{x_3}_{x_3,x_3}} \tag{4.13}$$

The designation *A* in the superscript is excluded above for brevity. The above equation can now be expressed in familiar terms as,

$$N^A_{33} = \frac{N^{Am}_{33}}{1 + m\omega^2 H^{Am}_{33}} \tag{4.14}$$

Here *m* in the superscript of the FRF implies that it is measured with the rotational accelerometer attached to the adapter. Therefore, the *H* and *N*-terms must be measured simultaneously with both, the translational and rotational accelerometers, attached to the adapter during impact testing. Note that the rotational sensor possesses inertia in all six DOFs and hence adds inertias along these DOFs to the adapter as well. With Eq. (4.14), the influence of mass (translational inertia) on N^{Am}_{33} can be cancelled. For the elimination of the influence of inertias in other DOFs, Eq. (4.12) has to be solved recursively [CAKA05]. Thus, the rotational inertia J_{yy} of the sensor about $\theta^A_{y,3}$ can also be cancelled with ($p = \theta^A_{y,3}; q = x^A_3; r = \theta^A_{y,3}$),

$$N^A_{33} = \frac{N^{Am}_{33}}{1 + J_{yy}\omega^2 P^{Am}_{33}} \tag{4.15}$$

where, N^{Am}_{33} is taken as the FRF obtained by solving Eq. (4.14). The information about the rotational inertia of the sensor about different axis is not available from manufacturer's datasheet. Thus, it is merely estimated here by creating a corresponding model in a Computer Aided Design (CAD) environment and assuming a uniform material density based on the mass of the sensor. The corresponding estimated collocated rotational inertias at the plane of the adapter (coordinate *3*) are: $J_{xx} = 2.97\times10^{-6}$ kgm^2, $J_{yy} = 3.3\times10^{-6}$ kgm^2, $J_{zz} = 2.36\times10^{-6}$ kgm^2. Apart from the rotational inertia, Eq. (4.15) also requires the measurement of P^{Am}_{33}, which cannot be acquired directly. Therefore, it is proposed to estimate it by using the finite backwards difference method applied to the rotation-to-force FRFs. For this, the dynamic exciter is moved to coordinates *2* and *1* (separated by a constant distance, d) and the rotation-to-force

FRFs (N_{32}^{Am}, N_{31}^{Am}) are measured. Now the formulation proposed by ALBERTELLI et al. [ALBE13b] can be adjusted such that the *N*-terms are used for estimating P_{33}^{Am},

$$P_{33}^{Am} = \frac{3N_{33}^{Am} - 4N_{32}^{Am} + N_{31}^{Am}}{2\mathrm{d}}. \tag{4.16}$$

Eq. (4.15) can now be solved based on the above synthesized value. The removal of further inertia effects by the recursive solution of Eq. (4.12) requires the knowledge of cross compliance functions, which cannot practically be measured. Hence, further mass cancellation is not viable and therefore not conducted. Apart from mass loading, another minor effect that must be corrected is the longer lever-arm effect of the rotational sensor. Due to the mounting situation and location of transducers, the rotational acceleration is measured at about 8 mm away from the location of the accelerometer, which is the assumed location of coordinate *3*. This leads to greater acceleration amplitudes which are linearly compensated here. In this way, the mass cancelled and corrected rotation-to-force FRF at coordinate *3* of the adapter shown in Figure 4.9 is achieved.

Figure 4.10 shows the comparison between the mass-cancelled (N_{33}^{A}) and the raw rotation-to-force FRF (N_{33}^{Am}) measured by the rotational accelerometer. Additionally, N_{33}^{Abd} obtained by applying the second order backwards difference method to three displacement-to-force FRFs, H_{33}^{A}, H_{32}^{A}, H_{31}^{A} is also plotted. This serves as an indicative reference because the displacement-to-force FRFs are measured at the adapter without the assembly of the rotational accelerometer. Note that N_{33}^{Abd} is also subject to experimental as well as approximation errors associated with the finite difference method.

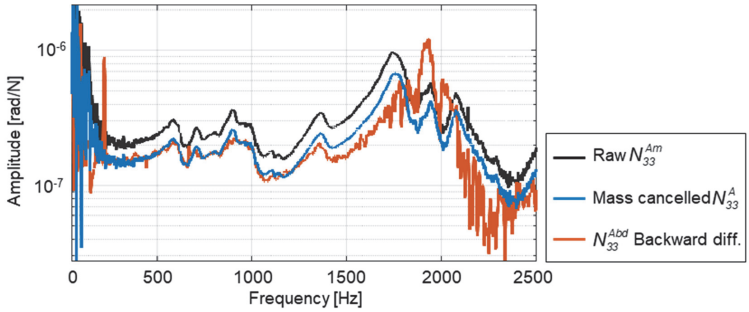

Figure 4.10 Comparison of rotation-to-force FRFs at coordinate *3*, N_{33}^{A}

Vergleich der Rotation-zu-Kraft FRFs an Koordinate 3, N_{33}^{A}

The amplitude of the raw, measured FRF N_{33}^{Am}, however, deviates significantly from the N_{33}^{Abd} and justifies the need to apply mass cancellation before utilization for estimating the rotation-to-moment FRF P_{33}^{A}.

The mass-cancelled FRF N_{33}^{A}, on the other hand, matches very well with the indicative reference FRF up to ca. 1400 Hz. Above this, both have a similar run, but a deviation

in amplitudes is observed. The uncancelled inertia effects most likely cause this deviation from the indicative reference as inertia effects from only two DOFs can be cancelled. Similar to the observations in [DROZ18a], lower frequencies show a significant noise contamination. A high level of noise is also observed in N_{33}^{Abd} due to the inherent noise amplification associated with the finite difference method [KUMA12].

Nevertheless, the proposed mass-cancellation method considerably improves upon the raw measured FRF and can therefore be applied to the non-collocated measured FRFs N_{32}^{Am} and N_{31}^{Am} using Eq.(4.12). The resulting mass-cancelled FRFs, N_{33}^{A}, N_{32}^{A} and N_{31}^{A} are substituted in the following equation to obtain the mass-cancelled rotation-to-moment FRF, P_{33}^{A},

$$P_{33}^{A} = \frac{3N_{33}^{A} - 4N_{32}^{A} + N_{31}^{A}}{2\mathrm{d}}. \tag{4.17}$$

Thus, with the proposed method, the formulation by ALBERTELLI can be applied using merely three rotation-to-force FRFs instead of the measurement of nine displacement-to-force FRFs required in [ALBE13b]. This represents a significant reduction of measurement effort.

For clarity, the developed method for obtaining rotational FRFs is summarized below in four steps:

i) Experimentally obtain the following FRFs at the adapter with the assembled rotational accelerometer: H_{33}^{Am}, N_{33}^{Am}, N_{32}^{Am} and N_{31}^{Am}
ii) Calculate P_{33}^{Am} based on the above measurements and Eq. (4.16)
iii) Obtain mass-cancelled N_{33}^{A} using Eq. (4.14) and (4.15). Similarly calculate mass-cancelled, non-collocated FRFs N_{32}^{A} and N_{31}^{A}
iv) Based on N_{33}^{A}, N_{32}^{A} and N_{31}^{A}, calculate the mass-cancelled rotation-to-moment FRF, P_{33}^{A} using Eq. (4.17)

4.3.3 Comparison of methods and recommendation

Vergleich der Methoden und Empfehlungen

In this subsection, first, the P_{33}^{A} terms derived by complex division, modal parameter expansion and rotational accelerometer are compared with each other, followed by an evaluation of each method. All three methods are applied to the same ø35 mm cylindrical adapter assembled in the spindle as shown in Figure 4.9. The linearly actuated impact hammer is utilized for impulse excitation for all FRFs. For the modal expansion method, the modal parameters of H_{33}^{A} and N_{33}^{A} were estimated till 2000 Hz and P_{33}^{A} was obtained as described in Section 4.3.1. The four-step method developed in Section 4.3.2 for obtaining the *P*-term using the lateral rotational accelerometer is also applied to the same adapter. In Figure 4.11, the amplitude and phase plots of P_{33}^{A} derived from the three methods are plotted.

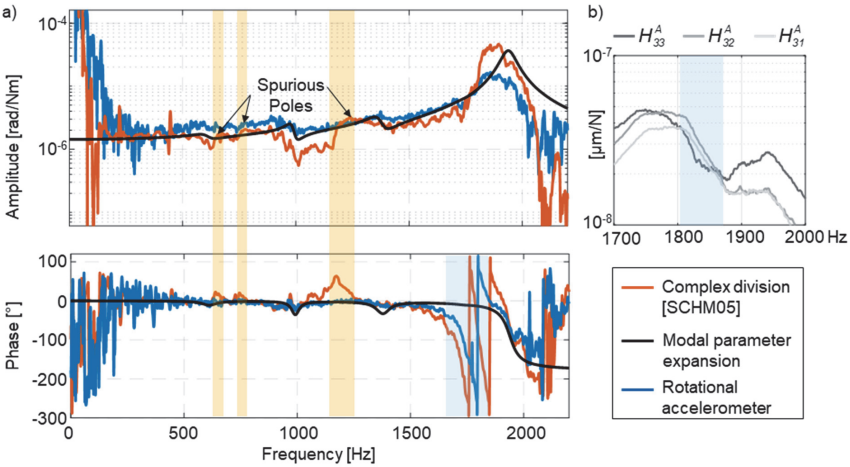

Figure 4.11 a) Comparison of the identified rotation-to-moment FRFs, P^A_{33};
b) Characteristics of *H*-terms at phase shift beyond -180°

a) Vergleich der identifizierten Rotation-zu-Drehmoment FRFs, P^A_{33};
b) Verlauf der H-Terme bei Phasenverschiebung unter -180°

All the three methods provide very similar estimates in the frequency range of interest. As expected, the complex division method leads to spurious poles at several frequencies (640 Hz, 740 Hz and 1165 Hz). These are noticeable at the positive deviations of the phase. However, these are not as prominent as those observed in the simulated example in Figure 4.8b. Apart from this, a high level of noise is observable in the FRFs estimated from the rotational accelerometer as well as from complex division. Both these methods use the finite difference method, which inherently amplifies noise from the measured FRFs [KUMA12]. Furthermore, a phase shift beyond -180° is visible above ca. 1750 Hz, which is most likely caused by the violation of the assumption of the second order backwards difference method that $|H^A_{33}|>|H^A_{32}|>|H^A_{31}|$ and $\angle H^A_{33}>\angle H^A_{32}>\angle H^A_{31}$. The same is valid for the N-terms. As an example, the amplitudes of H^A_{33}, H^A_{32}, H^A_{31} are plotted in Figure 4.11b and show a higher compliance at the inner coordinates than at the free end at the highlighted frequencies. The erroneous phase shift can therefore be avoided by reducing the constant distance between the impact coordinates 1, 2 and 3, such that all of them lie far enough from the nodes of adapter bending modes. The utilized constant gap of 20 mm between successive coordinates is clearly excessive for the 55 mm long adapter.

The modal parameter expansion method offers the key advantage that measurement noise does not propagate to the estimated FRF. The adopted LSCF approach enables the identification of structural poles even for noisy FRFs and ignores spurious and computational poles. Another advantage of the modal domain is that estimations can be obtained at static and quasi-static frequencies, independent of the sensor used for

measurement. The main drawback of this method is that the modal truncation errors are unavoidable. They can, however, be minimized by fitting a wider frequency zone than required (usually 1.5 times the frequency range of interest). The benefits and drawbacks of all three methods are summarized and compared in Table 4.2.

Table 4.2 Comparison of the three methods for identification of rotational compliances
Vergleich der drei Methoden zur Identifikation von rotatorischen Nachgiebigkeiten

SCHMITZ's Method	Modal Parameter Expansion	Using Rotational Accelerometer
Measurement setup: 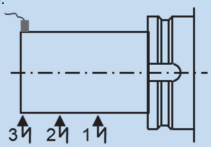		Measurement setup: 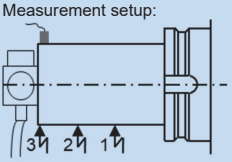
Required measurements: H_{33}^{A}, H_{32}^{A}, H_{31}^{A}		H_{33}^{Am}, N_{33}^{Am}, N_{32}^{Am}, N_{31}^{Am}
N_{33}^{A} obtained from backwards difference method	N_{33}^{A} obtained from backwards difference method	N_{33}^{Am} measured directly. Mass cancellation required
+ Only three FRFs must be measured + No domain transformation necessary + Simple formulation for calculating P_{33}^{A}	+ Only three FRFs must be measured + No measurement noise + No spurious poles created + Static and quasi-static compliance estimated independent of sensor used	+ No spurious poles created + Direct measurement of N_{33}^{Am} + No domain transformation necessary + Low noise above ca. 200 Hz
– Spurious poles are created in P_{33}^{A} – Prone to 'noisy' estimations	– Transformation to modal domain necessary – Modal truncation errors are unavoidable – Difficult to automate; requires manual intervention	– Significant mass loading effect – Frequency range of sensor limited to 2000 Hz – High noise content at low frequencies (<200 Hz)
Not suitable for structures and adaptors with dominant poles and zeros.	Wide applicability as long as backwards difference method provides reliable estimation of *N*.	Applicability limited by frequency range and low signal-to-noise ratio.

Recommended application

The applicability of the SCHMITZ's method of complex division strongly depends on the dynamics of the structure under consideration. An observation of the spurious poles in Figure 4.8b, Figure 4.11 and results from [JI18] indicate, that amplitudes of the spurious poles and zero-shifting are directly related to the amplitudes of poles of the underlying structure. Therefore, the errors caused by complex division are more dramatic for lowly damped structures with dominant poles and zeros. For milling machines (without

tool assembly) with non-dominant poles and low dynamic amplification, the complex division formulation may still be applied to achieve acceptable tool coupling results.

Rotational accelerometers allow for the direct measurement of rotation-to-force FRFs. Their use in experimental response modelling of machines is limited due their frequency range, high measurement noise at low frequencies and substantial mass loading effect. Nevertheless, the presented method for mathematical mass cancellation and synthesis of rotation-to-moment FRF, makes it possible to obtain the corrected response models within the limited frequency range. Because of their low sensitivity (35 μV/rad/s^2), their application is best suited to large machine tools which exhibit relatively high dynamic compliances (e.g.: portal milling machines with overhanging z-carriage and compliances > 1 μm/N). Better sensor SNR is expected for such applications.

The developed modal parameter expansion method enjoys a much wider applicability due to its robustness against measurement noise. A reliable estimate of P_{33}^{A} is possible for any adapter-machine combination as long as care is taken in obtaining *H* and *N*-terms and the structure exhibits linear behavior. Successful tool coupling using the modal parameter expansion method is already demonstrated in [BREC16a].

5 Analytical Response Modelling and Validation

Erstellung und Validierung von analytischen Response-Modellen

Unlike experimental response modelling, where modelling errors result from bias errors, set-up errors, measurement noise, etc., errors in analytical response models result from the various abstractions and assumptions made in the representation of the structure and its behavior. The accurate representation of the holder-tool assemblies is essential for successful coupling. This chapter first introduces an efficient approach for tool assembly modelling called the Extended Tool Model Updating approach (ETMU) (Section 5.1). Then, different beam modelling approaches for obtaining the analytical response model are compared and their suitability for the ETMU approach is evaluated (Section 5.2). Furthermore, methods for modelling typical features of a shrink fit holder such as balancing holes, tapered geometry, composite beam segments, etc. are introduced and validated (Section 5.3). Subsequently the ETMU approach is implemented to obtain the unknown holder-tool joint parameters (Section 5.4) as well as the effective diameter of the fluted segment (Section 5.5) of real holder-end mill assemblies. The obtained results are validated against reference measurements.

5.1 Extended tool model updating approach

Ansatz des erweiterten Werkzeugmodellabgleichs

Within the framework of analytical tool modelling, three main questions have to be answered: i) which modelling approach should be used (EULER-BERNOULLI beam, TIMOSHENKO beam, FEM model, etc.), ii) how should different tool features such as holder-tool joint, balancing holes, composite beam segment, holder taper, etc. be modeled and iii) how should the features be validated or updated in case they cannot be accurately described a priori?

In literature, mainly the modelling and updating of the tool feature of holder-tool joint has been studied extensively. The modelling and subsequent validation (or updating) of other tool features has not been explored adequately. Furthermore, the tool tip FRF in the clamped state is utilized for updating the joint feature model. As seen in the literature survey (Subsection 2.4.3), this brings with itself several disadvantages: i) errors associated with experimental response modeling are propagated to the identified joint model parameters [FILI09], ii) model parameters can be estimated incorrectly [MATT16] and iii) machine availability is reduced. Hence, there is a strong motivation for a completely offline estimation and validation of unknown model parameters of tool feature models.

The aim of this chapter is therefore to introduce an approach for allowing the validation and updating of tool model parameters in an offline manner based on reference FRFs of the tool assembly obtained in a freely constrained state. In order to enable such a direct comparison between the freely constrained tool assembly and the analytical model, it is proposed to extend the freely constrained holder-tool assembly to include

the accurate dynamics of the spindle-holder interface (*I*) for parameter updating. The 'extension' is achieved by means of frequency based substructuring. This approach is termed as the Extended Tool Model Updating (ETMU) approach. Using this approach, the two important challenges in modelling of thermal shrink fit holder and end mill assemblies are addressed: efficient identification of the holder-end mill joint properties and the modelling of the complex fluted segment feature of shaft mills. The validation of different tool feature models is also demonstrated using this approach.

Thermal shrink fit tool assemblies used in milling and drilling spindles with automatic tool changers consist of an end mill, a tool holder and a standard spindle-holder interface. Depending on the type of spindle and tool changer, different standard spindle-holder interfaces can be used, for example, the Morse taper (DIN 228), SK (DIN ISO 7388), HSK (DIN 69893), TS (DIN ISO 26622), etc. [BREC19b]. For a particular spindle, this normed geometry and shape of the interface remains constant. Hence, for the purpose of modelling, the tool assembly is divided into two parts: the normed interface (*I*) and the holder-tool assembly (*ThT*) (see Figure 5.1a).

The geometry of the normed interface may contain complex groves, tapered shanks, balancing holes, clamping holes, notches, etc. Modelling these complex features as uniform cylindrical beam segments and subsequently using receptance coupling (as proposed in [MATT16]), can introduce significant and avoidable modelling errors. Furthermore, merely a one-time accurate modelling is necessary as the interface geometry is normed. Hence, the ETMU approach proposes a one-time ad-hoc FEM modelling of the freely constrained spindle-holder interface. This model is then used to obtain the compliance matrix at the coupling point of the interface flange. In [DANI17] it was shown that ad-hoc FEM models of metal structures without joints or mechanisms can represent the dynamic behavior with high accuracy, such that model updating with a physical prototype is not necessary.

The second part of the tool model consists of the tool holder and the end mill. Since this part changes with each unique holder-tool combination, it can be abstracted as a series of uniform cylindrical beam segments. The fluted segment can be modelled as a uniform beam of equivalent diameter. The compliance matrices at the ends of the 2D beam segments are obtained by solving the characteristic equation of the freely constrained analytical beam. The principal sketch of the implementation of the ETMU approach for a thermal shrink fit tool holder and end mill with an HSK-A 63 interface is shown in Figure 5.1. Here the coordinate *5* is reserved of the SIDS plane as shown in Figure 4.1. Apart from this, the blank tip is also assigned the coordinate *3* as it represents an auxiliary structure like the adapter.

Due to the presence of slots, holes and the orientation groove, the HSK interface has a slightly varying dynamic behavior along different radial directions. Thus, before creating the extended analytical tool model, it is important to know the direction in which the reference FRFs for model updating will be measured. The response model of the HSK should then be created exactly in this direction.

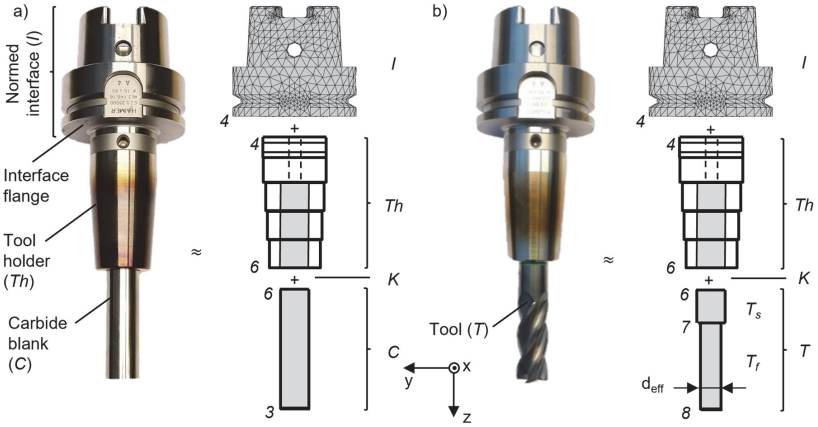

Figure 5.1 Extended analytical tool models for a) carbide blank and b) end mill assembly
Erweiterte Werkzeugmodelle für a) Hartmetallrohling und b) Schaftfräser

In this chapter, as an example, reference FRFs are measured in the y-direction of the local coordinate system shown in Figure 5.1 and hence the coupling calculations are considered only for this direction. Thus, in the freely constrained FEM model of the interface, a force $F^I_{y,4}$ and moment $M^I_{x,4}$ are applied at the master node of the multi-point constraint at coordinate *4*. The subsequent translational y^I_4 and rotational displacement $\theta^I_{x,4}$ are then recorded. The resulting direct compliance matrix of the interface coordinate is given by,

$$\boldsymbol{G}^I_{44} = \begin{bmatrix} H^I_{44} & L^I_{44} \\ N^I_{44} & P^I_{44} \end{bmatrix} = \begin{bmatrix} \dfrac{y^I_4}{F^I_{y,4}} & \dfrac{y^I_4}{M^I_{x,4}} \\ \dfrac{\theta^I_{x,4}}{F^I_{y,4}} & \dfrac{\theta^I_{x,4}}{M^I_{x,4}} \end{bmatrix}. \tag{5.1}$$

The analytical model of the holder or the tool is obtained by end-to-end rigid coupling of beam segments. Now, any given analytical holder model (*Th*) or holder-tool assembly model (*ThT*) can be augmented with the above interface model (*I*) to create an extended model. The rigid coupling of the holder with the interface compliance matrix allows for the calculation of the compliance function at, for example, the end of the extended holder (*ITh*) at coordinate *6* (without tool),

$$\boldsymbol{G}^{ITh}_{66} = \boldsymbol{G}^{Th}_{66} - \boldsymbol{G}^{Th}_{64}(\boldsymbol{G}^{Th}_{44} + \boldsymbol{G}^{I}_{44})^{-1}\boldsymbol{G}^{Th}_{46} \tag{5.2}$$

or at the end of the extended holder-tool assembly (*IThT*),

$$\boldsymbol{G}^{IThT}_{88} = \boldsymbol{G}^{T}_{88} - \boldsymbol{G}^{T}_{86}(\boldsymbol{G}^{ITh}_{66} + \boldsymbol{G}^{T}_{66})^{-1}\boldsymbol{G}^{ITh}_{68} \tag{5.3}$$

or at any other required point on the extended holder-tool assembly. The augmentation of the analytical beam model allows for a direct comparison of analytical calculated

FRFs with the FRFs obtained experimentally in freely constrained state. This comparison can then be used to validate or update the analytical model in a completely offline manner. A higher efficiency and accuracy of the method can be expected because the measurement and analysis of the clamped-free reference FRFs are avoided.

5.2 Analytical beam modelling

Analytische Balkenmodellierung

The accurate analytical modelling of the static and dynamic behaviors of the holder-tool assembly is of fundamental importance for reliable coupling calculations. Here, the choice of modelling approach determines the required computation effort and achievable accuracy of the coupling calculations. In this section, the TIMOSHENKO Beam Model (TBM) is implemented, validated, and compared with the EULER-BERNOULLI Beam Model (EBBM). With this comparison, the suitability of the TBM for implementing the ETMU approach is justified.

There exists relatively simple closed-form expressions for determining the transverse vibration behavior at the ends of an EBBM under different constraint conditions [BISH11]. These are computationally inexpensive but ignore shear deformation and rotational inertia effects, which are relevant for modelling non-slender beams. The TBM, on the other hand, considers these effects but no closed-form equations are available for obtaining the compliance matrices. Although the mathematical formulation for a TBM with generalized end conditions has been given in [ARIS04], its practical implementation for obtaining the compliance matrices at the beam-ends is relatively complex. Hence, for the sake of understanding and completeness, the adopted mathematical implementation based on [HAN99; ARIS04; ERTÜ06; ÖZŞA15] is compiled and explained in the following.

The first step for obtaining the compliance matrix is to find the eigenfrequencies of the free-free TBM. For this, equations of motion from Eq. (2.6) and (2.9) are decoupled into lateral and angular deflections and written in the homogeneous form as,

$$\frac{\partial^4 v}{\partial x^4} - \left(\rho I + \frac{\rho}{k' G}\right)\frac{\partial^4 v}{\partial x^2 \partial t^2} + \rho A \frac{\partial^2 v}{\partial t^2} + \frac{\rho^2 I}{k' G}\frac{\partial^4 v}{\partial t^4} = 0 \tag{5.4}$$

$$\frac{\partial^4 \psi}{\partial x^4} - \left(\rho I + \frac{\rho}{k' G}\right)\frac{\partial^4 \psi}{\partial x^2 \partial t^2} + \rho A \frac{\partial^2 \psi}{\partial t^2} + \frac{\rho^2 I}{k' G}\frac{\partial^4 \psi}{\partial t^4} = 0. \tag{5.5}$$

Assuming harmonic excitation and applying constraints for free-free end conditions, the characteristic equation can be written as [ERTÜ06],

$$\begin{vmatrix} D_{11} & D_{12} \\ D_{21} & D_{22} \end{vmatrix} = D_{11} D_{22} - D_{12} D_{21} = 0 \tag{5.6}$$

where,

$$D_{11} = (a - \lambda)\cdot(\cos a - \cosh b) \tag{5.7}$$

$$D_{12} = (\lambda - a)\cdot \sin a + \frac{\lambda\cdot a}{b\cdot\delta}\cdot(b - \delta)\cdot \sinh b \tag{5.8}$$

$$D_{21} = -\lambda\cdot a\cdot \sin a + \frac{a - \lambda}{\delta - b}\cdot\delta\cdot b\cdot \sinh b \tag{5.9}$$

$$D_{22} = \lambda\cdot a\cdot(\cosh b - \cos a) \tag{5.10}$$

$$\lambda = a - \frac{B^2\cdot s^2}{a};\ \delta = b + \frac{B^2\cdot s^2}{b}. \tag{5.11}$$

Here,

$$a = \sqrt{\Omega + \varepsilon}\ ;\ b = \sqrt{-\Omega + \varepsilon} \tag{5.12}$$

represent the dimensionless frequency numbers. These are expressed in terms of geometric and material properties of the beam as,

$$\Omega = \frac{B^2\cdot(s^2 + R^2)}{2};\ \varepsilon = B\cdot\sqrt{\frac{1}{4}\cdot B^2\cdot\left(s^2 + R^2\right)^2 - \left(B^2\cdot s^2\cdot R^2 - 1\right)}$$
$$B^2 = \frac{\rho\cdot A\cdot\omega^2\cdot L^4}{E\cdot I};\ s^2 = \frac{E\cdot I}{k'\cdot A\cdot G\cdot L^2};\ R^2 = \frac{I}{A\cdot L^2}. \tag{5.13}$$

In order to solve the transcendental characteristic equation, the term 'B' is taken as the unknown variable such that Eq. (5.6) is expressed as a polynomial equation in B. The remaining terms are available from the material and geometric properties. Note that the transcendental Eq. (5.6) is nonlinear and has infinite roots (Figure 5.2). The frequencies at which value of the equation is zero (roots) are also marked in the figure. In literature, iterative numerical approaches such as Newton-Raphson [IRVI99] and golden search method [TUNC18] are suggested for calculating the roots.

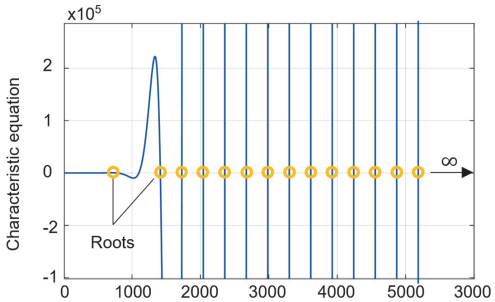

Figure 5.2 Plot of a typical transcendental characteristic equation
Verlauf einer typischen transzendentalen charakteristischen Gleichung

In this thesis, a numerical solution for the characteristic equation is obtained for a certain frequency range by using the Symbolic Math Toolbox from THE MATHWORKS, INC. [MATL22]. As initial guesses of the roots for the numerical solution, multiples of the π/s

terms are taken. Once the r^{th} root of the characteristic equation is available, the corresponding eigenfrequency ω_r as well as the dimensionless frequency numbers a_r and b_r are calculated along with λ_r and δ_r from Eq. (5.13), (5.12) and (5.11), respectively. Using these inputs, the r^{th} lateral and rotational mode shape of the beam at any point (x) can be obtained from,

$$\bar{v}_r(x) = A_r\left[C_1\cdot\sin\left(\frac{a_r}{L}\cdot x\right) + C_2\cdot\cos\left(\frac{a_r}{L}\cdot x\right) + C_3\cdot\sinh\left(\frac{b_r}{L}\cdot x\right) + C_4\cdot\cosh\left(\frac{b_r}{L}\cdot x\right)\right] \quad (5.14)$$

$$\bar{\psi}_r(x) = \frac{A_r}{L}\left[\lambda_r\cdot\left(C_1\cdot\cos\left(\frac{a_r}{L}\cdot x\right) - C_2\cdot\sin\left(\frac{a_r}{L}\cdot x\right)\right) + \delta_r\cdot\left(C_3\cdot\cosh\left(\frac{b_r}{L}\cdot x\right) + C_4\cdot\sinh\left(\frac{b_r}{L}\cdot x\right)\right)\right] \quad (5.15)$$

where,

$$C_1 = L;\ C_2 = -\frac{D_{11}}{D_{12}}\cdot C_1;\ C_3 = \frac{a_r - \lambda_r}{\delta_r - b_r}\cdot C_1;\ C_4 = -\frac{\lambda_r\cdot a_r}{b_r\cdot\delta_r}\cdot\frac{D_{11}}{D_{12}}\cdot C_1\,. \quad (5.16)$$

Note that A_r is a constant scaling term which mass normalizes the r^{th} eigenvector. In order to find this term, the modal mass matrix must first be calculated using the expression for each mode,

$$\hat{M}_r = \int_{x=0}^{L}\begin{Bmatrix} v_r(x) \\ \psi_r(x)\end{Bmatrix}\begin{bmatrix}\rho\cdot A & 0 \\ 0 & \rho\cdot I\end{bmatrix}\{v_r(x) \quad \psi_r(x)\}\cdot dx\,. \quad (5.17)$$

The scaling term required for achieving unity modal mass is thus obtained as follows,

$$A_r = \frac{1}{\sqrt{\hat{M}_r}}. \quad (5.18)$$

In this way, the flexible mode shape functions of the freely constrained TIMOSHENKO beam are achieved. Due to the free-free end conditions, there also exist rigid body beam modes that are derived from simple inertia properties,

$$\bar{v}_{RBM}(x) = \sqrt{\frac{1}{\rho\cdot A\cdot L}};\ \bar{\psi}_{RBM}(x) = \sqrt{\frac{12}{\rho\cdot A\cdot L^3 + 12\rho\cdot I\cdot L}}\cdot\left(x - \frac{L}{2}\right). \quad (5.19)$$

Note that the above modes are already mass normalized. Now, the rigid and flexible body mode shapes at the ends of the beams (x = [0, L]) are derived from appropriate substitution in the mode shape functions Eq. (5.19), (5.14) and (5.15). Subsequently, the FRFs at the beam-ends are derived by applying modal superposition of each of the calculated modal parameters (see Eq. (4.10)). As an example, the equation for collocated displacement-to-force FRF at one end of the TIMOSHENKO beam (x = L) is shown,

$$H_{LL}(\omega) = -\frac{1}{\rho\cdot A\cdot L\cdot\omega^2} - \frac{3L}{\left(\rho\cdot A\cdot L^2 + 12\rho\cdot I\right)\cdot\omega^2} + \sum_{r=1}^{n}\left(\frac{\bar{v}_r(L)\cdot\bar{v}_r(L)}{(1 + j\cdot\xi)\cdot\omega_r^2 - \omega^2}\right). \quad (5.20)$$

Where, ξ represents the structural damping loss factor. Similarly, the FRFs at different degrees of freedom and beam-ends can be obtained by modal superposition, giving the compliance matrices required for substructure coupling: $\boldsymbol{G}_{LL}, \boldsymbol{G}_{0L}, \boldsymbol{G}_{L0}, \boldsymbol{G}_{00}$.

Validation and comparison of modelling approaches

The developed ETMU approach involves the comparison and updating of analytical models in freely constrained states, where the resonance frequencies lie at significantly higher ranges than in the fix-free state. Hence, for the successful implementation of the ETMU approach, it is necessary that the modelling approach accurately represents beam dynamics till higher frequency (ca. 20 kHz). Therefore, the adopted TBM described in this section, the EBBM as well as FEM modelling are compared here with each other and their suitability for ETMU implementation is evaluated. The displacement-to-force FRF at an end of a uniform steel cylinder (ø30 mm, length = 120 mm, material no. 1.0503) in the freely constrained state is derived analytically using different approaches and compared with a reference measurement in Figure 5.3. The FEM model of the cylinder was created using quadratic tetrahedral elements of edge length of 5 mm. Identical material properties are taken for each approach (E = 206.9 GPa, ν = 0.3, ρ = 7780 kg/m^3, ξ = 0.001).

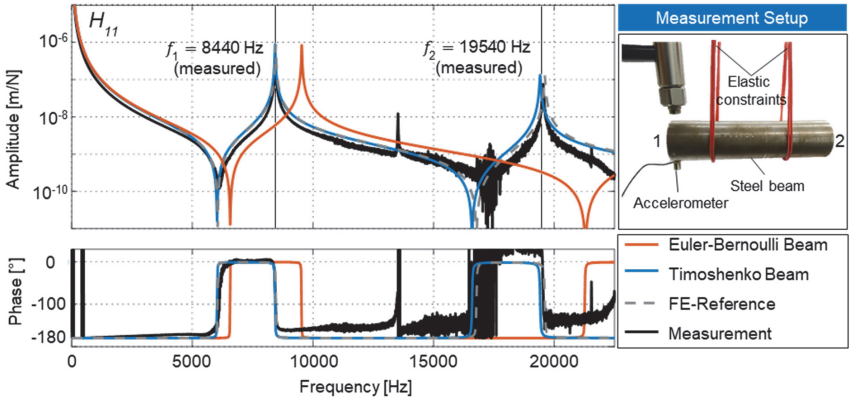

Figure 5.3 Comparison of beam FRFs obtained from different approaches
Vergleich der mit verschiedenen Ansätzen erhaltenen FRFs des Balkens

All approaches show nearly identical response behaviors until about 5 kHz. Beyond this, only the TBM and the FEM model show an excellent correspondence with the reference FRF. The measured bending frequencies at 8440 and 19540 Hz as well as the anti-resonances match very well with the TBM. The EBBM, on the other hand, overestimates the resonance frequencies despite the relatively slender d/L ratio of 0.25. In order to evaluate the influence of beam slenderness on the modelling accuracy, thick cylinders of d/L ratios of 0.5 and 1 are also modelled with the same diameter of 30 mm. Such thick beams are common in tool modelling because of the segmentation of the tool assembly into short, non-slender beams. Therefore, it is important to accurately depict their dynamic behavior. Figure 5.4 shows a lists the frequencies of

the first and second bending modes obtained from the beam and FEM modelling approaches. Since the eigenfrequencies exceed the excitation and measurement range of conventional equipment, the FEM model serves as the reference for validation. The EBBM consistently overestimates the eigenfrequencies independent of chosen slenderness due to the neglecting of shear distortion and rotational inertia effects. This overestimation is observable in the calculated relative errors in Figure 5.4 and increases with each mode. This is consistent with the findings in literature (refer to [HAN99; ERTÜ06]). Despite the overestimation, EBBM can still reliably predict low frequency dynamics, especially for slender beams and has been used for analytical modelling in several works (for example [SCHM04; SCHM05; SCHM06; SCHM07; SCHM19; KUMA12]). This is because, the prediction of the tool tip FRF is usually required in the first few kilo Hertz range. In this frequency range, the convenient closed form solution of the EBBM can still provide sufficiently accurate models for receptance coupling as seen in the example from Figure 5.3. However, for the case of ETMU, where the accurate prediction of the eigenfrequencies is required till much higher frequencies for different d/L ratios, the EBBM approach is not suitable.

The TBM accurately and reliably predicts the bending mode frequencies of beams irrespective of slenderness and is thus ideally suited for the implementation of the ETMU approach. Even the eigenfrequencies of the thick beam of d/L ratio of 1 could be calculated with good accuracy through the numerical solution of the characteristic equation (Eq. (5.6)). For model updating using the ETMU approach, the accurate prediction of the eigenfrequencies (usually the first bending mode) of the tool assembly is of great importance. Therefore, the TBM is chosen for the implementation of the ETMU approach.

d/L- Ratio	0.25		0.5		1	
FEM-Reference	1st Mode [Hz]	2nd Mode [Hz]	1st Mode [Hz]	2nd Mode [Hz]	1st Mode [Hz]	2nd Mode [Hz]
	8459	19610	26140	48360	69930	134400
Measurement	8440	19540	-	-	-	-
Modelling approach	**Relative Error [%]**					
EULER-BERNOULLI	+14	+36	+46	> +100	> +100	> +100
TIMOSHENKO	-0.003	-0.010	-0.12	-0.29	-2.1	-8.6

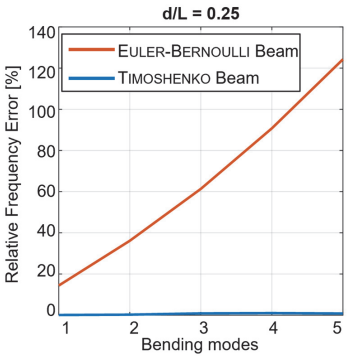

Figure 5.4 Comparison of beam modelling approaches
Vergleich von Balkenmodellierungsansätzen

Apart from model updating, another important aspect for analytical response modelling is the correct calculation of the location (frequency) of the first anti-resonance or zero. This is because the first zero of the free-free beam FRFs may lie within the relevant frequency range required for predicting tool dynamics. The calculation of their location

depends significantly on the number of roots of the characteristic equation considered in the modal superposition equation (modal truncation). Although the error in location reduces with the number of roots considered, this relationship is non-linear. Practical implementation of the TBM approach showed that the first 12 to 15 roots were sufficient for locating the first zero with reasonable accuracy.

5.3 Modelling of shrink fit holder features

Modellierung der Merkmale von Schrumpffuttern

In the following subsections, methods for the analytical response modelling of three common holder features of the shrink fit holder as segmented TIMOSHENKO beams are introduced. The features considered here are: balancing holes, the tapered segment of the holder and the holder segment with the inserted tool (Figure 5.5). The proposed method for modelling each feature is subsequently validated either (where possible) with measurements by extending the model as per the ETMU approach or by FEM simulations. Here, the emphasis is also laid on the accurate prediction of the eigenfrequencies. This is because the subsequent model updating assumes that the only difference between the simulated and measured resonance frequencies results from the unknown model parameter and not modelling errors. Once the methods for feature modelling are validated, accurate analytical tool holder models can be reliably obtained. This then allows for the correct identification of holder-end mill joint parameters as well as the subsequent modelling of the fluted segment. The accompanying implementation of the feature modelling methods in a MATLAB-based program for analytical tool modelling and coupling named ‘CouplingTools’ is also discussed briefly.

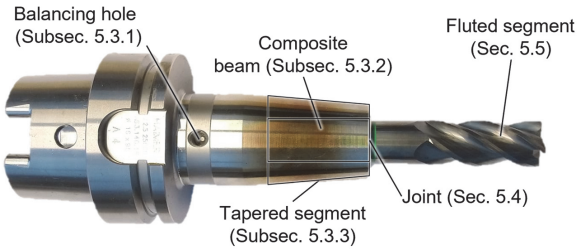

Figure 5.5 Typical features of a shrink fit holder and end mill assembly
Typische Merkmale einer Schrumpffutter-Schaftfräser-Baugruppe

5.3.1 Modelling of balancing holes

Modellierung von Wuchtbohrungen

Unsymmetrical mass distribution in the milling tool assembly creates unbalance forces and moments on the spindle shaft bearing system. These forces and moments are directly proportional to the square of the spindle speed and hence can cause vibrations, machining errors as well as reduce bearing and tool life at high spindle speeds. Therefore, tool holders are provided with one or more balancing planes in the form of radially distributed, threaded blind holes. Grub screws of appropriate weight can be inserted in

the threaded holes to compensate the unbalance vector. Usually, shrink fit holders have a balancing plane at the root-end (Figure 5.5), such that the unoccupied holes can cause a structural weakening of the holder shaft and affect the bending mode frequencies. This effect is of course amplified for smaller shaft diameters with large balancing hole diameters and depths. Although balancing holes are a common feature in tool holders and can influence dynamic behavior, their accurate modelling has not been considered in literature.

Figure 5.6 shows a typical shrink fit holder model with four balancing holes and a coolant channel. The taper of the holder is intentionally left out to consider the effect of the balancing holes in isolation. Now in the beam modelling approach, tool features can only be represented as hollow or full cylinders. Therefore, it is proposed to calculate an effective outer diameter (d_{eff}) of the balancing hole segment, area moments of inertia (I) and cross-section area (A) based on the section (X-X) passing through the middle of balancing holes. The inner diameter of the segment corresponds to the coolant channel diameter (d_{cc}).

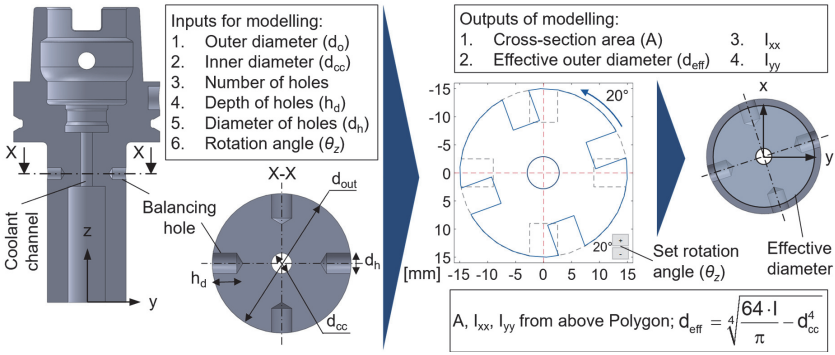

Figure 5.6 Method for modelling the balancing hole feature

Verfahren zur Modellierung von Abschnitt der Wuchtbohrungen

The balancing hole cross-section provides all the inputs required for calculating the effective geometric properties of the equivalent beam. Using the parametric inputs listed in Figure 5.6, a closed polygon representation of the cross-section can be created without any CAD model. Based on this polygon, the cross-section area, area moments of inertia and subsequently the effective diameter can easily be calculated for any rotational position of the holder. The cross-section properties are then attributed to a beam segment which is as thick as the diameter of a balancing hole. This feature modelling method is integrated in the 'Analytical Response Modelling Routine' of the developed 'CouplingTools' software (see Appendix A.1).

For the validation of the proposed feature modelling method, two holders with outer diameter of 35 mm and length 70 mm were custom manufactured with balancing holes and without any taper (identical to the one in Figure 5.6): one with four balancing holes (*Th4H*) and one with six holes (*Th6H*) as described in Figure 5.7. Analytical beam

models of each holder were created as a four-segment TIMOSHENKO beam, where the effective diameter and moments of inertia were calculated using the above proposed method. The compliance matrix at the ends of each of the beam segments were calculated using the described TBM method (Section 5.2) and rigidly coupled with each other to obtain he compliance matrix at the ends of the complete beam model. In accordance with the ETMU approach, the analytical response model was extended by coupling the HSK-interface at one end applying Eq (5.2). Subsequently the displacement-to-force collocated FRF at coordinate *6* (H^{lTh}_{6y6y}) of the extended holder model was calculated and obtained experimentally. The comparisons are presented in Figure 5.7.

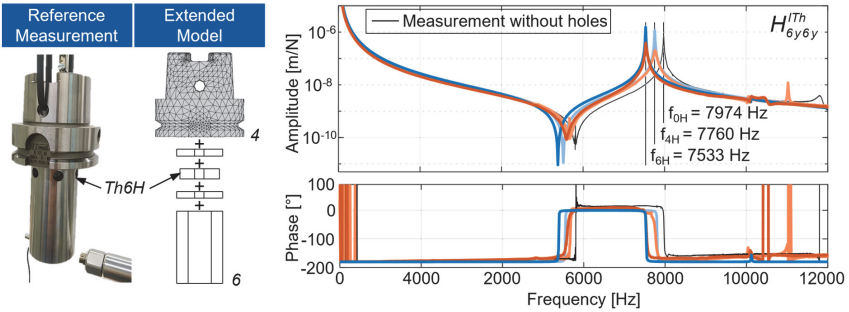

Th4H	Four balancing holes: ø 6.8 x 10 mm	d_{eff} = 31.51 mm	Model	Reference
Th6H	Six balancing holes: ø 6.8 x 10 mm	d_{eff} = 29.5 mm	Model	Reference

Figure 5.7 Validation of method for modelling balancing hole feature
Validierung der Methode zur Modellierung von Wuchtbohrungen

The predicted and reference FRFs show a very good correspondence for both tool holders. The resonance frequency as well as the anti-resonances could be predicted with good accuracy, indicating that the validity of the feature modelling method. The dynamic weakening effect is clearly observable in the shifting of the first bending mode from 7760 Hz to 7533 Hz for *Th4H* and *Th6H* respectively. For further comparison, an identical tool holder without any balancing holes was also experimentally analyzed. The corresponding first mode lies higher at 7974 Hz. This indicates that the effect of loss of dynamic stiffness due to the presence of balancing holes is greater than the effect of reduced mass. The proposed method can also be implemented in cases, where balancing masses in form of grub screws are inserted in the balancing holes. In these cases, the merely the shape of the section polygon must be modified by reducing the corresponding hole depth (h_d).

5.3.2 Modelling of holder-inserted tool segment

Modellierung des Halter-Werkzeug-Abschnitts

Since the tool and holder are made of different materials, the part of the holder with the inserted end mill is often modelled as a uniform composite beam, whose properties are a combination of the properties of the individual concentric beams [SCHM05;

SCHM06]. Here, it is assumed that the concentric beams share a common neutral axis during deflection and the effect of the holder-end mill joint stiffness and damping is not included. As an alternative, the internal, multipoint coupling along the length of the holder and end mill beams as EBBM is proposed in [SCHM06; SCHM19]. This requires the calculation of a large number of receptances and is hence not suitable for TIMOSHENKO beam modelling due to the comparatively higher computational effort. In [SCHM06], the equivalent mass (m_{eq}) and equivalent modulus-inertia product (EI_{eq}) of the reference composite beam are derived easily because of their relation with beam diameter,

$$EI_{eq} = \frac{\pi}{64}\left(E_o\left(d_o^4 - d_i^4\right) + E_i d_i^4\right); m_{eq} = \frac{\pi}{4}\left(\rho_o\left(d_o^2 - d_i^2\right) + \rho_i d_i^2\right)L. \tag{5.21}$$

Here, the subscript 'o' refers to the outer hollow beam (holder) and 'i' refers to the inner full beam (end mill or carbide blank). The calculation of other material properties of the composite beam such as density and damping loss factor are not explicitly described in literature. In the proposed feature modelling method, the relation of the individual beam's cross-section area to the total cross-section area (A) is used for attributing properties to the composite beam. For example, the density of the composite beam is,

$$\rho_{eq} = \left(\frac{A_o}{A}\right)\rho_o + \left(\frac{A_i}{A}\right)\rho_i. \tag{5.22}$$

In this way, all the equivalent geometric and material parameters of the composite beam can be obtained and the analytical response modelled can be derived by applying Eq. (5.6) to (5.20).

For validation and analysis of the proposed feature modelling method, holder-tool segments of varying inner and outer diameters were created. As an analysis object, a hollow steel cylinder of length 64 mm outer diameter of 32 mm (d_o) and inner diameter d_i along with an inner carbide cylinder of the same diameter d_i was considered (Figure 5.8a). Here again, the taper present on a real tool holder was left out in order to study the composite beam model in isolation. The diameter ratio d_i/d_o was varied from 0.25 to 0.75. Real tool holders have a d_i/d_o-ratio that usually varies from 0.3 to 0.5 along the length of the taper. Values above 0.5 are not realistic and have been included merely for the sake of completeness. Now for each ratio, a composite beam was created using the proposed TBM approach. For validation, corresponding FE models of the concentric beams were built, where the properties of inner and outer cylinders were retained. Figure 5.8b shows the plot of the relative error between the eigenfrequencies of the r^{th} mode (first and second bending modes) obtained from the composite beam (ω_r^{Comp}) and FEM model (ω_r^{FEM}) over the diameter ratio. Additionally, the eigenfrequencies of uniform steel and carbide TIMOSHENKO beams are also calculated as reference.

The negative values of relative error show that the composite beam slightly underestimates the eigenfrequencies of the analysis object for all diameter ratios. Additionally, magnitude of relative error increases with increase in inner diameter. Nevertheless, the maximum relative errors are limited to merely -2.7 % and -4.2 % for the first and second bending modes for d_i/d_o-ratio between 0.3 and 0.5. This analysis gives an idea

about the scale of error introduced due the composite beam abstraction using the proposed method. The small error is deemed to be acceptable and the proposed method is implemented for the analytical modelling of the holder-tool segment.

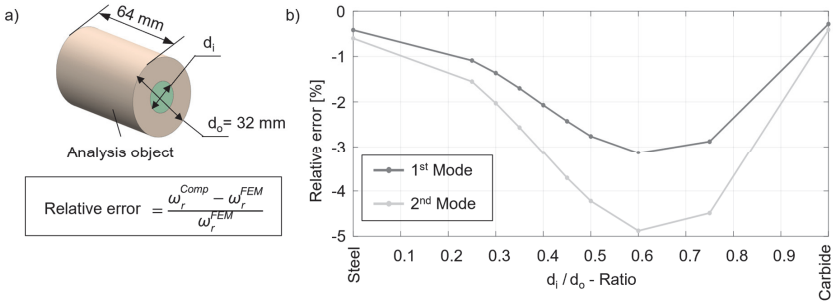

Figure 5.8 a) Dimensions of the analysis object;
b) characteristics of relative frequency error
a) Abmessung des Analyseobjekts; b) Verlauf des relativen Frequenzfehlers

5.3.3 Modelling of tapered holder

Modellierung des kegelförmigen Werkzeughalters

Shrink fit holders are provided with a slight taper to allow for ease of clamping and unclamping of end mills. Since beam modelling can represent tool features only as hollow or full cylinders, the tapered section of the holder is usually modelled by multiple discrete slices of varying outer diameters. Now the following question arises: how many discrete slices are required to model the dynamics of the tapered segment with sufficient accuracy and reasonable computational effort? Although previous works have utilized the slicing of tapered holder into shorter cylindrical beams [SCHM05; SCHM06; FILI09], the question of optimum number of discreet beams has not been analyzed.

For the systematic analysis of this question, three different taper angles (3°, 4.5° and 7°) are considered based on a brief survey of commercially available shrink fit holders. Thus, three non-hollow tapered steel cylinders of length 50 mm, lager diameter of 40 mm and different taper angles are chosen as analysis objects. Each analysis object is now modelled using an FEM model with quadratic tetrahedral elements as well as using a sliced model of TIMOSHENKO beams. For the slicing, each analysis object is divided into one to seven number of cylindrical slices, where the outer diameters of the slices are varied linearly. The rigid, frequency based coupling of a set of slices represents the approximate dynamic behavior of the tapered analysis object. Applying the presented TBM approach and rigid coupling, the free-free FRFs at the ends of the tapered segment are obtained. Subsequently, the first bending frequencies are compared with those derived from the FEM model and the relative errors are calculated for each analysis object and sliced sets (Figure 5.9a).

Based on the course of the relative errors, three main observations can be made: i) the smallest relative error is observed for the case of a single equivalent slice; ii) the error converges rapidly to about 3 to 4.5% with increasing number of slices; iii) for the 7°-tapered analysis object, two slices lead to a significant relative error, whereas odd number of slices lead to smaller errors up to a point. The most probable cause for observation iii) is that the first bending mode results in the largest strain near the middle of the tapered beam. With the division of the beam into even number of equal slices (with different diameters), an interface lies exactly at the location of high strain. This amplifies the discretization error for even slices, especially for the two-slice model.

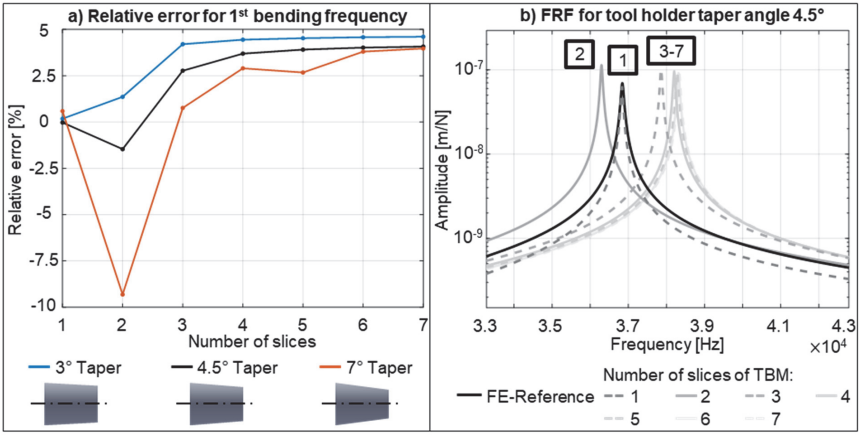

Figure 5.9 a) Relative frequency errors of the first bending mode;
b) Displacement-to-force FRF at the end of the 4.5°-tapered analysis object
a) Relative Frequenzfehler der ersten Biegemode;
b) Verlagerung-zu-Kraft-FRF am Ende des Untersuchungsobjekts mit 4,5°-Kegel

It is interesting to note that irrespective of the taper angle, a single slice with the mean diameter of the tapered segment results in the smallest error. For further analysis, the FRF of the 4.5°-tapered analysis is illustrated in Figure 5.9b. Here, frequency range at the first bending mode is magnified for analysis. Increasing the number of slices seems to cause a certain stiffening effect, which leads to the shifting of eigenfrequency to higher frequencies than the reference. On the other hand, with merely two slices, the interface in the middle seems to dynamically weaken the assembly and shift the eigenfrequency to the lower frequencies. The best correspondence and lowest computational time are achieved with the single slice approach. Therefore, based on the above analysis, a single equivalent slice with a mean diameter of tapered geometry is used for modelling the tapered holder segment.

5.4 Identification of joint properties and validation

Identifikation von Fügestelleneigenschaften und Validierung

The stiffness and damping effects between the holder and the clamped tool are caused mainly by the elastic deformation and the non-conservative slip of the micro asperities of the surfaces in contact. As seen in Subsection 2.4.3, several methods are proposed in literature for representing this joint behavior. In this thesis, the discreet massless SDE with one translational and one rotational degree of freedom is selected for mathematical modelling of the holder-tool joint feature. The complex stiffness matrix of such a spring-damper element is given by,

$$\boldsymbol{K} = \begin{bmatrix} k_{xF} + j\omega c_{xF} & 0 \\ 0 & k_{\theta M} + j\omega c_{\theta M} \end{bmatrix} \tag{5.23}$$

where k_{xF} corresponds to the translational stiffness and c_{xF} to the equivalent translational frequency-dependent damping. Similarly, $k_{\theta M}$ and $c_{\theta M}$ correspond to the rotational stiffness and damping factor, respectively. The cross-stiffness and damping terms are ignored for simplicity. Here, it is assumed that the SDE acts at the interface between the composite holder-tool segment and the overhanging tool, as shown in Figure 5.1. Such a feature model has been extensively used in literature and is hence an appropriate first case for demonstrating the efficiency of the ETMU approach. However, the proposed approach can also be applied for efficient parameterization of other joint models such as the uniform elastic layer or multiple point joint model as well. For this, merely the objective function formulation must be modified.

For identifying the joint parameters between the shrink fit holder and a particular tool, first, a carbide blank of the same length and diameter as the tool is inserted in the holder with the same insertion depth. Subsequently, the joint model is parameterized based on the measured, freely constrained blank tip FRF. The assumption here is that the joint parameters identified for the carbide blank can be transferred to the joint between the holder and the end mill. This assumption is valid as long as the carbide blank and the tool are subject to identical geometric tolerances and surface roughness limits.

As an example, the ETMU approach for joint identification is implemented for a shrink fit tool holder from HAIMER GMBH of the type A63.140.16 with an internal diameter of 16 mm and an insertion depth of 50 mm. The holder of length 69 mm possesses four balancing holes and a tapered segment of 4° taper angle. The analytical beam model of the holder was created based on the findings from Section 5.3, which are implemented in the developed 'CouplingTools' software. The equivalent diameter of the unbalance hole segment was estimated to be 15.72 mm (refer Subsection 5.3.1). The tapered segment is modelled as a single cylindrical composite beam of the mean diameter of the tapered segment (refer Subsection 5.3.3). The properties of the single composite beam are derived based on the ratio of the beam's cross-section area to the total cross-section area (refer Subsection 5.3.2). Once the dimensions and properties of the individual beams of the holder model are defined, the TBM is used to obtain the compliance matrix at the ends of each beam. The individual slices are then

rigidly coupled to each other to get the analytical model of the holder including the inserted carbide cylinder denoted by '*Th*'. This is extended using Eq. 5.1 to obtain the compliance matrix at coordinate *6*, $\boldsymbol{G}_{66}^{ITh}$. Now for obtaining analytical blank-tip FRF of the extended tool assembly, the interface-holder assembly (*ITh*) is elastically coupled with the carbide blank (*C*) using the following coupling equation,

$$\begin{bmatrix} H_{33}^{IThC} & L_{33}^{IThC} \\ N_{33}^{IThC} & P_{33}^{IThC} \end{bmatrix} = \boldsymbol{G}_{33}^{IThC} = \boldsymbol{G}_{33}^{C} - \boldsymbol{G}_{36}^{C}(\boldsymbol{G}_{66}^{ITh} + \boldsymbol{G}_{66}^{C} + \boldsymbol{K}^{-1})^{-1}\boldsymbol{G}_{63}^{C}. \tag{5.24}$$

Here, the carbide blank is modelled as a single segment TIMOSHENKO beam. Considering only the displacement-to-force FRF,

$$H_{33}^{IThC} = H_{33}^{C} - \begin{bmatrix} H_{36}^{C} & L_{36}^{C} \end{bmatrix} \left[\begin{bmatrix} H_{66}^{ITh} & L_{66}^{ITh} \\ N_{66}^{ITh} & P_{66}^{ITh} \end{bmatrix} + \begin{bmatrix} H_{66}^{C} & L_{66}^{C} \\ N_{66}^{C} & P_{66}^{C} \end{bmatrix} + \begin{bmatrix} k_{xf} + j\omega c_{xf} & 0 \\ 0 & k_{\theta M} + j\omega c_{\theta M} \end{bmatrix}^{-1} \right]^{-1} \begin{bmatrix} H_{63}^{C} \\ N_{63}^{C} \end{bmatrix}. \tag{5.25}$$

Initially, the above displacement-to-force FRF is calculated without the joint stiffness term, as the parameters are still unknown. This blank tip FRF of the rigidly coupled analytical tool assembly model is plotted in Figure 5.10b for the extended tool holder with carbide blanks of overhang lengths (L_o) of 50 mm and 100 mm. The corresponding blank tip FRFs are measured using the freely constrained measurement setup shown in Figure 5.10a.

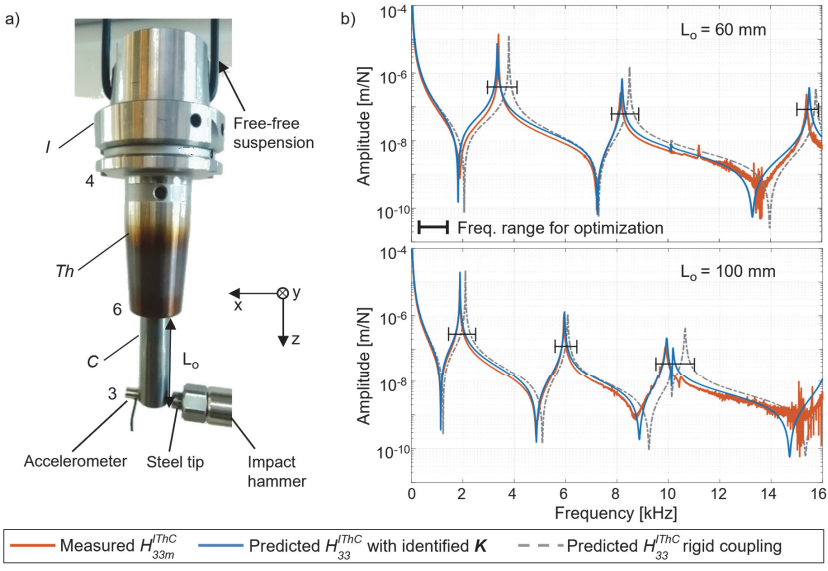

Figure 5.10 a) Freely constrained measurement setup; b) comparison of blank tip FRFs
a) Messaufbau im freihängenden Zustand; b) Vergleich von Rohling FRFs

The influence of sensor mass loading on the measured FRF is compensated using the structural modification method [ÖZŞA10]. The rigidly coupled and measured FRFs have similar courses, however, due to the missing joint parameters, the predicted FRF has resonance peaks located at relatively higher frequencies. The resonance peaks as well as anti-resonances are clearly observable in the FRF with a high SNR even up to 16 kHz. This is in contrast to the noisy reference measurements achieved using the experimental setup proposed in [MATT16]. Therefore, this comparison provides an ideal basis for updating the unknown joint parameters.

The importance of accurate analytical modeling is also apparent from the Figure 5.10. The difference in the location of the eigenfrequencies is an indication of the unknown joint parameters. Only for an appropriately modelled extended tool assembly, can the difference in the rigidly coupled and measured system be attributed to the missing joint dynamics. Any errors in analytical tool modelling itself can be falsely compensated by the identified joint parameters. This is the reason for choosing the TBM and the systematic analytical holder-tool modelling proposed in this chapter.

Three dominant eigenfrequencies are observable for both holder-blank assemblies in Figure 5.10b. These correspond to the first three bending modes of the feely constrained assembly as seen in the simulated vibration modes in Figure 5.11. The first bending mode mainly involves the vibration of the overhanging blank. A deformation of the holder and blank is observable in each of the mode shapes and therefore, the joint dynamics is expected to influence each of these modes. Thus, all three resonances can be utilized for the identification of joint parameters.

L_o	1st Bending Mode	2nd Bending Mode	3rd Bending Mode
50 mm	 f_1 = 4087 Hz	 f_2 = 8959 Hz	 f_3 = 17140 Hz
100 mm	 f_1 = 1899 Hz	 f_2 = 5887 Hz	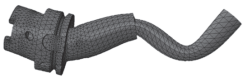 f_3 = 10035 Hz

Figure 5.11 Mode shapes of the first three dominant resonance frequencies
Schwingungsformen der ersten drei dominanten Resonanzfrequenzen

Efficient optimization approach for joint identification

Literature provides several approaches for identifying holder-tool joint parameters based on reference measurements. Some of them are: manual or visual tuning of parameters [ÖZŞA15; SCHM19], parameter variation [AHMA07] and curve fitting or nonlinear optimization [PARK08; MATT16]. These approaches use an objective function, which reduces the difference between the predicted and measured FRF amplitudes within a large frequency range. This is suitable for reference FRFs measured in the clamped-free state in the spindle. For the freely constrained case, however, a much

better indicator of the influence of the joint stiffness is the location of the resonance peaks. This is because any change in joint properties results in a clear shifting of the relevant resonance frequencies. Hence, in the proposed approach, the objective function is defined to reduce the weighted difference between the location (frequency) of the predicted and measured resonance peaks. Additionally, the weighted difference of the absolute values of the FRF at the resonance peak is also considered,

$$\min\left(\sum_{i=1}^{n} W_i^f \cdot |f_i^{\mathrm{m}} - f_i| + W_i^{\mathrm{abs}} \cdot \left(\left\|H_{33,m}^{I\mathrm{ThC}}(\sim f_i^{\mathrm{m}})\right\| - \left\|H_{33}^{I\mathrm{ThC}}(\sim f_i)\right\|\right)\right) \tag{5.26}$$

where, f_i^{m} corresponds to the frequency of the i-th resonance peak of the measurement and f_i to that of the calculated peak. $W_i^f, W_i^{\mathrm{abs}}$ are the weightages assigned to the i-th frequency and absolute error, respectively. Where, the weightage on the frequency difference is set much higher ($W_i^f \gg W_i^{\mathrm{abs}}$) to enable a faster convergence of the optimization problem. The efficiency of this formulation results from two aspects:

- First, the calculation of the objective function is simplified as only the FRF values at the resonance frequencies are required.
- Second, the analytical response model has to be calculated only in the neighborhood of the resonance frequencies as shown in Figure 5.10b.

A genetic algorithm was utilized to solve the optimization problem so that a global minimum to the bounded problem could be found. The identified joint parameters were used to elastically couple the interface-holder assembly with the one segment beam representing the blank using Eq. (5.25). The resulting FRF is also plotted in Figure 5.10b. A very good correspondence can be observed between the measurements and the prediction with identified join parameters. Both, the poles as well as the zeros could be matched very well and indicate accurate estimation. A summary of the proposed ETMU approach for joint identification is provided in Figure 5.12 in the form of a flowchart. Further analysis and validation are presented in the following.

Analysis and validation

A tool holder can be fitted with tools of varying lengths. Hence it is necessary to analyze the validity of the proposed approach for blanks with different (overhang) lengths. For this, the selected HAIMER holder was fitted with six carbide blanks of 16 mm diameter and varying lengths of 100, 110, 120, 130, 140 and 150 mm. Utilizing the maximum insertion length of 50 mm, gives overhang lengths L_o, ranging from 50 to 100 mm. Using the setup in Figure 5.10a, the freely constrained blank tip FRF $H_{33m}^{I\mathrm{ThC}}$ was measured for each holder-blank combination. Corresponding extended tool models were also created and the blank tip FRF predicted for the rigidly coupled assembly. Table 5.1 lists the used blanks with the corresponding measured and predicted (without joint parameters) resonance frequencies for the first and second modes. These values are also plotted against overhang length in Figure 5.13.

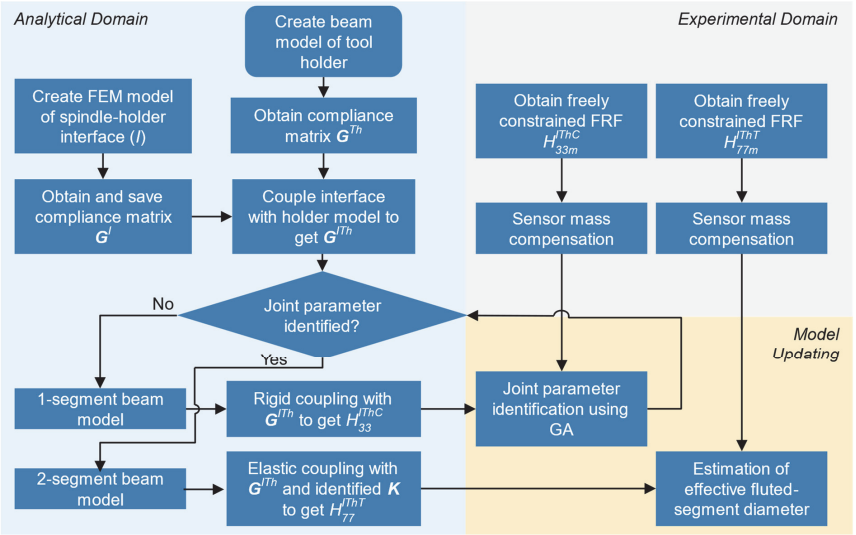

Figure 5.12 The ETMU approach for joint identification and fluted segment modelling
Der ETMU-Ansatz zur Fügestellenidentifikation und Spannutmodellierung

Both translational (k_{xf}) and rotational ($k_{\theta M}$) stiffness show a decreasing trend with increasing overhang. Between the minimum and maximum overhang, the identified translational stiffness reduces by 50.5 % and rotational stiffness declines by 25.0 %, indicating that the location of the resonance frequency of the assembly is more sensitive to change in rotational than in translational stiffness. The decreasing trend corroborates well with the decreasing relative difference between the predicted (without ***K***) and measured resonance frequencies because a smaller magnitude of additional stiffness is required to compensate for a small difference in resonance frequencies.

Table 5.1 Details of carbide tools and identified joint stiffness
Details der Werkzeugbaugruppen und ermittelte Fügestellensteifigkeit

Tool holder	Overhang length, L_o [mm]	Identified stiffness		Free-free measured frequency		Free-free predicted freq. (*without* ***K***)		Relative difference (*without* ***K***)		Adjusted joint damping	
		k_{xF} [N/m]	$k_{\theta M}$ [Nm/rad]	1st Mode [Hz]	2nd Mode [Hz]	1st Mode [Hz]	2nd Mode [Hz]	1st Mode [%]	2nd Mode [%]	c_{xf} [Ns /m]	$c_{\theta M}$ [Nms /rad]
HAIMER A63.140.16	50	3.51 x10^9	2.67 x10^5	4030	8789	4495	9463	11.54	7.67	150	30
	60	3.39 x10^9	3.22 x10^5	3344	8181	3796	8502	13.52	3.92	150	30
	70	3.41 x10^9	2.15 x10^5	2869	7552	3227	7771	12.48	2.90	150	30
	80	2.98 x10^9	2.39 x10^5	2471	7026	2766	7140	11.94	1.62	150	30
	90	2.34 x10^9	2.22 x10^5	2150	6485	2422	6595	12.65	1.70	150	18
	100	1.70 x10^9	2.00 x10^5	1884	5935	2100	6084	11.46	2.51	150	10

However, for the same insertion length, there is no physical change in the joint when the overhang is increased. Other complex joint models that consider the variation of contact pressure and stiffness along insertion length like the continuous uniform distributed SDE model by REZAEI et al. [REZA12] or the multipoint RSCA joint model by SCHMITZ et al. [SCHM19] do not show a sensitivity to overhang length. These models provide a more realistic joint representation. The variation of joint parameters for the same insertion length is probably due to the composite beam-lumped SDE model, where the contact between the inserted tool and the holder is assumed to be rigid and the joint compliance is assumed to be acting at the interface between the composite beam and the overhanging tool. Therefore, a drawback of the SDE feature model is that the joint parameters have to be identified for each overhang length. However, this model can still accurately depict the joint behavior at different overhangs and is chosen in this work because of its simplicity and because the focus is on the method of identification. As mentioned previously, the proposed ETMU approach can also be implemented to parameterize other joint models.

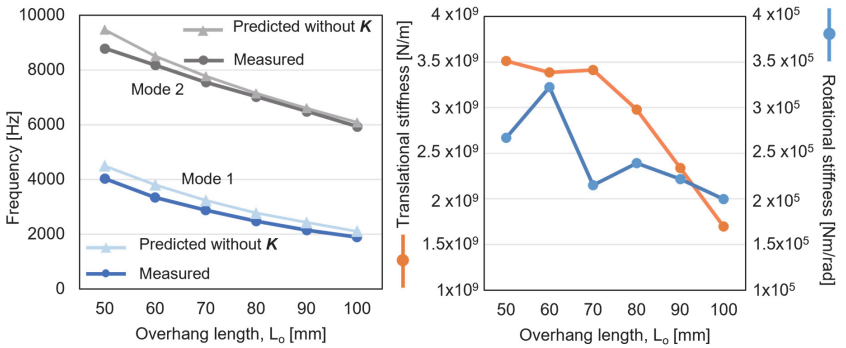

Figure 5.13 Variation of resonance frequencies and identified joint stiffness with overhang

Veränderung der Resonanzfrequenzen und der identifizierten Fügestellensteifigkeit mit der Überhanglänge

The identification of joint damping factors c_{xf} and $c_{\theta M}$ in the freely constrained state still remains a challenge for lowly damped structures. It was observed that the amplitude of the resonance frequencies in this state is extremely sensitive to the quality of impact and measurement setup such that a consistent, repeatable identification of joint damping was not possible. Hence, literature values for joint damping [ÖZŞA15] were used as starting values in this study.

Taking these values and the identified joint stiffness, the one-segment beam can be elastically coupled with the beam model of the holder to get the updated holder-blank assembly '*ThC*'. This can further be coupled to the experimental response model of any machine tool spindle such that the blank tip FRF in the clamped state (H_{33}^{SThC}) can be predicted. In this way, the blank tip FRF was predicted in x-direction for all six combinations from Table 5.1. Here, the analytical models were coupled to the ERM of MCT

A, which was obtained using the combination of accelerometer and actuated impact hammer. The predicted blank tip FRFs for the analyzed overhang lengths are plotted in Figure 5.14. The corresponding reference FRFs H_{33m}^{SThC} were measured with the help of a single-beam laser Doppler vibrometer and an impact hammer (Figure 5.15).

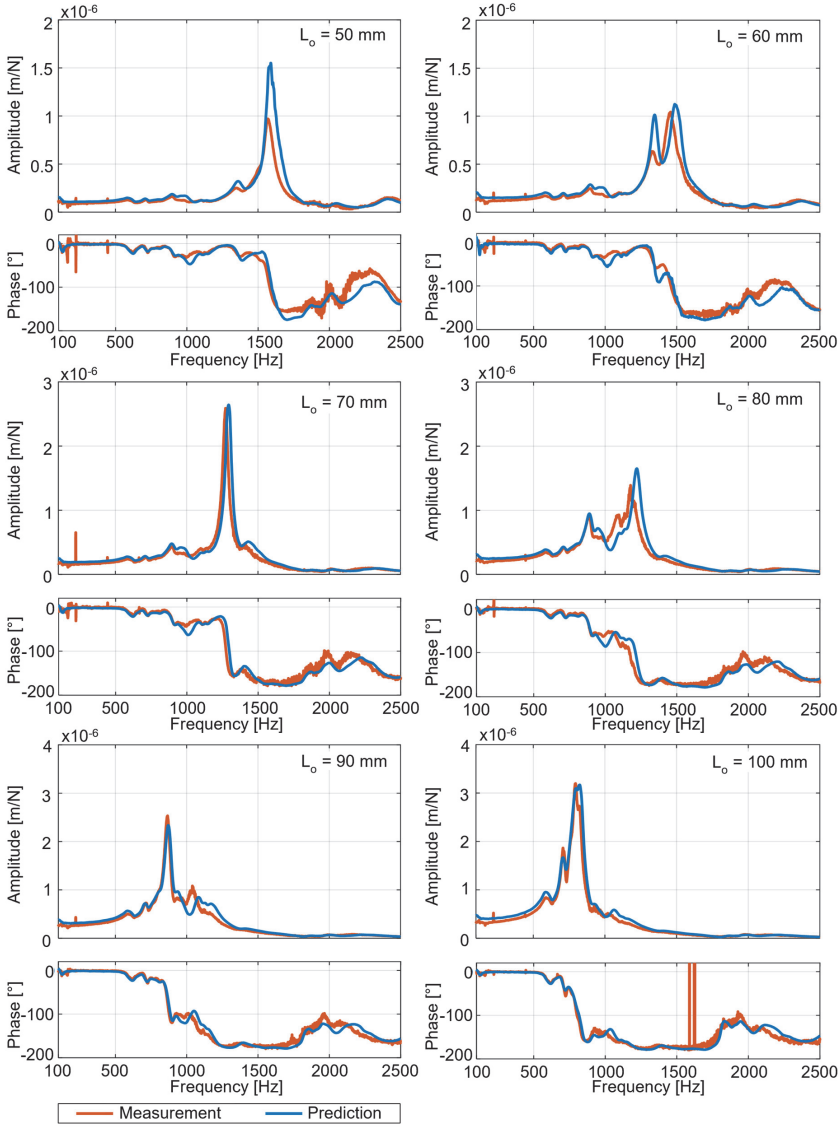

Figure 5.14 Comparison of measured and predicted blank tip FRFs

Vergleich der gemessenen und vorhergesagten FRFs an der Rohlingsspitze

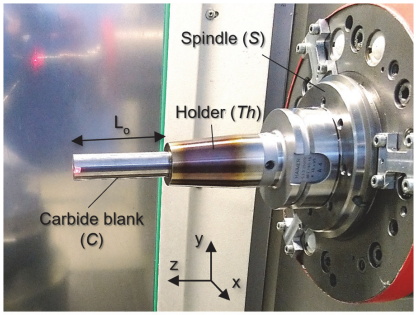

Figure 5.15 Measurement of blank tip FRF at MCT A
Messung des FRF an der Rohlingsspitze an der WZM A

The comparisons in Figure 5.14 show a very good correspondence in the amplitude and phase plots. The locations of the blank modes are also accurately predicted for all overhang lengths. This shows that the stiffness of the SDE model can be parameterized accurately and reliably in the freely constrained state using the ETMU approach. The effect of decreasing blank vibration frequencies with increasing overhang length can also be observed in the predictions. The assumed values of equivalent viscous damping values taken from [ÖZŞA15] resulted in acceptable correspondence at the resonance peaks. These were adjusted posteriori only for long overhangs of 90 and 100 mm. However, the a priori experimental identification of the joint damping should be investigated in future works.

5.5 Identification of effective fluted segment dia. and validation

Idenifikation des effektiven Durchmessers des Spannutsegments und Validierung

In the framework of the ETMU approach, once the joint stiffness parameters have been identified, the carbide blank is replaced with the corresponding real tool with the same insertion and overhang length. The extended tool model is also modified by replacing the one-segment beam with the elastic coupling of a two-segment beam using the identified stiffness matrix (refer to Figure 5.1). The two segments are intended to represent the overhanging shank part of the real tool (T_s) and the fluted segment (T_f), respectively. Now, the collocated displacement-to-force FRF at coordinate *7*, $H_{77}^{ITh T}$ is chosen for updating the fluted segment model. The corresponding method is described below.

Initially, the fluted segment beam diameter is taken as the shank diameter (d_s). The shank segment T_s is then coupled elastically using the identified joint properties with the extended holder at coordinate *6* giving the compliance matrix at the free end of the shank as,

$$\boldsymbol{G}_{77}^{ITh T_s} = \boldsymbol{G}_{77}^{T_s} - \boldsymbol{G}_{76}^{T_s}(\boldsymbol{G}_{66}^{T_s} + \boldsymbol{G}_{66}^{ITh} + \boldsymbol{K}^{-1})^{-1}\boldsymbol{G}_{67}^{T_s}. \tag{5.27}$$

Applying the force equilibrium and compatibility conditions between the shank and the fluted segment at *7*, gives the expression for the direct compliance matrix at coordinate *7* of the complete, extended tool assembly,

$$\boldsymbol{G}_{77}^{lThT} = \boldsymbol{G}_{77}^{T_f} - \boldsymbol{G}_{77}^{T_f}(\boldsymbol{G}_{77}^{T_f} + \boldsymbol{G}_{77}^{lThT_s})^{-1}\boldsymbol{G}_{77}^{T_f}. \tag{5.28}$$

The compliance matrix $\boldsymbol{G}_{77}^{lThT}$ includes collocated displacement-to-force FRF at coordinate *7*. Writing the above equation for the displacement-to force term,

$$H_{77}^{lThT} = H_{77}^{T_f} - \begin{bmatrix} H_{77}^{T_f} & L_{77}^{T_f} \end{bmatrix} \left[\begin{bmatrix} H_{77}^{T_f} & L_{77}^{T_f} \\ N_{77}^{T_f} & P_{77}^{T_f} \end{bmatrix} + \begin{bmatrix} H_{77}^{lThT_s} & L_{77}^{lThT_s} \\ N_{77}^{lThT_s} & P_{77}^{lThT_s} \end{bmatrix} \right]^{-1} \begin{bmatrix} H_{77}^{T_f} \\ N_{77}^{T_f} \end{bmatrix} \tag{5.29}$$

The corresponding reference FRF $H_{77\mathrm{m}}^{lThT}$, required for model updating, is obtained using the freely constrained measurement setup shown in Figure 5.16a. Here as well, an acceleration sensor is used to enable reliable measurement till higher frequencies (16 kHz) and its mass loading effect is compensated. A simple test bench for the quick measurement of freely constrained tool assemblies is described in Appendix A.2.

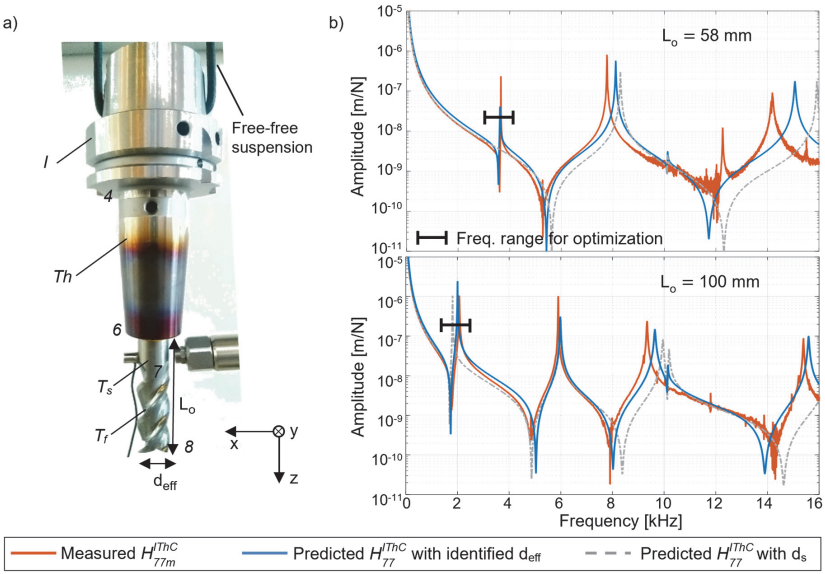

Figure 5.16 a) Freely constrained measurement setup; b) comparison of FRFs at coord. *7*
a) Messaufbau im freihängenden Zustand; b) Vergleich der FRFs an Koord. 7

Now, the unknown compliance matrix $\boldsymbol{G}_{77}^{T_f}$ in coupling Eq. (5.28) depends on the geometric parameters of the equivalent fluted segment beam. Since the reference FRF is available, the geometric parameter (effective diameter, d_{eff}) can be varied until a good correspondence between the measured and predicted FRF is achieved. For this, the

same objective function (Eq. (5.26)) for minimizing the weighted error between the location of simulated and measured eigenfrequencies is utilized. However, instead of the genetic algorithm, a simple, iterative, linear optimization algorithm was sufficient to arrive near the optimum.

The choice of the reference FRF at coordinate 7 for model updating has two main advantages:

i) In the required coupling formulation (Eq. (5.28)), out of the four compliance matrices of the fluted segment beam T_f, only a single analytical compliance matrix $\boldsymbol{G}_{77}^{T_f}$ is required. This improves the efficiency of the optimization algorithm, as only the compliance matrix at one end needs to be calculated.
ii) The measurement of H_{77m}^{lThT} on the shank is more convenient than tap testing on the free end of the fluted segment. This is because of the difficulty of attaching accelerometers on the tool edges and the risk of damage to impact hammer during tap testing.

As an example, the H_{77}^{lThT} FRF obtained experimentally and analytically for two real end-mills with tool diameter of 16 mm and overhang lengths of 58 mm (GARANT 20225716) and 100 mm (HOLEX 20305916) are plotted in Figure 5.16b. For the analytical model, the initial diameter of the fluted segment is taken as the diameter of the shank ($d_{eff} = d_s$). The simulated modal analysis of the tool assembly in Figure 5.11 has already shown that the bending of the overhanging tool or blank contributes significantly to the first mode shape. Therefore, the first resonance provides an excellent reference for identifying the equivalent effective diameter. The higher bending modes do not include significant modal strains of the fluted segment alone. Hence, the correspondence of the predicted FRF with d_{eff} is much more important at the first resonance than the higher ones. This can be considered in the optimization algorithm by adjusting the corresponding weightage for the frequency difference of the first mode.

Similar to joint identification, the optimization is conducted only at frequency ranges near the resonance peaks. The effective diameter identified by the linear optimization algorithm is then used to modify the second beam of the two-segment beam. As a check, displacement-to-force FRFs H_{77}^{lThT} with the identified effective diameters are also plotted in Figure 5.16b. Here as well, a good correspondence between the measured and predicted FRFs can be observed. Especially the first bending mode could be represented accurately. Clearly, the effective diameter is a simplification of the complex tool geometry and cannot capture all dynamic effects corresponding to the higher modes. The following experimental implementation and validation shows that this simplification provides sufficiently accurate prediction without extensive modelling effort.

Analysis and Validation

Four carbide end mills of different diameters, lengths, number of teeth, fluted lengths and helix angles were chosen for validating the identification of the effective diameter.

Each assembly of end mill and holder was analyzed for its joint stiffness using a corresponding carbide blank as proposed in Subsection 5.4. The details of the used holders, tools and identified joint stiffness are listed Table 5.2. Effective diameter of the fluted segment for each tool was identified based on the measured FRF H_{77m}^{lThT} of the extended tool assembly as already introduced in this subsection.

Table 5.2 Details of end mills used for validation and identified parameters

Angaben zu den für die Validierung verwendeten Schaftfräsern und den identifizierten Parametern

Assembly	Holder	End mill	Overhang [mm]	No. of teeth	Helix [°]	d_s [mm]	Tool dia. [mm]	d_{eff} [mm]	Fluted segment [mm]	Joint stiffness k_{xF} [N/m]	Joint damping $k_{\vartheta M}$ [Nm/rad]
A	GÜHRING 472625063	GARANT 20304125	85	4	38	24.5	25	20.66	80	2.87 x10^{10}	6.34 x10^{5}
B	HAIMER A63.140.20	GARANT 20227120	74	3	45	19.5	20	15.9	49	2.40 x10^{10}	5.95 x10^{5}
C	HAIMER A63.140.16	GARANT 20303816	100	4	38	15.5	16	12.8	41	1.70 x10^{9}	2.00 x10^{5}
D	HAIMER A63.140.10	GARANT 20702810	58	2	45	9.4	10	6.22	31	8.43 x10^{8}	3.85 x10^{4}

The identified translational and rotational joint stiffness show a decreasing trend with decreasing contact surface area (smaller diameter shafts have shorter insertion depths and thus lesser contact area compared to bigger diameter shafts). This trend is coherent with the findings of [LIAO17], where a nearly linear relation between insertion depth and joint stiffness could be observed. However, further study is required to establish correlations between contact area, radial interference, surface roughness and joint stiffness. This is not within the scope and aims of this thesis.

For validation, each tool assembly was clamped in the main spindle of the 4-axis MCT A and the tool tip FRF in x-direction was obtained using the vibrometer and the impact hammer. For the analytical model, the updated two-beam sub-assembly representing the end mill is elastically coupled to the tool holder model. The resulting updated holder-tool model (*ThT*) is then rigidly coupled with an appropriate ERM of MCT A to give the tool tip FRF H_{88}^{SThT} (refer Eq. (4.2)). Note that the four different tool holders have different diameters at the interface end. Therefore, four cylindrical adapters of corresponding diameters were used for obtaining four ERMs at MCT A. The predicted and measured tool tip FRFs of the clamped tool holder assemblies are plotted in Figure 5.17.

Assembly A: The four fluted end mill of ø25 mm and 85 mm overhang represents the largest considered holder-tool assembly. The FRF of the updated model corresponds well with the reference FRF in Figure 5.17. Two tool vibration modes at 1305 Hz and 1430 Hz could be predicted, but with a certain error. Due to the relatively long fluted segment, any estimation errors of the effective diameter will have a significant influence on the predicted FRF.

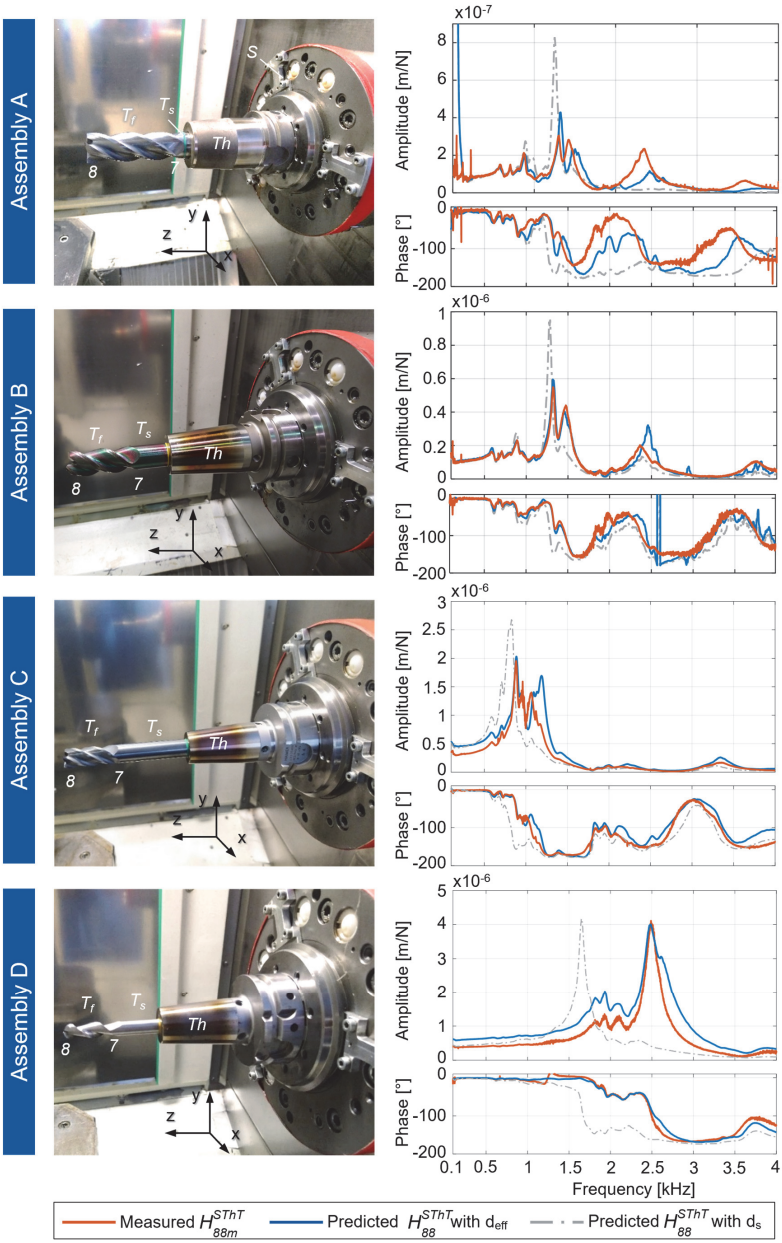

Figure 5.17 Comparison of measured and predicted tool tip FRFs

Vergleich der gemessenen und vorhergesagten FRFs an der Werkzeugspitze

Nevertheless, the dominant modes, the quasi-static and dynamic behavior at lower frequencies (<1300 Hz) could be estimated with sufficient accuracy. Modelling the fluted segment as a full cylinder leads to erroneous predictions and motivates the need for a reduced level of abstraction.

Assembly B: For the ø20 mm end mill with three teeth, eigenfrequencies of the tool bending modes (1320 Hz and 1471 Hz) as well as the quasi-static, dynamic compliance could be predicted with good accuracy. In this case, the phase drop below -90° at the resonance frequencies could be accurately predicted.

Assembly C: Due to the long overhang of the four fluted end mill, the tool bending modes are located at lower frequencies and thus interact with the machine and spindle modes (at 880 Hz). Although a certain deviation is observed at around 1120 Hz, the dominant vibration mode as well as the quasi-static stiffness could be estimated with sufficient accuracy.

Assembly D: The ø10 mm ball nose cutter with only two teeth represents a challenging case for modelling as well as for reference measurement. The excitation and displacement measurement at the very end of the tool and exactly in x-direction is difficult due to the rounded ball nose and the smaller number of flutes. The dominant tool mode at 2494 Hz could be predicted accurately using the estimated effective diameter of 6.22 mm. The dynamic characteristics at lower frequencies matches with the run of the reference, but a deviation in amplitude is observed. This results from the simplified equivalent model as well as the difficulties in exact reference FRF measurement.

Independent of the fluted segment properties (helix angle, fluted length, diameter, teeth, etc.), the proposed approach for fluted segment modelling and subsequent updating resulted in sufficiently accurate predictions of the considered tool tip FRFs. This is despite the low modelling and measurement effort required. An estimation of the dominant tool mode as well as the quasi-static behavior without extensive modelling is enough for predicting the surface location error due to tool deflection and for avoiding excitation of dominant resonance frequencies through the milling process.

Conclusions

This chapter proposes the extension of the beam model of the holder and tool or blank such that it can be updated using experimentally obtained FRFs of the tool assembly in freely constrained state. In this way, different unknown parameters can be identified accurately and without blocking the machine tool. For model updating in the freely constrained condition, the analytical response modelling using TIMOSHENKO beam theory is indispensable. Inaccurate modelling of holder features leads to a significant shifting of eigenfrequencies. Therefore, different feature models are developed, analyzed and validated.

The prediction of carbide blank tip FRF of the extended model with the rigid coupling of the one-segment beam led to resonance frequencies, which were slightly higher than the measured resonance frequencies. This difference was a reliable indicator of the joint stiffness such that elastic coupling with the identified stiffness resulted in a

good conformance with the measured free-free FRF up to 16 kHz. The validation by comparing the measured and analytical tip FRF of the holder-blank assembly in a machine spindle confirmed that the stiffness values were correctly identified. Similarly, the comparison of freely constrained FRFs between the shank and flutes (at point *7*) showed that an effective diameter of fluted segment could appropriately describe the dynamic behavior of the real tool for the first modes. The choice of point *7*, for comparing the dynamics, greatly facilitates the identification problem. The tool tip FRF could be predicted with reasonable accuracy for different tool diameters, fluted lengths, helix angels and number of teeth. This rough prediction can be used for process planning by avoiding the excitation of critical chatter frequencies. If a more accurate prediction of stability boundaries is required, a more detailed flute model is necessary. Hence, a sufficiently accurate, updated model of the holder-tool assembly could be achieved with only two offline reference FRF measurements, thereby increasing the efficiency of the tool modelling process.

6 Tool Tip-SIDS Transfer Function Prediction and Uncertainty Propagation

Prognose der Werkzeug-SIDS Übertragungsfunktion und Unsicherheitsfortpflanzung

In this chapter, the developed tool coupling framework is extended by including the spindle integrated sensor plane in the coupling calculations (Section 6.1). A key element for the coupling calculation is the development of a method for experimental modelling and uncertainty quantification of the transfer function between the spindle-holder interface and the sensor unit, $\boldsymbol{G}_{54}^{S}$ (Section 6.2). Subsequently, the uncertainty on the transfer function matrix is propagated onto the predicted tool tip-SIDS transfer function and systematically analyzed (Section 6.3). Here, the influence of uncertainty of individual FRFs of the spindle substructure on predicted transfer functions is also studied. The obtained transfer-functions with uncertainty bounds for different tools are then validated by comparing with the measured transfer functions (Section 6.4).

6.1 Extension of tool coupling planes

Erweiterung der Kopplungsebenen

The motor spindle concept used and analyzed in this chapter was developed at the WZL as part of a research project. Here, the motor spindle consists of a shaft-mounted aluminum alloy disc with six eddy-current sensors, three of which measure orbital displacements and three measure axial displacements of the disc [BREC18b; BREC19c]. An abstracted sketch of the spindle and the coupling planes is provided in Figure 6.1, where the disc with the SIDS is represented as plane *5*.

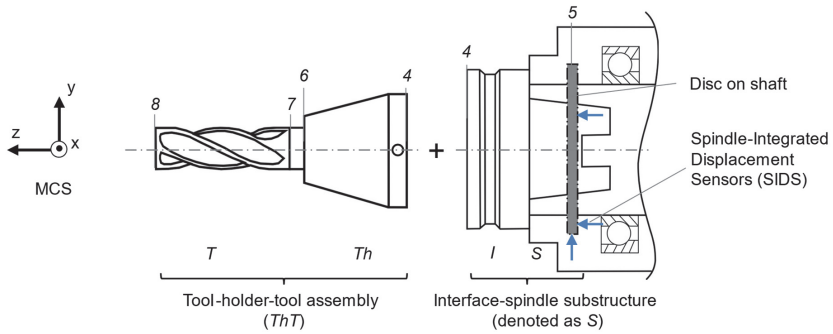

Figure 6.1 Coupling planes for the prediction of the tool tip-SIDS transfer function

Kopplungsebenen für Prognose der Werkzeug-SIDS Übertragungsfunktion

The orbital as well as the axial sensors are radially separated from each other, for example by 120°. Due to this radial separation, the difference in displacements at the three axial sensors can be used to estimate the rotational deflections about both the

radial directions, $\theta_{x,5}$ and $\theta_{y,5}$. Additional to the displacements, the angular position of the shaft (θ_z) from the encoder signal is also recorded synchronously. This is required for compensating systematic errors occurring every revolution of the spindle such as run-out (including roundness and concentricity error of the disc) and errors due to spindle kinematics [BREC18b; BREC19c]. These kinematic errors are first recorded during an air-cutting step and subsequently removed from the measurement during cutting. The tool interface of the spindle is of type HSK-63 A and is assembled in MCT B.

For the prediction of the tool tip-SIDS transfer function matrix $\boldsymbol{G}_{58}^{STHT}$, the updated analytical tool substructure *ThT* must be rigidly coupled with the interface-spindle substructure *S* at coordinate *4*. Here, the spindle substructure consists of two coupling planes: *4* representing the interface flange-end and *5* representing the disc with the SIDS. As an example, the derivation of coupling equation is obtained for the yz-plane. Applying compatibility condition for rigid coupling at *4* gives,

$$y_4^{ThT} = y_4^S \text{ and } \theta_{x,4}^{ThT} = \theta_{x,4}^S \tag{6.1}$$

or in vector form,

$$u_4^{ThT} = \begin{Bmatrix} y_4^{ThT} \\ \theta_{x,4}^{ThT} \end{Bmatrix} = u_4^S = \begin{Bmatrix} y_4^S \\ \theta_{x,4}^S \end{Bmatrix}. \tag{6.2}$$

The compliance matrices of the individual substructures to be coupled as shown in Figure 6.1 are,

$$u_4^{ThT} = \boldsymbol{G}_{48}^{ThT} q_8^{ThT};\ u_4^{ThT} = \boldsymbol{G}_{44}^{ThT} q_4^{ThT} \tag{6.3}$$

for the analytical tool-holder-tool substructure and,

$$u_4^S = \boldsymbol{G}_{44}^S q_4^S;\ u_5^S = \boldsymbol{G}_{54}^S q_4^S \tag{6.4}$$

for the experimentally obtained response model of the spindle substructure. Here, q represents the two DOF excitation vector at the unassembled substructure coordinates. In order to obtain the tool tip-SIDS transfer function matrix, an excitation vector Q_8^{STHT} is applied at coordinate *8* (U_8^{STHT}) of the spindle-holder-tool assembly. Assuming collocation of u_8^{THT} and U_8^{STHT}, the displacements at coordinate *4* are given by,

$$u_4^{ThT} = \boldsymbol{G}_{44}^{ThT} q_4^{ThT} + \boldsymbol{G}_{48}^{ThT} Q_8^{STHT};\ u_4^S = \boldsymbol{G}_{44}^S q_4^S. \tag{6.5}$$

Substituting above equation in the compatibility condition (Eq. (6.2)) gives,

$$\boldsymbol{G}_{44}^S q_4^S - \boldsymbol{G}_{44}^{ThT} q_4^{ThT} - \boldsymbol{G}_{48}^{ThT} Q_8^{STHT} = 0. \tag{6.6}$$

Applying force equilibrium condition at the coupling or interface coordinate *4*,

$$q_4^{ThT} + q_4^S = 0. \tag{6.7}$$

Substituting the above equation in Eq. (6.6) and solving for q_4^S by eliminating q_4^{ThT},

$$q_4^S = \left(\boldsymbol{G}_{44}^S + \boldsymbol{G}_{44}^{ThT}\right)^{-1} \boldsymbol{G}_{48}^{ThT} Q_8^{STHT}. \tag{6.8}$$

Now the required transfer function is ratio of the dynamic response at coordinate *5* due to an excitation at coordinate *8* for the assembled system,

$$\boldsymbol{G}_{58}^{SThT} = \frac{U_5^{SThT}}{Q_8^{SThT}} = \frac{\boldsymbol{G}_{54}^{S} q_4^{S}}{Q_8^{SThT}} = \frac{\boldsymbol{G}_{54}^{S}\left(\boldsymbol{G}_{44}^{S} + \boldsymbol{G}_{44}^{ThT}\right)^{-1}\boldsymbol{G}_{48}^{ThT} Q_8^{SThT}}{Q_8^{SThT}}. \tag{6.9}$$

Here as well, it is assumed that for the assembled system, the DOFs at *5* are collocated ($u_5^S = U_5^{SThT}$). Cancelling the common term in numerator and denominator,

$$\boldsymbol{G}_{58}^{SThT} = \boldsymbol{G}_{54}^{S}\left(\boldsymbol{G}_{44}^{S} + \boldsymbol{G}_{44}^{ThT}\right)^{-1}\boldsymbol{G}_{48}^{ThT} = \begin{bmatrix} H_{58}^{SThT} & L_{58}^{SThT} \\ N_{58}^{SThT} & P_{58}^{SThT} \end{bmatrix} = \begin{bmatrix} \dfrac{y_5^{SThT}}{F_8^{SThT}} & \dfrac{y_5^{SThT}}{M_8^{SThT}} \\ \dfrac{\theta_{x,5}^{SThT}}{F_8^{SThT}} & \dfrac{\theta_{x,5}^{SThT}}{M_8^{SThT}} \end{bmatrix}. \tag{6.10}$$

One can arrive at the same equation as above by applying the LAGRANGE multiplier formulation for frequency based substructuring. The utilized approach was chosen, as it is simpler and provides a more intuitive representation of the coupling terms. The LM FBS formulation is used in the next section for the propagation of uncertainties from the individual FRFs to the coupled system FRFs. Using Eq. (6.10), the complete 2x2 tool tip-SIDS transfer function can be calculated. Now the question arises: which of the elements of the matrix $\boldsymbol{G}_{58}^{SThT}$ should be used for force prediction? The aim of this work is to estimate the process forces at the tool tip (perpendicular to rotation axis) and not the occurring bending moment. This represents an important boundary condition for answering the previous question and thus precludes the use of P_{58}^{SThT} and L_{58}^{SThT} for force prediction. Since the SIDS system can measure translation as well as rotation (y_5^S, $\theta_{x,5}^S$), both, the displacement at SIDS to force at tool tip FRF (H_{58}^{SThT}) as well as rotation-to-force FRF (N_{58}^{SThT}) can be used for force estimation. Considering only the terms for calculating H_{58}^{SThT} from equation (6.10),

$$H_{58}^{SThT} = \begin{bmatrix} H_{54}^{S} & L_{54}^{S} \end{bmatrix}\left[\begin{bmatrix} H_{44}^{S} & L_{44}^{S} \\ N_{44}^{S} & P_{44}^{S} \end{bmatrix} + \begin{bmatrix} H_{44}^{ThT} & L_{44}^{ThT} \\ N_{44}^{ThT} & P_{44}^{ThT} \end{bmatrix}\right]^{-1}\begin{bmatrix} H_{48}^{ThT} \\ N_{48}^{ThT} \end{bmatrix}. \tag{6.11}$$

Now considering only the terms for calculating N_{58}^{SThT},

$$N_{58}^{SThT} = \begin{bmatrix} N_{54}^{S} & P_{54}^{S} \end{bmatrix}\left[\begin{bmatrix} H_{44}^{S} & L_{44}^{S} \\ N_{44}^{S} & P_{44}^{S} \end{bmatrix} + \begin{bmatrix} H_{44}^{ThT} & L_{44}^{ThT} \\ N_{44}^{ThT} & P_{44}^{ThT} \end{bmatrix}\right]^{-1}\begin{bmatrix} L_{48}^{ThT} \\ P_{48}^{ThT} \end{bmatrix}. \tag{6.12}$$

The terms $\boldsymbol{G}_{48}^{ThT}$ and $\boldsymbol{G}_{44}^{ThT}$ in Eq. (6.10) are obtained analytically from the updated holder-tool assembly as shown in Chapter 1. The terms corresponding to the collocated dynamics at coordinate *4* ($\boldsymbol{G}_{44}^{S}$) are obtained experimentally by the decoupling of an adapter using the methods developed in Chapter 4. Now the terms associated with the transfer function matrix between the holder-spindle interface and SIDS, $\boldsymbol{G}_{54}^{S}$, must

also be obtained experimentally. Thus, the prediction of the tool tip-SIDS transfer function is based on two different experimental compliance matrices ($\boldsymbol{G}_{44}^{S}$, $\boldsymbol{G}_{54}^{S}$) obtained from two different measurement campaigns. Although the ERM of a substructure contains all the necessary compliance matrices, the spindle-interface substructure is defined to have two ERMs for the sake of clarity and differentiation.

Now, depending on whether H_{58}^{SThT} or N_{58}^{SThT} is to be predicted for process force estimation, different elements of the $\boldsymbol{G}_{54}^{S}$ matrix have to be measured or calculated.

As seen in Eq. (6.11), for predicting H_{58}^{SThT}, the knowledge of L_{54}^{S} is required. This refers to the FRF obtained by applying a moment excitation at *4* and measuring the lateral displacement at *5*. Such an FRF cannot be measured directly as application of pure moment excitation is not practically realizable. Additionally, the displacement-to-moment FRF L_{54}^{S} cannot be equated to the rotation to force FRF N_{54}^{S} by application of MAXWELL's reciprocity theorem,

$$L_{54}^{S} \neq N_{54}^{S}. \tag{6.13}$$

Thus, the convenience of direct measurement of N_{54}^{S} using SIDS cannot be utilized and L_{54}^{S} must be obtained using a different approach. The modal parameter expansion approach, which was used in Subsection 4.3.1 for the estimation of rotation-to-moment FRFs, is adopted here again for the calculation of L_{54}^{S}. The proposed procedure is introduced in Subsection 6.2.4.

For predicting N_{58}^{SThT} using Eq. (6.12), the required rotation-to-force FRF at the spindle substructure N_{54}^{S} can be measured by applying a dynamic radial force at the spindle interface (coordinate *4*) and measuring the corresponding rotation using SIDS. However, the rotation-to-moment FRF P_{54}^{S} can neither be measured nor be calculated using SCHMITZ's formulation because of the inequality in Eq. (6.13). Here again, the modal parameter expansion approach can be applied.

Thus, both options require modal parameter expansion for the estimation of the unknown FRF and involve comparable analysis effort. In this chapter, the prediction of the displacement to force FRF H_{58}^{SThT} is demonstrated. Indeed, the same approach can be applied for predicting N_{58}^{SThT}.

6.2 Measurement of interface-SIDS transfer function and uncertainty quantification

Vermessung der Schnittstelle-SIDS Übertragungsfunktion und Quantifizierung von Unsicherheiten

As seen in the previous section, the response models of the unassembled spindle substructure at coordinate *4* and *5* ($\boldsymbol{G}^S_{44}$, $\boldsymbol{G}^S_{54}$) must be obtained experimentally for subsequent coupling calculations. Clearly, both these compliance matrices contain certain magnitude of additive measurement noise. However, the focus of this chapter is on the quantification and propagation of measurement uncertainty of the $\boldsymbol{G}^S_{54}$ transfer function. The measurement of the relevant terms of the transfer function $\boldsymbol{G}^S_{54}$ requires dynamic excitation at coordinate *4* at the holder-spindle interface and displacement measurement at the SIDS coordinate *5*. Due to the spatial separation between excitation and measurement coordinates, a poorer signal-to-noise ratio is observed at the SIDS compared to collocated measurements. The presence of the significant GAUSSIAN random noise on the true displacement signal introduces measurement uncertainty, which affects not only the transfer function but also the subsequent coupling calculations. It is therefore advantageous to estimate the experimental transfer functions H^S_{54} and N^S_{54} along with the quantification of measurement uncertainties on each FRF. Although N^S_{54} and its uncertainty quantification is not required for the prediction of H^{STht}_{58}, it is still considered for the sake of completeness and comparison. The focus is on the quantification of uncertainty purely due to additive measurement noise and not due to systematic errors, thermal effects, mass loading, etc. This section is organized as follows:

1. Firstly, the excitation method and measurement setup are introduced for estimating the transfer functions while also enabling the subsequent statistical analysis for uncertainty quantification (Subsection 6.2.1).
2. Secondly, a method for consistent transformation of time data to frequency domain transfer function is provided (Subsection 6.2.2).
3. Thirdly, the uncertainty on the transfer functions is quantified and analyzed (Subsection 6.2.2)

6.2.1 Measurement and excitation method

Mess- und Anregungsmethode

Aim of the measurement campaign is to obtain the displacement-to-force transfer function H^S_{54} and rotation-to-force transfer function N^S_{54} along with uncertainty bounds in the same experimental setup. This means that the measurements must be repeated multiple times in order to perform statistical analysis for uncertainty quantification. The 'moment method' proposed in [KLER08a; VOOR10; TRAI20] is used here for the quantification and propagation of uncertainties. The key idea is that statistical moments can be used for describing the probability distribution of variables, which can then be used to obtain bounds of uncertainty with a certain confidence level. Random measurement noise follows a GAUSSIAN distribution and only the first two moments, i.e. mean and

variance are sufficient to fully describe the distribution function [BEND10]. The assumption here is that the input and output signals contain only random errors and negligible systematic errors. Presence of systematic errors changes the probability distribution and further moments are necessary for its description. Thus, an important criterion for the choice of the excitation setup is that purely measurement noise is overlapped with true displacement or force signals.

During dynamic excitation with manually operated impact hammers, the orientation and impact location can only be controlled to a certain extent. Even automated impact hammers have a finite impact location accuracy and precision. Thus, impact based excitation introduces a certain bias error in the measurements (referred to as 'operator bias' in [MEGG18]). Although these errors can be expected to be small [KIM07], they can be avoided by using a modal shaker or a piezoelectric actuator. Once setup, the excitation location and orientation does not change for these actuators. Hence, the operator and instrument bias which can cause inter-FRF correlation between the simultaneously measured FRFs [MEGG18] is prevented. This implies that, if identical excitation signals are repeated, the difference in force and displacement amplitudes would most likely occur only due to random external influences (measurement noise). Therefore, an excitation using piezoelectric actuator is chosen for FRF measurement and uncertainty quantification. Although this corresponds to a relative excitation, the approximate equivalence of relative and absolute excitations is applied by confirming the preconditions stated in Subsection 4.2.1. Table 6.1 compares the different excitation approaches with respect to their suitability for measurement uncertainty quantification.

Table 6.1 Suitability of excitation methods for transfer function measurement
Eignung der Anregungsmethoden zur Vermessung von Übertragungsfunktionen

Excitation method	Frequency range	Excitation type	Errors	Repeatability
Impact hammer	Dependent on tip	Absolute	Operator bias error w.r.t. location and orientation; Inter-FRF correlation possible	Low
Automatic impact hammer	Dependent on tip	Absolute	Instrument bias error w.r.t. location and orientation; Inter-FRF correlation possible	High
Piezoelectric actuator	0 – 10000 Hz	Relative	Negligible excitation location and orientation error; negligible inter-FRF correlation	High

The motor spindle described in Section 6.1 with the integrated displacement sensors is assembled in the 5-axis horizontal milling machine (MCT B). To enable the excitation of the unassembled interface-spindle substructure at *4*, a dummy tool with an HSK-A 63 interface was sawed off and the interface part was clamped in the spindle (Figure 6.2). This is termed as a stub. For demonstration, the measurements and coupling calculations are conducted for the yz-plane. Therefore, the interface is excited in the y-direction and the displacements are measured at the y and θ_x degrees of freedom of

the SIDS. The rough location of the plane of the SIDS is also shown in Figure 6.2. A piezoelectric actuator with a capacitive force sensor is oriented in the y-direction and placed between the workpiece table and the interface. A static preload of about 250 N was applied. For the dynamic excitation, a ten-second bidirectional quadratic sine sweep between 0 Hz and 2000 Hz was chosen. The quadratic nature ensures that sufficient spectral energy is available at lower frequencies as more time is allotted to long-wavelength frequencies. A single bidirectional sweep is considered one measurement block and the displacement response to this excitation is used to estimate a single FRF. For statistical analysis, the same sweep is applied repeatedly with a pause of one second between two blocks. The pause acts as a trigger for the recognition of the start and end time of one measurement block. The use of multiple, identical excitation blocks is similar to the Operational System Identification method from [KLER07] but instead of using fully deterministic pseudo-random noise, the quadratic sine sweep is utilized as it resulted in better signal quality. Figure 6.2 shows schematically how each measurement block is transformed to the frequency domain and then the FRF is estimated for the corresponding block.

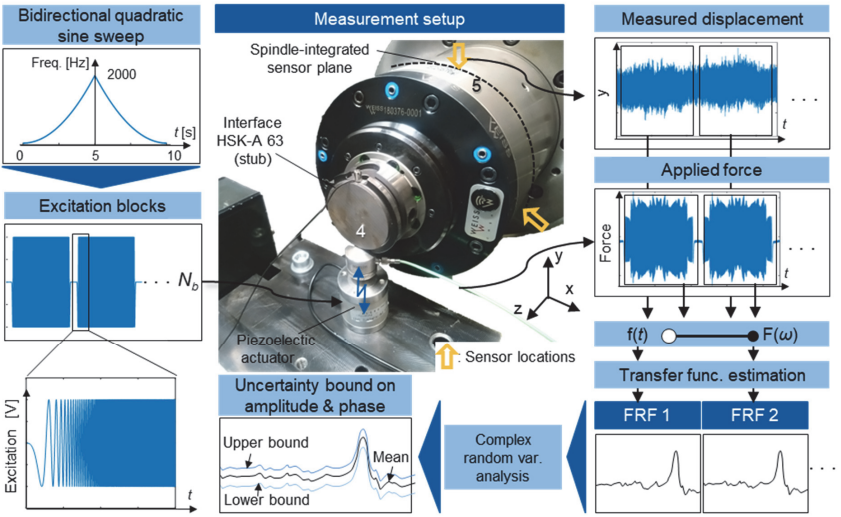

Figure 6.2 Transfer function measurement setup and schematic signal processing

Messaufbau zur Ermittlung der Übertragungsfunktion und Ablauf der Signalverarbeitung

6.2.2 Transfer function estimation

Schätzung der Übertragungsfunktion

The raw displacement response to the force excitation measured at the six SIDS must be first transformed to the displacements y and θ_x of the coordinate *5*. This is realized by solving the rigid plane equation based on the geometry of the sensor arrangement. The simultaneous measurement of y and θ_x due to excitation force corresponds to a SIMO system. However, both the output directions are taken to be independent variables and their inter-FRF correlation is assumed negligible. Each measurement block now has to be windowed and transformed to the frequency domain using a Fast FOURIER Transformation (FFT) algorithm. Although the blocks are periodic and have a common start at end value, a multi-window approach is adopted instead of a single-window approach as in [VOOR10]. This ensures that no leakage occurs due to measurement noise and discretization errors of excitation (volt) signal. Indeed, it is recognized that a higher number of windows averages out random errors and hence influence the magnitude of uncertainty. Especially if zero padded FFTs are calculated. On the other hand, windowing reduces unnecessary high frequency resolutions. Therefore, a minimum number of windows, which give the desired frequency resolution of the FFT without zero-padding, is chosen. In the case of the used data acquisition system, which samples at 50 kHz, ten HANN windows of 2 seconds each are applied with an overlap of 50 %, so that a frequency resolution of 0.5 Hz is achieved (Figure 6.3, left). This signal processing must be applied identically to each measurement block to avoid bias errors. The non-parametric FRF of the corresponding block is then estimated using an H1 estimator which assumes noise on the output signal. The FRFs of the first five measurement blocks estimated using the proposed windowing and estimation method are also shown in Figure 6.3, right.

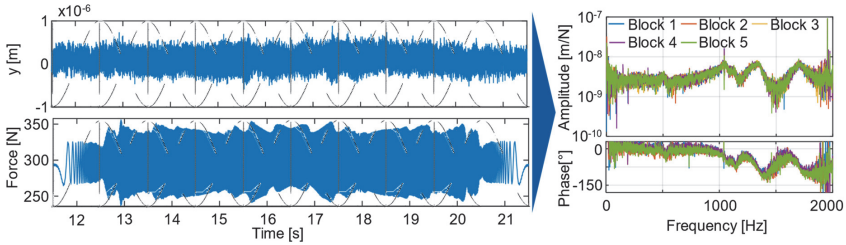

Figure 6.3 Windowing of a force and displacement block and five exemplary block FRFs

Fensterung von Kraft und Verlagerungssignal eines Blocks und FRFs von fünf exemplarischen Blöcken

6.2.3 Uncertainty quantification

Quantifizierung von Unsicherheiten

The multiple measurement blocks serve as a basis for the statistical analysis required for uncertainty quantification. Now, this analysis can be applied at different stages of FRF estimation: i) on the time domain data of force and displacement, ii) FOURIER

transform of the time domain data [KLER08a; VOOR10], or iii) the FRF itself can be treated as a random variable [TRAI20]. All approaches should produce equivalent results, however, options i) and ii) require the additional step of propagating uncertainties to the FRF estimate. Therefore, to avoid this additional step, statistical moments are calculated here on the complex FRF itself, which significantly reduces the analysis effort.

It is important to note that measured FRFs are complex-valued random variables and that the treatment of uncertainty differs significantly from real-valued variables. For example, the calculation of the statistical moment of variance requires not only the calculation of variance of the real and imaginary parts but also the covariance between them. For a complex random variable, $z = Re + jIm$, the bivariate variance-covariance matrix is given as [RIDL02; MEGG18],

$$var(z) = \begin{bmatrix} var(Re) & covar(Re,Im) \\ covar(Re,Im) & var(Im) \end{bmatrix}. \tag{6.14}$$

The analysis is simplified here by ignoring the correlation between the real and imaginary parts (intra-FRF correlation). This reduces the above matrix to a diagonal matrix. Apart from this, an assumption was made in Section 6.2.2 that the inter-FRF correlation is negligible as operator and instrument bias is avoided by the piezoelectric actuator. This gives the correlation between the two measured complex random variables, $var(H^S_{54}, N^S_{54}) = 0$, which further simplifies the statistical analysis.

Quantification of Uncertainty on *H* and *N*-terms

The measurement blocks obtained from the test setup in Figure 6.2 are now analyzed statistically. Let us say that N_b number of blocks are measured giving N_b FRFs of each transfer function: $H^S_{54,1}, H^S_{54,2}, H^S_{54,3}, \ldots H^S_{54,N_b}$ and $N^S_{54,1}, N^S_{54,2}, N^S_{54,3}, \ldots N^S_{54,N_b}$. Each FRF is a complex-valued vector of length N_f. For brevity, the statistical analysis of only the displacement-to-force transfer function H^S_{54} is shown here. The sample mean of the real and imaginary components at each frequency step are given by,

$$\overline{Re(H^S_{54})} = \frac{1}{N_b}\sum_{b=1}^{N_b} Re(H^S_{54,b}); \overline{Im(H^S_{54})} = \frac{1}{N_b}\sum_{b=1}^{N_b} Im(H^S_{54,b}) \tag{6.15}$$

where, b is the block number. Similarly, the dispersion of the random variables about the mean is estimated from the standard deviation,

$$\sigma_{ReH} = \sqrt{\frac{1}{N_b}\sum_{b=1}^{N_b}\left(\left(Re(H^S_{54,b}) - \overline{Re(H^S_{54})}\right)^2\right)} \tag{6.16}$$

$$\sigma_{ImH} = \sqrt{\frac{1}{N_b}\sum_{b=1}^{N_b}\left(\left(Im(H^S_{54,b}) - \overline{Im(H^S_{54})}\right)^2\right)}. \tag{6.17}$$

The above moments describe or estimate the probability distribution of the sample real and imaginary terms. However, this is based on one random sample of N_b blocks and the true or expected value of the statistical moments can deviate from those of the sample. Now, the statistical moment of interest for frequency based substructuring is indeed the mean of the real and imaginary parts of the FRFs [KLER08a]. Therefore, it is important to estimate how the sample mean deviates from the true mean. This can be estimated by the calculating the standard deviation of the sampling distribution of the sample mean (also called standard error), given as [BEND10],

$$\sigma_{\overline{ReH}} = \frac{\sigma_{ReH}}{\sqrt{N_b}};\ \sigma_{\overline{ImH}} = \frac{\sigma_{ImH}}{\sqrt{N_b}} \tag{6.18}$$

Note that the sampling distribution of the sample mean will also have a GAUSSIAN distribution [KIRK06]. Now, the standard error is a point estimator of the true mean and offers only a limited amount of information. It is much more useful to estimate an interval within which, the true mean value lies with a certain confidence level. This interval represents the uncertainty associated with the mean value of the random variable. For a given confidence level, the corresponding standard normal variable Z is calculated and the interval on the true mean value is established as,

$$\left[\overline{Re(H_{54}^S)} - Z\frac{\sigma_{ReH}}{\sqrt{N_b}} \leq \overline{Re(H_{54}^S)} \leq \overline{Re(H_{54}^S)} + Z\frac{\sigma_{ReH}}{\sqrt{N_b}}\right] \tag{6.19}$$

for the real part and,

$$\left[\overline{Im(H_{54}^S)} - Z\frac{\sigma_{ImH}}{\sqrt{N_b}} \leq \overline{Im(H_{54}^S)} \leq \overline{Im(H_{54}^S)} + Z\frac{\sigma_{ImH}}{\sqrt{N_b}}\right] \tag{6.20}$$

for the imaginary part. Now the uncertainties on the means of the real and imaginary components of the FRF for a 95% confidence level can be expressed by the terms,

$$\Delta_{\overline{ReH}} = 1.96\frac{\sigma_{ReH}}{\sqrt{N_b}};\ \Delta_{\overline{ImH}} = 1.96\frac{\sigma_{ImH}}{\sqrt{N_b}} \tag{6.21}$$

and the complex uncertainty is thus,

$$\Delta\overline{H}_{54}^S = \Delta_{\overline{ReH}} + j\Delta_{\overline{ImH}}. \tag{6.22}$$

Although the uncertainties are now quantified on the real and imaginary parts, a more desirable representation of the uncertainty is in the form of upper and lower bounds on the amplitude and phase plot. The bounds on the amplitude are calculated in the conventional way,

$$LB_{amp} = \left\|\overline{H}_{54}^S\right\| - \left\|\Delta\overline{H}_{54}^S\right\|;\ UB_{amp} = \left\|\overline{H}_{54}^S\right\| + \left\|\Delta\overline{H}_{54}^S\right\| \tag{6.23}$$

Now, the phase of the uncertainty is not merely dependent on its real and imaginary components but also on the amplitude of mean FRF as shown in [TRAI20],

$$\angle\Delta\bar{H}^{S}_{54} = \tan^{-1}\left(\frac{\left\|\Delta\bar{H}^{S}_{54}\right\|}{\left\|\bar{H}^{S}_{54}\right\|}\right). \tag{6.24}$$

The bounds on the phase can now be calculated,

$$LB_{pha} = \angle\bar{H}^{S}_{54} - \angle\Delta\bar{H}^{S}_{54};\ UB_{pha} = \angle\bar{H}^{S}_{54} + \angle\Delta\bar{H}^{S}_{54}. \tag{6.25}$$

As part of the measurement campaign using the test setup from Figure 6.2, the coordinate *4* was excited with N_b = 100 blocks of the sweep function. Subsequently, the corresponding 200 transfer function FRFs were analyzed statistically using the method described in this section. The uncertainties on the mean of the real and imaginary parts are represented in terms of bounds on amplitude and phase of the FRFs in Figure 6.4 along with the corresponding mean values.

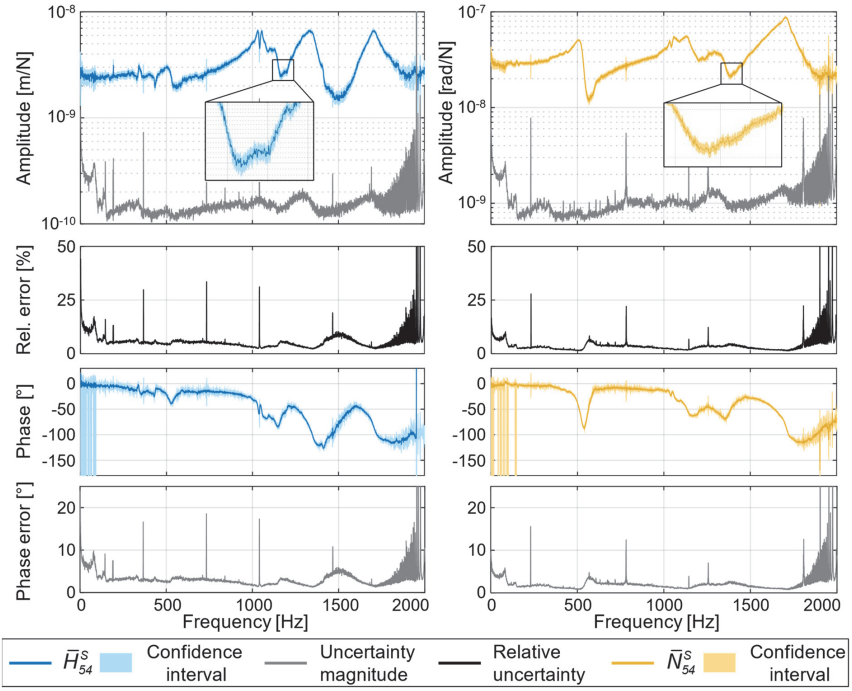

Figure 6.4 Uncertainty quantification and confidence intervals on $\bar{H}^{S}_{54}$ (left) and $\bar{N}^{S}_{54}$ (right)

Unsicherheitsquantifizierung und Konfidenzintervalle für $\bar{H}^{S}_{54}$ (links) und $\bar{N}^{S}_{54}$ (rechts)

It can be observed that, for both measured FRFs, the uncertainty amplitudes are an order of magnitude smaller than the mean values. Comparatively higher amplitude and phase uncertainties are observed at quasi-static frequencies between 0 - 100 Hz. The course of the relative amplitude error shows increases at zeros (or anti-resonances) of

the FRF. For example, at ca. 1170 Hz, 1500 Hz for H^S_{54} and 580 Hz, 1400 Hz for N^S_{54}. This behavior is expected due to the higher dynamic stiffness of the structure at its anti-resonances. Whereas a 4 - 5 % relative amplitude error is observed for the displacement-to-force FRF, a slightly lower relative error of 3 - 4 % is seen for the rotation-to-force FRF. The absolute uncertainty on the phase remains mostly in the range of 2° - 4° for both FRFs. Overall, it can be said that the quantified measurement uncertainty for N_b = 100 blocks and at a confidence level of 95 % appears to be insignificant at frequencies above 100 Hz. Clearly, increasing the number of measurement blocks can further reduce the uncertainty levels. It is also necessary to understand how these uncertainties are propagated and amplified through the coupling calculation. This aspect dealt later in Section 6.3.

6.2.4 Estimation of the *L*-term with modal parameter expansion

Schätzung des L-Terms durch Erweiterung der modalen Parameter

The coupling calculations for predicting the tool tip-SIDS FRFs (Eq. (6.11), (6.12)) include one term each, which cannot directly be measured. For the prediction of H^{SThT}_{58}, the displacement-to-moment FRF at the interface-spindle substructure, L^S_{54} is required. Figure 6.5a shows the compliance matrix of this substructure and highlights the required and measurable FRF. The inspection of the first column of the matrix, $\left[H^S_{44}\ N^S_{44}\ H^S_{54}\ N^S_{54}\right]^T$ shows that all the terms of this column can either be directly measured (H^S_{54}, N^S_{54}) or obtained by decoupling of the adapter (H^S_{44}, N^S_{44}). The latter can also be obtained by the attachment of additional sensors at coordinate *4* during the measurement of the interface-SIDS FRFs. For example, by attaching an accelerometer for measuring y_4, the H^S_{44} FRF can be obtained in the same measurement setup (Figure 6.5b). Similarly, with use of a rotational accelerometer, the FRF N^S_{44} can also be directly measured. However, this option was not explored in this work and FRF was obtained through adapter decoupling. Figure 6.5b summarizes the sources of the FRFs used for modal parameter estimation.

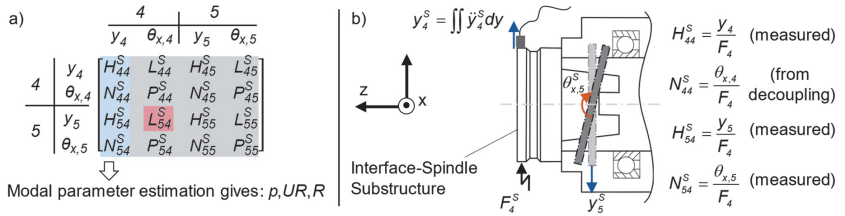

Figure 6.5 a) Compliance matrix of the interface-spindle substructure
b) Sketch of interface-spindle substructure with excitation and response DOFs
a) Nachgiebigkeitsmatrix der HSK-Spindel-Baugruppe
b) Skizze der HSK-Spindel-Baugruppe mit Anregungs- und Antwortfreiheitsgrade

Once the four FRFs in the first column are obtained, first, the global poles of the substructure are identified using the LSCF algorithm [PEET04], as in Subsection 4.3.1.

Second, the residues and residuals are estimated using the Least Squares Frequency Domain Residue estimator [GUIL03]. Thus, each identified FRF in the compliance matrix can be expressed in terms of its modal parameters in the pole-residue form as,

$$\mathrm{FRF}(j\omega) = \sum_{\mathrm{k}}^{\mathrm{n}} \left(\frac{R_{\mathrm{k}}}{j\omega - p_{\mathrm{k}}} + \frac{R_{\mathrm{k}}^{*}}{j\omega - p_{\mathrm{k}}^{*}} \right) - \frac{LR}{\omega^2} + UR \tag{6.26}$$

The frequency range for modal parameter estimation of the four FRFs was 0 - 2000 Hz, such that the lower residual term (*LR*) was not necessary. As an example, the amplitude plots of the measured and 'fitted' FRFs H_{54}^{S} and N_{54}^{S} are compared in Figure 6.6. A good correspondence between the two is observed. Now, the calculation of eigenvectors from the residue matrix $\boldsymbol{R}$ is not as straight forward here as in Subsection 4.3.1. This is because non-collocated FRFs are involved. The complete residue matrix for the interface-spindle substructure can be written in terms of mode shapes as,

$$\boldsymbol{R}_{\mathrm{N_o}\times\mathrm{N_i}\times\mathrm{n}} = \begin{bmatrix} \Phi_{y,4}\Phi_{y,4} & \Phi_{y,4}\Phi_{\theta,4} & \Phi_{y,4}\Phi_{y,5} & \Phi_{y,4}\Phi_{\theta,5} \\ \Phi_{\theta,4}\Phi_{y,4} & \Phi_{\theta,4}\Phi_{\theta,4} & \Phi_{\theta,4}\Phi_{y,5} & \Phi_{\theta,4}\Phi_{\theta,5} \\ \Phi_{y,5}\Phi_{y,4} & \Phi_{y,5}\Phi_{\theta,4} & \Phi_{y,5}\Phi_{y,5} & \Phi_{y,5}\Phi_{\theta,5} \\ \Phi_{\theta,5}\Phi_{y,4} & \Phi_{\theta,5}\Phi_{\theta,4} & \Phi_{\theta,5}\Phi_{y,5} & \Phi_{\theta,5}\Phi_{\theta,5} \end{bmatrix} \tag{6.27}$$

Note that in the above matrix, only the first column is known through identification. For the estimation of L_{54}^{S}, the eigenvectors $\Phi_{y,5}$ and $\Phi_{\theta,4}$ are required. These are obtained based on the knowledge of the first column by the following formulations,

$$\Phi_{y,4} = \sqrt{\boldsymbol{R}(1,1,\mathrm{n})} \tag{6.28}$$

$$\Phi_{\theta,4} = \boldsymbol{R}(2,1,\mathrm{n})/\Phi_{y,4} \tag{6.29}$$

$$\Phi_{y,5} = \boldsymbol{R}(3,1,\mathrm{n})/\Phi_{y,4}\,. \tag{6.30}$$

The calculated eigenvectors ($\Phi_{y,5}$ and $\Phi_{\theta,4}$) can now be substituted in Eq. (6.26) to obtain L_{54}^{S} by modal superposition. The resulting estimate of L_{54}^{S} is plotted in Figure 6.6. As expected, the *L* and the *N*-term differ in their amplitude, while sharing the same poles. This is unlike the case of collocated DOFs, where the *L*-term can be equated to *N*-term applying reciprocity. Although both the terms have a similar course, the amplitude difference can shift the predicted tool tip-SIDS FRF along the y-axis. Therefore, it is necessary to estimate the *L*-term. The estimated L_{54}^{S} and the measured H_{54}^{S} can now be used for prediction of the tool tip-SIDS FRF.

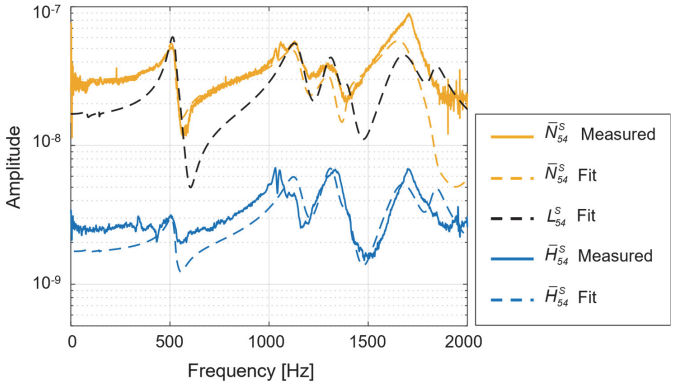

Figure 6.6 Comparison of measured, fitted and estimated FRFs of $\boldsymbol{G}^S_{54}$

Vergleich der gemessenen, gefitteten und geschätzten FRFs von $\boldsymbol{G}^S_{54}$

Note that the fitted FRF H^S_{54} can also be used in the coupling calculations instead of the measured FRF. While this may avoid errors due to measurement noise, it introduces other errors related to modal transformation, parameter estimation and truncation. In Figure 6.6, although a good correspondence between the fit and measured H^S_{54} can be observed, some deviation in the amplitude plots are noticeable. Since these deviations from the mean are greater than the quantified measurement uncertainty at certain frequencies, it was decided not to utilize the fitted *H*-term for coupling calculations.

6.3 Uncertainty propagation in tool tip-SIDS coupling calculations

Fortpflanzung von Unsicherheiten in Werkzeug-SIDS Kopplungsrechnungen

In this section, the uncertainty quantified on the measured FRFs of the spindle substructure is propagated through the coupling calculations for estimating the uncertainty on tool tip-SIDS transfer function. As mentioned in Section 6.1, the coupling equation Eq. (6.10) can also be derived using the LM-FBS formulation. This formulation is used here because the illustration of the propagation of individual FRF uncertainties to the predicted FRF is more convenient and intuitive. The general LM FBS formulation from [KLER06] applied to the coupling of the spindle and analytical tool substructure using the mean FRFs of the spindle substructure is,

$$\overline{\boldsymbol{Y}}^c = \overline{\boldsymbol{Y}}^\mu - \overline{\boldsymbol{Y}}^\mu \boldsymbol{B}^\mathrm{T}\left(\boldsymbol{B}\overline{\boldsymbol{Y}}^\mu \boldsymbol{B}^\mathrm{T}\right)^{-1} \boldsymbol{B}\overline{\boldsymbol{Y}}^\mu \tag{6.31}$$

where, $\overline{\boldsymbol{Y}}^\mu$ is the block diagonal matrix of the mean uncoupled substructure FRFs,

$$\overline{\boldsymbol{Y}}^{\mu} = \begin{bmatrix} \boldsymbol{G}^{ThT} & \boldsymbol{0} \\ \boldsymbol{0} & \overline{\boldsymbol{G}}^{S} \end{bmatrix} = \begin{bmatrix} \boldsymbol{G}_{88}^{ThT} & \boldsymbol{G}_{84}^{ThT} & & \boldsymbol{0} \\ \boldsymbol{G}_{48}^{ThT} & \boldsymbol{G}_{44}^{ThT} & & \\ & & \boldsymbol{G}_{44}^{S} & \overline{\boldsymbol{G}}_{45}^{S} \\ \boldsymbol{0} & & \overline{\boldsymbol{G}}_{54}^{S} & \boldsymbol{G}_{55}^{S} \end{bmatrix} \tag{6.32}$$

and $\overline{\boldsymbol{Y}}^{c}$ is the fully occupied matrix of the coupled substructure FRFs,

$$\overline{\boldsymbol{Y}}^{c} = \begin{bmatrix} \overline{\boldsymbol{G}}_{88}^{SThT} & \overline{\boldsymbol{G}}_{84}^{SThT} & \overline{\boldsymbol{G}}_{84'}^{SThT} & \overline{\boldsymbol{G}}_{85}^{SThT} \\ \overline{\boldsymbol{G}}_{48}^{SThT} & \overline{\boldsymbol{G}}_{44}^{SThT} & \overline{\boldsymbol{G}}_{44'}^{SThT} & \overline{\boldsymbol{G}}_{45}^{SThT} \\ \overline{\boldsymbol{G}}_{4'8}^{SThT} & \overline{\boldsymbol{G}}_{4'4}^{SThT} & \overline{\boldsymbol{G}}_{4'4'}^{SThT} & \overline{\boldsymbol{G}}_{4'5}^{SThT} \\ \overline{\boldsymbol{G}}_{58}^{SThT} & \overline{\boldsymbol{G}}_{54}^{SThT} & \overline{\boldsymbol{G}}_{54'}^{SThT} & \overline{\boldsymbol{G}}_{55}^{SThT} \end{bmatrix}. \tag{6.33}$$

Here, coordinate *4* of the spindle substructure is denoted as *4*' in the assembled state for distinction. $\boldsymbol{B}$ is the signed Boolean matrix representing the compatibility conditions for dual assembly in FBS. Note that the compliance matrices represented by $\boldsymbol{G}$ are of size 2x2 such that the matrices $\overline{\boldsymbol{Y}}^{\mu}$ and $\overline{\boldsymbol{Y}}^{c}$ are of size 8x8 each. Now applying the uncertainty propagation formulation for matrices to the coupling Eq. (6.31), we get the uncertainty of the mean values of the coupled substructure FRFs [KLER08a],

$$\begin{aligned} \Delta\overline{\boldsymbol{Y}}^{c} &= \sqrt{\left\{\sum_{r=1}^{R}\sum_{c=1}^{C}\left\{\frac{\partial\overline{\boldsymbol{Y}}^{c}}{\partial Y_{(r,c)}^{\mu}}\Delta Y_{(r,c)}^{\mu}\right\}^{2}\right\}} \\ &= \sqrt{\left\{\sum_{r=1}^{R}\sum_{c=1}^{C}\left\{(\boldsymbol{P}_{rc} - \boldsymbol{E}_1\boldsymbol{P}_{rc} - \boldsymbol{P}_{rc}\boldsymbol{E}_2 + \boldsymbol{E}_1\boldsymbol{P}_{rc}\boldsymbol{E}_2)\Delta Y_{(r,c)}^{\mu}\right\}^{2}\right\}} \end{aligned} \tag{6.34}$$

where,

$$\boldsymbol{E}_1 \triangleq \overline{\boldsymbol{Y}}^{\mu}\boldsymbol{B}^{\mathrm{T}}\left(\boldsymbol{B}\overline{\boldsymbol{Y}}^{\mu}\boldsymbol{B}^{\mathrm{T}}\right)^{-1}\boldsymbol{B};\ \boldsymbol{E}_2 \triangleq \boldsymbol{B}^{\mathrm{T}}\left(\boldsymbol{B}\overline{\boldsymbol{Y}}^{\mu}\boldsymbol{B}^{\mathrm{T}}\right)^{-1}\boldsymbol{B}\overline{\boldsymbol{Y}}^{\mu}. \tag{6.35}$$

The matrix $\boldsymbol{P}_{rc}$ has the same size as $\boldsymbol{Y}$ with all entries $\boldsymbol{P}_{rc}(i,j) = 0$ for $i \neq r$, $j \neq c$ and $\boldsymbol{P}_{rc}(i,j) = 1$ for $i = r$, $j = c$. The curly brackets denote the requirement of elementwise calculation of squares and square roots.

Now, the Jacobian matrix $\frac{\partial\overline{\boldsymbol{Y}}^{c}}{\partial Y_{(r,c)}^{\mu}}$ determines how uncertainty of the FRF at the r^{th} row and c^{th} column of the uncoupled system, $\Delta\overline{Y}_{(r,c)}^{\mu}$, propagates to all other uncertainties of the coupled FRF matrix, $\Delta\overline{\boldsymbol{Y}}^{c}$. Therefore, the analysis of the Jacobian matrix is an important aspect in understanding how individual uncertainties propagate. The uncertainty of interest in the 8x8 $\Delta\overline{\boldsymbol{Y}}^{c}$ matrix is the one propagated to the tool tip-SIDS transfer function of the coupled system, $\Delta\overline{H}_{58}^{SThT}$. This uncertainty occupies the seventh row and first column in $\Delta\overline{\boldsymbol{Y}}^{c}$ matrix (denoted by $\Delta\overline{Y}_{(7,1)}^{c}$). In the following analysis, the propagation of uncertainties on individual FRFs through the Jacobian is analyzed such that a quantitative statement about the amplification or attenuation of uncertainties can be

achieved. The relevant terms of the interface-SIDS transfer function matrix, $\overline{\boldsymbol{G}}_{54}^{S}$ for MCT B have already been obtained in Section 6.2. The direct compliance matrix at coordinate *4*, $\overline{\boldsymbol{G}}_{44}^{S}$ is obtained experimentally by the decoupling of a cylindrical adapter using SCHMITZ's formulation for complex division. As the analytical tool model, the previously validated model of the HAIMER holder (A63.140.16) with a fully inserted carbide blank of overhang length of 50 mm and diameter of 16 mm is chosen. With this constellation of experimental and analytical models, the propagation of uncertainty on the compliance matrix of the uncoupled interface-spindle substructure ($\overline{\boldsymbol{G}}^{S}$) is analyzed. Note that coordinate *4* of this substructure represents the interface coordinate where mathematical constraints are applied to couple the analytical tool model. On the other hand, the coordinate *5* represents an internal coordinate (SIDS) where no coupling constraints are applied. Thus, the compliance matrices of the interface-spindle substructure can be grouped as: interface ($\boldsymbol{G}_{44}^{S}$), internal ($\boldsymbol{G}_{55}^{S}$) and interface-to-internal ($\boldsymbol{G}_{45}^{S}$, $\boldsymbol{G}_{54}^{S}$). The propagation of uncertainties on the FRFs of these matrices is considered in the following sub-sections.

6.3.1 Propagation of uncertainty on SIDS compliance matrix

Fortpflanzung der Unsicherheit in der SIDS-Nachgiebigkeitsmatrix

For the propagation analysis, first, the unmeasurable compliance matrix at the internal coordinate *5* (SIDS) of the spindle substructure, $\boldsymbol{G}_{55}^{S}$ is considered. Although this matrix is part of the complete coupling equation (see Eq. (6.32), it plays no role in calculating the FRF of interest, $\overline{H}_{58}^{STHT}$ (see Eq. (6.11)). Nevertheless, as an example, the average amplitude of the Jacobian $\frac{\partial \overline{Y}^{c}}{\partial Y_{(7,7)}^{u}}$ for the uncertainty on H_{55}^{S} is calculated using Eq. (6.34) and illustrated in Figure 6.7. As expected, no propagation of uncertainty on the internal coordinate FRF to other FRFs takes place as indicated by the zeros in the matrix. Previous works have also shown that uncertainties of internal-to-internal coordinates do not propagate to any of the FRFs of the coupled system [VOOR10; TRAI20].

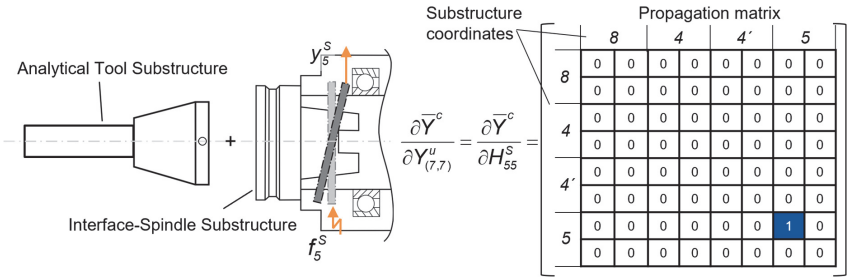

Figure 6.7 Sketch of excitation and measurement DOFs for H_{55}^{S} (left) with corresponding uncertainty propagation matrix (right)

Skizze der Anregungs- und Antwortfreiheitsgrade für H_{55}^{S} (links) sowie die zugehörige Fortpflanzungsmatrix (rechts)

6.3.2 Propagation of uncertainty on the interface compliance matrix

Fortpflanzung der Unsicherheit in der Schnittstellennachgiebigkeitsmatrix

Next, the propagation of uncertainty on the compliance matrix $\boldsymbol{G}_{44}^{S}$ of the isolated spindle-interface substructure (S) is analyzed. Although the uncertainties of this matrix are not quantified, it is still interesting to know how these would be propagated to other FRFs of the coupled system. The Jacobian for three terms of the compliance matrix, H_{44}^{S}, N_{44}^{S} and P_{44}^{S} are calculated. These are denoted as cases a, b and c respectively in Figure 6.8. The excitation and measurement degrees of freedom for each FRF are shown schematically in Figure 6.8 (top). The absolute values of the Jacobian averaged over N_f and rounded off, such that two to three significant figures are created, are shown in the matrix in Figure 6.8 (bottom). Being a coupling coordinate, it is expected that underlying uncertainty will propagate to every FRF of the coupled system. The Jacobian for the *H*-term is roughly an order of magnitude greater than that of the *N*-term, which is again an order of magnitude greater than the *P*-term. This is because of the difference in dimensional units of the respective uncertainties: m/N, rad/N and rad/Nm. Therefore, the propagation magnitudes can only be compared within each Jacobian matrix and not between each other. All three Jacobians seem to amplify the uncertainty propagated to the rotation-to-moment terms of the assembled system significantly, especially for the *P*-terms related to coordinate *8*. No significant propagation to the tool tip-SIDS transfer function located at (*7*,*1*) is observed for all Jacobians.

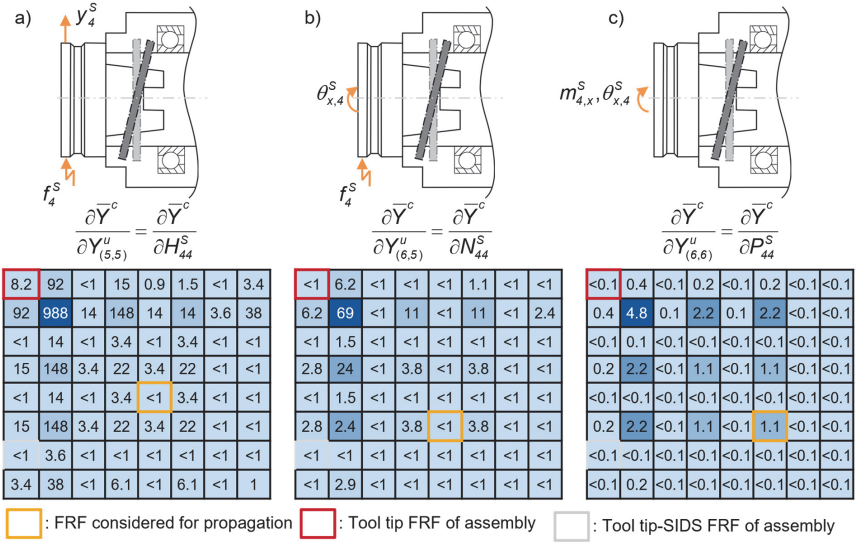

8.2	92	<1	15	0.9	1.5	<1	3.4
92	988	14	148	14	14	3.6	38
<1	14	<1	3.4	<1	3.4	<1	<1
15	148	3.4	22	3.4	22	<1	<1
<1	14	<1	3.4	<1	3.4	<1	<1
15	148	3.4	22	3.4	22	<1	<1
<1	3.6	<1	<1	<1	<1	<1	<1
3.4	38	<1	6.1	<1	6.1	<1	1

<1	6.2	<1	<1	<1	1.1	<1	<1
6.2	69	<1	11	<1	11	<1	2.4
<1	1.5	<1	<1	<1	<1	<1	<1
2.8	24	<1	3.8	<1	3.8	<1	<1
<1	1.5	<1	<1	<1	<1	<1	<1
2.8	2.4	<1	3.8	<1	3.8	<1	<1
<1	<1	<1	<1	<1	<1	<1	<1
<1	2.9	<1	<1	<1	<1	<1	<1

<0.1	0.4	<0.1	0.2	<0.1	0.2	<0.1	<0.1
0.4	4.8	0.1	2.2	0.1	2.2	<0.1	<0.1
<0.1	0.1	<0.1	<0.1	<0.1	<0.1	<0.1	<0.1
0.2	2.2	<0.1	1.1	<0.1	1.1	<0.1	<0.1
<0.1	<0.1	<0.1	<0.1	<0.1	<0.1	<0.1	<0.1
0.2	2.2	<0.1	1.1	<0.1	1.1	<0.1	<0.1
<0.1	<0.1	<0.1	<0.1	<0.1	<0.1	<0.1	<0.1
<0.1	0.2	<0.1	<0.1	<0.1	<0.1	<0.1	<0.1

Figure 6.8 Uncertainty propagation matrices for FRFs a) H_{44}^{S}, b) N_{44}^{S} and c) P_{44}^{S} with corresponding sketches of excitation and measurement DOFs.

Fortpflanzungsmatrizen für die FRFs a) H_{44}^{S}, b) N_{44}^{S} und c) P_{44}^{S} mit Skizzen von zugehörigen Anregungs- und Antwortfreiheitsgraden

The uncertainty on the displacement-to-force FRF, H^{S}_{44} (case a) is significantly amplified and propagates the uncertainty of the tool tip FRF. In other cases, the amplification to the tool tip FRF is not significant. Note that the Jacobian matrices only indicate the rough magnitude of amplification of the respective uncertainties and not the contribution of individual uncertainty to the total uncertainty of the assembly. For calculating the contribution to total uncertainty, the propagation terms must be multiplied with the quantified uncertainty.

6.3.3 Propagation of uncertainty on interface-SIDS compliance matrix

Fortpflanzung der Unsicherheit in der Schnittstellen-SIDS-Nachgiebigkeitsmatrix

The compliance matrix between the interface coordinate *4* and SIDS coordinate *5* represents a coupling-to-internal coordinate transfer function $\overline{\boldsymbol{G}}^{S}_{54}$. Only the *H* and *L*-terms of this matrix are required for the prediction of the required displacement-to-force tool tip-SIDS transfer function. Therefore, the Jacobian matrices for only these FRFs are calculated and shown in Figure 6.9 with illustrations of corresponding excitation and response degrees of freedom. Since this is a coupling-to-internal transfer function, the uncertainties are not propagated to all FRFs of the coupled system but rather to all FRFs in the respective row or column. A common trend observable in both the Jacobian matrices is that the uncertainty amplification is much greater for the FRFs which contain a rotational degree of freedom (terms (*7*,*2*), (*7*,*4*), (*7*,*6*) in both matrices in Figure 6.9). As expected, uncertainty is not propagated to the tool tip FRF as seen in the term (*1*,*1*). Apart from this, a significant amplification of uncertainty on $\overline{H}^{S}_{54}$ to the tool tip-SIDS FRF $\overline{H}^{STbT}_{58}$ can be observed Figure 6.9 (left).

As mentioned in the previous subsection, the Jacobians merely provide the amplification factors. The actual propagated uncertainty magnitude can only be assessed if the uncertainties on the measured FRFs are quantified. In the above case, $\overline{H}^{S}_{54}$ is measurable and its measurement uncertainty is quantified as proposed in Subsection 6.2.2. On the other hand, L^{S}_{54} is obtained by modal expansion and does not explicitly contain measurement noise uncertainty. Therefore, the propagated measurement uncertainty is only due to the quantified uncertainty on $\overline{H}^{S}_{54}$. Using this, the uncertainty matrix of the coupled spindle-holder-tool (*STbT*) assembly $\Delta\overline{\boldsymbol{Y}}^{\mathcal{C}}$ can be calculated from Eq. (6.34). For predicting the mean FRFs of the coupled system ($\overline{\boldsymbol{Y}}^{\mathcal{C}}$), Eq. (6.31) is solved. The required mean tool tip-SIDS force-to-displacement FRF ($\overline{H}^{STbT}_{58}$) as well as the total associated uncertainty are located at the seventh row and first column of $\overline{\boldsymbol{Y}}^{\mathcal{C}}$ and $\Delta\overline{\boldsymbol{Y}}^{\mathcal{C}}$ respectively. Note that $\overline{H}^{STbT}_{58}$ can also be obtained from Eq. (6.11) by taking the mean values of the interface-SIDS FRFs.

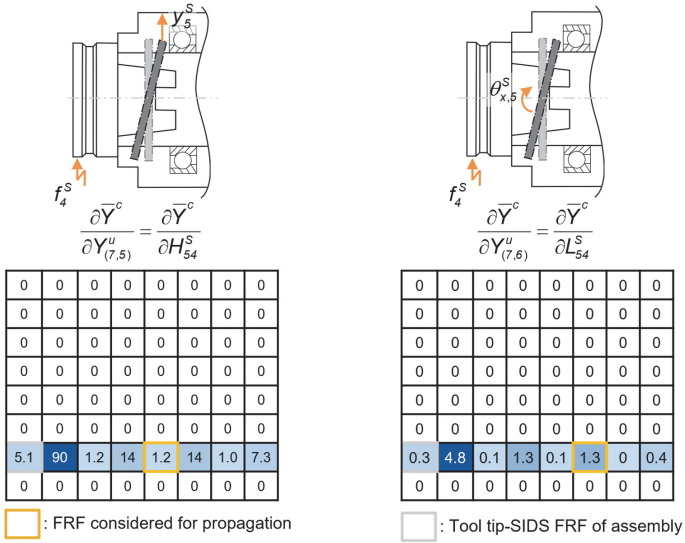

0	0	0	0	0	0	0	0
0	0	0	0	0	0	0	0
0	0	0	0	0	0	0	0
0	0	0	0	0	0	0	0
0	0	0	0	0	0	0	0
0	0	0	0	0	0	0	0
5.1	90	1.2	14	1.2	14	1.0	7.3
0	0	0	0	0	0	0	0

0	0	0	0	0	0	0	0
0	0	0	0	0	0	0	0
0	0	0	0	0	0	0	0
0	0	0	0	0	0	0	0
0	0	0	0	0	0	0	0
0	0	0	0	0	0	0	0
0.3	4.8	0.1	1.3	0.1	1.3	0	0.4
0	0	0	0	0	0	0	0

Figure 6.9 Uncertainty propagation matrices for $\overline{H}^S_{54}$ (left) and L^S_{54} (right) with corresponding sketches of excitation and measurement DOFs

Unsicherheitsfortpflanzungsmatrizen für $\overline{H}^S_{54}$ (links) und L^S_{54} (rechts) mit Skizzen von zugehörigen Anregungs- und Antwortfreiheitsgrade

Figure 6.10a shows the amplitude of the predicted tool tip-SIDS FRF along with the total propagated amplitude uncertainty corresponding to a 95% confidence level. It can be observed that, the uncertainty on the amplitude is more than an order of magnitude smaller than the predicted FRF and thus indicates an acceptable level of random error. In addition, the course of the propagated uncertainty roughly corresponds to the predicted FRF from around 600 Hz onwards. Below this frequency, the uncertainty is strongly influenced by the poles and zeros of the uncoupled spindle-interface substructure, even though these are not seen dominantly in the predicted FRF. At low frequencies (0 - ca. 50 Hz), a relatively high uncertainty amplitude is observed. This is due to presence of accelerometer based FRFs in the propagation calculations. These FRFs have high noise content in this range.

For comparison, the uncertainties quantified on both of the measurable interface-SIDS FRFs ($\overline{H}^S_{54}$, $\overline{N}^S_{54}$) are also plotted in Figure 6.10a). The measurement of $\overline{N}^S_{54}$ is a by-product of the measurement campaign and the procedure of uncertainty quantification is identical to the *H*-term. The uncertainty amplification effect due to the coupling calculations is clearly observable by comparing the quantified uncertainty $\Delta\overline{H}^S_{54}$ with the propagated uncertainty $\Delta\overline{H}^{SThT}_{58}$. The propagated uncertainty possesses a comparatively higher amplitude throughout the frequency range. Both have a similar course below 600 Hz.

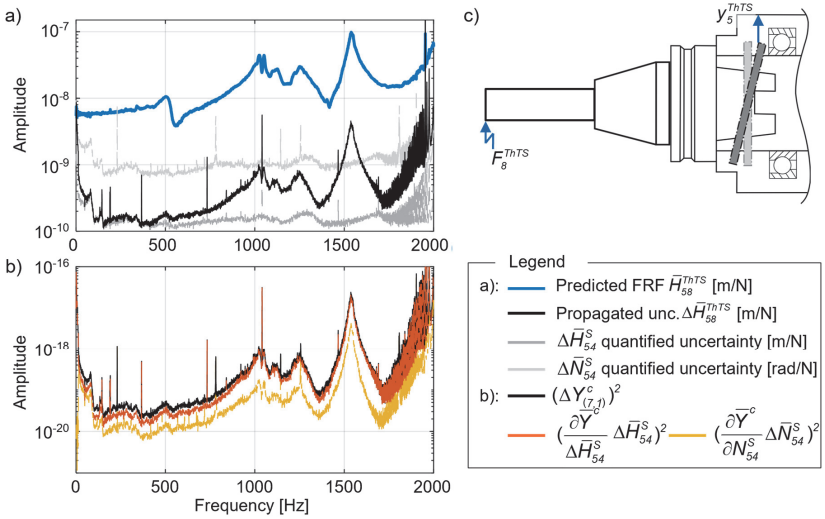

Figure 6.10 a) Predicted tool tip-SIDS FRF with propagated uncertainty
b) contribution of individual uncertainties to total uncertainty
c) sketch of input and output DOFs
a) Prognose der Werkzeug-SIDS FRF mit propagierter Unsicherheit
b) Beitrag der einzelnen Unsicherheiten zur Gesamtunsicherheit
c) Skizze der Anregungs- und Messkoordinaten

Now, although the fitted transfer function L_{54}^{S} does not contain random noise, it is still subject to errors such as modal truncation and parameter estimation errors. Therefore it is important to understand how potential errors on this FRF can propagate to the coupled tool tip-SIDS FRF. For the purpose of this contribution analysis, the quantified uncertainty $\Delta\overline{N}_{54}^{S}$ is taken as the uncertainty on L_{54}^{S}. The contribution analysis is conducted here by considering the squared value of propagated uncertainty matrix in Eq. (6.34). Expanding the equation for the quantified uncertainties, we get,

$$\left(\Delta\overline{\boldsymbol{Y}}^{c}\right)^{2} = \left(\frac{\partial\overline{\boldsymbol{Y}}^{c}}{\partial\overline{H}_{54}^{S}}\cdot\Delta\overline{H}_{54}^{S}\right)^{2} + \left(\frac{\partial\overline{\boldsymbol{Y}}^{c}}{\partial L_{54}^{S}}\cdot\Delta\overline{N}_{54}^{S}\right)^{2}. \tag{6.36}$$

The left-hand side of the above equation represents the matrix of the squared value of the total propagated uncertainty. The term of interest $(\Delta\overline{Y}_{(7,1)}^{c})$ is plotted along with the two terms on the right-hand side of the above equation in Figure 6.10b. It can be seen that the majority of the propagated (squared) uncertainty is contributed by $\Delta\overline{H}_{54}^{S}$. This is notable, given the fact that the amplitude of uncertainty of $\Delta\overline{N}_{54}^{S}$ is roughly one order of magnitude greater (Figure 6.10a). However, as seen in the averaged Jacobian matrix (Figure 6.9, right) the uncertainty on $\Delta\overline{N}_{54}^{S}$ is attenuated for propagation to the *H*-

terms and amplified for most of the *N*-terms of the matrix column. Therefore, the resulting contribution to propagated uncertainty is significantly smaller than the quantified uncertainty itself. On the other hand, the Jacobian of $\Delta\overline{H}_{54}^{S}$ amplifies uncertainty to the FRF of interest (Figure 6.9, left) and thus has a dominant contribution to the propagated uncertainty.

The following observations can be summarized based on the analysis in this section:

i) Uncertainty on the *H*-term of the interface compliance matrix ($\Delta\overline{H}_{44}^{S}$), is significantly amplified to the tool tip FRF ($\overline{H}_{88}^{SThT}$).
ii) Uncertainty on the *H*-term of the interface-SIDS transfer function matrix ($\Delta\overline{H}_{54}^{S}$), is significantly amplified to the tool tip-SIDS transfer function ($\overline{H}_{58}^{SThT}$).
iii) Uncertainty on the *N* and *P*-terms are attenuated for both $\overline{H}_{88}^{SThT}$ and $\overline{H}_{58}^{SThT}$.
iv) The contribution analysis also shows that, the total uncertainty propagated to $\overline{H}_{58}^{SThT}$ is dominated by the $\Delta\overline{H}_{54}^{S}$ term, although $\Delta\overline{N}_{54}^{S}$ has a greater absolute magnitude.

This implies that for the reliable prediction of force-to-displacement FRFs (at tool tip as well as tool tip-SIDS), the accurate measurement of the *H*-terms of the compliance matrices is of greater importance. Special care should be taken in the design of the measurement setup for force-to-displacement FRFs such that propagation of bias errors is reduced as well.

6.4 Prediction of tool tip-SIDS FRFs and validation

Prognose von Werkzeug-SIDS Übertragungsfunktionen und Validierung

The proposed method for experimental determination of the interface-SIDS transfer function matrix is validated in this section. In addition, the quantified uncertainty, $\Delta\overline{H}_{54}^{S}$ is propagated through the coupling calculation using Eq. (6.34) such that confidence bounds on the predicted tool tip-SIDS FRFs are obtained.

Experimental setup

The 5-axis MCT B with SIDS is utilized here again for the experimental implantation. The ERMs at the spindle-holder interface were obtained by decoupling of cylindrical adapters of 32 mm and 35 mm diameter. These correspond to the interface end diameters of the tool holders used for the validation. The compliance matrices at the free end of the adapters were measured using a piezoelectric excitation in the y-direction and measurement of accelerations at the usual three coordinates (see Section 4.1). The rotational compliances were calculated using the backwards difference method and by applying complex division as shown in [SCHM05].

For validation, four different holder-tool assemblies with tool (or blank) diameter of 10 mm and 16 mm were considered. Shrink-fit holders from HAIMER of type A63.140.10 and A63.140.16 were taken here. First, carbide blanks were fully inserted in each holder and the reference blank tip-SIDS transfer functions in the y-direction were

measured using an impact hammer with a steel tip (Figure 6.11, left). Carbide blanks were chosen first so as to avoid errors associated with analytical modelling of complex flute geometries and observe prediction errors only due to experimental and random errors as well as their propagation. In a second step, two end mills of ø10 mm (FRAISA P8400450) and ø16 mm (FRAISA P8410610) were fully inserted and the tool tip-SIDS transfer functions were measured. Both end mills have four flutes. The analytical modelling, joint identification and effective fluted segment calculation was carried out as described in Sections 5.3, 5.4 and 5.5 respectively. Subsequently, Eq. (6.11) is solved to obtain the predicted $\bar{H}_{58}^{STht}$ FRF. The corresponding reference and predicted FRFs are plotted in the Bode plots in Figure 6.11, right.

Results

The frequency range of the predicted FRFs results from the frequency range of excitation used for the measurement of the interface-SIDS transfer functions (0 – 2 kHz). A very good correspondence between the reference and predicted amplitudes and phases can be observed throughout the frequency range, except the first dominant mode at about 1 kHz. In the static and quasi-static frequency range, the predicted and measured values match very well. Prediction accuracy in this range is of high relevance as both, the static as well as dynamic process force estimations depend on the prediction in this range.

An amplitude deviation in the range of around 2.5 % to 9.5 % is observed between the mean predicted and reference transfer functions. The good matching with the reference also indicates correct analytical tool modelling and updating.

The first tool bending modes are predicted at ca. 1663 Hz for assembly A and C and at ca. 1537 Hz for assembly B and D. This indicates that the SIDS coordinate does not lie at any node of the tool mode shape. However, the comparison of the predicted tool vibration modes with measured transfer function is made difficult by the poor coherence of reference FRFs above ca. 1500 Hz. The reason for the poor coherence, especially in case of end mills, is the difficulty in applying high impulse force on the narrow flutes using the impact hammer. A maximum of 800 N of impulse force could be applied to the end mill with the steel tip hammer, which did not result in sufficient spectral energy above 1500 Hz at the SIDS. In future works, the reference tip-SIDS FRFs should be measured using piezoelectric actuators.

Figure 6.11, right also shows the amplitude plots of the propagated uncertainties corresponding to 95 % confidence level for each prediction. The uncertainty bounds on amplitude and phase are also plotted. The magnitude of propagated uncertainty remains below 3.3 % to 4 % of the mean values for most of the frequency range. At low frequencies (< 50 Hz), again, the influence of accelerometer based FRFs is observable. Despite the spatial separation between the interface flange and the SIDS, the amplitude of uncertainty propagated to the mean tip-SIDS FRFs remain low for all predictions. Note that the level of uncertainty for a specific confidence level is inversely proportional to the number of samples or repeated measurements (see Eq. (6.21)).

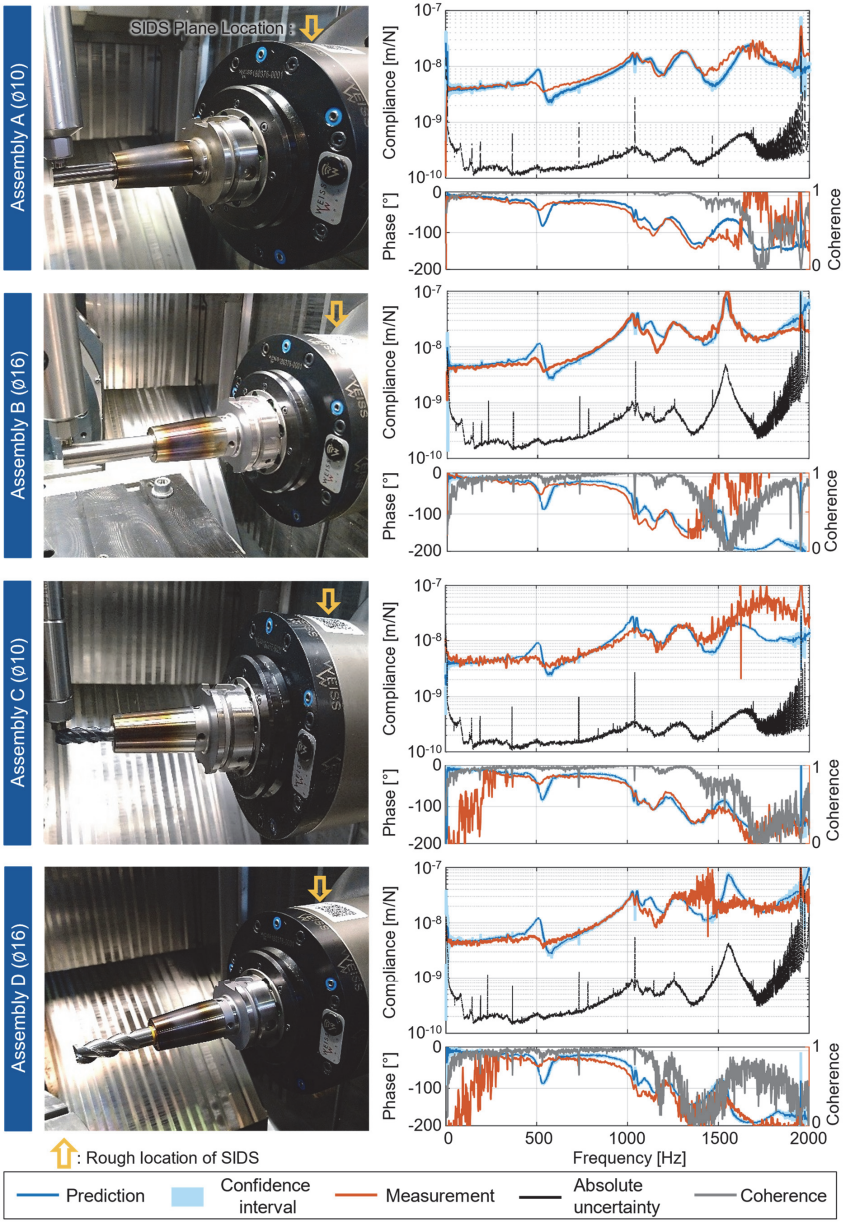

Figure 6.11 Comparison of measured and predicted tool tip-SIDS transfer functions

Vergleich von gemessenen und prognostizierten Werkzeug-SIDS Übertragungsfunktionen

Thus, with sufficient number of repeated measurements of H_{54}^{S} and N_{54}^{S}, the propagated uncertainty due to measurement noise can be kept at a low level. A repetition of N_b = 100 blocks used in this thesis seems to be sufficient for attaining narrow intervals on the predicted FRFs.

The proposed methods are demonstrated here for the case of a stationary spindle. The tool tip-SIDS transfer function is expected to vary with increasing spindle speeds. However, the proposed methods for one-time experimental response modelling of the interface-SIDS dynamics, uncertainty quantification and propagation can be applied to response models measured under rotation as well. Such a measurement of the interface-SIDS transfer function under rotation is conceivable with the help of the actuated impact hammer or a radial dynamic loading unit as shown in [BREC20c].

7 Process Force Estimation and Integration in Virtual Quality Framework

Ermittlung von Prozesskräften und Integration in ein Rahmenwerk der virtuellen Qualität

The developed framework for efficient experimental analytical tool coupling provide two predictions: tool tip-SIDS transfer function with confidence intervals and the tool tip FRF. These predictions, along with displacements at SIDS and an engagement simulation, enable process parallel computation of milling forces and workpiece quality monitoring. A model-based framework for virtually monitoring the workpiece surface quality was developed at the WZL and is introduced in [KÖNI18]. This framework is referred as Workpiece Quality Monitoring (WQM). Aim of this chapter is to demonstrate the utility of the predicted dynamic behaviors in the context of virtual quality monitoring. For this, a method for estimation of forces on the milling tool based on the deflections measured at the SIDS is first introduced and validated (Section 7.1). Here, a method for the propagation of the quantified uncertainty to the force estimates is also proposed. Subsequently, an approach for the integration of the developed tool coupling framework with an existing WQM framework is provided (Section 7.2). Finally, this integration is demonstrated for an exemplary milling operation (Section 7.3).

7.1 Method for process force estimation

Methode zur Prozesskraftschätzung

As introduced in the literature survey (Subsection 2.1.2), there are two main model-based approaches for estimating process forces by using structural deflections and appropriate transfer functions. These are the disturbance KALMAN filter approach and the transfer function inversion approach. Since the aim here is merely to demonstrate the potential of efficient tool compliance function prediction within the context of process and quality monitoring, the relatively simpler inversion approach is implemented for force estimation. Thus, the proposed method is based on the transfer function inversion approach from [BREC18b; BREC19c].

Under the assumption of negligible cross compliance between the radial directions ($H_{5x8y}^{SThT} \approx H_{5y8x}^{SThT} \approx 0$), the force acting on the tool tip in a radial direction can be estimated based on the inversion of the corresponding tool tip-SIDS transfer function. Note that cross-compliance between a radial force at tool tip and axial SIDS displacement was shown to be non-negligible in [BREC19c]. However, this cross compliance only plays a role for estimating axial forces. In this section, only the estimation of radial process forces is demonstrated and hence the cross compliance is ignored.

The proposed method for process force estimation is illustrated schematically in Figure 7.1. The starting point for the method is the prediction of the mean tool tip-SIDS transfer functions in the radial directions, which are obtained by applying the proposed tool coupling framework. Next, the displacements measured by the six axially and radially

arranged spindle integrated sensors during milling are considered. These are corrected to remove the systematic run-out and kinematic errors during rotation as introduced in [BREC18b; BREC19c]. Subsequently, orbit and rigid plane calculations are performed to obtain radial and rotational deflections of the shaft-mounted disc from the corrected measurements.

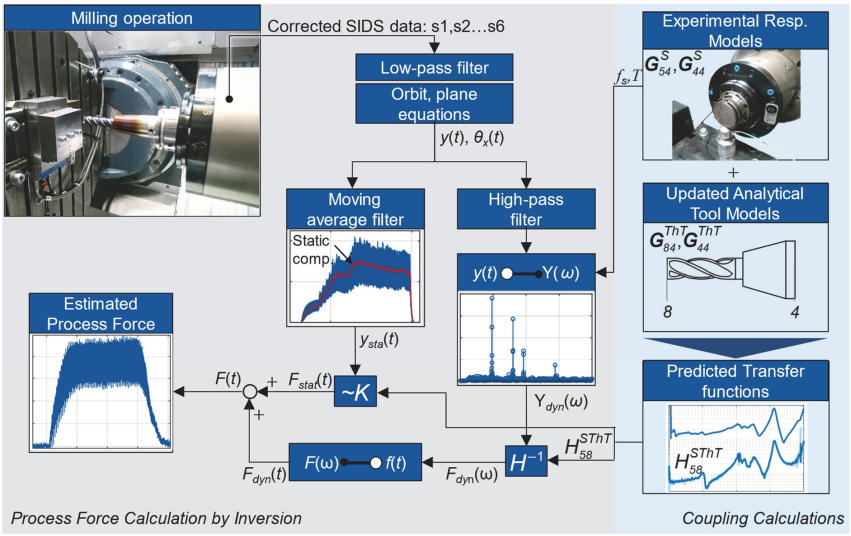

Figure 7.1 Process force estimation using SIDS and predicted transfer function
Prozesskraftschätzung mittels SIDS und vorhergesagte Übertragungsfunktion

A moving average as well as a high-pass filter then concurrently filters the resulting radial and rotational deflections of the spindle-mounted disk (or SIDS coordinate). This gives respectively the static and dynamic components of the displacement signals. The dynamic component is transformed to the frequency domain such that the sampling frequency (f_s) and resolution ($1/T$) match those of the experimental response model. This is realized by adjusting the FFT window length as described in Subsection 6.2.2. Apart from this, the experimental response models must be zero-padded, as the SIDS measurements occur at a much higher sampling rate of 51.2 kHz. In this way, the temporal resolution of the predicted force can be conserved. Thus, the zero-padded, predicted tool tip-SIDS transfer function is inverted and multiplied with the frequency domain dynamic deflections to give the frequency domain force at the tool tip,

$$\bar{F}_8^{SThT}(\omega) = \left(\bar{H}_{58}^{SThT}(\omega)\right)^{-1} \cdot \bar{y}_5^{SThT}(\omega). \tag{7.1}$$

It is then transformed back to the time domain by taking the inverse FOURIER transform. The estimated static deflection at the SIDS coordinate is multiplied with the averaged quasi-static component of the transfer function, giving the static force. The addition of the force components then results in the estimate of the total process force. Although the above calculations can be performed process-parallel, the dead time associated

with transformation from time to frequency domain is unavoidable in the transfer function inversion method. A method for the propagation of uncertainty to the force predictions is now introduced in the following.

Propagation of uncertainty to force estimates

It is important to understand how the quantified uncertainty on the interface-SIDS transfer function as well as the measurement noise on the SIDS signals propagate to the force estimates. The treatment of uncertainty and its propagation depends on the method of force estimation. For example, in the disturbance KALMAN filter approach, uncertainties can be considered in the system noise matrix as part of the noise contaminated state space model [ALBR05]. In case of the inversion approach, the propagation formulation is applied to the expression for force calculation such that,

$$\Delta\bar{F}_8^{SThT} = \sqrt{\left(\frac{\partial\bar{F}_8^{SThT}}{\partial\bar{H}_{58}^{SThT}}\cdot\Delta\bar{H}_{58}^{SThT}\right)^2 + \left(\frac{\partial\bar{F}_8^{SThT}}{\partial\bar{y}_5^{SThT}}\cdot\Delta\bar{y}_5^{SThT}\right)^2} \tag{7.2}$$

where,

$$\frac{\partial\bar{F}_8^{SThT}}{\partial\bar{H}_{58}^{SThT}} = -\bar{y}_5^{SThT}(\omega)\cdot\left(\Delta\bar{H}_{58}^{SThT}\right)^{-2};\ \frac{\partial\bar{F}_8^{SThT}}{\partial\bar{y}_5^{SThT}} = \left(\Delta\bar{H}_{58}^{SThT}\right)^{-1}. \tag{7.3}$$

Note that apart from the uncertainty quantified on the mean tool tip-SIDS FRF ($\Delta\bar{H}_{58}^{SThT}$), the uncertainty associated with the displacement measured by SIDS ($\Delta\bar{y}_5^{SThT}$) is also required for the above equation. This is quantified by considering the time domain displacements during the interface-SIDS transfer function measurement campaign from Section 6.2. These are transformed to frequency domain to get 100 blocks of FFTs. Now the quantification of the complex uncertainty on the mean FFT is achieved using the method proposed in Subsection 6.2.3. The only difference is that the uncertainty is quantified on the mean FFT and not the mean transfer function.

Thus, Eq. (7.2) can be solved for each tool assembly, where the propagated uncertainty on the tool tip-SIDS transfer function is known. Subsequently, the propagated frequency domain uncertainty can be utilized for representing the 95 % confidence interval on the mean of the estimated forces. Finally, these are transformed to the time domain analogous to the procedure in Figure 7.1 to get upper and lower confidence bounds on the mean estimated process force during milling.

Estimation of dynamic forces at stationary operating point

Before the proposed method can be applied for estimating the cutting forces in real milling operations, it is first necessary to empirically show that predicted transfer functions accurately estimate the dynamic tool tip forces with the inversion method. Since the experimental response models were acquired at the stationary operation point in Chapter 1, the validation is also conducted for the case of stationary spindle of MCT B.

The two holder-blank assemblies, whose transfer functions in y-direction were validated in Section 6.4, are chosen: the 16 mm and a 10 mm tool holder with corresponding fully inserted carbide blanks. For introducing dynamic forces during stationary operation, a piezoelectric actuator (Type: PSt 1000/25/125 from PIEZOSYSTEM JENA GMBH) and a force sensor (Type: 9102 from KISTLER INSTRUMENTE GMBH) are aligned in the y-direction as shown in Figure 7.2. Carbide blanks are chosen because of the ease of force application at the free end compared to the fluted segment of an end mill.

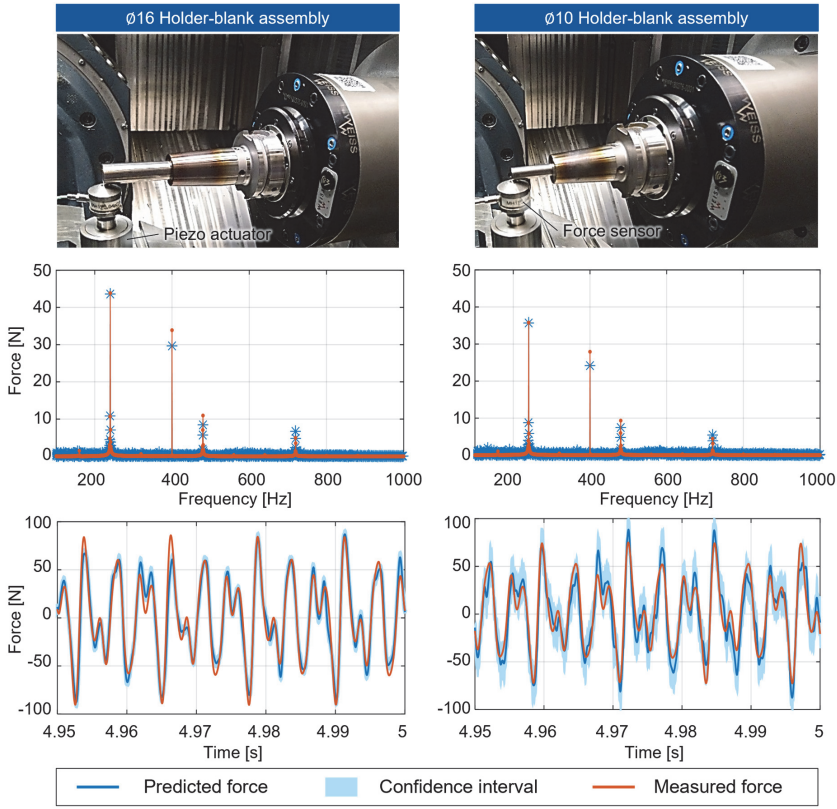

Figure 7.2 Comparison of predicted and measured dynamic forces at the blank tip for two different tools

Vergleich der vorhergesagten und gemessenen dynamischen Kräfte an der Rohlingsspitze für zwei verschiedene Werkzeuge

Stable milling process forces usually contain dynamic components corresponding to tool-passing frequency, its higher order harmonics and structural vibration frequencies. Therefore, an excitation signal was created, which contains a dominant tooth-passing frequency of 240 Hz, harmonics at 480 Hz, 720 Hz and structural vibration frequency at 400 Hz. The FOURIER transform of the applied dynamic force at the tool tip is also shown in Figure 7.2. The deflections at the SIDS caused by the piezo excitation are

filtered and processed as proposed in Figure 7.1 to obtain the force estimates at the tool tip for both assemblies. The time domain as well as frequency domain estimates of the force are plotted in Figure 7.2 and match very well with the measured forces in both domains. Each frequency component could be estimated correctly with a maximum amplitude error of 13.9 % and 15.4 % at 400 Hz for the ∅16 mm and ∅10 mm blank, respectively. The amplitude errors at 240 Hz are merely 0.6 % and 0.3 %. Additionally, the uncertainty bounds on the time domain force estimates are also calculated using Eq. (7.2) and plotted in Figure 7.2. The uncertainty bounds show a plausible course for both tool assemblies. A wider uncertainty bound is observed in case of the ∅10 mm blank assembly. This is due to two reasons: i) amplitude of the applied dynamic load is comparatively lower and ii) the overhang of the ∅10 mm blank assembly results in a smaller lever-arm effect. Both these aspects lead to a comparatively smaller deflections at the SIDS, which correspond to greater uncertainty due to poor SNR for small deflections.

Note that the maximum dynamic excitation of 70 N at 240 Hz for the 10 mm blank corresponds to a deflection of approximately 0.3 µm at the SIDS. This dynamic force is much lesser than what can be expected in a conventional milling (roughing) operation. Despite the small deflection at SIDS and low SNR, the dynamic forces could be estimated with sufficient accuracy. Therefore, the proposed method is considered to be acceptable for integration in the quality framework.

7.2 Integration in a virtual quality framework

Integration in ein Rahmenwerk zur virtuellen Qualitätsüberwachung

Virtual workpiece quality monitoring drastically reduces long quality feedback loops by running an efficient, online material removal simulation based on concurrent NC-signal data and estimated process forces [KÖNI18]. The key idea behind virtual quality is the model-based recreation of the real TCP path in the material removal simulation such that the generated virtual workpiece replicates the surface structure deviations of the real workpiece. The main inputs required for this are:

i) Geometric meta-information of tool and workpiece along with kinematic information of the machine tool.
ii) NC-Signal data with models for correcting TCP set path.
iii) Online process force estimates.
iv) Knowledge of tool and workpiece compliance functions in clamped state.

In this section, the potential of experimental-analytical milling tool coupling in providing inputs iii) and iv) from above to the existing WQM framework is demonstrated. Here the focus is on use-cases, where the influence of tool side deflection is significantly greater than the workpiece-side, such that only the TCP FRFs of different tool have to be predicted. Figure 7.3 schematically illustrates the proposed integration of experimental-analytical tool coupling with the WQM framework for machine tools with spindle integrated sensors.

Consider an end milling operation on such a machine equipped with an edge computer, a 'Machine Data Gateway' communicating with the NC and a target computer as proposed in [WELL19]. For substructure coupling calculations, first, a one-time experimental response modelling of the interface ($\boldsymbol{G}^{S}_{44}$) and the interface-SIDS transfer functions (H^{S}_{54}, N^{S}_{54}) are necessary (Figure 7.3, top left). For obtaining the interface response model, the working room of the machine is divided into a grid of measurement points. Two to three adapters with different diameters ($\emptyset_{A1}$, $\emptyset_{A2}$,…$\emptyset_{An}$) are measured at each machine grid position (Pos_1, Pos_2,…Pos_n) and discretized spindle speeds (ω_1, ω_2,…ω_n). The excitation, measurement and analysis strategies for obtaining the ERM are based on insights from Chapter 4. The effort required for the measurement campaign is mainly dependent on the degree of position-dependent and spindle speed-dependent dynamic behavior of the machine tool.

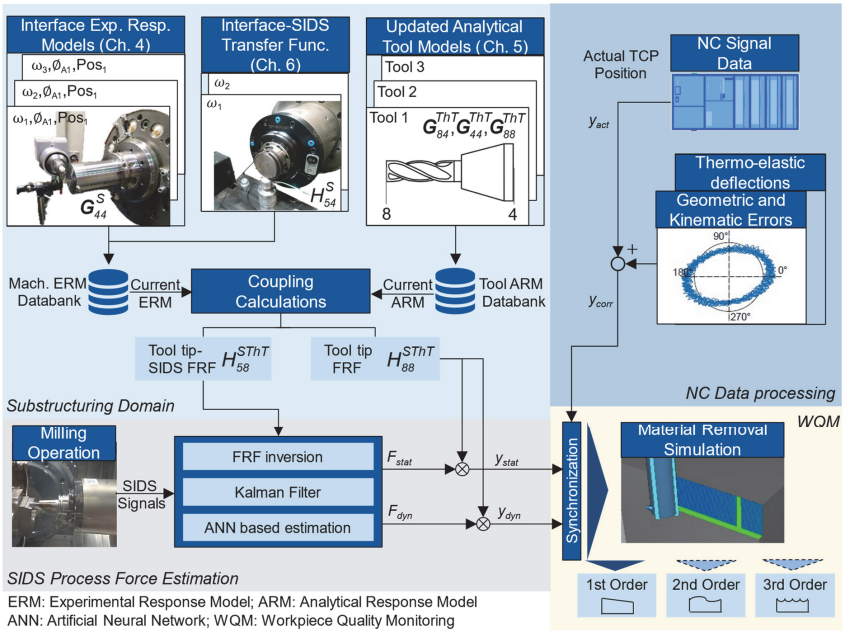

Figure 7.3 Experimental-analytical tool coupling within the framework of virtual quality
Experimentell-analytische Werkzeugankopplung im Rahmen virtueller Qualität

The one-time measurement of the interface-SIDS transfer functions (see Chapter 6) can usually be conducted independent of machine position and excitation direction. This is due to the rotational symmetry of the spindle and measurement of relative displacement between spindle shaft and housing. The spindle speed influence can be considered by conducting impact tests at discretized speeds using an automatic impact hammer instead of a piezoelectric actuator. However, the same method for obtaining the transfer function proposed in Chapter 6 can be applied. The ERMs of each machine

are then saved on a database available to the edge computer. Similarly, a priori created and updated ARMs of different tool assemblies (see Chapter 5) are saved on another databank. Depending on the current tool in use and the machine operating point, the respective models can be coupled process parallel using the computationally inexpensive coupling calculations (Eq. (4.2), (6.11)). The predicted tool tip-SIDS transfer function along with the SIDS deflections during milling are fed to a process force estimation algorithm. For this, alternative to the utilized FRF inversion approach, a disturbance KALMAN filter design [ALBR05; POST19] can also be applied. Another conceivable approach is the use of Artificial Neural Networks (ANNs), where the predicted tool tip-SIDS FRF serves to enrich the basis of process force estimation using SIDS. Such an approach has the advantage that, model errors can be reduced by adjusting a parametric model of the transfer function in the training phase of the ANN. Similar concepts for ANN based identification of force model parameters have already been demonstrated in [KÖNI17; BREC17b; POST20; BREC20b].

In this way, process force estimates as well as tool tip FRFs for any combination of machine, operating point and tool can be obtained efficiently without having to measure FRFs for each arrangement.

The estimated process force components, F_{stat} and F_{dyn} together with the predicted tool tip FRFs give the deviation of the TCP from the ideal set point. However, deviations of the TCP path are not only due to process forces but also due to geometric and kinematic errors, thermo-elastic behavior, tool run-off, etc. These deviations are corrected in the existing WQM framework using a model-based approach. For example, the kinematic and geometric errors are removed from the actual TCP position y_{act} using a previously measured volumetric correction model [WELL19]. Similarly, temperature-dependent deviations are compensated using a previously parameterized thermo-elastic model of the machine tool spindle and structure [BREC20a]. Note that the corrected TCP position y_{corr} is usually available at a low sampling rate of the servo frequency (for e.g., 500 Hz for certain Sinumerik 840D SL controllers). On the other hand, SIDS deflections measured with independent hardware can be acquired with a much higher sampling frequency (up to 51.2 kHz). Thus, the two independent sources must be synchronized before they are superimposed to give the estimated real TCP path. The subsequent material removal simulation of the existing WQM framework generates the workpiece surface by passing a simplified end mill geometry along the real TCP path over a multi-dexel workpiece representation (refer to [BREC17c; KÖNI18] for further details). Finally, an evaluation of the virtual surface quality with respect to first order (straightness) surface errors can now be achieved. The prediction of the second order (waviness) and third order kinematic deviation (roughness) is also possible, provided that the angular location of the cutting edges is known over time along with end mill geometry, radial and axial run outs as well as high resolution axes position signals. In the present work, however, only straightness errors are considered as the above-mentioned prerequisites are not satisfied.

Clearly, the knowledge of static and dynamic behavior of the tool is central for estimating workpiece quality, especially for achieving realistic estimations of surface waviness and roughness. Within the current WQM framework, the static and dynamic behavior of each relevant milling tool is obtained experimentally at each machine. The substructuring techniques developed in this work allow for a reliable estimation of tool dynamics for various spindle-holder-end mill combinations without significant experimental and computational effort. Therefore, the integration of these methods in the virtual quality framework as shown in Figure 7.3 offers the potential to drastically reduce experimental effort and increase industrial acceptance of virtual quality undertakings.

7.3 Experimental implementation and empirical proof

Experimentelle Umsetzung und empirischer Nachweis

The goal of the experimental implementation is to empirically demonstrate the prediction of milling forces and workpiece quality using the developed substructuring and force estimation methods. For this, several simple cutting tests were conducted using ø10 and ø16 end mills. The utilized measurement and validation setup are introduced in the following.

7.3.1 Experimental setup

Messaufbau

Two down milling operations with different tool assemblies and process parameters were chosen for validation. For this, the workpiece table of MCT B was equipped with a tri-axial dynamometer from KISTLER INSTRUMENTE GMBH (Type: 9257A). A quadratic workpiece of dimensions 100 x 100 x 40 mm and material, C45 medium carbon steel (No. 1.0503) was used in the cutting trials. The measurement setup is shown in Figure 7.4 and the details of the end mill used are listed in Table 7.1.

The two consecutive cuts are conducted on the same top edge of the workpiece such that the second cut (ø10 mm end mill) passes over the surface milled from the first cut (ø16 mm end mill). Both the cuts are conducted without coolant, in the negative x-direction and within the xy-plane. With such an arrangement, a component of static and dynamic cutting force in the y-direction is expected along with the corresponding tool deflection. Since the experimental response models of MCT B have already been obtained and validated in the y-direction in Chapters 4 and 6, the prediction of process forces and tool deflection is also demonstrated in this direction. In order to clearly observe and validate the tool deflection and form error due to static process force, the milling cuts were interrupted by stopping only the feed during machining. This results in a drop of the chip load and forces, such that a notch is created on the machined surface. The depth of the notch corresponds to the static tool deflection error.

In the current version of the WQM-software, process forces are assumed to be acting on the tool tip of a rigid cylinder. Thus, only tool tip–based compliances are used for predictions for validation. However, depending on the milling conditions, the fluted segment of the end mills with helix angles allows for multiple points of contact in the axial

direction. The proposed substructuring methods for tool modelling can easily be extended to consider tool compliances at multiple axial locations. For this, the two-beam fluted segment model can be further discretized into shorter beams and the compliance response can be predicted at the ends of each beam. In this way, future versions of the WQM-software can consider multiple axial tool contact for end mills with helix angles.

Table 7.1 Details of used tool assemblies and identified model parameters

Details der verwendeten Werkzeugbaugruppen und identifizierte Modellparameter

Assly.	Holder	End mill	Over hang [mm]	No. of teeth	No. of slices	Tool dia. [mm]	d_{eff} [mm]	Fluted segment [mm]	Joint stiffness k_{xf} [N/m]	Joint damping $k_{\theta M}$ [Nm/rad]
1	HAIMER A63.140.10	FRAISA P8400450	30	4	8	10	8.5	29	$8.23x10^9$	$4.47x10^4$
2	HAIMER A63.140.16	FRAISA P8410610	58	4	8	16	12.4	55	$3.39x10^9$	$3.22x10^5$

The efficient methods for analytical response modelling and updating introduced in Chapter 5 were applied for obtaining the ARMs of tool assemblies 1 and 2. The identified effective diameters and joint parameters are also listed in Table 7.1. The Eq. (4.2) and (6.11) are applied, as usual, for coupling the analytical and experimental models to predict the tool tip-SIDS transfer functions as well as the tool tip FRFs.

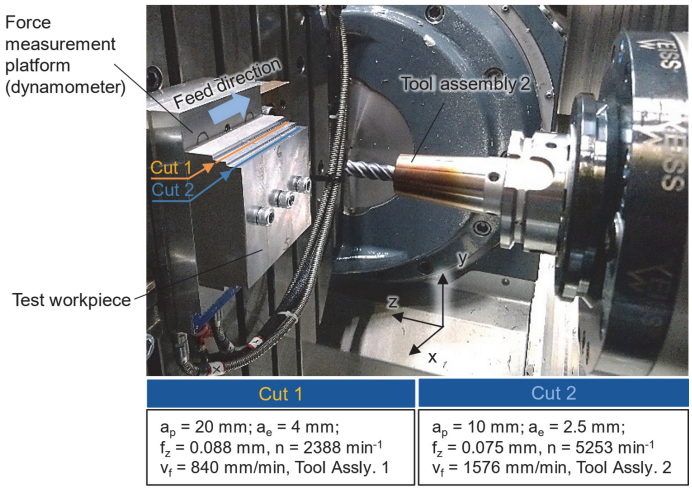

Figure 7.4 Measurement setup for milling trials at MCT B

Messaufbau für die Fräsversuche an WZM B

7.3.2 Process force estimation

Prozesskraftschätzung

In this subsection, the force estimates in the y-direction for the two milling trials are analyzed and compared to the reference force measured by the dynamometer. The period of time from the workpiece-tool engagement up to stoppage of feed for each cut is analyzed here as an example. The comparison of the estimated and measured process forces during this period is illustrated in Figure 7.5. Additionally, magnified time ranges are shown along with corresponding frequency domain transformations. In the time-plots, the static and dynamic component of the resultant milling force are clearly observable. The increasing trend of force in Cut 1 is a result of misalignment in the parallelism of the workpiece along the feed axis (x-axis). The FFTs for both cuts confirm that the tooth passing frequency is the dominant component in the dynamic process force. Apart from this, clear sidebands are observable around the tooth passing frequency but have relatively minor amplitudes. These occur at intervals corresponding to the spindle rotation frequency. For example, in case of Cut 1, the tooth passing frequency, $f_t = 159.2$ Hz represents the carrier frequency with a modulation of 39.8 Hz representing the spindle speed (2388 min^{-1}).

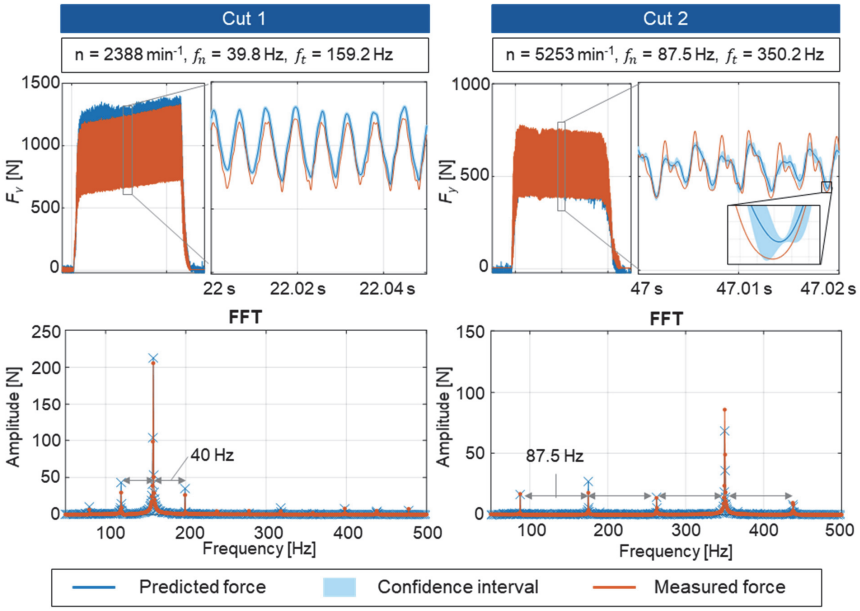

Figure 7.5 Comparison of estimated and measured process forces in y-direction

Vergleich der geschätzten und gemessenen Prozesskräfte in y*-Richtung*

Considering the force estimation for Cut 1, the magnified time range revels an acceptable match between the estimated and reference forces in y-direction. An overestima-

tion of the static force amplitude by approx. 9.6 % is observed. The inaccuracy in prediction of $\bar{H}_{58}^{STHT}$ in the quasi-static range is also of similar magnitude (refer Section 6.4) and thus it is the probable reason for the static force estimation error. Whereas the FFT comparison shows a dynamic amplitude estimation error of merely 3.4 % at f_t. The large dynamic force amplitude ensures a good SNR and thus narrow propagated confidence levels (ca. 0.4 % on the mean estimates).

In case of Cut 2, much lower static and dynamic forces are observable due to the small tool diameter and cutting conditions. Correspondingly, the propagated uncertainty shows a wider confidence interval of about 5 % on the mean force estimates. This is plausible because the 85 N of dynamic force amplitude results in poorer SNR compared to the 206 N for Cut 1. Apart from this, the FFT comparison shows an estimation error of approx. 19 % on the dynamic force amplitude at tooth passing frequency. This error is most probably due to the deviation between the predicted tool tip-SIDS FRF and actual FRF under spindle rotation. Since the predictions are based on the experimental response modelling of the stationary spindle, their validity at 5253 min^{-1} is limited. The prediction accuracy can presumably be further improved by experimental response modelling of spindle under rotation and at the corresponding spindle speed.

Although experimental and analytical modelling errors can be reduced, they are not completely avoidable. Especially for predicting the tool tip-SIDS transfer function, where, in addition to the analytical tool models, two ERMs are required: one at the spindle-holder interface and one between the interface-SIDS. The prediction is thus susceptible to three sources of modelling errors. Therefore, the use of error-tolerant approaches like the KALMAN-filter or adaptive models that utilize the predicted FRF can probably deliver more robust estimations of the process force.

7.3.3 Form error prediction

Prognose der Formabweichung

In this subsection, the surfaces milled by the Cuts 1 and 2 are analyzed with respect to their form errors (straightness) using the introduced WQM framework with inputs from the substructuring calculations. The conducted down milling operations in the x-direction cause a static deflection of the end mill such that an undercut results in the y-direction. The extent of the static deflection is reflected in the depth of the notch created by feed stoppage. This artificial feature serves to assess the virtual quality framework with the substructuring predictions.

The four main inputs required for generation of virtually milled surfaces using workpiece-tool material removal simulation are collected as follows:

i) The simplified geometry of the tool assemblies and the 3D Modell of the raw workpiece are made available to the framework as STL data.
ii) The geometric, kinematic and thermo-elastic models of MCT B are experimentally obtained in a previous step. NC-Signal data during machining is recorded and prepared such that NC-Trace instances of setups, events and measurements are available as suggested in [WELL19].

iii) Process force estimates based on SIDS deflections and the predicted tool tip-SIDS transfer function are obtained as described in the previous subsection.

iv) The updated ARMs of the two tool assemblies are coupled to the ERMs at co-ordinate *4* to predict the tool tip FRFs. The ERMs of MCT B were obtained using two adapters of 35 mm and 32 mm diameters. A combination of actuated impact hammer and a low mass accelerometer was taken as the experimental strategy.

Figure 7.6 compares the predicted tool tip FRFs with the reference FRFs measured using an impact hammer and a Doppler laser vibrometer. As seen in the amplitude and phase plots, a very good match could be achieved between the two. Since the ERM is measured using an accelerometer, the predicted displacement-to-force FRF cannot predict the static compliance. Therefore, the lowest frequency without integration distortion (30 Hz) is read out for determining static compliance. The comparison of these values with the reference static values shows good agreement and are made available to the WQM framework. Subsequently, the tool tip deflections due to static process force are calculated based on the estimated forces and corresponding predicted tool stiffness. Here, the uncertainty on the force estimation is not considered in the current version of the WQM and thus, only the mean estimated values are taken.

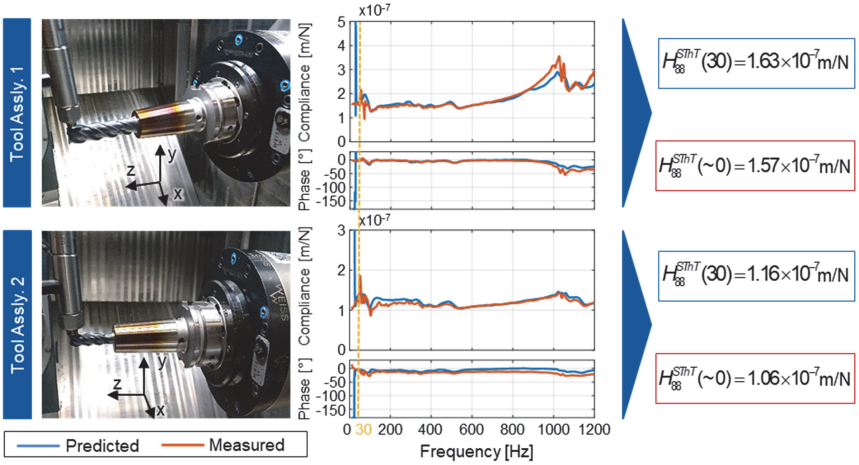

Figure 7.6 Comparison of predicted and measured tool tip FRFs

Vergleich der vorhergesagten und gemessenen FRFs an der Werkzeugspitze

Using the model-based correction of the TCP path, a cylindrical model of the tool is moved relative to a multi-dexel representation of the workpiece to subtractively generate the end contour of the milled surface. A software module representing a virtual Coordinate Measurement Machine (vCMM) then analyses the resulting point cloud. Thus, the profiles of the virtually milled surfaces of Cut 1 and 2 are analyzed for form deviations (straightness) along the x-direction as shown in Figure 7.7. In the 3D repre-

sentation of the vCMM, the surface notches created by feed stoppage are clearly visible for both cuts. Since the material removal simulation utilizes a rigid tool model, the axial location of the virtual profile measurement does not play any role.

For comparison, the surface profile is also measured with a CMM using a ø3 mm probe. Subsequently, the profile data is filtered by a spline filter with a cut-off wavelength of 1.5 mm. This is done to ensure that kinematic surface roughness (third order form deviation) is filtered out, as it is also not available in the virtual profile. A comparison of the measured and virtual straightness profiles for both cuts is also shown in Figure 7.7.

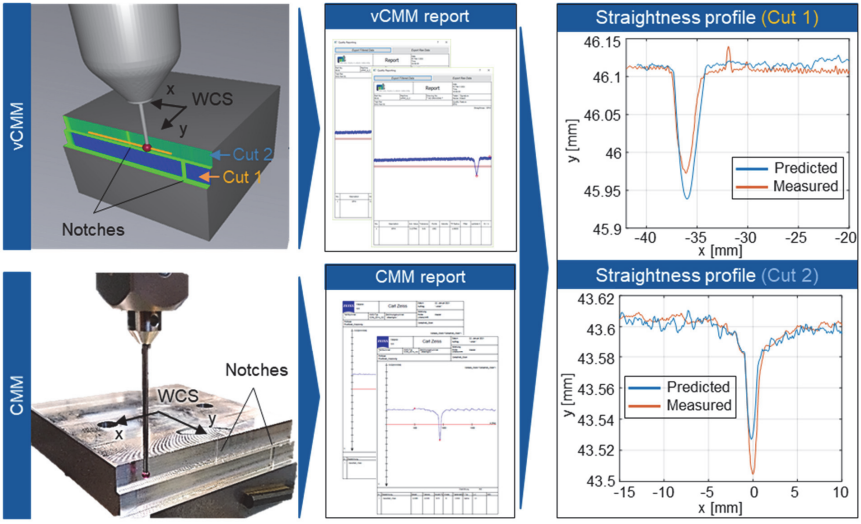

Figure 7.7 Comparison of straightness deviations from real and virtual evaluation

Vergleich der Geradheitsabweichungen aus realer und virtueller Ermittlung

In both the down milling operations, the static tool compliance and resulting deflection leads to the removal of lesser material than required. Once the feed is stopped during cutting, the cutting forces cease to exist, and the tool returns to the required position, thereby creating a notch. In both cuts, the profile and depth of the notch could be predicted with reasonable accuracy. In case of Cut 1, a slight overestimation of the depth can be observed (45.942 mm instead of 45.972 mm). Most probably, this error is due to overestimation of the static force by 9.6 % observed in Figure 7.5. However, other sources of errors in the underlying models of WQM cannot be excluded completely. This is also valid for Cut 2, where an underestimation of the notch depth is observed (43.527 mm instead of 43.506 mm).

A probable factor contributing to the error is, that the predicted FRFs are based on measurements of the adapter and spindle conducted in a stationary state. The change in the dynamic behavior of the spindle under rotation is not reflected in the predicted tool tip and tool tip-SIDS FRFs. In general, the accuracy of substructuring predictions

for WQM can be expected to improve if the ERMs are obtained for spindle under rotation. Nevertheless, a residual error in modelling is unavoidable, such that an adaptive parametric spindle model based on the FRF predictions may be more suitable for improving the accuracy of force and displacement estimations. Furthermore, the accuracy of the virtually generated surface can possibly be improved by considering a non-rigid tool cylinder in the material removal simulation instead of a rigid cylinder. The compliance at different axial positions of the tool could then be obtained by considering additional coupling planes in the ARM of the tool.

8 Summary and Outlook

Tool change in milling process represents a significant structural modification, which not only influences the process stability behavior but also the milled surface errors under stable cutting conditions. Since the measurement of the tool tip dynamics for each tool and machine combination is not feasible, an efficient prediction of the tool tip FRF is highly desirable. Additionally, the use of main spindle integrated displacement sensors for the estimation of process forces and virtual workpiece quality also requires the knowledge of the transfer function between the tool tip and the sensor unit. Thus, the efficient prediction of the spindle-holder-tool dynamics is indispensable for a variety of applications such as prediction of stability behavior, process forces, tool deflection during cutting as well as virtual surface quality.

Dynamic substructuring in the frequency domain offers a possibility for a realistic prediction of the spindle-holder-tool dynamics by coupling experimentally obtained response models of the machines with the analytical models of the holder-tool assembly. In the comprehensive and systematic analysis of the available literature, key deficits were identified, which contribute to limiting the widespread application of the frequency based tool coupling approach in industrial practice. These deficits were categorized under the aspects of experimental and analytical response modelling. Therefore, appropriate research questions were formulated in this thesis for researching substructuring methods for the reliable and efficient prediction of the tool tip as well as the tool tip-SIDS FRFs.

With the goal of obtaining high-quality ERMs, the previously unexplored aspect of using relative excitation actuators (such as piezoelectric actuators) was addressed. It was shown mathematically and practically that relative excitation can still be used to obtain the absolute vibration behavior under certain preconditions. With this background, different strategies for the measurement of displacement-to-force FRFs were implemented and systematically compared with respect to derived criteria. It was found that the use of piezoelectric actuator and accelerometer is most advantageous due to the flexible allocation of spectral energy to quasistatic frequencies, wide frequency range and low scope of bias errors.

Furthermore, two new methods for the identification of rotational compliances at the free end of an adapter are proposed: a modal parameter based and a rotational accelerometer based method. These avoid the characteristic drawback of creation of spurious poles using the complex division approach from [SCHM05]. For the use of rotational accelerometer, a method for the cancellation of inertia effects from the directly measured rotation-to-force FRFs is proposed. A comparison of the developed methods with the complex division approach showed that the modal parameter expansion approach delivered noise free estimation of the rotation-to-moment FRF using only three measured displacement-to-force FRFs. Based on the methodical comparison and analysis, the recommended applications for each method were also derived.

A major challenge in the accurate and efficient analytical tool modelling is that certain features of the tool assembly (like joint parameters) cannot practically be modeled a

priori and require additional reference measurements for their parametrization. Instead of using a FRF of the tool clamped in the machine spindle, this thesis proposes the measurement of reference FRFs in an offline, freely constrained state of the tool assembly using low mass accelerometers. This enables an accurate, economical and rapid identification process. Such model updating is realized by the proposed ETMU approach, where the ARM of the tool assembly is extended by considering the FEM based dynamics of the standard interface. Using the ETMU approach and an efficient optimization formulation, the SDE joint models of six holder-blank assemblies with different overhangs were identified. Based on the ETMU approach, a method for the identification of the effective diameter of the geometrically complex fluted tool segment is also proposed and validated for four exemplary holder-end mill assembles with different diameters, lengths, helix angles, number of teeth, tooth geometries, etc. Despite the vastly different tool assemblies, the ETMU approach could efficiently identify model parameters and predict the tool tip FRFs with good accuracy.

An important prerequisite for model updating using ETMU is the accurate modelling of different features such as balancing holes, holder taper and composite beam. For this, the TIMOSHENKO beam theory was implemented, compared and shown to be most suitable for analytical modelling. Furthermore, methods for the accurate beam modelling of holder features were developed. The structured analysis and validation of these methods offers valuable insights for the accurate tool holder modelling.

In this thesis, the tool coupling framework is extended to include the SIDS plane, such that tool tip-SIDS transfer functions can be predicted for different tools. The key enabler of the prediction is the developed experimental strategy, which delivers the required two transfer functions (H_{54}^{S} and L_{54}^{S}) between the interface and the SIDS. The strategy involves the measurement of the *H*-term using a piezoelectric actuator and an interface without the holder ('stub'). The displacement-to-moment transfer function (*L*-term), which cannot be directly measured could be identified using the developed modal parameter expansion method. Using this strategy, accurate predictions of the tool tip-SIDS transfer function could be achieved for four geometrically different holder-tool assemblies.

The statistical moments method was successfully implemented for the quantification of uncertainty due to GAUSSIAN random noise on the measured transfer functions. It was shown that for 100 repetitions of the FRF measurements, the 95 % confidence interval corresponded to about 4 - 5 % average amplitude error of the *H*-term. This was slightly lower for the directly measurable *N*-term (N_{54}^{S}), especially at the lower frequencies. The systematic propagation of the quantified uncertainties through the coupling calculations revealed that the uncertainties on the displacement-to-force FRFs strongly propagate to the predicted tool tip-SIDS transfer function ($\bar{H}_{58}^{STht}$). This implies that the careful measurement of displacement-to-force FRFs is crucial to reduce uncertainty propagation to the predictions. The derived uncertainty bounds on the amplitude and phase of the predicted transfer functions remained below 4 % of the mean values for most of the frequency range.

This thesis also demonstrates the utility of the predicted tool tip and tool tip-SIDS FRFs for the estimation of process forces and virtual workpiece quality. To this end, a method for process force estimation was developed based on SIDS deflections and the transfer function inversion technique from [BREC18b]. It was also shown how the quantified uncertainties on the FRF as well as the SIDS measurements can be propagated to the force estimates. The methodical validation confirmed the intuition that smaller dynamic deflections at the SIDS lead to greater uncertainties on the estimated forces. An accurate estimation of process forces could be achieved for different tool assemblies with stationary spindle as well as for real down milling operations. However, it was noted that for more robust prediction of the process forces, fault tolerant or adaptive models may be necessary. This is because the prediction of tool tip-SIDS FRF requires one analytical and two experimentally obtained compliance matrices (see Eq. (6.10)), which may contribute to greater residual modelling errors.

The developed substructuring methods provide two key inputs required for virtual quality undertakings for different holder-tool assemblies without significant measurement effort. These include the process force estimates and the static and dynamic tool tip compliance in the clamped state. Therefore, a possible integration of the substructuring methods with an existing WQM framework is proposed and validated. For the considered down milling operations, the form error due to tool deflection could be estimated based on the predicted FRFs of the different tool assemblies. Provided that the axes positions are available at higher temporal resolutions (not limited by servo frequency), the integrated substructuring-virtual quality framework can potentially also estimate surface waviness due to dynamic process force dependent tool deflections. This aspect can further increase the utility of the integrated framework and should be investigated and verified in future works.

Outlook

Consideration of dynamic behavior of the spindle shaft-bearing system under rotation offers potential for further improving the experimental response models. Spindle dynamics is not only influenced by the centrifugal forces but also by thermal and mechanical loads. Therefore, more research is necessary to develop methods for considering the operating-point and load dependent dynamic behavior of the spindle substructure. One possibility is the conception of an abstracted, adaptive model of the spindle-bearing system, whose parameters can be adjusted based on initial empirical trials at different operating points.

Measurement effort for experimental response modelling of the spindle substructure with SIDS may be considerably reduced if the interface as well as the interface-SIDS compliance matrices are obtained in a single measurement setup. This is imaginable if the stub interface used in this thesis is further modified, such that rotational deflections can also be measured directly at the stub using T-block or rotational accelerometers. In this way, adapter decoupling would be avoided and the same measurement setup could deliver all required dynamic compliances.

With respect to analytical modelling, the use of beam theories is convenient because detailed CAD or FEM models of the vast combinations of holders and end mills are often not available. However, it is conceivable that abstracted CAD models for many of the holder-tool combinations may be available in the future. This is indicated by the current industrial efforts towards the aggregation of CAD databanks from different manufacturers for computer-aided manufacturing simulations [CIMS22]. Thus, development efforts are required for the automated generation of FEM models from the CAD data, such that compliance matrices at different substructure coordinates can be calculated. Such an automated generation of ARMs based on the CAD data can considerably reduce modelling effort.

Another aspect that requires further research is the experimental identification of joint damping behavior for lowly damped structures. The damping effect due to microslip at the asperities between the holder and end mill surfaces could not be consistently identified using impact testing in freely constrained state. Therefore, alternate experimental strategies should be researched for the unambiguous modelling and identification of the holder-tool joint. An experimental method for the identification of damping due to microslip in bolted joints is proposed in [SANA18] and could be adjusted for the holder-tool joint.

The presented potential improvements of the substructuring methods can further increase prediction accuracy, economic utility and thus the industrial acceptance.

Zusammenfassung und Ausblick

Der Werkzeugwechsel stellt bei der Fräsbearbeitung eine wesentliche Strukturmodifikation dar, die nicht nur das Prozessstabilitätsverhalten, sondern auch die Oberflächengüte bei stabilen Schnittbedingungen beeinflusst. Da die Messung des Nachgiebigkeitsfrequenzgangs (engl.: Frequency Response Function, FRF) für jede Werkzeug- und Maschinenkombination nicht wirtschaftlich ist, ist eine effiziente Vorhersage der Werkzeugdynamik unerlässlich. Darüber hinaus erfordert der Einsatz von hauptspindelintegrierten Wegsensoren zur Abschätzung der Prozesskräfte und der virtuellen Werkstückqualität weiterhin die Kenntnis der Übertragungsfunktion zwischen Werkzeugspitze und Sensoreinheit (engl.: Spindle Integrated Displacement Sensors, SIDS). Daher bildet die effiziente Vorhersage der Spindel-Halter-Werkzeug-Dynamik bei der spanenden Bearbeitung die Grundlage für eine Vielzahl von Anwendungen wie die Vorhersage des Stabilitätsverhaltens, der Prozesskräfte sowie der virtuellen Oberflächenqualität.

Die dynamische Substrukturierung im Frequenzbereich bietet eine Möglichkeit zur realistischen Vorhersage des dynamischen Verhaltens an der Werkzeugspitze. Dies wird durch Kopplung von experimentell ermittelten Response-Modellen der Maschinen mit den analytischen Modellen der Halter-Werkzeug-Baugruppe realisiert. Bei der umfassenden und systematischen Analyse der verfügbaren Literatur wurden wesentliche Defizite identifiziert, die bisher eine breite Anwendung des frequenzbasierten Ansatzes zur Werkzeugankopplung in der industriellen Praxis einschränken. Diese Defizite wurden unter den Aspekten der experimentellen und analytischen Response-Modellierung kategorisiert. Daraus wurden zentrale Forschungsfragen abgeleitet, anhand derer Substrukturierungsmethoden für die zuverlässige Vorhersage von FRFs am Werkzeug sowie zwischen dem Werkzeug und den SIDS erforscht wurden.

Mit dem Ziel, qualitativ hochwertige experimentelle Response-Modelle (ERM) zu erhalten, wurde der bisher unerforschte Aspekt der Verwendung von Aktoren mit relativer Anregung (z. B. piezoelektrische Aktoren) untersucht. Es konnte mathematisch und praktisch gezeigt werden, dass mit relativer Anregung unter bestimmten Voraussetzungen das absolute Schwingungsverhalten errechnet werden kann. Vor diesem Hintergrund wurden verschiedene Strategien zur Messung von Weg-zu-Kraft-FRFs implementiert und systematisch hinsichtlich abgeleiteter Kriterien verglichen. Es zeigte sich, dass der Einsatz von piezoelektrischen Aktoren und Beschleunigungsaufnehmern aufgrund der flexiblen Aufteilung der spektralen Energie, des großen Frequenzbereichs und des geringen Umfangs von Bias-Fehlern am besten geeignet ist.

Darüber hinaus wurden zwei neue Methoden zur Identifikation von rotatorischen Nachgiebigkeiten am freien Ende eines Adapters erarbeitet: eine auf modalen Parametern basierende und eine auf Rotationsbeschleunigungssensoren basierende Methode. Diese vermeiden den charakteristischen Nachteil des komplexen Divisionsansatzes, welcher in [SCHM05] vorgestellt wurde. Für die Verwendung von Rotationsbeschleunigungssensoren wurde eine Methode zur Kompensation von Trägheitseffekten aus

den direkt gemessenen Rotation-zu-Kraft-FRFs erarbeitet. Ein Vergleich der entwickelten Methoden mit dem komplexen Divisionsansatz zeigte, dass die Methode der Erweiterung modaler Parameter eine Schätzung der Rotation-zu-Moment-FRF mit nur drei gemessenen translatorischen FRFs ohne Messrauschen erlaubt. Auf der Grundlage des systematischen Vergleichs und der Analyse wurden die empfohlenen Anwendungen für jede Methode abgeleitet.

Eine wesentliche Herausforderung bei der genauen und effizienten analytischen Modellierung von Werkzeugbaugruppen besteht darin, dass bestimmte Eigenschaften (z. B. Fügestellenparameter) a priori praktisch nicht modelliert werden können. Die Parametrisierung dieser Eigenschaften erfordert zusätzliche Referenzmessungen der Baugruppe. In dieser Arbeit wurden solche Referenzmessungen in Form von FRFs nicht am eingebauten Werkzeug gemessen, sondern offline im frei eingespannten Zustand. Dies ermöglichte eine präzise, wirtschaftliche und schnelle Identifikation der a priori unbekannten Eigenschaften der Werkzeugbaugruppe. Die Modellparametrierung wird durch den erarbeiteten ETMU-Ansatz (engl.: Extended Tool Model Updating) realisiert, bei dem das analytische Response-Modell (ARM) der Werkzeugbaugruppe um die Dynamik der Werkzeugschnittstelle erweitert wird.

Eine wichtige Voraussetzung für das Model-Updating mit ETMU ist die genaue Modellierung verschiedener Merkmale des Werkzeughalters wie Wuchtbohrungen, Kegelgeometrie, etc. Hierfür wurde die TIMOSHENKO-Balkentheorie umgesetzt, analysiert und mit der EULER-BERNOULLI-Balkentheorien verglichen. Die TIMOSHENKO-Balkentheorie erwies sich als am besten geeignet für das Model-Updating mit ETMU. Darüber hinaus wurden Methoden zur genauen Balkenmodellierung von Haltermerkmalen entwickelt. Die strukturierte Analyse und Validierung dieser Methoden bietet wertvolle Erkenntnisse für die korrekte Modellierung von Haltermerkmalen.

In dieser Arbeit wurde der Ansatz der Werkzeugankopplung um die SIDS-Ebene erweitert, so dass die Übertragungsfunktionen zwischen Werkzeugspitze und SIDS für verschiedene Werkzeuge vorhergesagt werden können. Dieser neue Ansatz wurde durch eine experimentelle Strategie befähigt, welche die beiden erforderlichen Übertragungsfunktionen zwischen der Werkzeugschnittstelle und dem SIDS bestimmt (H^{S}_{54} und L^{S}_{54}). Die Strategie beinhaltet die Messung des Weg-zu-Kraft-FRFs (H^{S}_{54}) mithilfe eines piezoelektrischen Aktors und einer speziellen Werkzeugschnittstelle ohne Halter. Der Weg-zu-Moment-FRF (L^{S}_{54}), welcher nicht direkt gemessen werden kann, konnte mit der entwickelten Methode der Erweiterung modaler Parameter ermittelt werden. Mit diesen Strategien konnten genaue Vorhersagen der Übertragungsfunktion zwischen Werkzeugspitze und SIDS für geometrisch unterschiedliche Halter-Werkzeug-Baugruppen erzielt werden.

Die statistische Momentenmethode wurde erfolgreich zur Quantifizierung der Unsicherheit durch das Gauß'sche Zufallsrauschen bei den Übertragungsmessungen eingesetzt. Es zeigte sich, dass bei 100 Wiederholungen der Schnittstelle-SIDS-FRF-Messungen das 95 %-Konfidenzintervall einem durchschnittlichen Amplitudenfehler

des Weg-zu-Kraft-FRFs von etwa 4 - 5 % entsprach. Dieser war für den direkt messbaren Rotation-zu-Kraft-FRF etwas geringer, insbesondere bei den niedrigeren Frequenzen. Die systematische Analyse der Unsicherheitsfortpflanzung durch die Kopplungsberechnungen zeigte, dass die Unsicherheiten der gemessenen Weg-zu-Kraft-FRFs eine stärkere Auswirkung auf die Prognose des Werkzeug-SIDS-FRFs hat. Die sorgfältige Messung von Weg-Kraft-FRFs ist daher von hoher Bedeutung, um die Unsicherheitsübertragung auf die Vorhersagen zu reduzieren. Die ermittelten Konfidenzintervalle für die Amplitude und Phase der vorhergesagten Übertragungsfunktionen blieben für die meisten Frequenzbereiche unter 4 % der Mittelwerte.

In dieser Arbeit wurde zudem der Nutzen der vorhergesagten Werkzeug- und Werkzeug-SIDS-FRFs für die Abschätzung der Prozesskräfte und der virtuellen Werkstückqualität demonstriert. Zu diesem Zweck wurde eine Methode zur Schätzung der Prozesskräfte entwickelt, die auf den SIDS-Auslenkungen und der Inversionsmethode der Übertragungsfunktion aus [BREC18b] basiert. Es konnte erfolgreich gezeigt werden, wie die quantifizierten Unsicherheiten der FRF sowie der SIDS-Messungen auf die Kraftschätzungen übertragen werden können. Die methodische Validierung bestätigte die Vermutung, dass kleinere dynamische Auslenkungen am SIDS zu größeren Unsicherheiten bei den geschätzten Kräften führen. Eine genaue Abschätzung der Prozesskräfte konnte sowohl für verschiedene Werkzeugbaugruppen mit stehender Spindel als auch für Fräsoperationen erreicht werden. Für eine noch robustere Vorhersage der Prozesskräfte sind allerdings fehlertolerante oder adaptive Modelle obligat. Dies liegt daran, dass die Vorhersage des Werkzeug-SIDS-FRF auf einer analytischen sowie auf zwei experimentell ermittelten Nachgiebigkeitsmatrizen basiert (siehe Gl. (6.10)), was zu größeren Restfehlern bei der Modellierung führen kann.

Die entwickelten Substrukturierungsmethoden bestimmen ohne hohen Messaufwand zwei wichtige Eingangsparameter, die für virtuelle Qualitätsuntersuchungen benötigt werden. Dazu gehören die Prozesskraftschätzungen auf Basis der prognostizierten Übertragungsfunktion sowie die statische und dynamische Nachgiebigkeit des Werkzeugs im eingespannten Zustand. Folglich wurde eine mögliche Integration der Substrukturierungsmethoden in ein bestehendes Rahmenwerk zur virtuellen Qualitätsüberwachung vorgestellt und validiert. Für die betrachteten Fräsoperationen konnte der abdrängungsbedingte Formfehler auf Basis der vorhergesagten FRFs der verschiedenen Werkzeugbaugruppen abgeschätzt werden. Mit einer genaueren Abbildung des Fräsers und höherer zeitlicher Auflösung der Achspositionen, kann die integrierte Substrukturierungsmethode potenziell auch die Oberflächenwelligkeit aufgrund von dynamischen, prozesskraftabhängigen Werkzeugauslenkungen bestimmen. Dieser Aspekt kann den Nutzen des integrierten Systems weiter erhöhen und sollte in zukünftigen Arbeiten untersucht und verifiziert werden.

Ausblick

Die Berücksichtigung des dynamischen Verhaltens des Spindellagersystems unter Drehzahl bietet Potenzial zur weiteren Verbesserung der ERM. Hierbei wird die Spindeldynamik nicht nur durch die Fliehkraft, sondern auch von thermo-elastischen und

mechanischen Belastungen beeinflusst. Es sind daher sind weitere Untersuchungen notwendig, um Methoden für die Betrachtung des betriebspunkt- und lastabhängigen dynamischen Verhaltens der Spindel-Substruktur zu entwickeln. Eine Möglichkeit ist die Konzeption eines abstrahierten, adaptiven Modells des Spindellagersystems, dessen Parameter auf Basis erster empirischer Versuche in verschiedenen Betriebspunkten angepasst werden können.

Der Messaufwand für die experimentelle Response-Modellierung einer Spindel-Substruktur mit SIDS kann erheblich reduziert werden, indem die Nachgiebigkeitsmatrix an der Werkzeugschnittstelle selbst sowie zwischen der Werkzeugschnittstelle und der SIDS in einem Messaufbau erfasst werden. Eine Möglichkeit stellt die Modifikation der in dieser Arbeit verwendeten Werkzeugschnittstelle (ohne Halter) dar, sodass auch rotatorische Nachgiebigkeiten direkt an der Schnittstelle mit einem T-Block oder einem Rotationsbeschleunigungssensor aufgenommen werden können. Durch Messung aller erforderlichen dynamischen Nachgiebigkeiten im selben Aufbau könnte somit eine Adapterentkopplung umgangen werden.

Im Hinblick auf die analytische Modellierung ist die Verwendung von Balkenmodellen geeignet, da detaillierte CAD- oder FEM-Modelle für die zahlreichen Kombinationen von Haltern und Fräsern oft nicht verfügbar sind. Zukünftig ist jedoch denkbar, dass abstrahierte CAD-Modelle für viele der Halter-Werkzeug-Kombinationen verfügbar sein werden. Darauf deuten die aktuellen industriellen Bestrebungen zur Zusammenführung von CAD-Datenbanken verschiedener Hersteller für die Computer-Aided-Manufacturing-Simulationen hin [CIMS22]. Somit sind Methoden zur automatischen Generierung von FEM-Modellen der Werkzeugbaugruppen aus den CAD-Daten notwendig, welche die Nachgiebigkeitsmatrizen an verschiedenen Kopplungskoordinaten liefern. Eine solche automatische Generierung von ARMs auf Basis der CAD-Daten kann den Modellierungsaufwand erheblich reduzieren.

Ein wichtiger Aspekt mit weiterem Forschungsbedarf ist die experimentelle Ermittlung der Fügestellendämpfung für das Model-Updating. Der Dämpfungseffekt durch Mikroschlupf an den Asperitäten zwischen Halter- und Schaftfräseroberflächen konnte durch Impulsanregungen im frei hängenden Zustand nicht eindeutig und wiederholbar identifiziert werden. Daher sollten für die eindeutige Modellierung und Identifizierung der Halter-Werkzeug-Verbindung andere experimentelle Strategien erforscht werden. In [SANA18] wird eine experimentelle Methode zur Ermittlung der Dämpfung aufgrund von Mikroschlupf in Schraubverbindungen vorgestellt, die für die Halter-Werkzeug-Fügestelle angepasst werden könnte.
Die vorgestellten, potenziellen Verbesserungen der Substrukturierungsmethoden können die Genauigkeit, den wirtschaftlichen Einsatz und damit die industrielle Akzeptanz weiter steigern.

9 Bibliography

Literaturverzeichnis

[ABEL10] Abele, E.; Altintas, Y.; Brecher, C.: Machine tool spindle units. In: CIRP Annals. Vol. 59, 2010. No. 2. p. 781–802.

[AHMA07] Ahmadi, K.; Ahmadian, H.: Modelling machine tool dynamics using a distributed parameter tool–holder joint interface. In: International Journal of Machine Tools and Manufacture. Vol. 47, 2007. No. 12-13. p. 1916–1928.

[ALBE13a] Albertelli, P.; Goletti, M.; Monno, M.: A new receptance coupling substructure analysis methodology to improve chatter free cutting conditions prediction. In: International Journal of Machine Tools and Manufacture. Vol. 72, 2013. p. 16–24.

[ALBE13b] Albertelli, P.; Goletti, M.; Monno, M.: An Improved Receptance Coupling Substructure Analysis to Predict Chatter Free High Speed Cutting Conditions. In: Procedia CIRP. Vol. 12, 2013. p. 19–24.

[ALBR05] Albrecht, A.; Park, S. S.; Altintas, Y.; Pritschow, G.: High frequency bandwidth cutting force measurement in milling using capacitance displacement sensors. In: International Journal of Machine Tools and Manufacture. Vol. 45, 2005. No. 9. p. 993–1008.

[ALLE20] Allen, M. S.; Rixen, D.; Seijs, M. v. d.; Tiso, P.; Abrahamsson, T.; Mayes, R.: Substructuring in Engineering Dynamics: Emerging Numerical and Experimental Techniques. Cham: Springer International Publishing AG. 2020.

[ALTI04] Altintas, Y.; Park, S. S.: Dynamic Compensation of Spindle-Integrated Force Sensors. In: CIRP Annals. Vol. 53, 2004. No. 1. p. 305–308.

[ALTI12] Altintas, Y.: Manufacturing automation. Metal cutting mechanics, machine tool vibrations, and CNC design. 2nd Ed. Cambridge: Cambridge University Press. 2012.

[ALTI92] Altintas, Y.: Prediction of Cutting Forces and Tool Breakage in Milling from Feed Drive Current Measurements. In: Journal of Engineering for Industry. Vol. 114, 1992. No. 4. p. 386–392.

[ANSI84] American National Standard. ANSI/ASA American National Standards Institute (ANSI), S2.34-1984 Part R2020 (1984). Experimental Determination of Rotational Mobility Properties and the Complete Mobility Matrix.

[ARIS04] Aristizabal-Ochoa, J. D.: Timoshenko beam-column with generalized end conditions and nonclassical modes of vibration of shear beams. In: Journal of Engineering Mechanics. Vol. 130, 2004. No. 10. p. 1151–1159.

[ASLA18] Aslan, D.; Altintas, Y.: Prediction of cutting forces in five-axis milling using feed drive current measurements. In: IEEE/ASME Transactions on Mechatronics. Vol. 23, 2018. No. 2. p. 833–844.

[BEND10] Bendat, J. S.; Piersol, A. G.: Random data - Analysis and measurement procedures. 4th Ed. Hoboken, NJ: Wiley. 2010.

[BISH11] Bishop, R. E. D.; Johnson, D. C.: The mechanics of vibration. 1st Ed. Cambridge: Cambridge Univ. Press. 2011.

[BISH55] Bishop, R. E. D.: The analysis of vibrating systems which embody beams in flexure. In: Proceedings of the Institution of Mechanical Engineers. Vol. 169, 1955. No. 1. p. 1031–1050.

[BOOS18] Boos, W.; Arntz, K.; Johannsen, L.; Prümmer, M.; Horstkotte, R.; Ganser, P.; Venek, T.; Gerretz, V.: Erfolgreich Fräsen im Werkzeugbau. URL: https://studien.werkzeugbau-akademie.de/de/unsere_studien/download [Retrieved: 01.10.2021].

[BRAV05] Bravo, U.; Altuzarra, O.; López de Lacalle, L. N.; Sánchez, J. A.; Campa, F. J.: Stability limits of milling considering the flexibility of the workpiece and the machine. In: International Journal of Machine Tools and Manufacture. Vol. 45, 2005. No. 15. p. 1669–1680.

[BREC14] Brecher, C.; Bäumler, S.; Daniels, M.: Prediction of dynamics of modified machine tool by experimental substructuring. In: Allen, M.; Mayes, R.; Rixen, D. (Ed.): Dynamics of Coupled Structures, Vol. 1. Cham: Springer International Publishing 2014. p. 297–305.

[BREC15] Brecher, C.; Daniels, M.; Wellmann, F.; Neus, S.; Epple, A.: Realisierung effizienter Zerspanprozesse. Ergebnisbericht des BMBF Verbundprojekts ReffiZ. Aachen: Shaker Verl. 2015.

[BREC16a] Brecher, C.; Chavan, P.; Fey, M.; Daniels, M.: A modal parameter approach for receptance coupling of tools. In: MM Science Journal. October 2016, No. 4. p. 1032–1034.

[BREC16b] Brecher, C.; Fey, M.; Tenbrock, C.; Daniels, M.: Multipoint constraints for modeling of machine tool dynamics. In: Journal of Manufacturing Science and Engineering. Vol. 138, 2016. No. 5.

[BREC17a] Brecher, C.; Weck, M.: Werkzeugmaschinen Fertigungssysteme 2: Konstruktion, Berechnung und messtechnische Beurteilung. 9th Ed. Berlin, Heidelberg: Springer. 2017.

[BREC17b] Brecher, C.; Wiesch, M.; Epple, A.: Entwicklung eines Kraftschätz-modells beim Fräsen. In: ZWF Zeitschrift für wirtschaftlichen Fabrikbetrieb. Vol. 112, 2017. No. 11. p. 792–796.

[BREC17c] Brecher, C.; Epple, A.; Fey, M.; Königs, M.; Neus, S.; Wellmann, F.: Lernende Produktionssysteme. Internet of Production für agile Unternehmen: AWK Aachener Werkzeugmaschinen-Kolloquium 2017. Aachen, 2017. p. 135–161.

[BREC18a] Brecher, C.; Chavan, P.; Spierling, R.; Fey, M.: A substructuring approach for simulation of time dependent workpiece dynamics during milling. In: MM Science Journal. Vol. 12, 2018. p. 2625–2632.

[BREC18b] Brecher, C.; Eckel, H.-M.; Fey, M.; Butz, F.: Prozesskraftmessung mit spindelintegrierter Sensorik. In: ZWF Zeitschrift für wirtschaftlichen Fabrikbetrieb. Vol. 113, 2018. No. 10. p. 660–663.

[BREC19a] Brecher, C.; Chavan, P.; Fey, M.: Experimentell-analytische Substrukturkopplung zur Ankopplung von Werkstücken. In: 2. VDI-Fachtagung Schwingungen 2019. Würzburg, 5th and 6th November. Düsseldorf: VDI-Verlag 2019. p. 229–240.

[BREC19b] Brecher, C.; Weck, M.: Werkzeugmaschinen Fertigungssysteme 1: Maschinenarten und Anwendungsbereiche. 9th Ed. Berlin: Springer Vieweg. 2019.

[BREC19c] Brecher, C.; Eckel, H.-M.; Motschke, T.; Fey, M.; Epple, A.: Estimation of the virtual workpiece quality by the use of a spindle-integrated process force measurement. In: CIRP Annals. Vol. 68, 2019. No. 1. p. 381–384.

[BREC20a] Brecher, C.; Spierling, R.; Wiesch, M.; Königs, M.; Fey, M.: Erweiterung der digitalen Prozesskette um das thermo-elastische Maschinenverhalten. In: ZWF Zeitschrift für wirtschaftlichen Fabrikbetrieb. Vol. 115, 2020. No. 1-2. p. 31–35.

[BREC20b] Brecher, C.; Wiesch, M.; Fey, M.: Mit datenbasierten Modellen Fräsprozesse optimieren : WZL-Forschungsergebnisse: Datengetriebene Ansätze steigern die Genauigkeit von Simulationsmodellen zum Auslegen von Fräsprozessen. In: NC-Fertigung. Vol. 41, 2020. No. 12. p. 32–33.

[BREC20c] Brecher, C.; Eckel, H.-M.; Neus, S.: Erforschung dynamischer Lagerlasten in Hauptspindeln. In: Zeitschrift für wirtschaftlichen Fabrikbetrieb. Vol. 12, 2020. No. 115. p. 920–923.

[BREC21] Brecher, C.; Chavan, P.; Fey, M.: Efficient joint identification and fluted segment modelling of shrink-fit tool assemblies by updating extended tool models. In: Production Engineering. Vol. 15, 2021. No. 1. p. 21–33.

[BREC22] Brecher, C.; Strachkov, A.; Chavan, P.; Fey, M.: Tool tip to spindle-integrated sensor transfer function prediction using receptance coupling. In: 21. ITG/GMA Fachtagung Sensoren und Messsysteme 2022.

[BUDA94] Budak, E.; Altintas, Y.: Peripheral milling conditions for improved dimensional accuracy. In: International Journal of Machine Tools and Manufacture. Vol. 34, 1994. No. 7. p. 907–918.

[BUDA96] Budak, E.; Altintas, Y.; Armarego, E. J. A.: Prediction of milling force coefficients from orthogonal cutting data. In: Journal of Manufacturing Science and Engineering. Vol. 118, 1996. No. 2. p. 216–224.

[CAKA05] Cakar, O.; Sanliturk, K.: Elimination of transducer mass loading effects from frequency response functions. In: Mechanical Systems and Signal Processing. Vol. 19, 2005. No. 1. p. 87–104.

[CAO17] Cao, H.; Zhang, X.; Chen, X.: The concept and progress of intelligent spindles: A review. In: International Journal of Machine Tools and Manufacture. Vol. 112, 2017. p. 21–52.

[CHAV20] Chavan, P.; Brecher, C.; Fey, M.; Loba, M.: Workpiece coupling in machine tools using experimental-analytical dynamic substructuring. In: Dynamic Substructures, Vol. 4. Proceedings of the 37th IMAC, a Conference and Exposition on Structural Dynamics 2019. Cham: Springer International Publishing AG 2020. p. 47–56.

[CHEN17] Cheng, K.; Niu, Z.-C.; Wang, R. C.; Rakowski, R.; Bateman, R.: Smart cutting tools and smart machining: Development approaches, and their implementation and application perspectives. In: Chinese Journal of Mechanical Engineering. Vol. 30, 2017. No. 5. p. 1162–1176.

[CIMS22] CIMSOURCE GmbH: What is ToolsUnited? URL: https://www.toolsunited.com/landingpage/en/content/ [Retrieved: 01.01.2022].

[CRAI06] Craig, R. R.; Kurdila, A.: Fundamentals of structural dynamics. 2nd Ed. Hoboken, NJ: Wiley. 2006.

[CRAI68] Craig, R. R.; Bampton, M. C. C.: Coupling of substructures for dynamic analyses. In: AIAA Journal. Vol. 6, 1968. No. 7. p. 1313–1319.

[CRAI77] Craig, R. R.: On the use of attachment modes in substructure coupling for dynamic analysis. In: 18th Structural Dynamics and Materials Conference. Reston, VA: American Institute of Aeronautics and Astronautics 1977.

[CROW84] Crowley, J.; Klosterman, A.; Rocklin, G.; Vold, H.: Direct structural modification using frequency response functions. In: Proceedings of the Second International Modal Analysis Conference 1984. p. 58–65.

[DANI17] Daniels, M.: Substrukturkopplung zur effizienten Schwingungsanalyse von Werkzeugmaschinen. Ph.D. Thesis. RWTH Aachen University, 2017.

[DENK11] Denkena, B.; Tönshoff; H. K.: Spanen: Grundlagen. 3rd Ed. Shaker Verlag, 2011.

[DENK12] Denkena, B.; Gümmer, O.: Process stabilization with an adaptronic spindle system. In: Production Engineering. Vol. 6, 2012. 4-5. p. 485–492.

[DFG21] DFG: Detailseite zu GEPRIS Projekten. URL: https://gepris.dfg.de/gepris/projekt/245846105 [Retrieved: 01.01.2022].

[DROZ18a] Drozg, A.; Rogelj, J.; Čepon, G.; Boltežar, M.: On the performance of direct piezoelectric rotational accelerometers in experimental structural dynamics. In: Measurement. Vol. 127, 2018. p. 292–298.

[DROZ18b] Drozg, A.; Čepon, G.; Boltežar, M.: Full-degrees-of-freedom frequency based substructuring. In: Mechanical Systems and Signal Processing. Vol. 98, 2018. p. 570–579.

[DUAR00] Duarte, M.; Ewins, D. J.: Rotational degrees of freedom for structural coupling analysis via finite-difference technique with residual compensation. In: Mechanical Systems and Signal Processing. Vol. 14, 2000. No. 2. p. 205–227.

[DUAR95] Duarte, M.; Ewins, D.: Some Insights into the Importance of Rotational Degrees-of-freedom and Residual Terms in Coupled Structure Analysis. In: Proceedings of SPIE - The International Society for Optical Engineering. January 1995. p. 164–170.

[DUMO16] Dumont, M.; Kinsley, N.: Using accelerometers for measuring rotational degrees-of-freedom. In: Sound and Vibration. Vol. 02, 2016. p. 11–13.

[ELLI12] Elliott, A. S.; Moorhouse, A. T.; Pavić, G.: Moment excitation and the measurement of moment mobilities. In: Journal of Sound and Vibration. Vol. 331, 2012. No. 11. p. 2499–2519.

[ERTÜ06] Ertürk, A.; Özgüven, H. N.; Budak, E.: Analytical modeling of spindle–tool dynamics on machine tools using Timoshenko beam model and receptance coupling for the prediction of tool point FRF. In: International Journal of Machine Tools and Manufacture. Vol. 46, 2006. No. 15. p. 1901–1912.

[FEY16] Fey, M.; Epple, A.; Kehne, S.; Brecher, C.: Patent application. DE 102016013890. Verfahren zur Bestimmung der Achslast auf Linear- und Rundachsen. RWTH Aachen University. Publication date: 24.05.2018.

[FEY19] Fey, M.; Brecher, C.; Eckel, H.-M.; Strachkov, A.: Patent application. DE 102019008025 A1. Verfahren zur Erfassung einer axialen Verlängerung einer rotierenden Welle relativ zu einem Gehäuse. RWTH Aachen University. Publication date: 02.06.2021.

[FILI09] Filiz, S.; Cheng, C.-H.; Powell, K. B.; Schmitz, T. L.; Ozdoganlar, O. B.: An improved tool–holder model for RCSA tool-point frequency response prediction. In: Precision Engineering. Vol. 33, 2009. No. 1. p. 26–36.

[FRAU15] Fraunhofer-Institut für Produktionstechnologie IPT: Sense4Tool – Der multisensorische Werkzeughalter. URL: https://www.ipt.fraunhofer.de/de/projekte/sense4tool.html [Retrieved: 01.02.2022].

[GASC21] Gasch, R.; Knothe, K.; Liebich, R.: Strukturdynamik. Diskrete Systeme und Kontinua. 3rd Ed. Berlin, Heidelberg: Springer Vieweg. 2021.

[GLAD64] Gladwell, G.: Branch mode analysis of vibrating systems. In: Journal of Sound and Vibration. Vol. 1, 1964. No. 1. p. 41–59.

[GUIL03] Guillaume, P.; Verboven, P.; Vanlanduit, S.; Auweraer, H. v. d.; Peeters, B.: A poly-reference implementation of the least-squares complex frequency-domain estimator. In: Proceedings of the Twenty First International Modal Analysis Conference. Vol. 2003, 2003. p. 183–192.

[HAEU21] Haeussler, M.: Modular sound & vibration engineering by substructuring. Ph.D Thesis. Technische Universität München, 2021.

[HAN99] Han, S.; Benaroya, H.; Wei, T.: Dynamics of transversely vibrating beams using four engineering theories. In: Journal of Sound and Vibration. Vol. 225, 1999. No. 5. p. 935–988.

[HOFF99] Hoffmann P., Scheer C., Zurich E., Kirchheim A., Shaffner G.: Spindle-integrated force sensors for monitoring drilling and milling processes. In: Proceedings of the 9th International Conference for Sensors, Transducers & Systems, Nürnberg, Germany. 1999. p. 18–20.

[IRVI99] Irvine, T.: Application of the Newton-Raphson Method to Vibration Problems, Vibrationdata.com. URL: https://citeseerx.ist.psu.edu/viewdoc/summary?doi=10.1.1.216.6997. [Retrieved: 01.02.2022].

[JEON02] Jeong, Y.-H.; Cho, D.-W.: Estimating cutting force from rotating and stationary feed motor currents on a milling machine. In: International Journal of Machine Tools and Manufacture. Vol. 42, 2002. No. 14. p. 1559–1566.

[JETM88] Jetmundsen, B.; Bielawa, R. L.; Flannelly, W. G.: Generalized Frequency Domain Substructure Synthesis. In: Journal of the American Helicopter Society. Vol. 33, 1988. No. 1. p. 55–64.

[JI18] Ji, Y.; Bi, Q.; Zhang, S.; Wang, Y.: A new receptance coupling substructure analysis methodology to predict tool tip dynamics. In: International Journal of Machine Tools and Manufacture. Vol. 126, 2018. p. 18–26.

[KIEN52] Kienzle, O.: Die Bestimmung von Kräften und Leistungen an spanenden Werkzeugen und Werkzeugmaschinen. In: VDI-Z. Vol. 94, 1952. No. 11. p. 299–305.

[KIM07] Kim, H. S.; Schmitz, T. L.: Bivariate uncertainty analysis for impact testing. In: Measurement Science and Technology. Vol. 18, 2007. No. 11. p. 3565–3571.

[KINS08] Kinsley, N.; Insalco, M. D.: European Patent. EP1292832B1. Piezoelectric rotational accelerometer. Kistler Holding AG. Publication date: 19.11.2008.

[KIRK06] Kirkup, L.; Frenkel, R. B.: Sampling a Gaussian distribution. In: Frenkel, B.; Kirkup, L. (Ed.): An Introduction to Uncertainty in Measurement. [Online Ed.]. Cambridge: Cambridge University Press 2006. p. 154–161.

[KIST19a] Kistler Instrumente GmbH: Dynamometers for cutting force measurement. URL: https://www.kistler.com/en/solutions/research-and-development-testing/dynamometers-for-cutting-force-measurement/stationary-dynamometer-for-measuring-cutting-forces [Retrieved: 01.06.2021].

[KIST19b] Kistler Instrumente GmbH: 4-Component Dynamometer (RCD) Rotating – for Measuring Cutting Forces on a Rotating Tool (Data Sheet). URL: https://www.kistler.com/files/document/000-995e.pdf [Retrieved: 01.06.2021].

[KIVA04] Kivanc, E. B.; Budak, E.: Structural modeling of end mills for form error and stability analysis. In: International Journal of Machine Tools and Manufacture. Vol. 44, 2004. No. 11. p. 1151–1161.

[KLER06] Klerk, D. de; Rixen, D.; Jong, J. de: The Frequency Based Substructuring (FBS) Method reformulated according to the Dual Domain Decomposition Method. In: A conference & Exposition on Structural Dynamics, IMAC XXIV. 2006. p. 1–14.

[KLER07] Klerk, D. de; Valentin, C. L.: Determination of an operating systems receptance FRF data. In: Proceedings of the Twenty Fifth International Modal Analysis Conference, Orlado, Florida. 2007. p. 1–14.

[KLER08a] Klerk, D. de; Voormeeren, S. N.: Uncertainty Propagation in Experimental Dynamic Substructuring. In: Proceedings of the Twenty Sixth International Modal Analysis Conference, Orlando, Florida. 2008.

[KLER08b] Klerk, D. de; Rixen, D. J.; Voormeeren, S. N.: General Framework for Dynamic Substructuring: History, Review and Classification of Techniques. In: AIAA Journal. Vol. 46, 2008. No. 5. p. 1169–1181.

[KLER11] Klerk, D. de: How bias errors affect experimental dynamic substructuring. In: Proulx, T. (Ed.) Structural Dynamics, Vol. 3. Conference Proceedings of the Society for Experimental Mechanics Series, New York, 2011. p. 1101–1112.

[KLOS71] Klostermann, A.: On the experimental determination and use of modal representations of dynamic characteristics. Ph.D. Thesis. University of Cincinnati, 1971.

[KÖNI17] Königs, M.; Wellmann, F.; Wiesch, M.; Epple, A.; Brecher, C.: A scalable, hybrid learning approach to process-parallel estimation of cutting forces in milling applications. In: Schmitt, R.; Schuh, G. (Ed.): 7. WGP-Jahreskongress. Aachen: Apprimus Wissenschaftsverlag 2017. p. 425-432.

[KÖNI18] Königs, M.; Brecher, C.: Process-parallel virtual quality evaluation for metal cutting in series production. In: Procedia Manufacturing. Vol. 26, 2018. p. 1087–1093.

[KOPS90] Kops, L.; Vo, D. T.: Determination of the equivalent diameter of an end mill based on its compliance. In: CIRP Annals. Vol. 39, 1990. No. 1. p. 93–96.

[KUMA12] Kumar, U. V.; Schmitz, T. L.: Spindle dynamics identification for Receptance Coupling Substructure Analysis. In: Precision Engineering. Vol. 36, 2012. No. 3. p. 435–443.

[LAW13a] Law, M.: Position-dependent dynamics and stability of machine tools. Ph.D. Thesis. University of British Columbia, 2013.

[LAW13b] Law, M.; Altintas, Y.; Phani, A. S.: Rapid evaluation and optimization of machine tools with position-dependent stability. In: International Journal of Machine Tools and Manufacture. Vol. 68, 2013. p. 81–90.

[LAW13c] Law, M.; Phani, A. S.; Altintas, Y.: Position-dependent multibody dynamic modeling of machine tools based on improved reduced order models. In: Journal of Manufacturing Science and Engineering. Vol. 135, 2013. No. 2. p. 021008.

[LIAO17] Liao, J.; Zhang, J.; Feng, P.; Yu, D.; Wu, Z.: Identification of contact stiffness of shrink-fit tool-holder joint based on fractal theory. In: The International Journal of Advanced Manufacturing Technology. Vol. 90, 2017. No. 5-8. p. 2173–2184.

[LINK14] Link, M.: Finite Elemente in der Statik und Dynamik. 4th Ed. Wiesbaden: Springer Vieweg. 2014.

[LIU99] Liu, W.; Ewins, D. J.: The Importance Assessment of RDOF in FRF Coupling Analysis, #67. In: Proceedings of the 17th International Modal Analysis Conference. Vol. 3727, 1999. p. 1481.

[MACN71] MacNeal, R. H.: A hybrid method of component mode synthesis. In: Computers & Structures. Vol. 1, 1971. No. 4. p. 581–601.

[MAIA97] Maia, N.; Silva, J.; Ribeiro, A.: Some applications of coupling/uncoupling techniques in structural dynamics Part 3: Estimation of Rotational Frequency-Response-Functions using MUM. In: Proceedings of the International Modal Analysis Conference 1997.

[MALI18] Mali, K. D.; Singru, P. M.: Study on the effect of the impact location and the type of hammer tip on the Frequency Response Function (FRF) in experimental modal analysis of rectangular plates. In: IOP Conference Series: Materials Science and Engineering. Vol. 330, 2018. p. 12102.

[MANC14] Mancisidor, I.; Urkiola, A.; Barcena, R.; Munoa, J.; Dombovari, Z.; Zatarain, M.: Receptance coupling for tool point dynamic prediction by fixed boundaries approach. In: International Journal of Machine Tools and Manufacture. Vol. 78, 2014. p. 18–29.

[MATL22] Matlab R2022a: Symbolic Math Toolbox User's Guide. URL: https://de.mathworks.com/help/pdf_doc/symbolic/symbolic_ug.pdf [Retrieved: 01.01.2022].

[MATS09] Matsubara, A.; Ibaraki, S.: Monitoring and control of cutting forces in machining processes: A review. In: International Journal of Automation Technology. Vol. 3, 2009. No. 4. p. 445–456.

[MATT16] Matthias, W.; Özşahin, O.; Altintas, Y.; Denkena, B.: Receptance coupling based algorithm for the identification of contact parameters at holder–tool interface. In: CIRP Journal of Manufacturing Science and Technology. Vol. 13, 2016. p. 37–45.

[MEGG18] Meggitt, J. W. R.: On the treatment of uncertainty in experimentally measured frequency response functions. In: Metrologia. Vol. 55, 2018. No. 6. p. 806–818.

[MEHR13] Mehrpouya, M.; Graham, E.; Park, S. S.: FRF based joint dynamics modeling and identification. In: Mechanical Systems and Signal Processing. Vol. 39, 2013. 1-2. p. 265–279.

[MILF05] Milfelner, M.; Cus, F.; Balic, J.: An overview of data acquisition system for cutting force measuring and optimization in milling. In: Journal of Materials Processing Technology. 164-165, 2005. p. 1281–1288.

[MÖHR10] Möhring, H.-C.; Litwinski, K. M.; Gümmer, O.: Process monitoring with sensory machine tool components. In: CIRP Annals. Vol. 59, 2010. No. 1. p. 383–386.

[NAMA07] Namazi, M.; Altintas, Y.; Abe, T.; Rajapakse, N.: Modeling and identification of tool holder–spindle interface dynamics. In: International Journal of Machine Tools and Manufacture. Vol. 47, 2007. No. 9. p. 1333–1341.

[ÖZŞA09] Özşahin, O.; Ertürk, A.; Özgüven, H. N.; Budak, E.: A closed-form approach for identification of dynamical contact parameters in spindle–holder–tool assemblies. In: International Journal of Machine Tools and Manufacture. Vol. 49, 2009. No. 1. p. 25–35.

[ÖZŞA10] Özşahin, O.; Özgüven, H. N.; Budak, E.: Analysis and compensation of mass loading effect of accelerometers on tool point FRF measurements for chatter stability predictions. In: International Journal of Machine Tools and Manufacture. Vol. 50, 2010. No. 6. p. 585–589.

[ÖZŞA15] Özşahin, O.; Altintas, Y.: Prediction of frequency response function (FRF) of asymmetric tools from the analytical coupling of spindle and beam models of holder and tool. In: International Journal of Machine Tools and Manufacture. Vol. 92, 2015. p. 31–40.

[PARK02] Park, S. S.; Altintas, Y.: Dynamic Compensation of Cutting Forces Measured From the Spindle Integrated Force Sensor System. In: Proceedings of IMECE2002. Vol. 2002. No. 320.

[PARK03] Park, S. S.; Altintas, Y.; Movahhedy, M.: Receptance coupling for end mills. In: International Journal of Machine Tools and Manufacture. Vol. 43, 2003. No. 9. p. 889–896.

[PARK04] Park, S. S.; Altintas, Y.: dynamic compensation of spindle integrated force sensors with Kalman filter. In: Journal of Dynamic Systems, Measurement, and Control. Vol. 126, 2004. No. 3. p. 443–452.

[PARK06] Park, S. S.: Identification of spindle integrated force sensor's transfer function for modular end mills. In: Journal of Manufacturing Science and Engineering. Vol. 128, 2006. No. 1. p. 146–153.

[PARK08] Park, S. S.; Chae, J.: Joint identification of modular tools using a novel receptance coupling method. In: The International Journal of Advanced Manufacturing Technology. Vol. 35, 2008. 11-12. p. 1251–1262.

[PCB 21] PCB Piezotronics, Inc.: Modal impact hammers. URL: https://www.pcb.com/Contentstore/mktgcontent/LinkedDocuments/Force-Torque/TM-FRC-Impact-Hammers_Lowres.pdf [Retrieved: 01.07.2021].

[PEET04] Peeters, B.; Auweraer, H. v. d.; Guillaume, P.; Leuridan, J.: The PolyMAX frequency-domain method: A new standard for modal parameter estimation? In: Shock and Vibration. Vol. 11, 2004. 3-4. p. 395–409.

[POST19] Postel, M.; Aslan, D.; Wegener, K.; Altintas, Y.: Monitoring of vibrations and cutting forces with spindle mounted vibration sensors. In: CIRP Annals. Vol. 68, 2019. No. 1. p. 413–416.

[POST20] Postel, M.: Model-supported improvement of stability limit predictions in milling through artificial neural networks. Ph.D. Thesis. ETH Zurich, 2020.

[PRO-21] Pro-micron GmbH: Spike. URL: https://www.pro-micron.de/spike [Retrieved: 01.07.2021].

[PRZE63] Przemieniecki, J. S.: Matrix structural analysis of substructures. In: AIAA Journal. Vol. 1, 1963. No. 1. p. 138–147.

[RAO06] Rao, V. S.; Rao, P.: Tool deflection compensation in peripheral milling of curved geometries. In: International Journal of Machine Tools and Manufacture. Vol. 46, 2006. No. 15. p. 2036–2043.

[REZA12] Rezaei, M. M.; Movahhedy, M. R.; Moradi, H.; Ahmadian, M. T.: Extending the inverse receptance coupling method for prediction of toolholder joint dynamics in milling. In: Journal of Manufacturing Processes. Vol. 14, 2012. No. 3. p. 199–207.

[RIDL02] Ridler M. N.; Salter, M. J.: An approach to the treatment of uncertainty in complex S-parameter measurements. In: Metrologia. Vol. 39, 2002. No. 3. p. 295–302.

[RIXE10] Rixen, D. J.: A substructuring technique based on measured and computed impulse response functions of components. In: Sas, P. (Ed.): Proceedings of ISMA 2010. Heverlee 2010. p. 1939–1954.

[RIXE11] Rixen, D. J.: Substructuring using Impulse Response Functions for Impact Analysis. In: Proulx, T. (Ed.): Structural Dynamics, Vol. 3. Conference Proceedings of the Society for Experimental Mechanics Series, New York, 2011. p. 637–646.

[ROMA94] Romanow, P.: Konstruktionsbegleitende Kalkulation von Werkzeugmaschinen. Ph.D. Thesis. Technische Universität München, 1994.

[RUBI75] Rubin, S.: Improved Component-Mode Representation for Structural Dynamic Analysis. In: AIAA Journal. Vol. 13, 1975. No. 8. p. 995–1006.

[SAAD18] Saadallah, A.; Finkeldey, F.; Morik, K.; Wiederkehr, P.: Stability prediction in milling processes using a simulation-based Machine Learning approach. In: Procedia CIRP. Vol. 72, 2018. p. 1493–1498.

[SANA18] Sanati, M.; Terashima, Y.; Shamoto, E.; Park, S. S.: Development of a new method for joint damping identification in a bolted lap joint. In: Journal of Mechanical Science and Technology. Vol. 32, 2018. No. 5. p. 1975–1983.

[SATT80] Sattinger, S. S.: Method for experimentally determining rotational mobilities of structures. In: Westinghouse-Bettis Atomic Power Lab., Pittsburgh, PA. Vol. 50, 1980.

[SCHM00] Schmitz, T. L.; Donalson, R. R.: Predicting High-Speed Machining Dynamics by Substructure Analysis. In: CIRP Annals. Vol. 49, 2000. No. 1. p. 303–308.

[SCHM01] Schmitz, T. L.; Davies, M. A.; Kennedy, M. D.: Tool point frequency response prediction for high-speed machining by RCSA. In: Journal of Manufacturing Science and Engineering. Vol. 123, 2001. No. 4. p. 700–707.

[SCHM03] Schmitz, T. L.; Burns, T. J.: Receptance coupling for high-speed machining dynamics prediction. In: International Modal Analysis Conference (IMAC XXI), Kissimmee, FL. 2003. February 3-6, 2003. p. 19.

[SCHM04] Schmitz, T. L.; Burns, T. J.; Ziegert, J. C.; Dutterer, B.; Winfough, W. R.: Tool length-dependent stability surfaces. In: Machining Science and Technology. Vol. 8, 2004. No. 3. p. 377–397.

[SCHM05] Schmitz, T. L.; Duncan, G. S.: Three-component receptance coupling substructure analysis for tool point dynamics prediction. In: Journal of Manufacturing Science and Engineering. Vol. 127, 2005. No. 4. p. 781.

[SCHM06] Schmitz, T. L.; Duncan, G. S.: Receptance coupling for dynamics prediction of assemblies with coincident neutral axes. In: Journal of Sound and Vibration. Vol. 289, 2006. 4-5. p. 1045–1065.

[SCHM07] Schmitz, T. L.; Powell, K.; Won, D.; Duncan, G. S.; Sawyer, W. G.; Ziegert, J. C.: Shrink fit tool holder connection stiffness/damping modeling for frequency response prediction in milling. In: International Journal of Machine Tools and Manufacture. Vol. 47, 2007. No. 9. p. 1368–1380.

[SCHM19] Schmitz, T.; Honeycutt, A.; Gomez, M.; Stokes, M.; Betters, E.: Multi-point coupling for tool point receptance prediction. In: Journal of Manufacturing Processes. Vol. 43, 2019. p. 2–11.

[SCIP15] Scippa, A.; Sallese, L.; Grossi, N.; Campatelli, G.: Improved dynamic compensation for accurate cutting force measurements in milling applications. In: Mechanical Systems and Signal Processing. 54-55, 2015. p. 314–324.

[SEIJ16] Seijs, M. v. d.: Experimental dynamic substructuring: Analysis and design strategies for vehicle development. Ph.D. Thesis. Delft University of Technology, 2016.

[SEMM19a] Semm, T.; Nierlich, M. B.; Zaeh, M. F.: Substructure coupling of a machine tool in arbitrary axis positions considering local linear damping models. In: Journal of Manufacturing Science and Engineering. Vol. 141, 2019. No. 7.

[SEMM19b] Semm, T.; Rebelein, C.; Zaeh, M. F.: Prediction of the position dependent dynamic behavior of a machine tool considering local damping effects. In: CIRP Journal of Manufacturing Science and Technology. Vol. 27, 2019. p. 68–77.

[SJÖV06] Sjövall, P.; McKelvey, T.; Abrahamsson, T.: Constrained state–space system identification with application to structural dynamics. In: Automatica. Vol. 42, 2006. No. 9. p. 1539–1546.

[SJÖV07a] Sjövall, P.; Abrahamsson, T.: State-space model identification for component synthesis. Modal Analysis Conference 2007. Bethel, CN.: SEM2007.

[SJÖV07b] Sjövall, P.; Abrahamsson, T.: Component system identification and state-space model synthesis. In: Mechanical Systems and Signal Processing. Vol. 21, 2007. No. 7. p. 2697–2714.

[SJÖV08] Sjövall, P.; Abrahamsson, T.: Substructure system identification from coupled system test data. In: Mechanical Systems and Signal Processing. Vol. 22, 2008. No. 1. p. 15–33.

[STRU77] Strutt, J. W.: Theory of sound. London: Macmillan Publications Co., Inc. 1877.

[SU94] Su, T.-J.; Juang, J.-N.: Substructure system identification and synthesis. In: Journal of Guidance, Control, and Dynamics. Vol. 17, 1994. No. 5. p. 1087–1095.

[TAYL07] Taylor, F. W.: On the art of cutting metals. In: American Society of Mechanical Engineers. 1907. No. 23.

[TIMO21] Timoshenko, S. P.: LXVI. On the correction for shear of the differential equation for transverse vibrations of prismatic bars. In: The London, Edinburgh, and Dublin Philosophical Magazine and Journal of Science. Vol. 41, 1921. No. 245. p. 744–746.

[TIMO22] Timoshenko, S. P.: X. On the transverse vibrations of bars of uniform cross-section. In: The London, Edinburgh, and Dublin Philosophical Magazine and Journal of Science. Vol. 43, 1922. No. 253. p. 125–131.

[TOL15] Tol, Ş.; Özgüven, H. N.: Dynamic characterization of bolted joints using FRF decoupling and optimization. In: Mechanical Systems and Signal Processing. 54-55, 2015. p. 124–138.

[TRAI20] Trainotti, F.; Haeussler, M.; Rixen, D. J.: A practical handling of measurement uncertainties in frequency based substructuring. In: Mechanical Systems and Signal Processing. Vol. 144, 2020. p. 106846.

[TSAI88] Tsai, J.-S.; Chou, Y.-F.: The identification of dynamic characteristics of a single bolt joint. In: Journal of Sound and Vibration. Vol. 125, 1988. No. 3. p. 487–502.

[TUNC18] Tunc, L. T.: Prediction of tool tip dynamics for generalized milling cutters using the 3D model of the tool body. In: The International Journal of Advanced Manufacturing Technology. Vol. 95, 2018. 5-8. p. 1891–1909.

[TUYS17] Tuysuz, O.; Altintas, Y.: Frequency domain updating of thin-walled workpiece dynamics using reduced order substructuring method in machining. In: Journal of Manufacturing Science and Engineering. Vol. 139, 2017. No. 7. p. 71013.

[VOOR10] Voormeeren, S. N.; Klerk, D. de; Rixen, D. J.: Uncertainty quantification in experimental frequency based substructuring. In: Mechanical Systems and Signal Processing. Vol. 24, 2010. No. 1. p. 106–118.

[WALL08] Wallichs, A.; Taylor, F. W.: Über Drehbarkeit und Werkzeugstähle. Berlin: Verlag von Julius Springer. 1908.

[WELL19] Wellmann, F.: Datengetriebene, kontextadaptive Produktivitätssteigerung von NC-Zerspanprozessen. Ph.D. Thesis. RWTH Aachen University, 2019.

[XI21] Xi, T.; Benincá, I. M.; Kehne, S.; Fey, M.; Brecher, C.: Tool wear monitoring in roughing and finishing processes based on machine internal data. In: The International Journal of Advanced Manufacturing Technology. Vol. 113, 2021. 11-12. p. 3543–3554.

A. Appendix

Anhang

A.1 Implementation of a tool coupling environment

Realisierung einer Werkzeugankopplungsumgebung

In this section, the validated methods for efficient experimental and analytical modelling are implemented in the form of a software called 'CouplingTools' in the Matlab environment. Thus, the software fulfills the following functions:

1. Creating ERMs
    a. Creating machine ERM based on FRFs from adapter measurements
    b. Evaluate the raw interface-SIDS force and displacement measurements to calculate the mean transfer functions along with confidence intervals
2. Creating ARMs
    a. TIMOSHENKO beam modelling of tools using an interactive Graphical User Interface (GUI) called the 'ToolBuilder'
    b. Tool model extension using ETMU approach
    c. Identification of joint stiffness using free-free reference FRFs
    d. Estimation of effective diameter of the fluted segment using free-free reference FRFs
3. Performing coupling calculations
    a. Predicting the tool tip and tool tip-SIDS FRFs with amplitude and phase uncertainty bounds
4. Loading and plotting reference FRFs

Figure A.1 shows the main Matlab-based GUI for realizing the above functions.

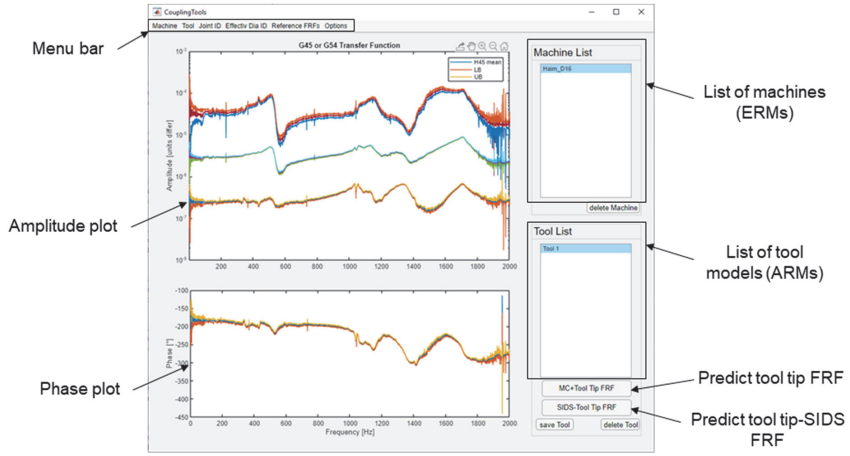

Figure A.1 Main GUI of the software CouplingTools

Haupt-GUI der Software CouplingTools

The main functionalities are accessible from the Menu bar located at the top of the GUI. An object-oriented paradigm is adopted, where the ERMs and ARMs are represented as tool and machine objects with corresponding properties and methods. Two plot axes are available for the plotting of amplitude and phase of different FRFs. A list of machines whose response models have been created based on adapter decoupling is displayed in the 'Machine List'. Similarly, a list of created ARMs of different tool assemblies is displayed in the 'Tool List'. Using the 'MC+Tool Tip FRF' button, the tool tip FRF can be predicted for the actively selected tool and machines from the lists. If the ERM of the machine in the Machine List also includes the evaluated transfer behavior between the interface and SIDS, the 'SIDS-Tool Tip FRF' button enables the prediction of the corresponding tool tip-SIDS FRF.

A.1.1 Creating ERMs

Erstellung von ERMs

Experimentally obtained FRFs of the adapter or interface-spindle substructure can be loaded and evaluated using the 'Machine' tap in the Menu bar. First, the displacement-to-force or rotation-to-force FRFs measured at the adapter are read-in and plotted using the 'Load Measurement' button in the drop-down menu (Figure A.2). With the 'Decoupling' option, the user is prompted about the method for the identification of rotational compliances as well as the dimensions and material of the adapter to be decoupled from the compliance matrix at the free end. With these inputs, the ERM of the machine at the interface flange is created and the corresponding object is created. Furthermore, the force and displacement signals for the interface-SIDS transfer function can be read-in and analyzed using the 'Load Transfer Function' option. This creates the corresponding transfer function using the proposed strategy along with the confidence intervals on the amplitude as phase.

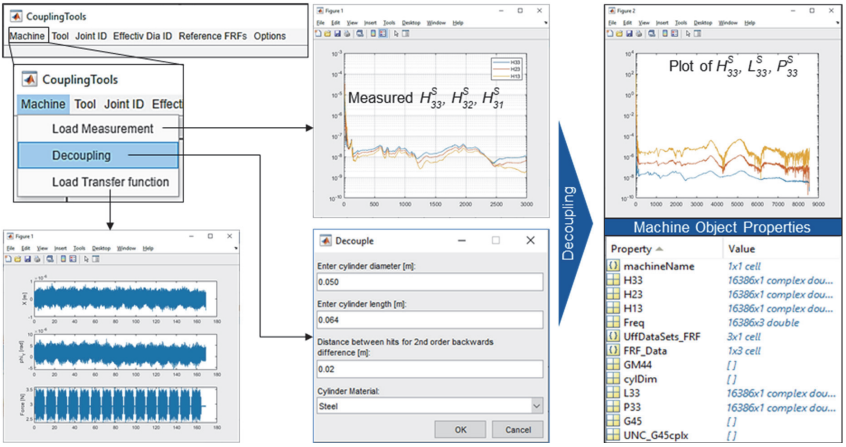

Figure A.2 Creation of the machine object using the 'Machine' menu

Erstellung des Maschinenobjekts mit dem ‚Machine'-Menu

A.1.2 Creating updated ARMs

Erstellung von ARMs und deren Parametrisierung

The ARM of new tool assembly can be created by selecting the 'Tool' option in the menu bar followed by the 'Create Tool' option in the drop-down menu. The interactive 'ToolBuilder' GUI appears in a pop-up window and shows the 2D representational plot of the normed interface along with a grid of green points (Figure A.3). For creating a slice, the button T.2 must be first clicked. With the subsequent crosshair cursor, a grid point corresponding to the length of the slice should be clicked. This then opens up a pop-up window, where the detail regarding the inner, outer diameter, material and number of sub-slices can be entered. In case of a composite beam, the inner as well as outer beam material can be specified. Thus, the tool assembly can be abstracted by creating successive slices of required geometry and material from left to right direction. If a DXF-file of the desired tool already exists, it can be imported as a template using T.1.

Once the holder-tool model is complete, the location of the balancing hole can be specified by selecting a grid point or entering the values manually. The inputs required for calculating the equivalent diameter, cross section area and area moments of inertia are entered in another pop-up window. Subsequently, a 2D representation of the balancing hole plane is plotted in the GUI and the calculated values are assigned to the tool object.

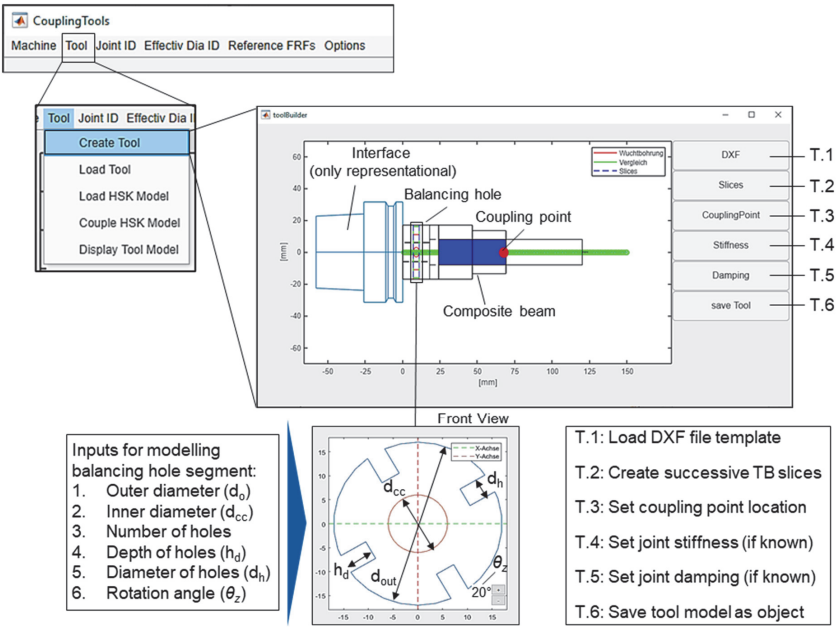

Figure A.3 Creation of the tool object using the ToolBuilder GUI

Erstellung eines Werkzeugobjekts mit ToolBuilder GUI

Furthermore, the location of the coupling point, where the joint parameters are assumed to work is specified with the T.3 button. Using T.4 and T.5, the stiffness and damping respectively can be entered if they are known a priori or roughly estimated. After all these steps, T.6 can be used to save the tool object for subsequent applications. Existing tool objects can be opened and plotted using the 'Load Tool' and 'Display Tool Model' of the drop-down menu respectively.

The free-free response model of the rigidly coupled holder-tool assembly is extended to include the interface dynamics by using the option 'Couple HSK Model'. This first requires the loading for the compliance matrix at the end of the interface obtained from the corresponding FEM model ('Load HSK Model').

The resulting extended tool assembly (interface-holder-tool) is now prepared for parameter identification. The 'Joint ID' tab of the menu bar (highlighted in Figure A.4) is dedicated to loading and evaluation of the reference free-free FRFs for joint identification. The reference FRF at the blank tip of the interface-holder-blank assembly is loaded using the 'Load H-Th-C FRF' option. Here, the letter H is used to denote the HSK interface substructure. Next, by clicking on the 'Identify Joint' option, the measured (H_{33m}^{lThC}) and the analytically obtained (H_{33}^{lThC}) blank tip FRFs are plotted such that the user can select one or multiple frequency ranges for the optimization process.

Similarly, in the 'Effectiv. Dia. ID' option loads and plots the tool tip FRF of the freely constrained interface-holder-tool assembly. Here, the analytical tool is represented by a two-segment beam.

Based on the user defined frequency ranges, the respective optimization algorithms are executed to identify joint stiffness and the effective fluted segment in two separate steps. The identified values as well as the measured FRFs are assigned to the object.

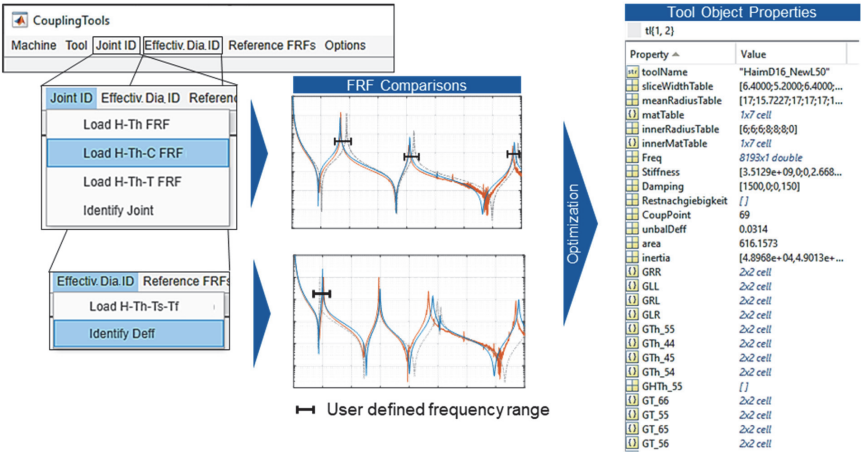

Figure A.4 Model updating of the ARM
Model-Updating des ARM

A.2 Setup for rapid free-free FRF measurement

Aufbau für die schnelle FRF-Messung im freihängenden Zustand

A simple test bench for the quick measurement of the interface-holder-tool or interface-holder-blank assembly in the freely constrained state using an actuated impact hammer is described here (Figure A.5). The tool assembly is hung from a flexible band at hooks, which can be moved along the length of the aluminum profile in x-direction. This allows for the quick hanging of tool assemblies using the drill holes of the HSK interface. An actuated impact hammer is placed on a carriage, which can be moved in the z-direction using a rack and pinion mechanism. This is necessary to enable quick adjustment of the actuation height for tool assemblies with different lengths. The base of the carriage can also be positioned along the x-direction, if required.

The test bench is designed such that the impact location always lies in the xy-plane which passes through the middle of the tool assembly. This allows for consistent and repeatable measurement of the reference FRFs required for model updating using the ETMU approach.

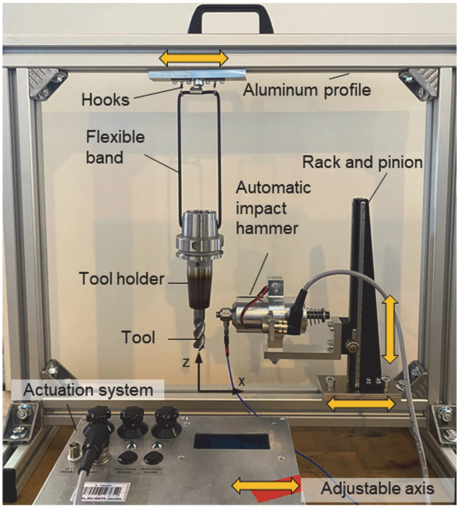

Figure A.5 Setup for quick measurement of reference FRFs for model updating

Aufbau zur schnellen Messung von Referenz-FRFs für die Modellaktualisierung